Modelling redshift-space distortion effects on spatial clustering and velocity statistics

Dissertation
zur
Erlangung des Doktorgrades (Dr. rer. nat.)
der
Mathematisch-Naturwissenschaftlichen Fakultät
der
Rheinischen Friedrich-Wilhelms-Universität Bonn

von
Joseph Kuruvilla
aus
Kottayam, Kerala, India

Bonn, August 2019

Angefertigt mit Genehmigung der Mathematisch-Naturwissenschaftlichen Fakultät der Rheinischen Friedrich-Wilhelms-Universität Bonn.

1. Gutachter:	Prof. Dr. Cristiano Porciani
2. Gutachter:	Prof. Dr. Peter Schneider
Tag der Promotion:	22.10.2019
Erscheinungsjahr:	2020

To my mom and dad

Acknowledgements

First and foremost, I would like to thank my supervisor Prof. Dr. Cristiano Porciani for his patience and guidance throughout these years. He has been extremely supportive and I very much appreciate the scientific freedom he has granted me. The regular feedback and discussions we have had helped me shape the final form of my research work. His meticulous nature and attention to details pertaining towards scientific research is something I would like to strive for in my scientific career.

I would like to thank Dr. Emilio Romano-Díaz for his constant support and for lending a patient ear to listen to me over the years. The discussions we have had related to science and computing was always enjoyable. The friendship we have formed is something I will cherish for years to come and the constant banter is something I will miss.

I am thankful to Prof. Dr. Peter Schneider for accepting to be my second supervisor. The passion and enthusiasm displayed by Peter and Cristiano during their 'cosmology' lecture is one of the main reasons that I got interested in the field of cosmology.

The constant help from our secretaries Sabine Derdau and Christina Stein-Schmitz with regards to all the administrative matters have helped me a lot over these years. I acknowledge the financial support I have received from the H2 grant of the Bonn-Cologne Graduate School (BCGS), and from the International Max Planck Research School (IMPRS) for Astronomy & Astrophysics.

I would like to acknowledge my group mates especially Dr. Enrico Garaldi for making my time with the group an enjoyable one. I would also like to thank Devina Misra for her support and for carefully reading parts of my thesis. The time in Bonn would not have been fun without my friends, especially Maitraiyee Tiwari, Gautam Ramola, Beatriz Hernandez, Ana Mikler and Hans Nguygen.

Lastly I would like to thank my parents, Kuruvilla and Molly, and my brother Austin for their support and encouragement throughout my life.

List of publications

The research projects during my PhD has lead to one peer-reviewed publication, one to be submitted and one in preparation for submission:

- (Chapter 2) **Kuruvilla, J**. and Porciani, C. (2018), *On the streaming model for redshift-space distortions*, Mon. Not. R. Astron. Soc., arXiv: 1710.09379
- (Chapter 3) **Kuruvilla, J**. and Porciani, C., *The n-point streaming model: how velocities shape correlation functions in redshift space*, To be submitted.
- (Chapter 4) **Kuruvilla, J**. and Porciani, C., *Cosmology with kSZ: using pairwise and triple-wise velocity*, In preparation.

Abstract

The nature of gravity as we know is that it pulls. Issac Newton's *Principia* generalised this gravity as a universal attractive force which weakens with distance. However in the late 1990s it was found that our Universe is undergoing an accelerated expansion, which has since then been confirmed by numerous independent cosmological probes. Thus on the scale of the Universe, we need a repulsive force. This acceleration is an unsolved puzzle which is one of the most exciting topics in cosmology. The accelerated expansion could be due to an unknown exotic component, which has been christened as the 'dark energy', or it could be that on the large scales there is a breakdown of our understanding of the gravitational theory. One of the observational methods through which we can test the theory of gravity at those scales is known as 'redshift-space distortions' (RSD), which is the main topic of this thesis. To probe the three-dimensional distribution of galaxies in the Universe, we require the redshift as the radial distance indicator in addition to the two-dimensional angular position in the sky. The recession velocity of any galaxy is proportional to the distance from us according to the Hubble expansion law. However the observed velocity has an additional contribution from peculiar velocities. These are generated due to the clustering dynamics and thus contaminate the distance information. Thus RSD causes a change in the clustering pattern as compared to the actual galaxy distribution.

The main aim of this thesis is to model the n-point spatial clustering statistics in redshift-space faithfully. The main motivation factor in undertaking this task is that the future redshift surveys will offer us an influx of (big) data as never seen before. For example *LSST* is poised to produce about 20 terabytes of raw data per night and about 60 petabytes of data during its operation period. However to take advantage of this plethora of data, we need accurate theoretical models.

In chapter 2, we focus on the two-point clustering information. The state-of-the-art constraints on the gravitational theory based on RSD come from the so called 'Gaussian streaming model' (GSM). We find that the success of the GSM appears to be fortuitous. We improve upon this by introducing the 'generalised hyperbolic streaming model', which we showcase to work extremely well at non-linear scales and does not have to rely on any fortuitous cancellations. The future redshift surveys will be able to measure higher-order correlation functions precisely. In light of this we develop the exact n-point streaming model in chapter 3. We also introduce a phenomenological model based on the GSM tailored for three-point clustering information in redshift space, in which all the ingredients were taken from the linear perturbation theory. This paves way for extracting the cosmological information from higher-order clustering statistics in a precise manner.

We also look at the effect of RSD on pairwise velocity statistics measured from the kinetic Sunyaev-Zeldovich effect in chapter 4, which will be measured precisely in future cosmic microwave background (CMB) experiments. We see that the mean pairwise velocity in redshift space undergoes a sign inversion and this comes about from the 'Finger-of-God' (FoG) effect. We also explore the effects of RSD on the three-point velocity statistics and further construct an estimator which is ideal to extract the cosmological parameters.

Contents

CHAPTER 1

Introduction

Cosmology is the scientific study of the origin, evolution, and fate of the Universe. Based on several observational evidences, the current standard cosmological model is the ΛCDM model. The name indicates its two main components: CDM stands for cold dark matter and Λ refers to the cosmological constant, which is a description of the dark energy (DE) that is used to explain the accelerated expansion of the Universe. According to the current consensus, the Universe is made up of 68% DE, and 27% dark matter. All the (baryonic) matter (such as atoms, chemical elements, plasma, gas, etc) we understand only accounts for about 5%. Thus we have an incomplete knowledge in many facets of the Universe, wherein what we understand is largely dwarfed by what is unknown to us. The ΛCDM model describes a dynamic universe with a flat spatial geometry. In this scenario, the Universe is thought to have undergone an early phase of exponential expansion known as inflation (Guth, 1981).

One of the current objectives of ongoing and future cosmological surveys is to obtain a better understanding of these components, especially the nature of DE and DM. However, one of the main things that sets the field of cosmology apart from other scientific fields is the fact that we only have one Universe that we can observe. This implies that what we deduce from our Universe can neither be repeated nor tested in another universe.

This chapter is divided into six different sections, in which we try introduce various concepts in the field of cosmology. In section 1.1, we begin with the description of our Universe by considering it in the isotropic and homogeneous limit. Starting from Friedmann-Lemaître-Robertson-Walker metric, we introduce the Friedmann equations and describe the time dependence for a given density component. We also introduce the concept of redshift which will be needed further on. Section 1.2 deals with a brief review about the thermal history of the Universe starting from the phase of big bang till the epoch of recombination. Furthermore we introduce the kinetic Sunyaev-Zeldovich effect which is a secondary anisotropy of the cosmic microwave background which we will discuss further in chapter 4. We introduce perturbations to the expanding background in section 1.3 and describe it using linear perturbation theory. However as the perturbations become highly non-linear, the analytical prescription is insufficient to describe it faithfully and hence the need of N-body simulations arises which we discuss in section 1.4. To describe these perturbations in a statistical manner, we introduce the two-point and three-point correlation function as well its Fourier pairs in section 1.5. We have mentioned that our Universe is isotropic, however the observed correlation function and power spectrum showcase anisotropy. The nature and the origin of this anisotropy in the observed field, which has matured into a useful probe the right theory of gravity, is further discussed in section 1.6.

1.1 The Homogeneous Universe

There has been considerable effort to understand the large-scale structure in our Universe. We believe that the gravitational force is the underlying force that governs the cosmic evolution, as the Universe is immense in size and neutral in charge. One of the fundamental assumptions in modern cosmology is that the Universe is isotropic and homogeneous on large scales. Isotropy implies that there are no special directions, and homogeneous means that there are no special places. This central tenet is known as the 'cosmological principle'. In other words, the Universe on average looks the same from any point. This is motivated from the Copernican argument that the Earth is neither a central nor a preferred position. The universe on small scales however is characterised by inhomogeneities, only when averaged over large scales the distribution of galaxies appears to be nearly homogeneous. Evidences for the isotropy and homogeneity can be seen in the early Universe as observed in measurements from the cosmic microwave background radiation (CMB) surveys and in the late Universe from galaxy redshift surveys like the 'Sloan Digital Sky Survey' (SDSS) which showed that the Universe is indeed homogeneous on scales larger than 70 h^{-1} Mpc (Yadav et al., 2005; P. Sarkar et al., 2009; Pandey and S. Sarkar, 2015). This motivates us to consider a homogeneous and isotropic model. This model gives the simplest solution of equations to the general relativity (GR) and lead to what is now known as the Friedmann-Lemaître-Robertson-Walker (FLRW) model which we explain in the below section.

1.1.1 Friedmann-Lemaître-Robertson-Walker metric

Einstein's field equations describe the gravitational effects produced by a given mass in general relativity and is given as

$$G_{\mu\nu} + \Lambda g_{\mu\nu} = \frac{8\pi G}{c^4} T_{\mu\nu}\,, \tag{1.1}$$

where c is the speed of light, $G_{\mu\nu}$ is the Einstein tensor, Λ is the cosmological constant which is proportional to the vacuum energy density, $g_{\mu\nu}$ is the metric tensor, G is Newton's gravitational constant, and $T_{\mu\nu}$ is the stress-energy tensor. The expression on the left hand side represents the curvature of spacetime as determined by the metric and the expression on the right hand side represents the matter/energy content of spacetime. The cosmological constant is of interest as it could provide a possible explanation for the dark energy.

As a result of the cosmological principle, we assume that there exists a set of 'fundamental observers' who follow the mean motion of matter and radiation in the universe. For such an idealised universe, as shown by Alexander Friedmann, Georges Lemaître, Howard P. Robertson and Arthur G. Walker independently, it is possible to define a metric as

$$\mathrm{d}s^2 = c^2\mathrm{d}t^2 - a(t)^2\left[\mathrm{d}\chi^2 + f_k^2(\chi)\left(\mathrm{d}\theta^2 + \sin^2\theta\,\mathrm{d}\phi^2\right)\right]\,, \tag{1.2}$$

where t is the cosmic time, θ and ϕ are the angular coordinates on a unit sphere, and $a(t)$ is the cosmic scale factor. The scale factor describes how distances expand or contract with time. This factor is normalized to $a(t_0) = 1$ for the present-day. Given that χ is the comoving radial coordinate, $f_k(\chi)$ is the comoving angular diameter distance that depends on the curvature parameter, k, given as

$$f_k(\chi) = \begin{cases} \sin(\sqrt{k}\chi)/\sqrt{k} & (k > 0) \\ \chi & (k = 0) \\ \sinh(\sqrt{-k}\chi)/\sqrt{-k} & (k < 0) \end{cases} . \tag{1.3}$$

From the cosmological observations we believe that $k = 0$, which corresponds to a flat universe and hence $f_k(\chi) = \chi$.

1.1.2 Friedmann equations

The FLRW metric is an exact solution of the Einstein's field equations. Assuming the cosmic fluid to be a perfect fluid and inserting the FLRW metric as given in equation (1.2) and into Einstein's field equations one obtains the so called Friedmann equations

$$\frac{\ddot{a}}{a} = -\frac{4\pi G}{3}\left(\rho + \frac{3p}{c^2}\right) + \frac{\Lambda}{3}\,, \tag{1.4}$$

$$\left(\frac{\dot{a}}{a}\right)^2 = \frac{8\pi G\rho}{3} - \frac{kc^2}{a^2} + \frac{\Lambda}{3}\,, \tag{1.5}$$

where ρ is the mass density, p is the pressure, and $a \equiv a(t)$. The Hubble parameter, or expansion rate is given by

$$H(t) = \frac{\dot{a}}{a}\,. \tag{1.6}$$

The symbol H_0 refers to the present rate of expansion and is often parameterised as $H_0 = 100\,h\,\mathrm{km\,s^{-1}\,Mpc^{-1}}$, where h is a dimensionless factor of order unity.

There are three main components in the universe: pressure-less matter, radiation and vacuum energy. The different species among matter and radiation in the early Universe are

$$\underbrace{\text{photons}\,(\gamma)\quad \text{neutrinos}\,(\nu)}_{\text{radiation (r)}} \qquad \overbrace{\underbrace{\text{electrons}\,(e)\quad \text{photons}\,(p)}_{\text{baryons (b)}}\quad \text{cold dark matter (cdm)}}^{\text{matter (m)}}\,.$$

Dark matter (DM) is the most dominant matter component. It is a hypothetical form of matter, thought to be non-baryonic in nature as can be seen from the classification above. There are two main supporting evidences to believe they are non-baryonic. Firstly that the CMB would have looked completely different if DM was composed of baryons (Peebles, 1982). Secondly the abundance of elements created during big-bang nucleosynthesis depends strongly on the baryon-to-photon ratio. In the standard model, DM moves at non-relativistic speed ($v \ll c$) and hence named as 'cold'. DM is considered dark because it weakly interacts, if at all, with electromagnetic radiation and is thus invisible to the entire electromagnetic spectrum. This renders the direct detection of DM extremely difficult. However there are various ongoing experiments to have a direct detection of DM (Schumann, 2019). Currently the evidences supporting the DM paradigm come from indirect indications based on the observation of gravitational effects. The pioneering work from Zwicky, 1933 measured the velocity dispersion of galaxies in the Coma cluster and found that they exceeded the expectation from considering only luminous matter. This was further substantiated by measuring the rotational

curves of spiral galaxies, where the observed rotational velocity, v_r, did not follow the Keplerian law $v_r \propto r^{-\frac{1}{2}}$ (e.g. Babcock, 1939; Rubin and Ford, 1970; Rubin, Ford and Thonnard, 1980). Further empirical evidence comes from the X-ray (A. D. Lewis, Buote and Stocke, 2003), gravitational lensing observations (Tyson, Kochanski and Dell'Antonio, 1998; Refregier, 2003), and the bullet cluster being an iconic example (Clowe et al., 2006). For more details on gravitational probes of DM, we refer the reader to Peter, 2012, and Buckley and Peter, 2018.

As mentioned earlier, from the CMB and the big bang nucleosynthesis we know that the baryonic matter constitutes about 5% of the total content in the Universe. However from the global baryon consensus at low redshift Universe, it is evident that there is a deficit of baryons (Fukugita, Hogan and Peebles, 1998). Galaxy surveys have shown that only about 10% of these baryons are in collapsed objects (Fukugita and Peebles, 2004) and roughly 50% have been accounted for in the intergalactic medium (Danforth and Shull, 2008). According to the latest picture, roughly 30% of the baryons are missing (Shull, B. D. Smith and Danforth, 2012), which is now known as the 'missing baryon problem'.

The accelerated expansion of the Universe has been one of the fascinating discoveries in the recent times. The interpretation of accelerated expansion was first facilitated by the measurement of supernova luminosity as a function of redshift (Riess, Filippenko et al., 1998; Perlmutter et al., 1999). This picture of accelerated expansion is strengthened by a plethora of other observations including CMB anisotropies (Larson et al., 2011; Planck Collaboration, Akrami et al., 2018), galaxy surveys (Alam, Albareti et al., 2015), and weak gravitational lensing (Schneider, 2005) among others. Dark energy is an unknown form of energy which could explain the accelerated expansion of the Universe. It mimics a negative and replusive pressure, which behaves opposite to gravity. The cosmological constant provides the simplest possible explanation for dark energy phenomena. One of the main objectives of future redshift surveys is to address the nature of dark energy (Weinberg et al., 2013).

To determine the time dependence of the density of these components, one employs the first law of thermodynamics which is given in the present context as

$$\mathrm{d}(\rho c^2 a^3) = -p\mathrm{d}a^3 \,. \tag{1.7}$$

In the case of pressureless matter, $p = 0$, equation (1.7) gives

$$\rho_{\mathrm{m}}(t) = \rho_{\mathrm{m}0} a^{-3}(t) \,, \tag{1.8}$$

where the subscript '0' indicates the value at the present time. Similarly for the case of radiation, one would get $\rho_{\mathrm{r}}(t) = \rho_{\mathrm{r}0} a^{-4}(t)$ and for vacuum energy it is given as $\rho_\Lambda = \rho_{\Lambda 0}$. The total density and pressure are given as the sum of these three components

$$\begin{aligned} \rho(t) &= \rho_{\mathrm{m}}(t) + \rho_{\mathrm{r}}(t) + \rho_\Lambda(t) \,, \\ p &= \frac{\rho_r c^2}{3} - \rho_\Lambda c^2 \,. \end{aligned} \tag{1.9}$$

The matter content of the Universe can be expressed in terms of the critical density

$$\rho_{\mathrm{crit}} = \frac{3H_0^2}{8\pi G} \approx 1.88 \times 10^{-29}\, h^2\, \mathrm{g/cm^3} \,. \tag{1.10}$$

A universe with density above this critical value will have $k > 0$, whereas a lower density one will have $k < 0$. This characteristic density is used to scale the matter densities by defining the density parameters

$$\Omega_{\rm m} = \frac{\rho_{\rm m}}{\rho_{\rm crit}}; \quad \Omega_{\rm r} = \frac{\rho_{\rm r}}{\rho_{\rm crit}}; \quad \Omega_{\Lambda} = \frac{\rho_{\Lambda}}{\rho_{\rm crit}} \,. \tag{1.11}$$

Making use of equations (1.9) and (1.11), the expansion equation (1.5) can be written as

$$H^2 = H_0^2 \left[\frac{\Omega_{\rm r0}}{a^4} + \frac{\Omega_{\rm m0}}{a^3} + \frac{(1 - \Omega_{\rm tot})}{a^2} + \Omega_{\Lambda 0} \right] , \tag{1.12}$$

where the subscript '0' indicates the density parameter value at present time and $\Omega_{\rm tot} = \Omega_{\rm r0} + \Omega_{\rm m0} + \Omega_{\Lambda 0}$ is defined as the total density parameter of the present-day universe. If we are able to measure the density parameters, we can describe the past, present, and future evolution of the universe.

1.1.3 Cosmological redshift

Light rays follow null geodesics, implying that for them $\mathrm{d}s^2 = 0$. For radial light rays ($\mathrm{d}\theta = \mathrm{d}\phi = 0$), we find that $c^2\mathrm{d}t^2 = a(t)^2\mathrm{d}\chi^2$ and for radial rays which arrive at the observer at the origin of the coordinate system we find

$$c\,\mathrm{d}t = -a(t)\,\mathrm{d}\chi \,, \tag{1.13}$$

which can be integrated to yield the radial coordinate as a function of cosmic time, with $\chi(t_0) = 0$,

$$\chi(t) = \int_t^{t_0} \frac{c\,\mathrm{d}t'}{a(t')} \,. \tag{1.14}$$

As a result of the expansion of the universe, the photons are redshifted. We can define the redshift z as

$$1 + z = \frac{\nu_{\rm em}}{\nu_{\rm obs}} = \frac{a(t_0)}{a(t)} \,, \tag{1.15}$$

where $\nu_{\rm em}$ is the frequency of the photon at the time of emission and $\nu_{\rm obs}$ is the frequency of the photon at the time of observation. Thus redshift is directly related to the expansion factor of the Universe. The photons we observe coming from a comoving source are all redshifted, provided that the scale factor was smaller than unity in the past. In the nearby Universe ($z < 0.1$), however the effects of expansion are minimal and the observed redshifts are dominated by peculiar motions of the galaxies.

1.2 Thermal history of the Universe

The origin of the Universe is an intriguing question which we often like to ask. This curiosity has found its way in many facets of philosophy, theology, and science. In our current scientific understanding, the Universe started with a 'big bang', a term which has become synonymous with the standard model of modern cosmology. Although the term implies that the Universe originated with a giant explosion, it is a misnomer. The big bang theory suggests that space itself expanded, rather than something exploding originating from a point in space. The origin of the term big bang also has an interesting history. In the late 1940s, there were two major schools of thought regarding the evolution of the

Universe. One school prescribed to the fact that the Universe originated and expanded from a very high-density and high-temperature state which is what we know as the 'big bang' model. The other school supported the idea that the Universe is always expanding but maintains a constant average density, in which it has no beginning or end. This is commonly known as the 'steady state' model. Some of the most influential cosmologists of that period including Hermann Bondi, Thomas Gold, and Fred Hoyle worked on steady state model and are accredited as the founders of this model (Bondi and Gold, 1948; Hoyle, 1948). Ironically, the term 'big bang' was coined by Fred Hoyle as pejorative term to make fun of an exploding Universe during a BBC radio show in 1949. While catchy, the term did not take off right away. It was revived again in late 1960s by Jim Peebles and cemented in the early 70s with two notable cosmology textbooks: Peebles' *Physical Cosmology* and Dennis Sciama's *Modern Cosmology*. For a more detailed history, the reader may refer to Kragh, 2013.

To give a brief thermal history of the Universe according to the standard model of cosmology, everything started from a high-density and high-temperature state around 13.8 billion years ago. We know that the CMB photons we observe today have been redshifted and should have been more energetic in the past. Its temperature at any epoch can be written down as $T(z) = T_0(1+z)$, where T_0 is the present temperature and is equal to 2.73 K. To understand the thermal history, the comparison between the interaction rate Γ with which particles interact and the expansion rate H is important. When the rate of interaction is greater than rate of expansion, thermal equilibrium is attained. As the Universe expands and cools, it might deviate from the thermal equilibrium and the particles will decouple from the thermal bath. Different species of particles may have different interaction and hence decouple at different epochs. If the equilibrium had been maintained until today, the Universe would have been mostly photons. Thus it is important to understand the deviations from equilibrium that led to freeze-out (after the epoch when $\Gamma = H$, the interactions become very unlikely and they cease to be in contact with other species). Neutrino is one of the first particle species to freeze-out when the Universe was about 1 second old ($z = 6 \cdot 10^9$), which corresponds to a decoupling temperature of about 1 MeV[1]. Shortly after this, as the Universe cools further, electrons and positrons annihilate

$$e^+ + e^- \rightarrow \gamma + \gamma \,. \tag{1.16}$$

This happens when the age of the Universe was about 6 seconds ($z = 2 \cdot 10^9$) and correspondingly the decoupling temperature was about 500 keV. The energy from the annihilation was injected to the photons and not to neutrinos as they had decoupled from the thermal bath already. This is the reason why the neutrino temperature we observe today is less than of the photons. The relation between the two temperatures is

$$T_\gamma = 1.4\, T_\nu \,, \tag{1.17}$$

where T_γ is the photon temperature and T_ν is the neutrino temperature. The present cosmic neutrino background has therefore a temperature, $T_{\nu 0} = 1.95$ K $= 0.17$ meV. Neutrino oscillation experiments have shown that it has a non-zero mass, hence they are non-relativistic today. Thus they behave as matter-like particles in the late Universe and radiation-like in the early epochs. As the Universe expanded and when it was around 3 minutes old ($z = 4 \cdot 10^8$), light atomic nuclei like hydrogen, helium and lithium were formed. This epoch is known as the 'big bang nucleosynthesis' (BBN, for a more detailed review see Steigman, 2007; Cyburt et al., 2016; Mathews, Kusakabe and Kajino, 2017). Finally as the Universe cooled down to temperature around 0.3 eV, which corresponds to

[1] 1 MeV $\approx 10^{10}$ K

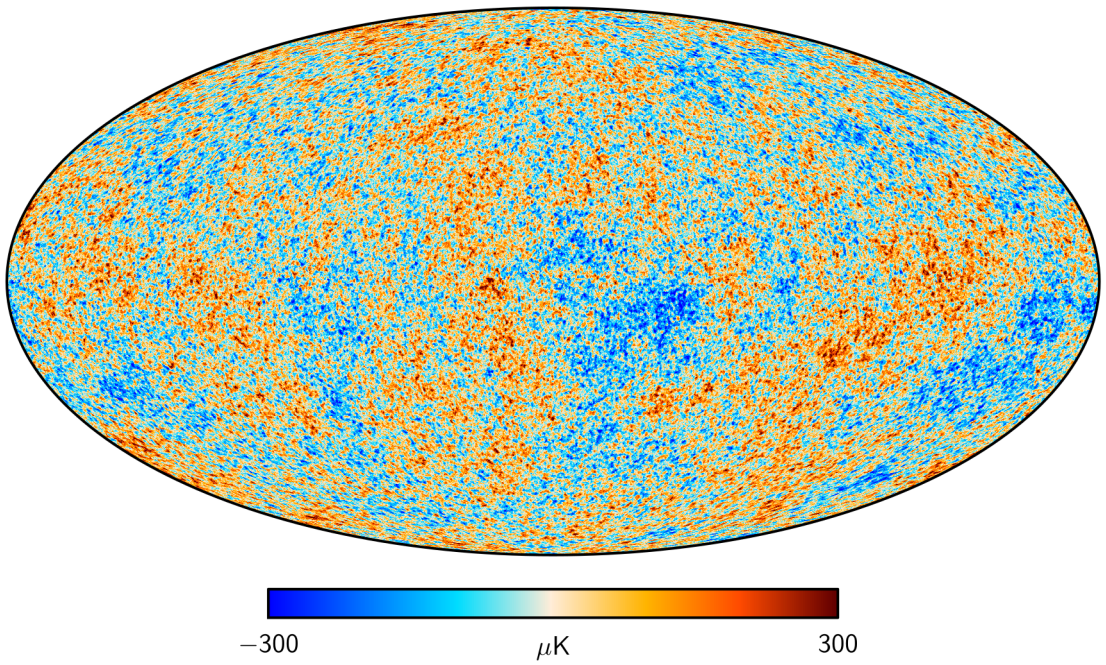

Figure 1.1: The leftover glow from the big bang, depicts the Universe when it was roughly 380,000 years old. A full sky map of the CMB as obtained from the *Planck* survey (Planck Collaboration, Akrami et al., 2018).

an epoch when the Universe was 380,000 years old and $z \sim 1100$, the atomic nuclei and electrons combined to form the neutral atoms. This epoch is commonly referred to as 'recombination'. Prior to recombination, the photons were coupled to the rest of the plasma through Thomson scattering ($e^- + \gamma \rightarrow e^- + \gamma$), which implies that the Universe was optically thick before this phase and we cannot observe the Universe prior to this as the information (photon) was not able to escape. However the sudden decrease in the free electron density as a result of the recombination implies that the scattering process turns out to be inefficient and the photons decouple at $z \sim 1100$. Today these photons are the CMB, which can be seen from experiments like *WMAP* (Larson et al., 2011) and *Planck* (Planck Collaboration, Akrami et al., 2018). Thus they provide us with a picture of how our Universe looked like when it was 380,000 years old[2]. The temperature fluctuation anisotropy as seen by Planck is shown in figure 1.1.

The fluctuations which originated at the epoch of recombination (at the surface of last scattering) are called 'primary anisotropies'. These CMB photons are again affected by a number of distortions along their way to us and are called 'secondary anisotropies'. In other words, all temperature fluctuations in the CMB generated since the epoch of matter-radiation decoupling at $z \sim 1100$. On small angular separation scales, these secondary effects are the dominant source of anisotropy and have the potential

[2] Light travels roughly 30 cm per nanosecond. So if you are reading this (on a screen or paper) 30 cm away from your face, you are seeing the screen/paper as it was about a nanosecond (10^{-9} s) ago. Everything we see, in essence, is in the past. We are seeing the moon as it was about one second ago. Light from our Sun takes about eight minutes to reach us and thus we are seeing it as it was eight minutes ago. We see the center of our own Galaxy as it was 26,000 years ago and the nearest galaxy to us, the Andromeda galaxy, as it was 2.5 million years ago. Thus when we look further out in the Universe, we are probing the shells of cosmic time. The CMB provides us with the farthest shell of cosmic time we can observe with electromagnetic waves.

to reveal intricate details about the history of our universe between the present and recombination epochs. Among the various secondary anisotropies that exist, we will focus on one of them, the so called kinetic Sunyaev-Zeldovich effect in this thesis and explain it below.

1.2.1 Sunyaev-Zeldovich effect

One of the best studied secondary CMB anisotropies is the Sunyaev-Zeldovich (SZ) effect (Sunyaev and Zeldovich, 1970; Sunyaev and Zeldovich, 1972; Sunyaev and Zeldovich, 1980). CMB photons interact with the free electrons of a hot ionised gas along the line-of-sight and causes a change in the apparent temperature of the CMB. This happens as a result of the inverse Compton scattering, in which if an electron has a significantly higher kinetic energy than photons, then the energy is transferred from electrons to resulting scattered photons. An important result is that the intensity change caused by the SZ effect is redshift-independent, depending only on intrinsic properties of the scattering medium and is therefore a remarkably robust indicator of gas properties at a wide range of redshifts. In this work, we focus on a secondary effect to this known as the kinetic Sunyaev-Zeldovich (kSZ) which arises if the scattering medium is moving relative to the Hubble flow. Galaxy clusters provide localised concentrations of free electrons and thus kSZ allows us to measure the cluster velocity directly. The fractional temperature fluctuation caused due to kSZ is

$$\begin{aligned}\left.\frac{\Delta T(\hat{n})}{T_{\rm cmb}}\right|_{\rm kSZ} &= -\int {\rm d}l\ \sigma_{\rm T}\left(\frac{\boldsymbol{v}_{\rm e}\cdot\hat{n}}{c}\right) n_{\rm e}\,, \\ &= -\tau\left(\frac{\boldsymbol{v}_{\rm e}\cdot\hat{n}}{c}\right)\,, \end{aligned} \tag{1.18}$$

where $\sigma_{\rm T}$ is the Thomson scattering cross-section, $T_{\rm cmb}$ is the CMB temperature, c is the speed of light, $\boldsymbol{v}_{\rm e}$ is the peculiar velocity of free electrons, and $n_{\rm e}$ is the physical free electron number density. The integral $\int {\rm d}l$ is computed along the line-of-sight (los) which is given by $\hat{n}$. The optical depth is defined as $\tau = \int {\rm d}l\ \sigma_{\rm T}\ n_{\rm e}$, i.e. the integrated electron density. The optical depth depends on various properties of the DM halo hosting the galaxy cluster, such as it concentration and mass. In addition it is affected by astrophysical effects such as star formation, and feedback from active galactic nuclei (AGNs) and supernova. Its effect on the optical depth - halo mass scaling relation was studied in Battaglia, 2016 using three different hydrodynamic simulations with varying input astrophysics.

The los velocity greater than zero corresponds to a cloud of free electrons moving away from the observer. Thus kSZ effect shifts the CMB temperature slightly while preserving the CMB power spectrum. Using the kSZ as a cosmological probe requires a strong detection of the kSZ signal for a large number of clusters. Currently the only direct kSZ detection is in a merging cluster systems with particularly large velocities (Sayers et al., 2013; Adam et al., 2017). The kSZ signal detection is challenging because of its small amplitude and its spectrum being identical to that of primary CMB temperature fluctuations. This difficulty has motivated for alternative methods. A different approach to detect the kSZ signal is to combine data from CMB and galaxy redshift survey, and employ a pairwise statistic (e.g. Hand et al., 2012; Planck Collaboration, P. A. R. Ade et al., 2016; Schaan et al., 2016; Soergel et al., 2016; De Bernardis et al., 2017; Y.-C. Li et al., 2017) which will be further described in section 1.5.

1.3 The Inhomogeneous Universe

The fundamental assumption of homogeneity of the universe is violated at small scales as the observed universe is far from homogeneous on these scales. There is a richness of structure in the universe, ranging from dwarf galaxies on the small scale to galaxy clusters on large scale. The theory of structure formation assumes that the structure grows due to gravitational instability. Primordial fluctuations, as a result of inflation, are amplified through gravity. These gravitational perturbations induce cosmic flows of matter; ultimately the over-dense regions decouple from the Hubble flow (expansion of the Universe) and collapse to form bound structures. Low density regions on the contrary become more and more empty, turning into even more under-dense regions. Gradually, through this gravitational instability scenario, cosmic structures emerge to form the universe as we know it. Furthermore, other effects like pressure, free-streaming of particles, etc. also affect the evolution of the structures in the universe.

1.3.1 Linear perturbation theory

A topic of great interest in cosmology is the growth of the density perturbations. When the fluctuations are small, the equations describing the structure growth can be linearised. The fluctuations can be parameterised using the density contrast which is defined as

$$\delta(\boldsymbol{x}) = \frac{\rho(\boldsymbol{x}) - \bar{\rho}}{\bar{\rho}}\,, \tag{1.19}$$

where $\bar{\rho}$ is the mean density in the Universe. As long as the density contrast is small, one can use linear perturbation theory. An assumption which is used here is that the dark matter particle distribution can be described as a fluid. This assumption will indeed break down on small scales. In general there is no well defined velocity field $\boldsymbol{u(r)}$ and multi-streams do occur as a result of the inter-particle crossings of collisionless dark matter particles. On large scales however, considering a non-relativistic, collisionless dark matter medium characterised by negligible thermal motions and using the fluid approximation, one gets the so called fluid equations for pressureless dust

$$\frac{\partial \hat{\rho}(\boldsymbol{r},t)}{\partial t} + \nabla_r \cdot [\hat{\rho}(\boldsymbol{r},t)\boldsymbol{u}(\boldsymbol{r},t)] = 0\,, \quad \text{(Continuity equation)} \tag{1.20}$$

$$\frac{\partial \boldsymbol{u}(\boldsymbol{r},t)}{\partial t} + [\boldsymbol{u}(\boldsymbol{r},t)\cdot\nabla_r]\,\boldsymbol{u}(\boldsymbol{r},t) = -\nabla_r\phi(\boldsymbol{r},t)\,, \quad \text{(Euler equation)} \tag{1.21}$$

$$\nabla_r^2\phi(\boldsymbol{r},t) = 4\pi G\hat{\rho}(\boldsymbol{r},t) - \Lambda\,. \quad \text{(Poisson equation)} \tag{1.22}$$

The continuity equation describes the conservation of matter. Euler equation is the equation of motion for the fluid elements. The Poisson equation relates the gravitational potential, ϕ, to the matter density as well as the cosmological constant. The fluid equations written in proper coordinates can be transformed to comoving coordinates defined by

$$\boldsymbol{x} = \frac{\boldsymbol{r}}{a(t)}\,. \tag{1.23}$$

The density and velocity fields are written in comoving coordinates as

$$\hat{\rho}(\boldsymbol{r},t) = \rho(\boldsymbol{x},t)\,, \tag{1.24}$$

$$\boldsymbol{u}(\boldsymbol{r},t) = \dot{a}\boldsymbol{x} + \boldsymbol{v}(\boldsymbol{x},t)\,. \tag{1.25}$$

The velocity field has been decomposed into the Hubble expansion of the homogeneous universe as given by the first term and peculiar velocity. Transforming from proper coordinates to comoving coordinates, the fluid equations become

$$\frac{\partial\delta(\boldsymbol{x},t)}{\partial t} + \frac{1}{a}\nabla_x\cdot(1+\delta(\boldsymbol{x},t))\boldsymbol{v}(\boldsymbol{x},t) = 0\,, \quad \text{(Continuity equation)} \tag{1.26}$$

$$\frac{\partial\boldsymbol{v}(\boldsymbol{x},t)}{\partial t} + \frac{1}{a}(\boldsymbol{v}(\boldsymbol{x},t)\cdot\nabla_x)\boldsymbol{v}(\boldsymbol{x},t) + \frac{\dot{a}}{a}\boldsymbol{v}(\boldsymbol{x},t) = -\frac{1}{a}\nabla_x\phi(\boldsymbol{x},t)\,, \quad \text{(Euler equation)} \tag{1.27}$$

$$\nabla_x^2\phi(\boldsymbol{x},t) = \frac{3H_0^2\Omega_\mathrm{m}}{2a}\delta(\boldsymbol{x},t)\,. \quad \text{(Poisson equation)} \tag{1.28}$$

Considering small perturbations in the density and small peculiar velocities, we can linearise equations (1.26) and (1.27) as

$$\frac{\partial\delta(\boldsymbol{x},t)}{\partial t} + \frac{1}{a}\nabla_x\cdot\boldsymbol{v}(\boldsymbol{x},t) = 0\,, \tag{1.29}$$

$$\frac{\partial\boldsymbol{v}(\boldsymbol{x},t)}{\partial t} + \frac{\dot{a}}{a}\boldsymbol{v}(\boldsymbol{x},t) = -\frac{1}{a}\nabla_x\phi(\boldsymbol{x},t)\,. \tag{1.30}$$

The Poisson equation (1.28) is already linear. We can combine these equations by taking the time derivative of equation (1.29) and the divergence of equation (1.30), to obtain

$$\frac{\partial^2\delta(\boldsymbol{x},t)}{\partial^2 t} + 2H(t)\frac{\partial\delta(\boldsymbol{x},t)}{\partial t} - \frac{3H_0^2\Omega_\mathrm{m}}{2a^3}\delta(\boldsymbol{x},t) = 0\,. \tag{1.31}$$

This equation does not contain derivatives with respect to $\boldsymbol{x}$ nor does it contain a term proportional to $\boldsymbol{x}$. Therefore the solution factorises and can be written as a product of functions of $\boldsymbol{x}$ and t. The general solution is given as

$$\delta(\boldsymbol{x},t) = D_+(t)\Delta_+(\boldsymbol{x}) + D_-(t)\Delta_-(\boldsymbol{x})\,. \tag{1.32}$$

where $D_\pm$ are two linearly independent solutions of equation (1.31).

1.3.2 The peculiar velocity field

In linear perturbation theory, the velocity field can be described by a gradient field [as vorticity decays as factor of $a^{-1}(t)$]. One can define a velocity potential $\psi(\boldsymbol{x},t)$ in terms of the peculiar velocity which can be written as

$$\boldsymbol{v}(\boldsymbol{x},t) = \nabla_x\psi(\boldsymbol{x},t)\,. \tag{1.33}$$

Employing the linearised continuity equation and using the linear evolution of the density contrast

$\delta(\boldsymbol{x},t) = D_+(t)\Delta_+(\boldsymbol{x})$, which implies $\dot{\delta}(\boldsymbol{x},t) = (\dot{D}_+(t)/D_+(t))\delta(\boldsymbol{x},t)$, then the Laplacian of the velocity potential is given as

$$\nabla_x^2\psi(\boldsymbol{x},t) = \nabla\cdot\boldsymbol{v}(\boldsymbol{x},t) = -a\frac{\dot{D}_+(t)}{D_+(t)}\delta(\boldsymbol{x},t) = -aHf\delta(\boldsymbol{x},t)\,, \tag{1.34}$$

where

$$f = \mathrm{d}\ln D_+/\mathrm{d}\ln a \approx \Omega_{\mathrm{m}}^{\gamma}(z)\,. \tag{1.35}$$

where $\gamma \simeq 0.545$ (Linder, 2005). Combining equations (1.33) and (1.34), one can obtain the linear peculiar velocity field as

$$\boldsymbol{v}(\boldsymbol{x},t) = \frac{aHf}{4\pi}\int \mathrm{d}^3y\,\delta(\boldsymbol{y},t)\frac{\boldsymbol{y}-\boldsymbol{x}}{|\boldsymbol{y}-\boldsymbol{x}|^3}\,. \tag{1.36}$$

Thus knowledge of the density contrast $\delta(\boldsymbol{x})$ in the linear regime enables one to calculate the velocity field $\boldsymbol{v}(\boldsymbol{x})$.

1.4 Numerical simulations

The last fifty years have seen huge progress in our understanding of the cosmic structure. Much of this has come from well motivated simple analytic arguments and insights. The analytical description of the Universe based on linear and higher-order perturbation theory however is inaccurate and starts to break down as the density becomes highly non-linear ($|\delta| > 0$). In general, it is extremely difficult to analytically describe the gravitational dynamics in detail. Thus numerical simulations have become one of the mainstay in the field of cosmology to explore and understand the properties of non-linear structure. N-body simulations treat all matter as collisionless DM. These simulations consists of N particles in a comoving volume V tracing the underlying matter distribution based on a specified cosmological model. Current state-of-the-art numerical simulations follow the dynamics of about 10^{12} particles [3]. In this work we make use of GADGET-2 (Springel, Yoshida and S. D. M. White, 2001; Springel, 2005), a publicly available and highly parallel code for numerical simulation of collision-less dark matter particles. Newtonian gravity is used to calculate the interaction between the DM particles, instead of GR, which is a valid approximation when the volume of the simulation boxes are small (Chisari and Zaldarriaga, 2011). GADGET-2 employs a hybrid algorithm to calculate the forces between particles. On the large scales, it uses particle-mesh (PM) technique to calculate the potential quickly. PM method constructs the density field on a grid, often using the cloud-in-cells (CIC) interpolation algorithm. This grid interpolation technique replaces constituent particles with a density value defined within a voxel. From the value in each voxel, the gravitational potential is calculated by solving the Poisson equation (1.22) in Fourier space. For scales below one to two mesh cells, the force is heavily suppressed. This technique is thus not well suited for numerical simulations which require high spatial resolution. To achieve this, GADGET-2 makes use of a hierarchical tree algorithm to compute the short-range gravitational force. In this method, particles are arranged in a hierarchy of cells in an oct-tree, which is a tree data structure in which each node has exactly eight children. It is ensured at the smallest level that no cell contains more than one particle, as the volume of simulation is divided into smaller cells. The gravitational force acting on each particle is then

[3] https://www.euclid-ec.org/?page_id=4133

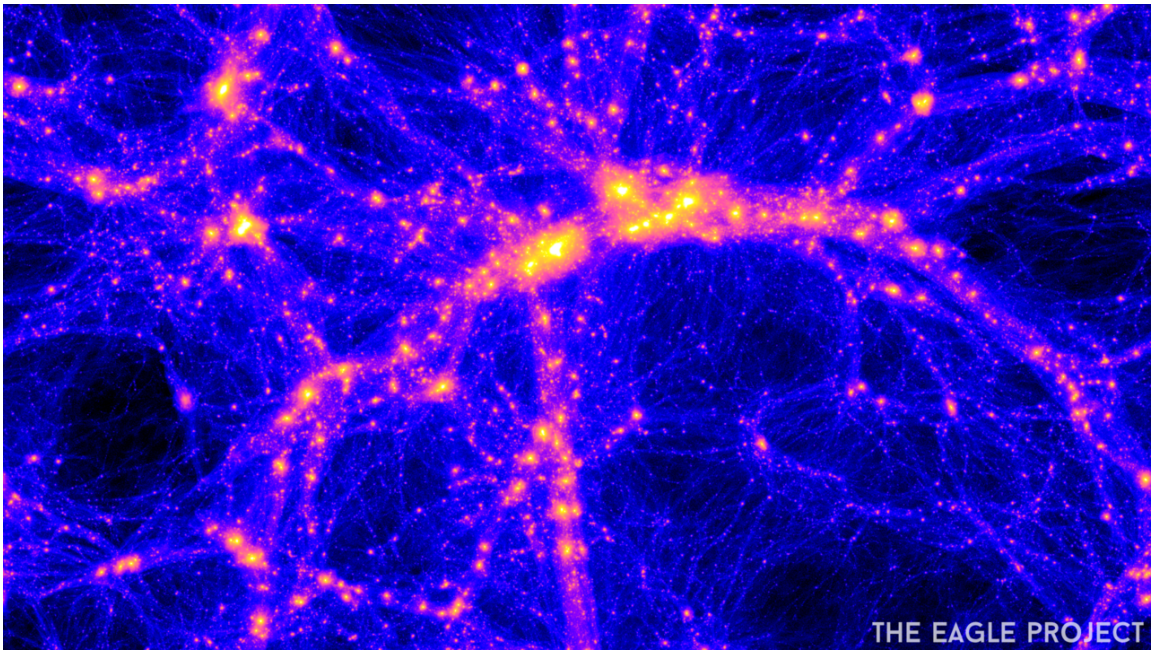

Figure 1.2: A slice taken from the EAGLE simulation (Schaller et al., 2015) which shows the intricately connected cosmic web. The high density regions are marked by orange/red color and the underdense regions which makes up the cosmic voids are shown in black.

calculated by summing the partial forces from neighbouring tree nodes. To first approximation, it treats the particles in an individual node as a single particle which is positioned at the center of mass.

An image from a simulation snapshot is shown in figure 1.2, which shows some striking features in the matter distribution of the Universe. This spatial organisation of tracers (DM, galaxies) forms an intricately connected network which is known as the cosmic web (Bond, Kofman and Pogosyan, 1996). The high-density regions which are gravitationally collapsed along the three principal axes (denoted by orange spots in the above figure) are known as knots/clusters. A prominent feature is the filament (collapsed along two principal axes) which act as the connecting structure between high density components (like clusters) in the cosmic web (e.g. Colberg, Krughoff and Connolly, 2005; Aragón-Calvo et al., 2010; Libeskind et al., 2018). They also appear to be the channels through which mass gets transported to higher dense regions. Length of the filaments may vary from few to 100 Mpc (e.g. Cautun et al., 2014). Regions of the Universe where matter has collapsed only along one principal axis constitute the sheets. Another prominent feature in the cosmic web are the voids. They are the most underdense region in the Universe and largely devoid of any matter, usually spherical in shape and occupying most of the volume in the Universe. Even though they are largely devoid of material, they contain a considerable amount of information about the underlying cosmological scenario. These complex patterns in the density field emerge as the growth of gravitational perturbation goes beyond a linear phase. They showcase the anisotropic nature of the gravitational collapse process which can be directly seen from the numerical simulations.

Future redshift surveys like *Euclid* (Amendola et al., 2013), Dark Energy Spectroscopic Instrument (*DESI*, Levi et al., 2013) and Large Synoptic Survey Telescope (*LSST*, LSST Science Collaboration et al., 2009) will cover large volumes. Numerical simulations will play a vital role in generating the

covariance matrix required for precise cosmological parameter estimation. For this purpose, it is essential that the simulations cover similar volumes as those surveys. It also requires the mass and force resolution to fully capture the non-linear clustering to obtain the desired percent level accuracy from future surveys.

1.5 Statistical approach

While the numerical simulations take care of the cosmological evolution of the underlying matter and velocity fields, one needs to characterise and quantify the information embedded in these systems. For this one can make use of statistical properties of the field. One of the main reason is that the cosmological evolution takes place over a timescale which is much longer than we can make observations. It is thus not possible to follow the evolution of single systems and must be done statistically.

1.5.1 Spatial clustering

The observable universe can be modelled as a random realisation out of many possibilities. This follows the assumption that the part of the universe we observe is a fair sample of the whole universe ('fair sample hypothesis'). The statistical approach within the context of galaxy distribution can be seen as early as 1930s where Edwin Hubble studied the frequency distribution of count N of galaxies in the field of a telescope [4]. The statistical approach to galaxy clustering developed considerably during the 1970s and autocorrelation function emerged as one of the favoured summary statistics. The physical interpretation of two-point correlation function, ξ, is that it measures the excess probability, compared with that expected for a random distribution, of finding a pair of particles at volume elements $\mathrm{d}V_1$ and $\mathrm{d}V_2$ which are separated by a distance r as shown in the left panel of figure 1.3.

$$\mathrm{d}P = \bar{n}^2 \left[1 + \xi(r)\right] \mathrm{d}V_1 \mathrm{d}V_2 \,, \tag{1.37}$$

where $\bar{n}$ is the mean density. If the particles are unclustered, then $\xi = 0$; which implies that it is randomly distributed. For clustered particles, $\xi > 0$ and if they are anticorrelated, $\xi < 0$. Similarly clustering analysis with regards to correlation function can be generalised to higher-orders. If the random field was to be Gaussian, all the information will be captured by the two-point clustering signal. Under the inflation paradigm, the observational evidences point towards the fact that the initial conditions of our Universe resemble a Gaussian random field Planck Collaboration, Akrami et al., 2018. The subsequent evolution of perturbations in both temporal (time) and spatial scales makes the present Universe far from a Gaussian random field. Thus there is additional cosmological information in the higher-order correlation function with respect to two-point statistics.

In the case of three-point correlation function, we consider three particles in triangular configuration (where $r_{12},\ r_{23}$ and r_{31} are the sides of the triangle) with volume elements $\mathrm{d}V_1$, $\mathrm{d}V_2$ and $\mathrm{d}V_3$ as shown in the right panel of figure 1.3. The excess probability to find a triplet, compared with that expected for a random distribution, can be written down as

$$\mathrm{d}P_{123} = \bar{n}^3 \left[1 + \xi(r_{12}) + \xi(r_{23}) + \xi(r_{31}) + \zeta(r_{12}, r_{23}, r_{31})\right] \mathrm{d}V_1 \mathrm{d}V_2 \mathrm{d}V_3 \,, \tag{1.38}$$

[4] For a more concise history, we refer the reader to Peebles, 1980; Peebles, 2001

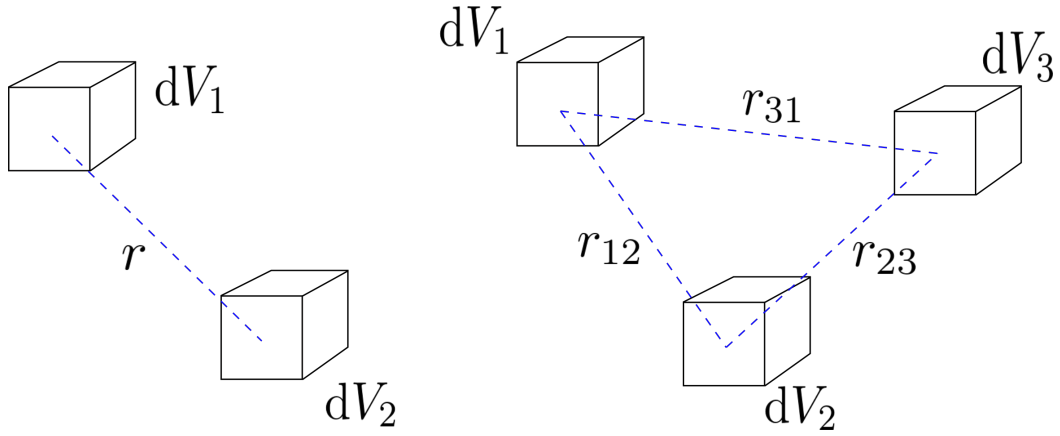

Figure 1.3: Left panel shows two particles in volume elements $\mathrm{d}V_1$ and $\mathrm{d}V_2$ separated by a distance r. Right hand panel shows three particles in volume elements $\mathrm{d}V_1$, $\mathrm{d}V_2$ and $\mathrm{d}V_3$ separated by distances r_{12}, r_{23} and r_{31} in a triangular configuration.

where $\zeta(r_{12}, r_{23}, r_{31})$ is the connected three-point correlation function. It is also possible to define these correlation functions as statistical properties of a cosmic density field (δ), which is a random field. The Universe is assumed to be statistically isotropic and homogeneous, as we have mentioned before. These properties are thus followed by the density field also. We can define the two-point correlation function as the joint ensemble average of densities at two different points separated by a distance r,

$$\xi(r) = \langle \delta(\boldsymbol{x}) \delta(\boldsymbol{x} + \boldsymbol{r}) \rangle \,, \tag{1.39}$$

which depends on the separation $\boldsymbol{r}$ as the density field is assumed to be homogeneous (invariant under translations) and depends on the norm of this separation vector due to the fact that the field is isotropic (invariant under rotation). The density contrast can be written in term of its Fourier components

$$\tilde{\delta}(\boldsymbol{k}) = \int \mathrm{d}^3 x \, \delta(\boldsymbol{x}) \, \exp(-i\boldsymbol{k} \cdot \boldsymbol{x}) \,, \tag{1.40}$$

We can define power spectrum[5], which is the Fourier pair of the correlation function, as

$$\langle \tilde{\delta}(\boldsymbol{k}) \tilde{\delta}(\boldsymbol{k}') \rangle = (2\pi)^3 \delta_{\mathrm{D}}(\boldsymbol{k} + \boldsymbol{k}') P(k) \,. \tag{1.41}$$

The Dirac delta $\delta_{\mathrm{D}}(\boldsymbol{k} + \boldsymbol{k}')$ expresses the statistical homogeneity (translational invariance) of clustering. The statistical isotropy is showed from the fact that the power spectrum depends only on the norm of the wavevector k. For homogeneous and isotropic fields, they are related to each other as

$$P(k) = 4\pi \int_0^\infty \mathrm{d}r \, r^2 \, \frac{\sin(kr)}{kr} \, \xi(r) \,, \tag{1.42}$$

$$\xi(r) = \frac{1}{2\pi^2} \int_0^\infty \mathrm{d}k \, k^2 \frac{\sin(kr)}{kr} \, P(k) \,. \tag{1.43}$$

[5] It is also valid to define the power spectrum as the covariance where one of the mode is taken to be a complex conjugate. In such a case, $\langle \tilde{\delta}(\boldsymbol{k}) \tilde{\delta}^*(\boldsymbol{k}') \rangle = (2\pi)^3 \delta_{\mathrm{D}}(\boldsymbol{k} - \boldsymbol{k}') P(k)$

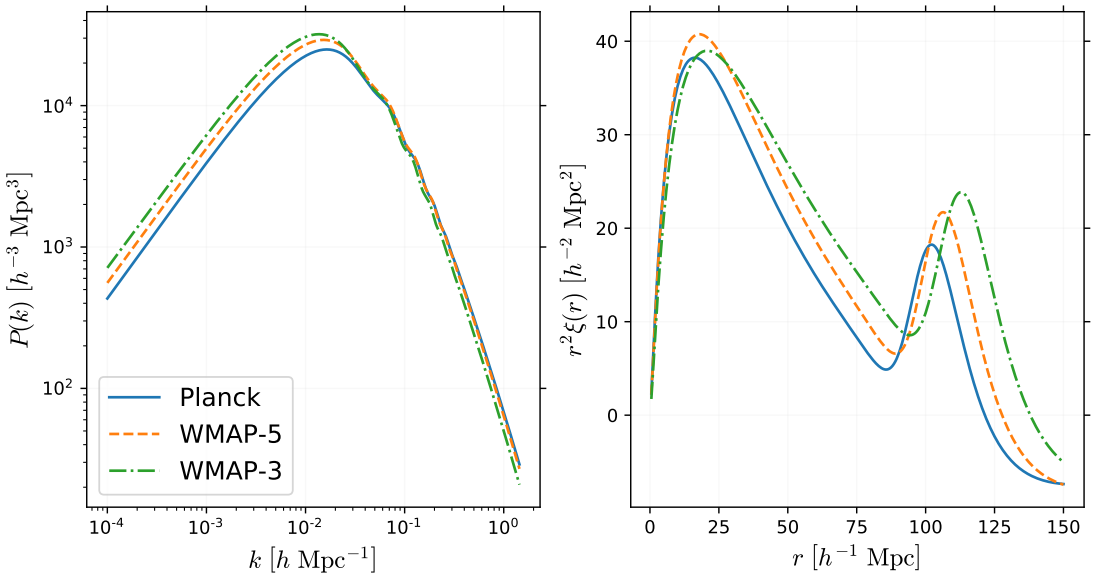

Figure 1.4: Left panel shows the linear matter power spectrum for three different cosmological parameters within the ΛCDM scenario at z=0. Right panel shows the corresponding Fourier transform pair, i.e. the linear correlation function.

Table 1.1: Cosmological parameters used for computing the power spectrum and correlation function in figure 1.4

Name	H_0	Ω_m	Ω_b	Ω_Λ	n_s	σ_8
Planck	67.74	0.3089	0.0486	0.6911	0.9667	0.8159
WMAP-5	70.10	0.2790	0.0462	0.7210	0.9600	0.8170
WMAP-3	73.00	0.2400	0.0420	0.7600	0.9500	0.7600

The clustering statistics depends on the underlying cosmological model and an example of this is shown in figure 1.4. The power spectrum and correlation function are computed at redshift, $z = 0$, where the input linear power spectrum for three different scenarios is obtained from the CAMB software and their respective correlation functions are numerically computed as per equation (1.43). The different cosmologies are summarised in the table 1.1, they were chosen based on the results from *WMAP* (third and fifth year data release, D. N. Spergel et al., 2007; Komatsu et al., 2009) and *Planck* (2018 data release, Planck Collaboration, Akrami et al., 2018) survey. The connected three-point correlation function in configuration space can be defined as

$$\zeta(r_{12}, r_{23}, r_{31}) = \langle \delta(\boldsymbol{x}_1)\delta(\boldsymbol{x}_2)\delta(\boldsymbol{x}_3)\rangle \,, \tag{1.44}$$

where $\boldsymbol{r}_{12} = \boldsymbol{x}_2 - \boldsymbol{x}_1$, $\boldsymbol{r}_{23} = \boldsymbol{x}_3 - \boldsymbol{x}_2$ and $\boldsymbol{r}_{31} = \boldsymbol{x}_1 - \boldsymbol{x}_3$ and ζ only depends on the norm of the triplet separation due to homogeneity and isotropy as mentioned before. We can also define the third order clustering statistics in Fourier space known as the bispectrum, which is the Fourier transform

pair of connected correlation function ζ.

$$\langle\tilde{\delta}(\boldsymbol{k}_1)\tilde{\delta}(\boldsymbol{k}_2)\tilde{\delta}(\boldsymbol{k}_3)\rangle = (2\pi)^3\delta_{\rm D}(\boldsymbol{k}_1+\boldsymbol{k}_2+\boldsymbol{k}_3)B(k_1,k_2,k_3)\,. \tag{1.45}$$

1.5.2 Velocity statistics

In addition to (particle) clustering statistics, studying the peculiar velocity field of the LSS is a powerful tool to probe the Universe. We have already seen that on large scales the peculiar velocity field is directly related to the underlying matter perturbation, it can thus be used to test the growth of structure. There have been various approaches in studying the velocity field including reconstruction of the linear velocity field from the density field and compare it with the measured velocity field. In this work we take a different approach and study few summary statistics based on the velocity field namely the pairwise and triple-wise velocities, and its moments. Los pairwise velocity is the relative los velocity difference between two particles and is defined as

$$w_{12\parallel} = (\boldsymbol{v}_2 - \boldsymbol{v}_1)\cdot\hat{n}\,, \tag{1.46}$$

where $\hat{n}$ is the unit vector along the los. The convention follows that if the particles are moving towards each other (infalling), the pairwise velocity will be negative and if they are moving away from each other, it will be positive. Similarly, the relative velocity differences can be obtained for higher-order, namely triple-wise velocity which refers to the third-order velocity statistics. In the case of triple-wise velocity difference, is possible to have three components of it

$$w_{12\parallel} = (\boldsymbol{v}_2 - \boldsymbol{v}_1)\cdot\hat{n}\,, \tag{1.47}$$
$$w_{23\parallel} = (\boldsymbol{v}_3 - \boldsymbol{v}_2)\cdot\hat{n}\,, \tag{1.48}$$
$$w_{31\parallel} = (\boldsymbol{v}_1 - \boldsymbol{v}_3)\cdot\hat{n}\,. \tag{1.49}$$

Pairwise and triple-wise velocities will be covered in detail in the coming chapters. Combining these velocity statistics with clustering information will help us in further constraining the cosmological model from future surveys.

1.6 Observational effect: redshift-space distortions

In a homogeneous Universe, we can use redshift directly as a distance indicator. However there is also a peculiar velocity component in addition to the Hubble flow. The observed redshift $z_{\rm obs}$ is thus a superposition of the cosmic expansion and the peculiar velocity of an object along the los (Harrison, 1974),

$$1 + z_{\rm obs} \approx (1+z_{\rm cos})\left(1+\frac{v_\parallel}{c}\right)\,, \tag{1.50}$$

where $z_{\rm cos}$ is the cosmological redshift induced due to Hubble expansion, $v_\parallel$ is the los component of the peculiar velocity and c is the speed of light. The position of an object in redshift-space $\boldsymbol{x}_s$, which is the observed reference frame, can be written as

$$\boldsymbol{x}_s = \boldsymbol{x} + \frac{v_\parallel}{\mathcal{H}}\hat{n}\,, \tag{1.51}$$

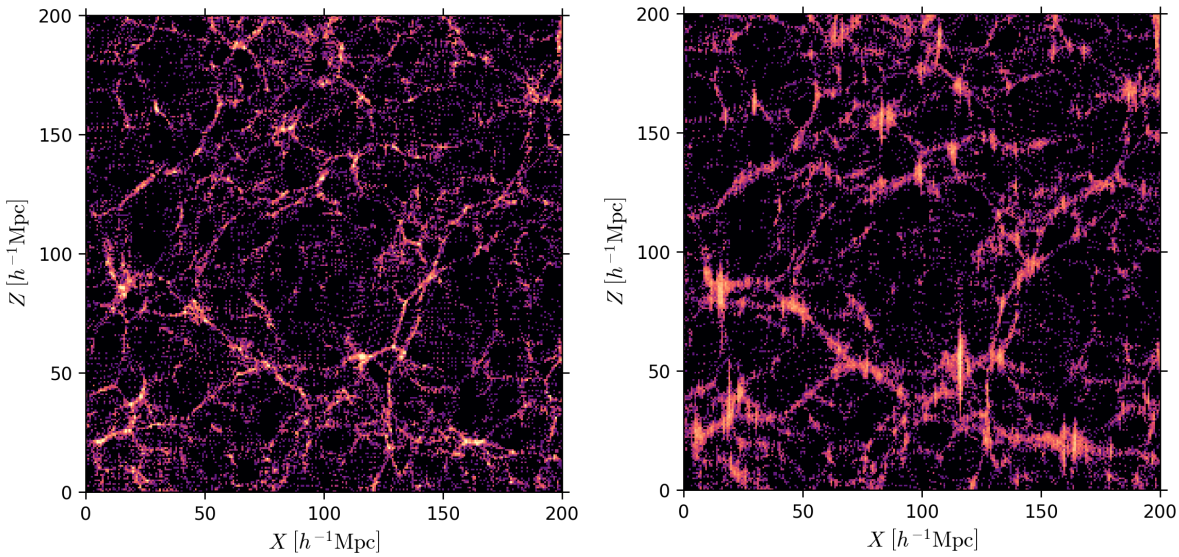

Figure 1.5: Slice of DM particles from a cosmological simulation in real-space on the left panel. The right panel shows the same slice in which the particle positions have been perturbed according to each particles' peculiar velocity along the los. This is the observed reference frame in which some spurious features including elongation of the structure along the los (Z-direction) can be seen.

where $\boldsymbol{x}$ is its true position in real space and $\mathcal{H} = aH$ is the conformal Hubble parameter. In figure 1.5, the left panel shows the particle position in real-space from a thin slice in a cosmological simulation and the right panel showcases the perturbed position of the particle distribution due to its peculiar velocity in redshift space or the observed reference frame. These distortions are referred to as redshift-space distortions (RSD).

These lead to two main effects which are shown in figure 1.6. Consider a spherical overdensity on which four galaxies are placed. The arrows denote the peculiar velocity of the object along the los, in which only galaxies 1 and 3 have a non-zero los velocity. On large scales or linear regimes, it results in an apparent squashing of structure along the los and this is known as the 'Kaiser effect' (Kaiser, 1987). In the non-linear regime, the overdensity appears to be elongated along the los as a result of the velocity dispersion inside collapsed structures like clusters of galaxies. This is commonly referred to as the 'Finger-of-God' (FoG) effect (Jackson, 1972; Sargent and Turner, 1977). An important consequence of RSD is that the correlation function (or its Fourier transform power spectrum) is no longer isotropic as RSD breaks the rotational invariance along the los. However the degree of anisotropy can be leveraged to measure the growth rate of structure.

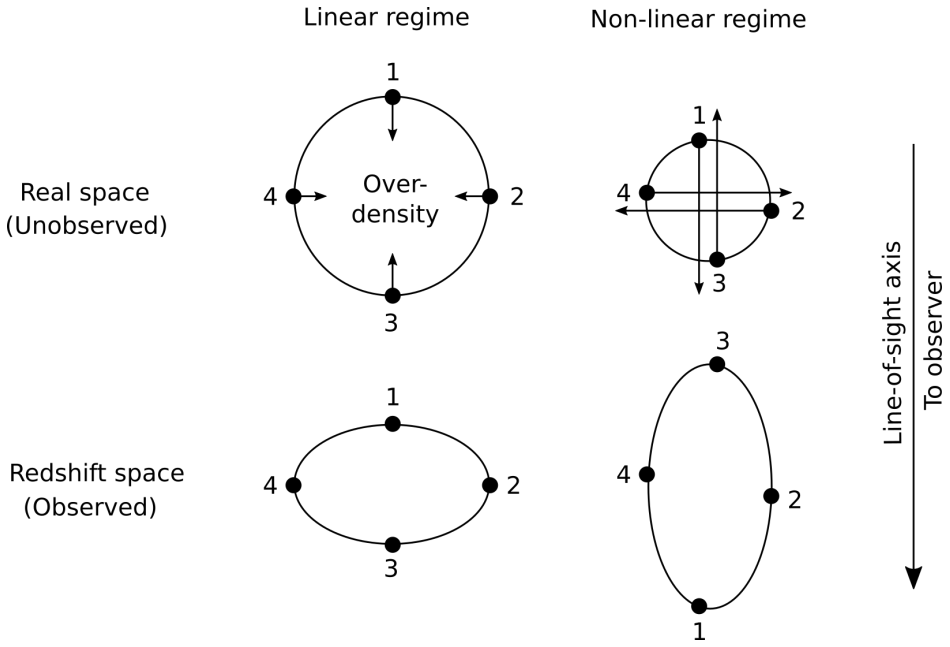

Figure 1.6: Illustration of effects of RSD. In linear regime, coherent flow towards overdense region causes the structures to appear squashed along the los. Collapsed structures in non-linear regions appear elongated along the los due to the velocity dispersion. Only objects having a peculiar velocity component along the los will be affected by RSD, which can be seen from the fact that objects 2 and 4 remain unchanged in real and redshift space.

CHAPTER 2

Two-point redshift-space correlation function

Galaxy redshift surveys provide us with three-dimensional maps of the Universe. However, the resulting charts are twisted by the fact that we convert redshifts into distances by assuming a homogeneous model of cosmic expansion. It is well known that the measured redshift is not a perfect distance indicator in the presence of density perturbations. Peculiar galaxy motions along the line of sight (los) generate the leading corrections and give rise to the so-called 'redshift-space distortions' (RSD) between the reconstructed configuration (in 'redshift space') and the actual galaxy distribution (in 'real' space).

The clustering pattern in redshift space predominantly showcases two spurious features. Collapsed structures appear highly elongated along the los due to the velocity dispersion of their constituent galaxies, a phenomenon known as the 'Finger-of-God' (FoG) effect (Jackson, 1972; Sargent and Turner, 1977). At the same time, large-scale flows towards overdense regions (or away from underdense regions) coherently deform the inferred galaxy distribution (Kaiser, 1987). Overall, RSD break the rotational invariance of galaxy N-point statistics which are anisotropic functions of the galaxy separations (in redshift space) along the los and in the plane of the sky. On large scales, the degree of anisotropy reflects the growth rate of cosmic structure and can thus be used to probe dark energy and gravity theories see Hamilton, 1998, for a comprehensive review.

RSD are clearly detected in measurements of galaxy clustering (e.g. Davis and Peebles, 1983; Fisher et al., 1994; Peacock, Cole et al., 2001; Guzzo, Pierleoni et al., 2008) and forthcoming surveys have the potential to extract valuable cosmological information from them (M. White, Song and Percival, 2009; Giannantonio, Porciani et al., 2012; Borzyszkowski, Bertacca and Porciani, 2017). The main limiting factor is modeling galaxy statistics in redshift space to the required accuracy for the widest possible range of scales. This is a formidable problem involving four non-linear quantities: the density and the velocity fields, galaxy biasing and the mapping from real to redshift space. Several lines of research have been pursued over the last decades with the aim of improving our understanding of RSD, including perturbative approaches for the largest scales (e.g Matsubara, 2008; Taruya, Nishimichi, Saito et al., 2009; Taruya, Nishimichi and Bernardeau, 2013; Senatore and Zaldarriaga, 2014), phenomenological models (e.g. Peacock and Dodds, 1994), and combinations of the two (e.g. B. A. Reid and M. White, 2011).

In this paper, we focus on the phenomenological approach introduced by Peebles, 1980 to model the galaxy two-point correlation function in redshift space and subsequently generalised by Fisher, 1995, who dubbed it the 'streaming model'. In this framework, the mapping from real to redshift space is

discussed in terms of the pairwise velocity distribution function. Basically, (one plus) the anisotropic correlation function in redshift space is written as an integral of (one plus) the spherically-symmetric correlation function in real space times the probability density of the relative los peculiar velocity. This model is exact in the distant-observer limit. Its properties in Fourier space have been thoroughly investigated by Scoccimarro, 2004.

The history of the streaming model is rich and varied. In its early applications, it was used to model the small-scale clustering of galaxies from the CfA survey (Davis and Peebles, 1983). The pairwise velocity distribution was assumed to be exponential[1]. The (scale-dependent) mean pairwise (or streaming) velocity along the los was determined by requiring the conservation of galaxy pairs under the stable-clustering hypothesis while the corresponding velocity dispersion (assumed to be scale independent to first approximation) was treated as a free parameter and measured from the suppression of the redshift-space correlations along the los at fixed transverse separation (e.g. Davis and Peebles, 1983; Bean et al., 1983; C. Li, Jing, Kauffmann, Börner, S. D. M. White et al., 2006). Later on, Fisher, 1995, see also Fisher et al. 1994 demonstrated that the streaming model with a Gaussian velocity distribution and a scale-dependent velocity dispersion is compatible with linear (Eulerian) perturbation theory on large scales. Therefore, it became clear that the character of the velocity PDF must change substantially with the galaxy separation, which makes the development of accurate theoretical models difficult. For this reason, hybrid models that combine linear perturbative predictions in redshift space with a (scale-independent) streaming term for the incoherent small-scale motions were introduced in order to describe galaxy clustering on a wider range of separations (Peacock and West, 1992; Park et al., 1994; Peacock and Dodds, 1994). These 'dispersion models' continue to be very popular (e.g. Hawkins et al., 2003; Guzzo, Pierleoni et al., 2008; Beutler et al., 2012; Chuang and Y. Wang, 2013) although they correspond to a streaming model with a discontinous velocity PDF (Scoccimarro, 2004) and may lead to biased estimates of the cosmological parameters (Kwan, G. F. Lewis and Linder, 2012).

Over time, the 'Gaussian streaming model' (GSM) has become the workhorse of RSD studies (B. A. Reid, Samushia et al., 2012; Samushia et al., 2014; Alam, Ho et al., 2015; Chuang, Pellejero-Ibanez et al., 2017; Satpathy et al., 2017). It requires three inputs: the real-space correlation function plus the mean and the dispersion of the los relative velocity distribution both as a function of the spatial separation and the orientation of the pairs. Several flavours of perturbation theory have been used to model these basic ingredients obtaining satisfactory agreement with N-body simulations at least for certain redshifts, tracers and scales (B. A. Reid and M. White, 2011; B. A. Reid, Samushia et al., 2012; Carlson, B. Reid and M. White, 2013; L. Wang, B. Reid and M. White, 2014; M. White, 2014; Vlah, Castorina and M. White, 2016; Kopp, Uhlemann and Achitouv, 2016).

Analytical considerations and numerical simulations show that the los pairwise velocity distribution is strongly non-Gaussian at all scales, being characterized by a net skewness and approximately exponential tails (Efstathiou, Frenk et al., 1988; Fisher et al., 1994; Juszkiewicz, Fisher and Szapudi, 1998; Scoccimarro, 2004). Different strategies have been employed to explain this shape ranging from the halo model (Sheth, 1996; Sheth and Diaferio, 2001; Tinker, 2007) to the superposition of environment-dependent Gaussian or quasi-Gaussian distributions (Bianchi, Chiesa and Guzzo, 2015; Bianchi, Percival and Bel, 2016). Given the non-Gaussian nature of the velocity PDF, the GSM corresponds to a cumulant expansion truncated at second order (B. A. Reid and M. White, 2011). An approximate extension to the third cumulant has been presented using the Edgeworth expansion

[1] Other analytical forms have also been considered but the exponential provided the best fit to the observational data.

Table 2.1: Cosmological parameters characterizing our N-body simulations.

Name	$f_{\rm NL}$	h	σ_8	$n_{\rm s}$	$\Omega_{\rm m}$	$\Omega_{\rm b}$	Ω_Λ
W0	0	0.7010	0.8170	0.9600	0.2790	0.0462	0.7210
W$f_{\rm NL}$	$\pm$27,$\pm$80	0.7010	0.8170	0.9600	0.2790	0.0462	0.7210
P0	0	0.6774	0.8159	0.9667	0.3089	0.0486	0.6911

around a Gaussian at first order (Uhlemann, Kopp and Haugg, 2015).

After discussing the limitations of the GSM, we introduce a new parameterization for the pairwise velocity PDF and show that it accurately reproduces the ouptut of N-body simulations both at the level of particles and haloes as well as for their 2-point correlation functions in redshift space. There is a growing interest in extending RSD studies to smaller scales as a test of modified gravity and interacting dark energy models (e.g. Jennings et al., 2012; Marulli, Baldi and Moscardini, 2012; Hellwing et al., 2014; Taruya, Nishimichi, Bernardeau et al., 2014; Zu, Weinberg et al., 2014; Xu, 2015; Barreira, Sánchez and Schmidt, 2016; Sabiu et al., 2016; Arnalte-Mur, Hellwing and Norberg, 2017). These future developments provide the main motivation for our work.

The paper is organized as follows. In Sections 2.1 and 2.2, we introduce the suite of N-body simulations used for our study and the basic principles of redshift-space distortions respectively. In Section 2.3, we present an original derivation of the streaming model starting from the 2-particle distribution function in phase space. We show that the model is regulated by different equations depending on whether one is considering ordered or unordered pairs. Here, we also review the applications of the streaming model to galaxy redshift surveys and test the basic assumptions of the GSM against N-body simulations. In Section 2.4, we illustrate how the relative los velocity and its cumulants are connected to the (isotropic) radial and tangential components of the pairwise velocity vector. We then characterise the scale dependence of the first 4 cumulants for dark-matter (DM) particles and haloes extracted from our numerical simulations. This allows us to discuss the pairwise velocity bias for the haloes. Further, we use the N-body simulations to decompose the matter pairwise velocity distribution into the contributions generated by DM haloes of different masses. In Section 2.5, we introduce the generalized hyperbolic distribution to model the PDF of the los pairwise velocity and show that it vastly improves upon previous approximations for both DM particles and haloes. Finally, in Section 2.6, we summarise our main achievements and conclude.

2.1 N-Body simulations

Our study combines analytical and numerical work. For the latter, we consider six N-body simulations run with the code GADGET-2 (Springel, Yoshida and S. D. M. White, 2001; Springel, 2005). As a reference, we use the zero-redshift output of the simulation that was labelled 1.0 in Pillepich, Porciani and Hahn, 2010 and we now dub W0. This run follows the formation of the large-scale structure from Gaussian initial conditions within a periodic cubic box with a side of 1200 h^{-1}Mpc. It assumes a flat ΛCDM cosmology with the best-fitting parameters determined by the 5-yr analysis of the WMAP mission (Komatsu et al., 2009) and considers 1024^3 particles with a mass of $1.246 \times 10^{11} h^{-1} \mathrm{M}_\odot$ (see Pillepich et al. 2010 for further details). To study the redshift evolution of our results, we consider other snapshots extracted from the same run. Furthermore, in order to explore the sensitivity of our findings to the underlying cosmological model and to the properties of the linear density perturbations, we use

other five simulations. Four of them (W-80, W-27, W+27, W+80) are also presented in Pillepich, Porciani and Hahn, 2010. Their only difference with respect to our reference run is the presence of non-Gaussian initial conditions of the local type with $f_{\rm NL} = -80, -27, +27$ and $+80$. The remaining simulation (P0), instead, has been run specifically for this work and assumes the best-fitting cosmological parameters from the Planck mission (Planck Collaboration, Adam et al., 2016). In all cases, we use the same box and softening lengths as well as the same number of particles and initial redshift. This implies that the P0 run has a slightly higher particle mass, $1.379 \times 10^{11} h^{-1}\mathrm{M}_{\odot}$. A comparison of the cosmological parameters used in the simulations is given in Table. 2.1.

We identify DM haloes using the ROCKSTAR halo finder (Behroozi, Wechsler and Wu, 2013) in the default configuration and only consider bound objects containing at least 100 particles within the virial radius.

2.2 Redshift-space distortions

We generally use redshift as a distance indicator assuming a homogeneous model of cosmic expansion with instantaneous scale factor a and Hubble parameter H. However, in the presence of peculiar velocities, we need to distinguish between the redshift-inferred distance of a generic tracer of the large-scale structure of the Universe (e.g. a galaxy or a galaxy cluster) $\boldsymbol{x}_{\rm s}$ and its true comoving distance $\boldsymbol{x}$. In the distant-observer (or plane-parallel) approximation (Hamilton, 1998),

$$\boldsymbol{x}_{\rm s} = \boldsymbol{x} + (\boldsymbol{v} \cdot \hat{\boldsymbol{z}})\, \hat{\boldsymbol{z}} \,, \tag{2.1}$$

where $\boldsymbol{v}$ denotes the peculiar velocity divided by the factor aH and $\hat{\boldsymbol{z}}$ denotes the los direction. The spurious displacement along the los distorts the clustering pattern of the tracers in redshift space from its actual configuration in real space. Let us consider two tracers with real-space separation $\boldsymbol{r} = \boldsymbol{x}_2 - \boldsymbol{x}_1$. The los component of their separation in redshift space is then

$$s_{\parallel} = (\boldsymbol{x}_{\mathrm{s}_2} - \boldsymbol{x}_{\mathrm{s}_1}) \cdot \hat{\boldsymbol{z}} = r_{\parallel} + w_{\parallel} \,, \tag{2.2}$$

where $r_{\parallel} = \boldsymbol{r} \cdot \hat{\boldsymbol{z}}$ and $w_{\parallel} = (\boldsymbol{v}_2 - \boldsymbol{v}_1) \cdot \hat{\boldsymbol{z}}$, while the transverse separation remains unchanged, i.e.

$$\boldsymbol{s}_{\perp} = \boldsymbol{r}_{\perp} \,. \tag{2.3}$$

If the spatial distribution of the tracers is statistically homogeneous in real space and their two-point correlation function $\xi(r)$ is invariant under rotations of the separation vector $\boldsymbol{r}$, it follows that the correlation function in redshift space $\xi_{\rm s}(s_{\perp}, s_{\parallel})$ is anisotropic between the parallel and transverse components and does not depend on $s = (s_{\parallel}^2 + s_{\perp}^2)^{1/2}$. An illustrative example is shown in Fig. 2.1 where we compare ξ and $\xi_{\rm s}$ for the DM particles in our N-body simulation (we have used one of the box axes as the los direction). Note that the iso-correlation contours for $\xi_{\rm s}$ are elongated along $s_{\parallel}$ at small transverse separations as a manifestation of the FoG effect and are squashed towards the bottom at large $s_{\perp}$ because of coherent infall motions as described in Kaiser, 1987.

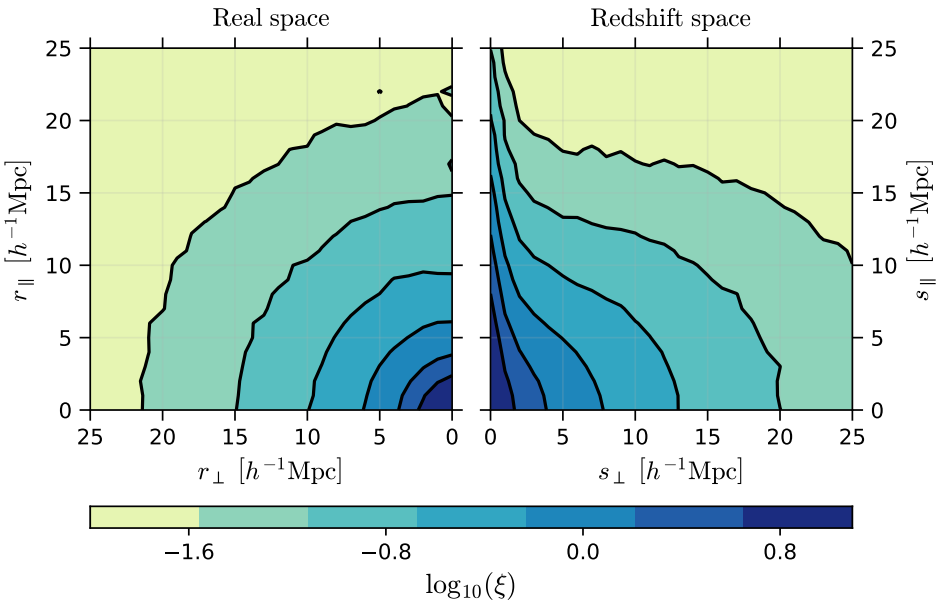

Figure 2.1: Two-point correlation function in real (left) and redshift space (right) for the DM particles in the W0 simulation at $z = 0$. The contour levels correspond to values of ξ and ξ_s ranging from 0.08 (outermost) to 2.56 (innermost) and differing by a factor of 2 between two consecutive levels. To facilitate comparisons, the same levels are used in all figures showing correlation functions.

2.3 The streaming model

The streaming model has been introduced to map $\xi(r)$ on to $\xi_\mathrm{s}(\boldsymbol{s})$ (Peebles, 1980; Fisher, 1995; Scoccimarro, 2004). Its basic equation is generally written as

$$1 + \xi_\mathrm{s}(\boldsymbol{s}_\perp, s_\parallel) = \int_{-\infty}^{+\infty} [1 + \xi\,(r)]\ \mathcal{P}_{w_\parallel}(s_\parallel - r_\parallel \mid \boldsymbol{r})\ \mathrm{d}r_\parallel\ , \tag{2.4}$$

where $r^2 = s_\perp^2 + r_\parallel^2$ and $\mathcal{P}_{w_\parallel}$ denotes the distribution function of the pairwise los velocity at fixed real-space separation vector $\boldsymbol{r} = (\boldsymbol{s}_\perp, r_\parallel)$ (i.e. a PDF which is differential in $w_\parallel$). In the remainder of this section, we will show that this classic result is exact provided that ordered pairs are used to define the correlation function and the correct definition of the velocity PDF is employed.

2.3.1 Ordered and unordered pairs

Two-point correlation functions are statistics of tracer pairs. A pair is a set composed of two elements. Still, we can define two kinds of pairs. If the order in which the elements appear in the pair is important (i.e. it makes sense to define a first element and a second element), we speak of an ordered pair (or 2-tuple). On the other hand, if the order does not matter, we speak of an unordered pair (or pair set). Ordered pairs can be represented by directed graphs (and vice versa), e.g. $A \to B \neq B \to A$, and unordered pairs by undirected graphs, e.g. $A \text{ — } B = B \text{ — } A$. From a set of N discrete objects, we can form $N\,(N-1)$ ordered pairs and $N\,(N-1)/2$ unordered pairs.

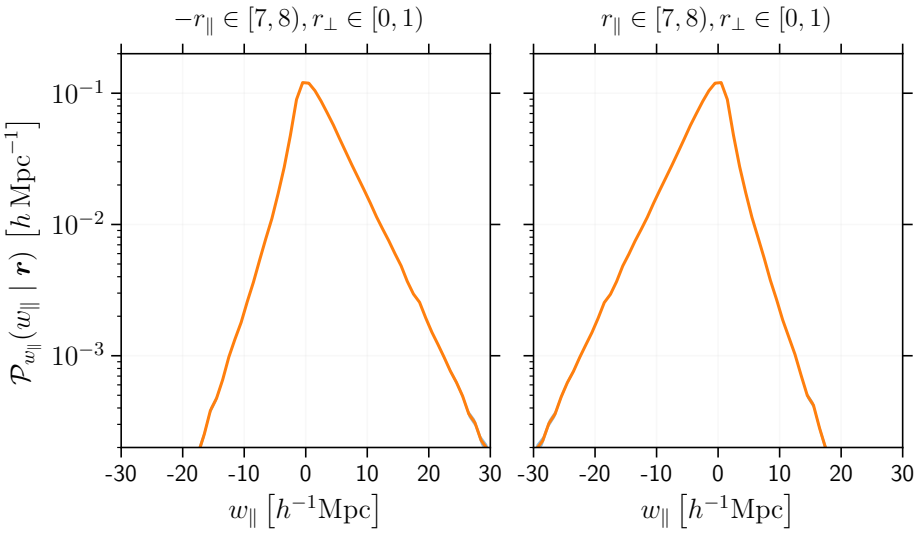

Figure 2.2: PDF of the relative los velocity for ordered pairs with fixed real-space separation (as indicated by the top labels in units of $h^{-1}\mathrm{Mpc}$). The left- and right-hand side panels correspond to a particle exchange and show the symmetry $\mathcal{P}_{w_\parallel}(w_\parallel \mid r_\perp, r_\parallel) = \mathcal{P}_{w_\parallel}(-w_\parallel \mid r_\perp, -r_\parallel)$.

If the two-point correlation function is built out of ordered pairs, the spatial separations $r_\parallel$ and $s_\parallel$ must be signed numbers (while $s_\perp = r_\perp \geq 0$ as they give the magnitude of the two-dimensional vector $\boldsymbol{s}_\perp = \boldsymbol{r}_\perp$). On the other hand, for unordered pairs, $r_\parallel$ and $s_\parallel$ are unsigned numbers.

2.3.2 The streaming model for ordered pairs

Let us consider a system of N particles with instantaneous comoving positions $\boldsymbol{x}_i$ and rescaled peculiar velocities $\boldsymbol{v}_i$ (where the subscript i identifies the different particles). Following a standard procedure in classical statistical mechanics, we introduce the one- and two-particle phase-space densities Yvon, 1935

$$f_1(\boldsymbol{x},\boldsymbol{v}) = \langle \hat{f}_1(\boldsymbol{x},\boldsymbol{v})\rangle = \langle \sum_{i=1}^{N} \delta_{\mathrm{D}}^{(3)}(\boldsymbol{x}-\boldsymbol{x}_i)\,\delta_{\mathrm{D}}^{(3)}(\boldsymbol{v}-\boldsymbol{v}_i)\rangle\ , \tag{2.5}$$

$$f_2(\boldsymbol{x}_\mathrm{A},\boldsymbol{x}_\mathrm{B},\boldsymbol{v}_\mathrm{A},\boldsymbol{v}_\mathrm{B}) = \langle \sum_{i=1}^{N}\sum_{j\neq i} \delta_{\mathrm{D}}^{(3)}(\boldsymbol{x}_\mathrm{A}-\boldsymbol{x}_i)\,\delta_{\mathrm{D}}^{(3)}(\boldsymbol{x}_\mathrm{B}-\boldsymbol{x}_j) \delta_{\mathrm{D}}^{(3)}(\boldsymbol{v}_\mathrm{A}-\boldsymbol{v}_i)\,\delta_{\mathrm{D}}^{(3)}(\boldsymbol{v}_\mathrm{B}-\boldsymbol{v}_j)\rangle\ , \tag{2.6}$$

where $\hat{f}_1(\boldsymbol{x},\boldsymbol{v})$ is the discrete one-particle phase density (also known as the Klimontovich or the microscopic density), the brackets denote averaging over an ensemble of realisations and $\delta_{\mathrm{D}}^{(n)}(\boldsymbol{x})$ is the Dirac delta distribution in $\mathbb{R}^n$. Note that f_1 is normalised to the total number of particles, i.e. $\int f_1\ \mathrm{d}^3x\ \mathrm{d}^3v = N$ and f_2 to the total number of ordered pairs, i.e. $\int f_2\ \mathrm{d}^3x_\mathrm{A}\ \mathrm{d}^3x_\mathrm{B}\ \mathrm{d}^3v_\mathrm{A}\ \mathrm{d}^3v_\mathrm{B} =$

$N\,(N-1)$. By definition, the spatial two-point correlation function of the particles is

$$1+\xi(\boldsymbol{x}_{\rm A},\boldsymbol{x}_{\rm B})=\frac{\int f_2\ {\rm d}^3v_{\rm A}\ {\rm d}^3v_{\rm B}}{\left(\int f_1\ {\rm d}^3v\right)^2}\ . \tag{2.7}$$

Assuming statistical isotropy (i.e. the invariance under rotations of the expectations over the ensemble) implies that f_1 can only depend on x^2, v^2 and $\boldsymbol{x}\cdot\boldsymbol{v}$. Requiring that ensemble averages are also invariant under translations (statistical homogeneity) fixes the dependence of the one-particle distribution function to $f_1=\bar{n}\,F(v^2)$ where the constant $\bar{n}=\int f_1\ {\rm d}^3v$ gives the mean particle number density per unit volume and F is an arbitrary function such that $4\pi\int F(v^2)\,v^2\ {\rm d}v=1$. Under the same assumptions and for $N\gg1$, $\int f_2\ {\rm d}^3v_{\rm A}\ {\rm d}^3v_{\rm B}=\bar{n}^2\,[1+\xi(r)]$.

Our goal is to introduce a new set of distribution functions which are defined in 'redshift phase space'. This can be easily achieved by performing the change of coordinates given in equations (2.1), (2.2) and (2.3):

$$g_1(\boldsymbol{x}_{\rm s},\boldsymbol{v})=f_1(\boldsymbol{x}_\perp,x_{{\rm s}\parallel}-v_\parallel,\boldsymbol{v})=\bar{n}\,F(v^2)\ , \tag{2.8}$$

$$g_2(\boldsymbol{s}_\perp,s_\parallel,\boldsymbol{v}_{\rm A},\boldsymbol{v}_{\rm B})=f_2(\boldsymbol{s}_\perp,s_\parallel-v_{{\rm B}\parallel}+v_{{\rm A}\parallel},\boldsymbol{v}_{\rm A},\boldsymbol{v}_{\rm B})\ . \tag{2.9}$$

The spatial two-point correlation function in redshift-space is then

$$1+\xi_{\rm s}(\boldsymbol{s}_\perp,s_\parallel)=\frac{\int g_2\ {\rm d}^3v_{\rm A}\ {\rm d}^3v_{\rm B}}{\left(\int g_1\ {\rm d}^3v\right)^2}=\frac{\int g_2\ {\rm d}^3v_{\rm A}\ {\rm d}^3v_{\rm B}}{\bar{n}^2}\ . \tag{2.10}$$

We now rewrite the rhs of equation (2.9) as

$$\int_{-\infty}^{+\infty}f_2(\boldsymbol{s}_\perp,s_\parallel-w_\parallel,\boldsymbol{v}_{\rm A},\boldsymbol{v}_{\rm B})\,\delta_{\rm D}^{(1)}(w_\parallel-v_{{\rm B}\parallel}+v_{{\rm A}\parallel})\ {\rm d}w_\parallel\ , \tag{2.11}$$

and we substitute it in equation (2.10). After multiplying the rhs of the resulting equation by the ratio

$$\frac{\bar{n}^2\ \left[1+\xi\left(\sqrt{s_\perp^2+(s_\parallel-w_\parallel)^2}\right)\right]}{\displaystyle\int f_2(\mathbf{s}_\perp,s_\parallel-w_\parallel,\boldsymbol{v}_{\rm A},\boldsymbol{v}_{\rm B})\,{\rm d}^3v_{\rm A}\ {\rm d}^3v_{\rm B}}\ , \tag{2.12}$$

(which is identically equal to one), we re-arrange the terms to define the relative line-of-sight velocity PDF for ordered pairs with real-space separation $\boldsymbol{r}=(\boldsymbol{s}_\perp,s_\parallel-w_\parallel)$ as

$$\begin{aligned}\mathcal{P}_{w_\parallel}(w_\parallel\mid\boldsymbol{r})&=\frac{\int f_2\,(\boldsymbol{r},\boldsymbol{v}_{\rm A},\boldsymbol{v}_{\rm B})\ \delta_{\rm D}^{(1)}(w_\parallel-v_{{\rm B}\parallel}+v_{{\rm A}\parallel})\ {\rm d}^3v_{\rm A}\ {\rm d}^3v_{\rm B}}{\int f_2\,(\boldsymbol{r},\boldsymbol{v}_{\rm A},\boldsymbol{v}_{\rm B})\,{\rm d}^3v_{\rm A}\,{\rm d}^3v_{\rm B}}\\&=\frac{\int f_2\,(\boldsymbol{r},\boldsymbol{v}_{\rm A},\boldsymbol{v}_{\rm B})\ \delta_{\rm D}^{(1)}(w_\parallel-v_{{\rm B}\parallel}+v_{{\rm A}\parallel})\ {\rm d}^3v_{\rm A}\ {\rm d}^3v_{\rm B}}{\bar{n}^2\,[1+\xi(r)]}\ ,\end{aligned} \tag{2.13}$$

and finally obtain

$$1+\xi_{\rm s}(\boldsymbol{s}_\perp, s_\parallel) = \int_{-\infty}^{+\infty} \left[1+\xi\left(r\right)\right]\, \mathcal{P}_{w_\parallel}(w_\parallel \mid \boldsymbol{r})\, \mathrm{d}w_\parallel$$
$$= \int_{-\infty}^{+\infty} \left[1+\xi\left(r\right)\right] \mathcal{P}_{w_\parallel}(s_\parallel - r_\parallel \mid \boldsymbol{r})\, \mathrm{d}r_\parallel\,, \tag{2.14}$$

which coincides with equation (2.4). The moment-generating function of the random variable $w_\parallel$ is

$$M_{w_\parallel}(t) = \frac{\int e^{t(v_{\rm B\parallel}-v_{\rm A\parallel})}\, f_2\left(\boldsymbol{r}, \boldsymbol{v}_{\rm A}, \boldsymbol{v}_{\rm B}\right)\, \mathrm{d}^3 v_{\rm A}\, \mathrm{d}^3 v_{\rm B}}{\bar{n}^2\left[1+\xi(r)\right]}\,. \tag{2.15}$$

Let us recap what we have done and achieved so far. Following a particle-based description and making use of the reduced distribution functions in phase-space, we have demonstrated that the streaming model is exact in the distant-observer approximation (and under the assumption of statistical homogeneity and isotropy in real space) provided that equation (2.13) is used to define $\mathcal{P}_{w_\parallel}$ or, equivalently, equation (2.15) is used to calculate the moment-generating function. It is worth stressing that our particle-based approach is completely rigorous also in multi-stream regions (where particles with different velocities are present at the same spatial location $\boldsymbol{x}$) and fully accounts for density-velocity correlations.

Alternative derivations of the streaming equation have been presented by other authors adopting more restrictive assumptions. They are generally based on a macroscopic description obtained by coarse graining $\hat{f}_1(\boldsymbol{x},\boldsymbol{v})$ either in space (over patches of intermediate size between the typical inter-particle separation and the cosmological scales of interest) or in time so that to erase discreteness effects and deal with a smooth function. Formally, a perfectly smooth distribution function, $\bar{f}_1(\boldsymbol{x},\boldsymbol{v})$, is obtained by taking the Rostoker-Rosenbluth fluid limit (Rostoker and Rosenbluth, 1960), i.e. by simultaneously letting $N\to\infty$ and the particle mass $m\to 0$ so that $Nm=$ constant. This provides an approximated description of the system which is accurate until discreteness effects (particle collisions and correlations) cannot be neglected any longer. In fact, the microscopic, n-particle, and macroscopic densities are distinct quantities that evolve very differently: $\hat{f}_1$ is exact and satisfies the Klimontovic equation, the n-particle densities, f_n, (which are exact ensemble averages) are solutions of the BBGKY hierarchy, while $\bar{f}_1$ is an approximation and fulfills the Vlasov equation. Equipped with these definitions, we are now ready to compare our results with previous derivations of the streaming equation. Scoccimarro, 2004 used the language of statistical field theory and characterized the matter content of the universe (in the single-stream regime) in terms of two continuous fields describing the density contrast $\delta(\boldsymbol{x})$ and the peculiar velocity $\boldsymbol{u}(\boldsymbol{x})$. In our notation, this is equivalent to assuming that $\bar{f}_1(\boldsymbol{x},\boldsymbol{v}) = \bar{n}\left[1+\delta(\boldsymbol{x})\right]\delta_{\rm D}^{(3)}[\boldsymbol{v}-\boldsymbol{u}(\boldsymbol{x})]$. Correlation functions were then computed by taking ensemble averages of the product of fields evaluated at different spatial locations. This method has been generalised to multi-streaming by Uhlemann, Kopp and Haugg, 2015 and Agrawal et al., 2017 see also Seljak and P. McDonald, 2011, who wrote $\bar{n}\left[1+\delta(\boldsymbol{x})\right] = \int \bar{f}_1(\boldsymbol{x},\boldsymbol{v})\, \mathrm{d}^3 v$ before computing the correlation function. In all cases, the authors were able to derive equation (2.4). However, since they rely on the collisionless fluid limit, all these approaches give a different velocity PDF and moment-generating function than our equations (2.13) and (2.15). In fact, our $f_2\left(\boldsymbol{r},\boldsymbol{v}_{\rm A},\boldsymbol{v}_{\rm B}\right)$ is replaced by the product $\bar{f}_1(\boldsymbol{x}_{\rm A},\boldsymbol{v}_{\rm A})\,\bar{f}_1(\boldsymbol{x}_{\rm B},\boldsymbol{v}_{\rm B})$ which completely neglects velocity correlations. While this is certainly an extremely good approximation for particle dark matter, it does not hold true

in general. Note that our derivation is exact and applies to any system of particles (e.g. galaxies or their host haloes) without making assumptions regarding their interactions.

Symmetry under particle exchange

By construction, the velocity PDF in equation (2.13) is symmetric under particle exchange (A↔B) or parity transformations, i.e.

$$\mathcal{P}_{w_\parallel}(w_\parallel \mid \boldsymbol{r}) = \mathcal{P}_{w_\parallel}(-w_\parallel \mid -\boldsymbol{r}) \ . \tag{2.16}$$

In fact, the ordered pairs that can be formed with two particles equally contribute to $(w_\parallel, \boldsymbol{r})$ and $(-w_\parallel, -\boldsymbol{r})$.

In order to visualise the velocity PDF for the DM particles of our N-body simulation, we build an estimator for $\mathcal{P}_{w_\parallel}$ by replacing the ensemble average in the definition of f_2 with an average over the simulation box (accounting for periodic boundary conditions). To speed the calculation up, we randomly sample 256^3 particles and consider all the ordered pairs between them. Each pair is classified in 1×1 $(h^{-1}\,\mathrm{Mpc})^2$ bins based on the values for $r_\parallel$ and $r_\perp$. Finally, we build an histogram for $w_\parallel$ in each bin. An example is shown in Fig. 2.2 where we examine real-space separations of $\pm r_\parallel \in [7,8)\,h^{-1}$ Mpc and $r_\perp \in [0,1)\,h^{-1}$ Mpc. In each branch, the distribution clearly shows strongly asymmetric exponential tails. For $r_\parallel > 0$, it has a negative skew meaning that the particles in the pairs tend to approach each other. The mean and rms values are $-2.4\,h^{-1}$ Mpc and $5.2\,h^{-1}$ Mpc, respectively, while the mode is very close to zero.

2.3.3 The streaming model for unordered pairs

Before moving to the main goal of our work, we briefly discuss an alternative formulation of the streaming equation which highlights an interesting feature of RSD.

N-body simulations provide valuable insights about the pairwise-velocity PDF. In this branch of the literature (Efstathiou, Frenk et al., 1988; Zurek et al., 1994; Fisher et al., 1994; Scoccimarro, 2004; Tinker, Weinberg and Zheng, 2006; B. A. Reid and M. White, 2011; Zu and Weinberg, 2013; Bianchi, Chiesa and Guzzo, 2015), it is customary to use the pairwise los velocity for unordered pairs,

$$w_{\rm los} = w_\parallel \frac{r_\parallel}{|r_\parallel|} = w_\parallel \,\mathrm{sgn}\left(r_\parallel\right) \ , \tag{2.17}$$

whose sign encodes physical information about the relative projected motion. If the elements of a pair approach (recede from) each other along the los, then $w_{\rm los}$ is negative (positive).

It is worth stressing that the PDF of $w_{\rm los}$ can not be inserted into equation (2.4) without first making some changes. In this section, we clarify the issue and derive the basic equation of the streaming model for unordered pairs. By construction, $w_{\rm los}$ does not depend on the order of the galaxy/particle pairs and

$$\mathcal{P}_{w_{\rm los}}(w_{\rm los}|\mathbf{r}) = \mathcal{P}_{w_{\rm los}}(w_{\rm los}|-\mathbf{r}) = \mathcal{P}_{w_{\rm los}}(w_{\rm los}|r_\perp, |r_\parallel|) \ . \tag{2.18}$$

For a generic x,

$$\mathcal{P}_{w_\parallel}(x \mid \boldsymbol{r}) = \begin{cases} \mathcal{P}_{w_{\rm los}}(\ \ x \mid r_\perp, |r_\parallel|) & \text{if } r_\parallel \geq 0 \ , \\ \mathcal{P}_{w_{\rm los}}(-x \mid r_\perp, |r_\parallel|) & \text{if } r_\parallel < 0 \ , \end{cases} \tag{2.19}$$

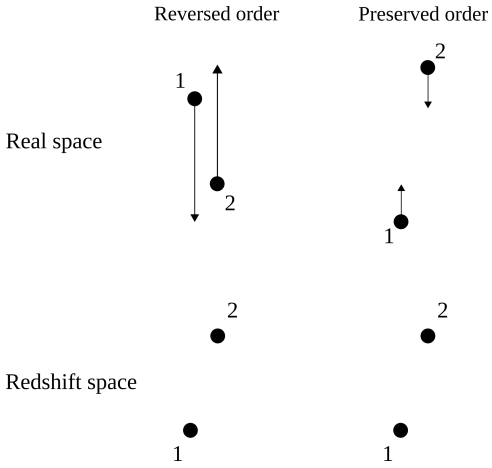

Figure 2.3: Schematic diagram illustrating how large relative infall velocities can reverse the order of a pair between real and redshift space (left-hand panel). The vertical arrows represent the los component of the individual velocities (assumed equal for simplicity). For comparison, the right-hand panel, shows a pair that preserves its order.

i.e. $\mathcal{P}_{w_{\rm los}}$ coincides with the positive $r_\parallel$ branch of $\mathcal{P}_{w_\parallel}$. Substituting in equation (2.4) and breaking the integral into two parts running over the positive and negative values of $r_\parallel$ respectively, we obtain

$$1+\xi_{\rm s}(s_\perp,s_\parallel)=\int_0^{+\infty}\left[1+\xi\left(r\right)\right]\,g(s_\parallel,|r_\parallel|,r_\perp)\,\mathrm{d}|r_\parallel|\,, \tag{2.20}$$

with

$$g(s_\parallel,|r_\parallel|,r_\perp)=\mathcal{P}_{w_{\rm los}}(-s_\parallel-|r_\parallel||r_\perp,|r_\parallel|)+\mathcal{P}_{w_{\rm los}}(s_\parallel-|r_\parallel||r_\perp,|r_\parallel|)\,. \tag{2.21}$$

This is the correct equation of the streaming model for unordered pairs. It can be re-written in compact form using the signed $r_\parallel$,

$$1+\xi_{\rm s}(s_\perp,s_\parallel)=\int_{-\infty}^{+\infty}\left[1+\xi_{\rm r}(r)\right]\mathcal{P}_{w_{\rm los}}[(s_\parallel-r_\parallel)\,\mathrm{sgn}(r_\parallel)\mid\mathbf{r}]\,\mathrm{d}r_\parallel\,, \tag{2.22}$$

which allows a direct comparison with equation (2.14) for the ordered pairs. As we illustrate in Fig. 2.3, the first term on the right-hand side of equation (2.21) and the region with $r_\parallel<0$ in equation (2.22) refer to pairs that reverse their order between real and redshift space (i.e. having separation $s_\parallel>0$ in redshift space and $-|r_\parallel|<0$ in real space). On the other hand, the remaining terms are connected with pairs that preserve their ordering (i.e. both $s_\parallel$ and $r_\parallel$ are positive).

Pair reversal takes place more frequently at smaller real-space separations. The reason is twofold: i) smaller pairwise velocities are needed to swap the order of a pair when $r_\parallel$ is small; ii) the distribution of $w_{\rm los}$ shows a larger mean infall velocity and is more negatively skewed at small r. A detailed discussion on the impact of pair reversal on ξ_s is presented in Appendix 2.A.1.

2.3.4 Applications of the streaming model

Pairwise velocities: mean infall and dispersion

Most of the discussion on pairwise velocities focus on their low-order statistical moments. In our notation, the mean pairwise velocity is defined as

$$\boldsymbol{v}_{12}(\mathbf{r}) = \frac{\int (\boldsymbol{v}_\mathrm{B} - \boldsymbol{v}_\mathrm{A})\, f_2\left(\boldsymbol{r}, \boldsymbol{v}_\mathrm{A}, \boldsymbol{v}_\mathrm{B}\right)\, \mathrm{d}^3 v_\mathrm{A}\, \mathrm{d}^3 v_\mathrm{B}}{\bar{n}^2\,[1+\xi(r)]}\,, \tag{2.23}$$

which, in the literature, is often written in the single-stream fluid approximation as (e.g. Juszkiewicz, Fisher and Szapudi, 1998; B. A. Reid and M. White, 2011)

$$\boldsymbol{v}_{12}(\mathbf{r}) = \frac{\langle (\boldsymbol{v}_\mathrm{B} - \boldsymbol{v}_\mathrm{A})\,[1+\delta(\boldsymbol{x}_\mathrm{A})]\,[1+\delta(\boldsymbol{x}_\mathrm{B})]\rangle}{1+\xi(r)}\,. \tag{2.24}$$

By symmetry, $\boldsymbol{v}_{12}(\mathbf{r}) = v_{12}(r)\,\mathbf{r}/r$ and the sign of $v_{12}(r)$ indicates whether the elements of a pair, on average, approach each other or not. For a set of self-gravitating particles, $v_{12}(r)$ regulates the growth of the 2-point correlation function through the pair-conservation equation that derives from the BBGKY hierarchy (Davis and Peebles, 1977).

Similarly, the second moment of the pairwise velocities defines a tensor of components,

$$\Sigma_{ij}(\boldsymbol{r}) = \frac{\int \Delta_i\, \Delta_j f_2\left(\boldsymbol{r}, \boldsymbol{v}_\mathrm{A}, \boldsymbol{v}_\mathrm{B}\right)\, \mathrm{d}^3 v_\mathrm{A}\, \mathrm{d}^3 v_\mathrm{B}}{\bar{n}^2\,[1+\xi(r)]}\,, \tag{2.25}$$

where $\Delta_i = (\boldsymbol{v}_\mathrm{B} - \boldsymbol{v}_\mathrm{A}) \cdot \hat{\boldsymbol{x}}_i$ denotes the Cartesian components of the pairwise velocity vectors with respect to a right-handed orthonormal basis $\hat{\boldsymbol{x}}_i$. By symmetry, Σ_{ij} can be expressed in terms of a few scalar functions

$$\Sigma_{ij}(\boldsymbol{r}) = \frac{\left[\Xi(r) + \frac{2}{3}\sigma_v^2\right]\delta_{ij} + \left[\Pi(r) - \Xi(r)\right]\frac{r_i\, r_j}{r^2}}{1+\xi(r)}\,, \tag{2.26}$$

where $\sigma_v^2 = \int v^2\, f_1\, \mathrm{d}^3 v / \int f_1\, \mathrm{d}^3 v$ denotes the mean square value of the peculiar particle velocity while $\Pi(r)$ and $\Xi(r)$ represent the contributions of correlations for the velocity components along $\hat{\boldsymbol{r}}$ and in the transverse directions, respectively (Davis and Peebles, 1977). The second moment of the pairwise-velocity component along the separation vector is

$$\Sigma_{ij}(\boldsymbol{r})\,\hat{r}_i\,\hat{r}_j = \frac{(2/3)\,\sigma_v^2 + \Pi(r)}{1+\xi(r)}\,, \tag{2.27}$$

while along any direction perpendicular to it ($\hat{\boldsymbol{t}} \cdot \hat{\boldsymbol{r}} = 0$)

$$\Sigma_{ij}(\boldsymbol{r})\,\hat{t}_i\,\hat{t}_j = \frac{(2/3)\,\sigma_v^2 + \Xi(r)}{1+\xi(r)}\,. \tag{2.28}$$

The second moment tensor is isotropic if $\Pi(r) = \Xi(r)$. When this is not the case, the velocity dispersion along the line of sight depends on the pair orientation with respect to it (see Section 2.4.2 for further details).

Some historical remarks

Since the advent of galaxy redshift surveys, the streaming model has been a key tool to interpret clustering data. As we briefly mentioned in the introduction, in its early applications, it was used to make inferences about galaxy motions which are otherwise difficult to probe. The anisotropies in $\xi_{\rm s}(s_\perp, s_\parallel)$ at small $s_\perp$ were translated into a typical pairwise velocity dispersion, σ_{12}, by assuming that (Peebles, 1976; Peebles, 1979)

$$\mathcal{P}_{w_\parallel}(w_\parallel \mid \boldsymbol{r}) = \frac{1}{\sqrt{2}\sigma_{12}} \exp\left(-\frac{\sqrt{2}\,|w_\parallel|}{\sigma_{12}}\right), \tag{2.29}$$

independently on the real-space separation. Quoting Peebles, 1976, the expression above was 'meant only as a simple fitting function with one free parameter'. It was actually motivated by theoretical considerations and early N-body simulations showing that, on the spatial separations of interest: (i) the velocity PDF should be only weakly scale dependent, (ii) the second-moment tensor should be approximately isotropic and (iii) the pairwise velocity dispersion should be significantly larger than the mean. The small data sets available at the time (containing a few hundred galaxy redshifts) were found to be consistent with these assumptions.

As samples grew bigger and the analysis was extended to larger $s_\perp$, it was no longer possible to neglect the so-called 'streaming motions' i.e. the fact that the average relative velocity between galaxy pairs at fixed spatial separation does not vanish. If clustering is stable on small scales (i.e. galaxy groups are in virial equilibrium), then $v_{12}(r) = -H\,r$. On the other hand, for large separations, it is expected that $v_{12}(r) \to 0$. In between these asymptotic regimes, $v_{12}(r) < 0$ and a net gravitational infall should be observed. As a natural generalization of equation (2.29), several authors then assumed that

$$\mathcal{P}_{w_\parallel}(w_\parallel \mid \boldsymbol{r}) = \frac{1}{\sqrt{2}\sigma_{12}} \exp\left[-\frac{\sqrt{2}\,|w_\parallel - \bar{w}_\parallel(\boldsymbol{r})|}{\sigma_{12}}\right], \tag{2.30}$$

where $\bar{w}_\parallel(\boldsymbol{r}) = \boldsymbol{v}_{12}(\mathbf{r}) \cdot \hat{\boldsymbol{z}} = v_{12}(r)\,\hat{\boldsymbol{r}} \cdot \hat{\boldsymbol{z}}$ denotes the line-of-sight component of the mean pairwise velocity and $v_{12}(r)$ is written as a function of $\xi(r)$ using approximate solutions to the pair-conservation equation calibrated against N-body simulations (Davis and Peebles, 1983; Bean et al., 1983; Hale-Sutton et al., 1989; Mo, Jing and Borner, 1993; Fisher et al., 1994; Zurek et al., 1994; Marzke et al., 1995; Loveday et al., 1996; Shepherd et al., 1997; Guzzo, Strauss et al., 1997; Jing, Börner and Suto, 2002; Zehavi et al., 2002; C. Li, Jing, Kauffmann, Börner, Kang et al., 2007).

The larger volumes covered by the current generation of redshift surveys lead to much more accurate measurements of galaxy clustering thus providing strong motivation for better models. Building upon the work by Fisher, 1995, B. A. Reid and M. White, 2011 proposed a Gaussian approximation for $\mathcal{P}_{w_\parallel}(w_\parallel \mid \boldsymbol{r})$ where the mean $v_{12}(r)\,\hat{\boldsymbol{r}} \cdot \hat{\boldsymbol{z}}$ and the scale-dependent dispersion $\sigma_{12}(\boldsymbol{r})$ are computed using standard perturbation theory by assuming that haloes are linearly biased tracers of the matter. At the same time, the real-space correlation function of the galaxies is evaluated using Lagrangian perturbation theory and also including higher-order bias terms. Finally, in order to account for the incoherent motion of galaxies within their host haloes (and also to mitigate the imperfections of perturbative calculations), the actual variance of the Gaussian PDF is written as $\sigma^2(\boldsymbol{r}) = \sigma^2_{12}(\boldsymbol{r}) + \sigma^2_{\rm FoG}$ with $\sigma^2_{\rm FoG}$ a nuisance parameter over which one needs to marginalize. The GSM has been later extended to use velocity statistics for biased tracers computed within the Convolution Lagrangian

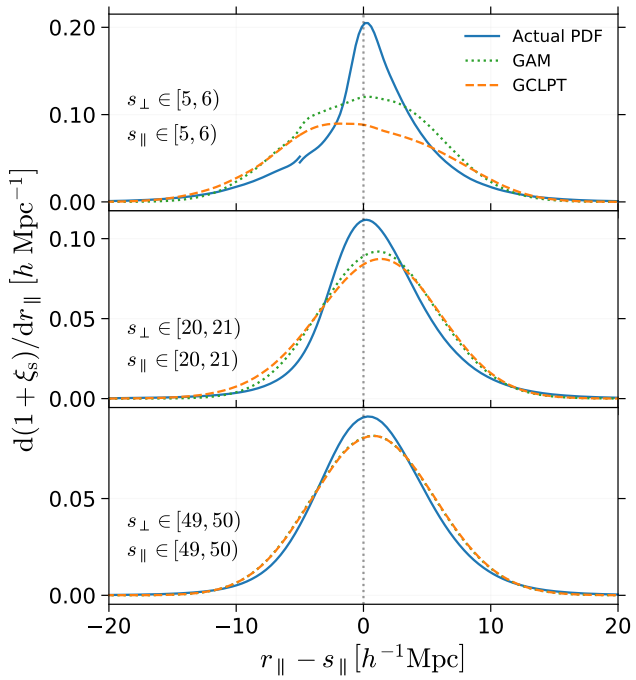

Figure 2.4: The integrand on the rhs of equation (2.4) is plotted as a function of $r_\parallel - s_\parallel$ for three redshift-space separation vectors (whose radial and transverse components are given in units of $h^{-1}\mathrm{Mpc}$). The bottom panel refers to scales that are usually treated perturbatively, the middle panel to intermediate scales, while the top panel considers separations in the fully non-perturbative regime. In each case, we show three curves corresponding to different assumptions for the PDF of pairwise velocities. The solid curve corresponds to the actual data for the DM-particle pairs in the W0 simulation at $z = 0$. The other curves are obtained by assuming a Gaussian PDF. For the dotted curve (GAM), the scale-dependent mean and variance are measured from the simulation while, for the dashed curve (GCLPT), they are estimated using CLPT. In all cases, we use the same real-space correlation function, $\xi(r)$, which has been measured from the N-body simulation.

Perturbation Theory (CLPT, L. Wang, B. Reid and M. White, 2014) and the Convolution Lagrangian Effective Field Theory (CLEFT, Vlah, Castorina and M. White, 2016). In its different versions, the GSM has been extensively applied to redshift surveys (B. A. Reid, Samushia et al., 2012; Samushia et al., 2014; Alam, Ho et al., 2015; Chuang, Pellejero-Ibanez et al., 2017; Satpathy et al., 2017).

Limitations of the Gaussian approximation

The GSM represents the state of the art in modelling RSD at the 2-point level. Considering DM haloes with masses between 10^{12} and $10^{13}\,h^{-1}\,\mathrm{M}_\odot$ at low redshift, L. Wang, B. Reid and M. White, 2014 showed that the two-point correlation $\xi_\mathrm{s}(\mathbf{s})$ predicted by the CLPT-based GSM agrees with N-body simulations to better than a few per cent for redshift-space separations larger than $\sim 20\,h^{-1}$ Mpc which are not too closely aligned with the line of sight (similar results are obtained for the CLEFT-based GSM, Vlah, Castorina and M. White, 2016). The accuracy of the model degrades rapidly on smaller scales. We find similar trends when we study the correlation of DM particles, although, in this case, the model already departs from the simulations on substantially larger scales (see below for more quantitative

information). It is instructive to investigate the origin of such behaviour and clarify the implications of the Gaussian ansatz for the pairwise-velocity PDF. To this goal, we focus on the DM particles in the W0 simulation at $z = 0$ as they form a much larger sample than the DM haloes and are thus less affected by statistical noise. In Fig. 2.4, we plot the integrand appearing in the rhs of equation (2.4) as a function of $r_\parallel - s_\parallel$ for three redshift-space separation vectors and using three different 'models' for $\mathcal{P}_{w_\parallel}(w_\parallel \mid \boldsymbol{r})$. The solid line is obtained by measuring the velocity PDF at different pair separation vectors directly from the simulation. The dotted line (GAM) corresponds to assuming a Gaussian PDF with the actual scale-dependent mean and variance measured in the simulation. Finally, the dashed line (GCLPT) uses CLPT to predict the mean and variance (up to an additive constant calibrated using simulations, see Section 2.4 and L. Wang, B. Reid and M. White, 2014 for further details) of the Gaussian PDF. In all cases, we do not compute $\xi(r)$ perturbatively but we measure it directly from the simulation. The top panel shows that both the Gaussian ansatz for $\mathcal{P}_{w_\parallel}$ and the CLPT calculations are very inaccurate at small scales. Integrating the different curves gives $\xi_\mathrm{s} = 0.64$ for the N-body based PDF while we obtain $\xi_\mathrm{s} = 0.70$ and 0.44 for the GAM and GCLPT models, respectively. The middle panel refers to a separation vector with components $s_\parallel = s_\perp \simeq 20.5\,h^{-1}$Mpc. In this case, pairs with $5 \lesssim r_\parallel \lesssim 35\,h^{-1}$Mpc contribute to ξ_s and those with $r_\parallel \simeq 20\,h^{-1}$Mpc give the largest signal. Both Gaussian approximations, however, reach their maximum for slightly larger values of $r_\parallel$ and give rise to less sharply peaked integrands in the streaming equation. Although the two curves based on the Gaussian approximations seem to be rather similar, once integrated, give rise to significantly different values of ξ_s. We find $\xi_\mathrm{s} = 0.049$ when the actual moments are used and $\xi_\mathrm{s} = 0.063$ for the CLPT predictions. This difference mainly originates from the regions on the lhs from the peak, i.e. for $r_\parallel < s_\parallel$ where perturbative calculations become less reliable. Note that the actual value of the redshift-space correlation is $\xi_\mathrm{s} = 0.048$ which nearly coincides with the best Gaussian approximation in spite of the fact that the corresponding integrals in Fig. 2.4 appear to be quite different. Even though we provided only one specific example here, we find that this serendipitous coincidence holds true for a broad range of redshift-space separation vectors $\mathbf{s}$. This result provides motivation for improving the GSM by combining it with enhanced estimates for the pairwise-velocity moments. However, the success of the GSM on these intermediate scales appears to be fortuitous as the model does not reproduce the correct shape of the integrand in the streaming equation. The bottom panel shows that the situation improves only slightly when we consider larger redshift-space separations. In this case, the CLPT calculations can be calibrated to accurately reproduce the first two moments of the pairwise velocities and no obvious difference can be noted between the GAM and GCLPT approximations. However, even at a separation of $s \simeq 70\,h^{-1}\mathrm{Mpc}$, the Gaussian models for the velocity PDF cannot accurately reproduce the shape of the function $\mathrm{d}(1+\xi_\mathrm{s})/\mathrm{d}r_\parallel$ measured in the simulation. In spite of this, once the integral over $r_\parallel$ is performed, they give values for ξ_s which are accurate at the few per cent level.

The aim of this paper is to introduce a more general fitting function for the pairwise-velocity PDF that, once inserted in the streaming model, provides more accurate results for the redshift-space correlation function than the GSM. The advantage is twofold: first, on large scales and in the era of precision cosmology, we would be able to make predictions that do not rely on fortuitous cancellations and, second, extending the accuracy of the streaming model to smaller spatial separations would allow us to probe modified gravity and interacting dark-energy models as mentioned in the introduction. Related work has been presented by Uhlemann, Kopp and Haugg, 2015; Bianchi, Chiesa and Guzzo, 2015 and Bianchi, Percival and Bel, 2016 who accounted for skewness in the PDF by using the

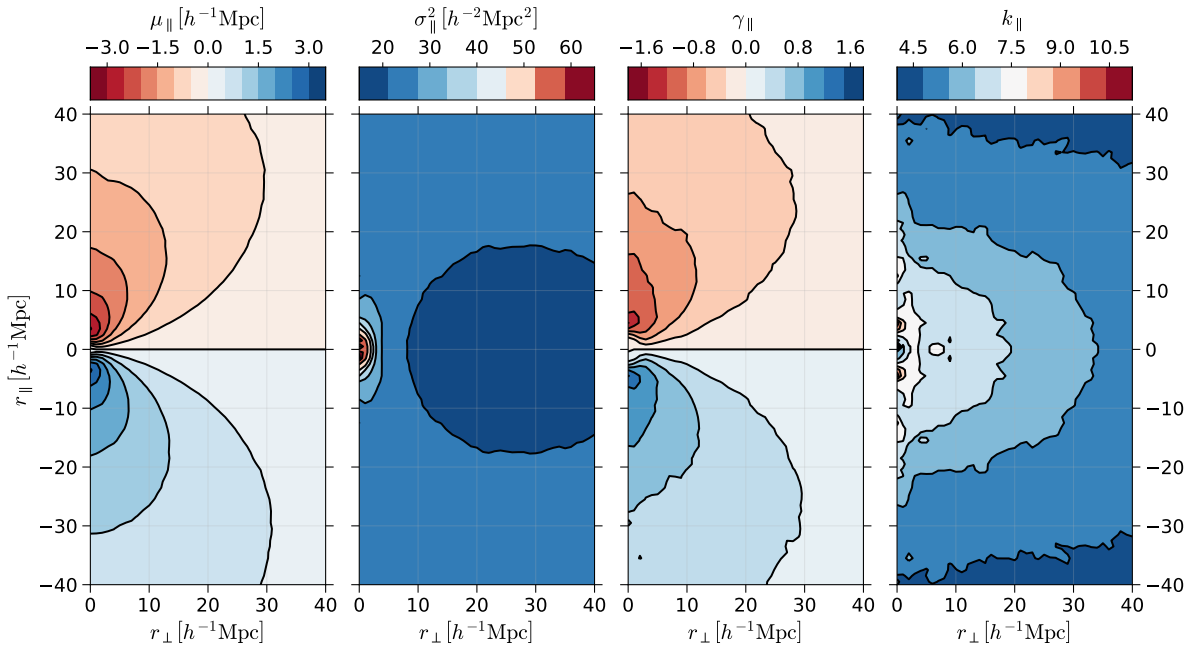

Figure 2.5: Normalised cumulants of the pairwise los velocity for ordered pairs of DM particles in the W0 simulation.

Edgeworth expansion around a Gaussian probability density and by superposing multiple Gaussian (or quasi-Gaussian) distributions, respectively.

2.4 Statistics of pairwise velocities

The streaming model is formulated in terms of $w_\parallel$ or $w_{\rm los}$ while analytical calculations (perturbative or not) generally deal with the radial and transverse components of the pairwise velocities. In this section, we derive the relation between the cumulants of these different components. In order to provide some illustrative examples, we compute several velocity statistics for the DM particles and the haloes in the W0 simulation at redshift $z = 0$.

2.4.1 Cumulants

In Fig. 2.5, we investigate how the first four normalised cumulants of $\mathcal{P}_{w_\parallel}$ for the DM particles, depend on the real-space separation vector $\mathbf{r}$. Specifically, we consider the mean $\mu_\parallel = \langle w_\parallel \rangle_{\rm c}$, the variance $\sigma^2_\parallel = \langle w^2_\parallel \rangle_{\rm c}$, the skewness $\gamma_\parallel = \langle w^3_\parallel \rangle_{\rm c}/\sigma^3_\parallel$ and the kurtosis $k_\parallel = \langle w^4_\parallel \rangle_{\rm c}/\sigma^4_\parallel$. As expected, the odd cumulants undergo parity inversion as the sign of $r_\parallel$ changes while the even cumulants are parity invariant. Note that the cumulants of $\mathcal{P}_{w_{\rm los}}$ can also be read from Fig. 2.5 by looking at the region with $r_\parallel > 0$. In this case, the mean velocity and the skewness are always negative meaning that $\mathcal{P}_{w_{\rm los}}$ is asymmetric as it is more likely to find infalling pairs at the scales we consider see also Scoccimarro, 2004. The velocity PDF is leptokurtic (i.e. $k > 3$) meaning that it has a sharper peak and heavier tails compared to a Gaussian distribution. Although both $|\gamma|$ and k decrease with increasing $r_\parallel$ and $r_\perp$,

$\mathcal{P}_{w_{\rm los}}$ always differs substantially from a Gaussian probability density.

2.4.2 Radial, transverse and los pairwise velocities

The peculiar shape of the contour levels in Fig. 2.5 is mainly regulated by the angle that the pair separation forms with the los. This can be shown as follows. The pairwise velocity of an ordered pair, $\boldsymbol{v}_2 - \boldsymbol{v}_1$, can be decomposed into radial (i.e. along the pair-separation vector) and transverse components:

$$w_{\rm r} = (\boldsymbol{v}_2 - \boldsymbol{v}_1) \cdot \hat{\boldsymbol{r}} \,, \tag{2.31}$$

$$\mathbf{w}_{\rm t} = (\boldsymbol{v}_2 - \boldsymbol{v}_1) - w_{\rm r}\, \hat{\mathbf{r}} \,. \tag{2.32}$$

In a homogenous and isotropic universe, the statistical properties of $w_{\rm r}$ and $\mathbf{w}_{\rm t}$ only depend on r. Introducing a preferential los direction, however, breaks the rotational invariance so that $\mathcal{P}_{w_\parallel}$ depends on both $r_\parallel$ and $r_\perp$. Let us consider the normal vector to the plane defined by the pair separation and the los,

$$\boldsymbol{n} = \hat{\boldsymbol{r}} \times \hat{\boldsymbol{z}} \,, \tag{2.33}$$

and form a right-handed orthonormal basis using $\hat{\mathbf{r}}$, $\hat{\mathbf{n}}$ and the additional unit vector $\hat{\mathbf{e}}$. Only the component of $\mathbf{w}_{\rm t}$ perpendicular to $\boldsymbol{n}$ (and thus parallel to $\hat{\mathbf{e}}$),

$$\boldsymbol{w}_{\rm e} = (\boldsymbol{w}_{\rm t} \cdot \hat{\boldsymbol{e}})\, \hat{\boldsymbol{e}} = (\boldsymbol{v}_2 - \boldsymbol{v}_1) - w_{\rm r}\, \hat{\boldsymbol{r}} - (\mathbf{w}_{\rm t} \cdot \hat{\boldsymbol{n}})\, \hat{\boldsymbol{n}} \,, \tag{2.34}$$

contributes to $w_\parallel$. By defining the angle θ so that $\cos\theta = \hat{\mathbf{r}} \cdot \hat{\boldsymbol{z}} = r_\parallel / r$, it follows that $\hat{\mathbf{e}} \cdot \hat{\boldsymbol{z}} = \pm \sin\theta$ depending on the relative orientation of the pair separation and the los. Eventually, we can write

$$w_\parallel = w_{\rm r} \cos\theta + w_{\rm p} \sin\theta \,, \tag{2.35}$$

with

$$w_{\rm p} = \mathrm{sgn}(\hat{\boldsymbol{e}} \cdot \hat{\boldsymbol{z}})\, w_{\rm e} \,. \tag{2.36}$$

The cumulants of $w_\parallel$ at fixed r and θ can then be expressed in terms of the cumulants and cross-cumulants of $w_{\rm r}$ and $w_{\rm p}$ at fixed r. It follows from equation (2.35) that

$$\langle w_\parallel^n \rangle_{\rm c} = \sum_{i_1=1}^{2} \sum_{i_2=1}^{2} \cdots \sum_{i_n=1}^{2} \langle w_{i_1} w_{i_2} \ldots w_{i_n} \rangle_{\rm c} \,, \tag{2.37}$$

where $w_1 \equiv w_{\rm r} \cos\theta$ and $w_2 \equiv w_{\rm p} \sin\theta$. Terms involving odd powers of $w_{\rm p}$ vanish due to statistical isotropy (i.e. the probability distribution of $w_{\rm p}$ is symmetric with respect to zero, reflecting the fact that all orientations of $\hat{\boldsymbol{r}}$ with respect to $\hat{\boldsymbol{z}}$ are equally likely). For the normalised cumulants shown in

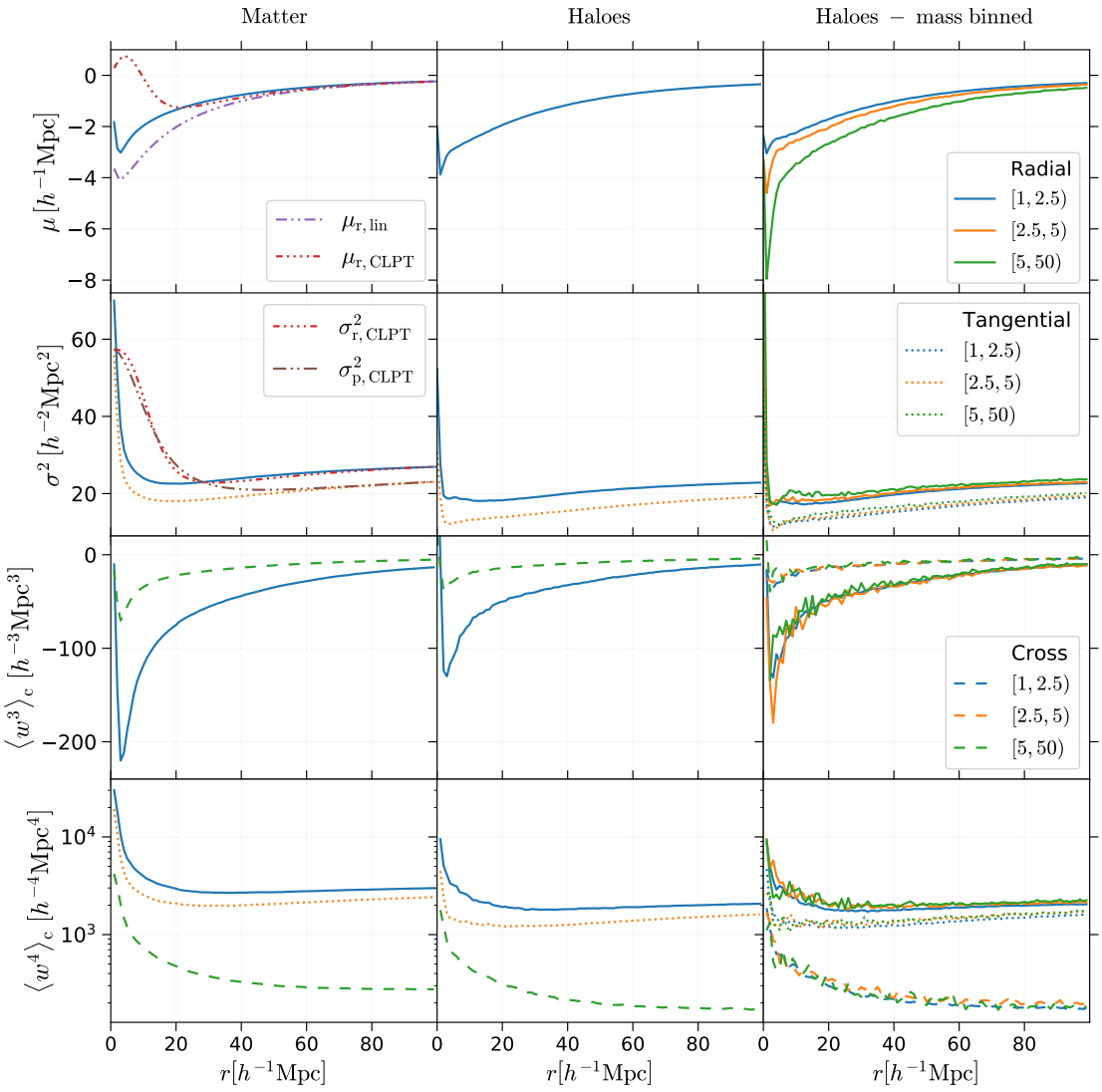

Figure 2.6: Cumulants and cross-cumulants of the radial and tangential pairwise velocities contributing to the first 4 normalised cumulants of $w_{\parallel}$, see equations (2.38) - (2.41). The solid, dotted and dashed lines represent the radial, tangential and cross components, respectively. In the left column, all quantities have been measured from the velocities of DM particles in the W0 simulation at $z = 0$. One-loop (and linear, for μ_r) CLPT predictions are also shown in the two topmost panels. A constant has been added to the CLPT results for σ^2_r and σ^2_p in order to match the simulation output at $r = 100\,h^{-1}$ Mpc. The middle column, shows the results for the bulk velocities of the DM haloes identified in the same simulation snapshot. Finally, the dependence of the results on the halo mass is investigated in the right column using different mass intervals indicated in units of $10^{13}h^{-1}\,\mathrm{M}_{\odot}$.

Fig. 2.5, we obtain:

$$\mu_{\parallel} = \mu_{\rm r} \, \cos\theta \; , \tag{2.38}$$

$$\sigma^2_{\parallel} = \sigma^2_{\rm r} \, \cos^2\theta + \sigma^2_{\rm p} \, \sin^2\theta \; , \tag{2.39}$$

$$\gamma_{\parallel} = \sigma^{-3}_{\parallel} \, \left[\langle w^3_{\rm r} \rangle_{\rm c} \cos^2\theta + 3 \, \langle w_{\rm r} \, w^2_{\rm p} \rangle_{\rm c} \, \sin^2\theta \right] \cos\theta \; , \tag{2.40}$$

$$k_{\parallel} = \sigma^{-4}_{\parallel} \, \Big\{ \langle w^4_{\rm r} \rangle_{\rm c} \, \cos^4\theta + \langle w^4_{\rm p} \rangle_{\rm c} \, \sin^4\theta + 6 \left[\langle w^2_{\rm r} \, w^2_{\rm p} \rangle_{\rm c} \, - 2 \, \mu_{\rm r} \, \langle w_{\rm r} \, w^2_{\rm p} \rangle_{\rm c} \right] \cos^2\theta \sin^2\theta \Big\} \; . \tag{2.41}$$

DM particles

In the left column of Fig. 2.6, we show the radial dependence of the different isotropic terms appearing in the equations above for the particles in the final snapshot ($z = 0$) of the W0 simulation. In the top row, we compare $\mu_{\rm r}$ measured in our simulation with the predictions of linear and one-loop Convolution Lagrangian Perturbation Theory (CLPT Carlson, B. Reid and M. White, 2013; L. Wang, B. Reid and M. White, 2014). In the second row, we plot $\sigma^2_{\rm r}$ and $\sigma^2_{\rm p}$ for the N-body particles and contrast them with the corresponding CLPT results at one loop (after shifting them vertically in order to match the simulation output at $r = 100\,h^{-1}$ Mpc). The figures indicate that state-of-the-art perturbative approaches qualitatively reproduce the scale dependence of the lowest-order cumulants for $r > 20 - 30\,h^{-1}$ Mpc. However, they provide accurate predictions only on much larger scales. Finally, the third and fourth rows present the various contributions to the skewness and kurtosis of $w_{\parallel}$. Note that the cross-cumulants of the correlated random variables $w_{\rm r}$ and $w_{\rm p}$ are sub-dominant but non-negligible.

DM haloes and pairwise velocity bias

We now contrast the previous results with the isotropic velocity statistics for the DM haloes identified at $z = 0$ in the W0 simulation. In the middle column of Fig. 2.6, we show the cumulants and cross-cumulants for the radial and tangential pairwise velocities measured using the halo bulk velocities. It is evident that halo pairs (that trace peaks in the density field) tend to approach each other at a slightly greater velocity than particle pairs (that also populate underdense regions where the velocity divergence is positive). Haloes have also smaller velocity dispersions, i.e. they trace a colder velocity field than the DM (see also Carlberg and Couchman, 1989; Couchman and Carlberg, 1992; Cen and Ostriker, 1992; Gelb and Bertschinger, 1994; Evrard, Summers and Davis, 1994; Summers, Davis and Evrard, 1995; Colıén, Klypin and Kravtsov, 2000). Following Carlberg, 1994, we introduce the pairwise velocity bias as the ratio between the halo and DM rms pairwise velocities. Its variation with the pair separation is shown in Fig. 2.7 for the radial and the tangential components of the velocity. In both cases, the 'antibias' assumes values ~ 0.8 on large scales and becomes very strong for $r < 15\,h^{-1}$ Mpc. Fig. 2.6 shows that also the higher-order cumulants for the haloes depart from those for the DM, especially at small separations. This reflects the fact that the shape of the pairwise velocity PDF is different for DM particles and haloes.

In the right column of Fig. 2.6, we investigate the dependence of the velocity cumulants on halo mass. More massive objects show larger mean infall velocities, dispersions, and fourth-order cumulants. On the other hand, we could not detect any mass dependence for the third-order cumulant. The

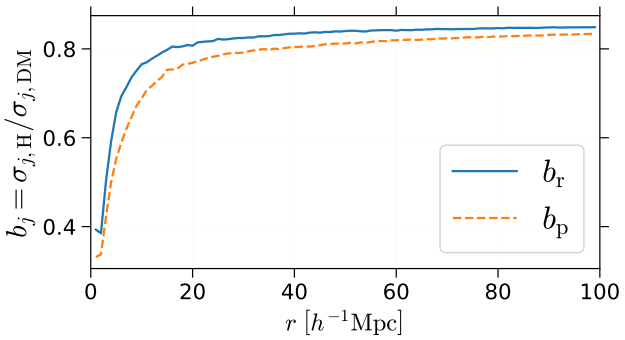

Figure 2.7: Pairwise-velocity bias for radial (solid) and tangential (dashed) motion.

latter, however, is always negative indicating the the halo velocity PDF is asymmetric (and thus non Gaussian) for all the separations and masses considered here. The amplitude of the fourth cumulant (invariably larger than 3) also shows that the PDF is leptokurtic with heavy tails.

2.4.3 Dissecting the pairwise-velocity distribution

The pairwise-velocity distribution of DM particles is shaped by the highly non-linear physics of gravitational instability and, for this reason, is very difficult to model analytically starting from first principles. A simplified approach relies on a phenomenological description that exploits the internal dynamics of DM haloes (e.g Sheth, 1996; Sheth and Diaferio, 2001; Tinker, 2007). To provide further insight into the importance of virialised structures, we investigate the halo contribution to $\mathcal{P}_{w_\mathrm{los}}$. We first classify the DM particles in our simulation according to whether they belong to haloes or to the field. We then partition $\mathcal{P}_{w_\mathrm{los}}$ into the contributions of halo-halo, halo-field and field-field pairs. Note that the concept of 'field particle' is not absolute as it depends on the mass resolution of the simulation and the minimum halo mass which is considered. In the W0 simulation, we classify 69.3 per cent of the particles as belonging to the field at $z = 0$. If we were resolving haloes with a mass $M < 1.2 \times 10^{13}\, h^{-1}\mathrm{M}_\odot$, then the fraction of field particles would decrease. Basically, our 'halo particles' account for the matter content of galaxy groups and clusters of galaxies. We show a few examples in Fig. 2.8. For real-space separations that are smaller than the typical halo size, $r < 1\, h^{-1}$ Mpc, halo-halo pairs give the dominant contribution to $\mathcal{P}_{w_\mathrm{los}}(w_\mathrm{los}|\mathbf{r})$ for all w_los whereas the field-field pairs only matter at very low w_los. For $r > 1\, h^{-1}$ Mpc, instead, the wings of $\mathcal{P}_{w_\mathrm{los}}$ are regulated by the halo-halo pairs while the core of the PDF is determined by the field-field pairs. Halo-field pairs are always subdominant. The field-field term peaks at $w_\mathrm{los} \simeq 0$, is negatively skewed (although it becomes practically symmetric for $r_\parallel < 1\, h^{-1}$ Mpc) and shows rapidly decaying exponential wings. Halo-halo pairs are characterized by larger mean infall velocities and velocity dispersions with respect to their field-field counterparts. The exponential tails of their negatively skewed distribution are also much fatter. In ξ_s, halo-halo pairs produce the FoG enhancement at small $s_\perp$, while field-field pairs completely dominate the signal at large s.

In Fig. 2.9, we further partition the halo-halo pairs into subsamples based on the halo mass (for simplicity, cross pairs formed by particles in different halo-mass bins are not considered here). This

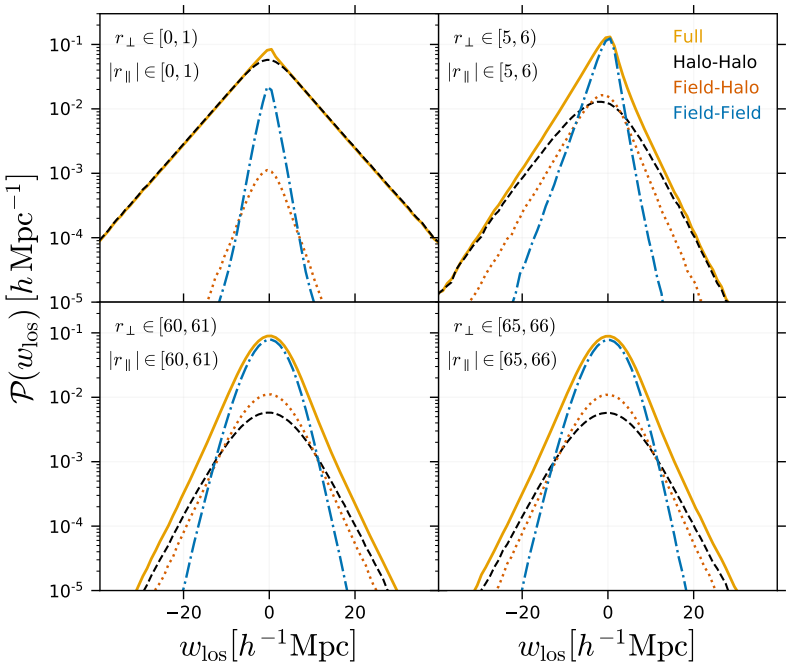

Figure 2.8: The los pairwise-velocity distribution of the particles in the W0 simulation at $z = 0$ is decomposed into simpler elements. The figure shows the contributions of halo-halo, field-halo and field-field pairs for six different real-space separation vectors (expressed in $h^{-1}\mathrm{Mpc}$).

procedure reveals that haloes of different masses[2] are characterized by very different pairwise-velocity distributions. Not only the velocity dispersion increases with the halo mass but also the mean infall velocity grows in magnitude. The skewness can even reverse sign for cluster-sized haloes. All this shows the complexity behind the overall distribution of $w_{\rm los}$ and clarifies why the PDF is so difficult to model accurately.

2.5 A new fitting function

It has been proposed that $\mathcal{P}_{w_{\rm los}}(w_{\rm los}|\mathbf{r})$ can be more easily described as a superposition of simpler elementary functions. The pairwise peculiar velocity dispersion depends on the (suitably defined) local density of the pairs (Kepner, Summers and Strauss, 1997) and its PDF can be modelled as a weighted sum of basic Gaussian terms evaluated at fixed halo masses and environment densities (Sheth, 1996; Sheth and Diaferio, 2001; Tinker, Weinberg and Zheng, 2006; Tinker, 2007). Integrating out the degrees of freedom due to the haloes, $\mathcal{P}_{w_{\rm los}}(w_{\rm los}|\mathbf{r})$ can be approximated as the superposition of univariate Gaussian (Bianchi, Chiesa and Guzzo, 2015) or quasi-Gaussian (Bianchi, Percival and Bel, 2016) distributions whose cumulants are drawn from a multivariate Gaussian distribution.

Although relatively new in the field of cosmology, similar techniques have actually been in use for over a century in statistics, finance and the theory of turbulence. The basic idea is to suitably

[2] We also considered additional variables as the halo spin parameter and triaxiality but their impact on $\mathcal{P}_{w_{\rm los}}$ was too small to be isolated.

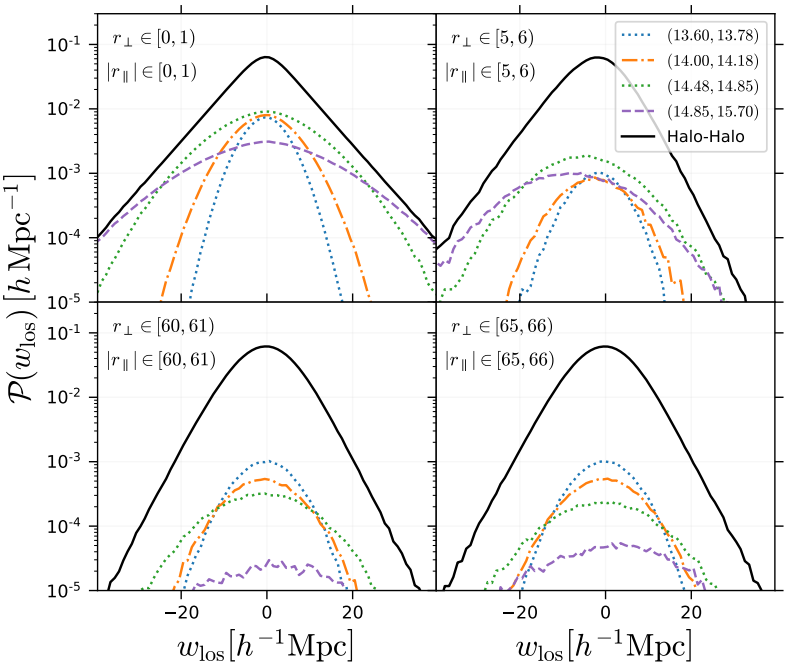

Figure 2.9: The los pairwise-velocity distribution of the halo-halo term is further partitioned into the contributions of various halo log-mass bins (the bin boundaries in $\log_{10}[M_{\rm vir}/(h^{-1}{\rm M}_\odot)]$ are indicated in the labels) for different real-space separation vectors (expressed in $h^{-1}{\rm Mpc}$). For simplicity, only 'diagonal' terms in which both particles reside in haloes of the same bin are shown.

combine uncountably many elements of a parametric family of PDFs to model heavy tailed and skewed distributions. In statistics, an (uncountable) 'mixture' or 'compound' probability distribution is defined by the relation

$$\mathcal{P}_x(x|\tau) = \int \mathcal{P}_x(x|\mathbf{f})\,\mathcal{P}_{\mathbf{f}}(\mathbf{f}|\tau)\,{\rm d}^n f = \mathcal{P}_x \circ \mathcal{P}_{\mathbf{f}}\ , \tag{2.42}$$

where x denotes the random variable of interest (subject to the condition τ) and $\mathbf{f}$ is a n-dimensional array containing the factors (or latent variables) that influence the distribution of x. The function $\mathcal{P}_x(x|\mathbf{f})$ gives the conditional probability density of x in a subpopulation with given $\mathbf{f}$ while the 'mixing distribution' $\mathcal{P}_{\mathbf{f}}$ is the joint probability density (or the statistical measure) of the factors. If $\mathcal{P}_x(x|\mathbf{f})$ is a Gaussian distribution, $\mathcal{N}_x(x;\mu,\sigma^2)$, then the variable x is called a mixture of Gaussians (or normals). Scale mixtures of normals (where mixing only involves σ^2) are widely used to model symmetric distributions with heavy tails. Location mixtures of normals (where mixing only involves μ) are commonly used to model skewed[3] distributions. Joint location and scale mixing gives rise to skewed distributions with heavy tails.

The above-mentioned models for $\mathcal{P}_{w_{\rm los}}(w_{\rm los}|\mathbf{r})$ can be phrased in this language. For instance, Bianchi, Chiesa and Guzzo, 2015 assume that $w_{\rm los}$ is a joint location and scale mixture of Gaussians with a bivariate Gaussian mixing distribution. In this case, the scatter in μ and σ is meant to represent

[3] Note, however, that a location mixture with Gaussian mixing distribution yields another Gaussian.

physical variability due to some latent (but not-so-well-specified) environmental density. This method compresses the information contained in $\mathcal{P}_{w_{\rm los}}(w_{\rm los}|\mathbf{r})$ into five parameters (the mean values for μ and σ and the three elements of their covariance matrix) that change smoothly with $\mathbf{r}$. Although the model matches well the outcome of numerical simulations on large scales, it has two drawbacks: i) by definition, σ is non negative and thus cannot follow a Gaussian distribution[4]; ii) the resulting $\mathcal{P}_{w_{\rm los}}(w_{\rm los}|\mathbf{r})$ cannot reproduce the large skewness measured at small separations ($r < 5 - 10\,h^{-1}$ Mpc depending on the redshift) for particles and haloes in N-body simulations (Bianchi, Percival and Bel, 2016). For this reason, Bianchi, Percival and Bel, 2016 replace the mixture of Gaussians with a mixture of skewed quasi-Gaussians obtained by applying the Edgeworth expansion to first order. However, in order to limit the number of degrees of freedom of the model, the skewness of $\mathcal{P}_x(x|\mathbf{f})$ is not used as a third factor over which the mixing is performed but is deterministically linked to the variances of σ and μ by means of an ansatz that introduces an additional free parameter.

While these recent efforts have led to the development of tools that can closely approximate $\mathcal{P}_{w_{\rm los}}(w_{\rm los}|\mathbf{r})$ on a wide range of scales, they are based on to a phenomenological description that provides little insight into the underlying physics. At the current stage of development, the models do not have predictive power. They essentially offer a language and a convenient class of fitting functions that can be used to describe the output of simulations with different gravity models and retrieve information on the cosmological parameters and the law of gravity from the observed $\xi_{\rm s}$ (assuming a functional form for the scale dependence of the model parameters). Their complexity, however, is growing rapidly and, as we discussed above, ad hoc assumptions are required to limit their degrees of freedom while extending their range of validity. Given this premise, we follow here a pragmatic and complementary approach by proposing a fitting function for $\mathcal{P}_{w_{\rm los}}(w_{\rm los}|\mathbf{r})$ that closely reproduces the features seen in N-body simulations and provides an excellent fit to them at all scales. For this purpose, we search the statistics literature for a family of analytic PDFs with the following characteristics: i) unimodality; ii) presence of quasi-exponential tails; iii) highly tunable low-order cumulants (in particular skewness); iv) possibility of reducing to the Gaussian distribution in some limit. We end up selecting the generalised hyperbolic distribution (GHD) which will be precisely defined in the next section. As in Peebles, 1976 and B. A. Reid and M. White, 2011, we do not give any physical motivation in support of our choice but we note that, interestingly enough, the GHD describes a particular mixture of normals.

2.5.1 The generalised hyperbolic distribution

The inverse Gaussian distribution

Let us consider a one-dimensional standard Wiener process with drift $\nu \in \mathbb{R}_{>0}$ and diffusion coefficient $\sigma \in \mathbb{R}_{>0}$. At time t, the position x of a Brownian particle follows the distribution $\mathcal{N}_x(x; \nu t, \sigma^2 t)$. The first-passage time of the level $\ell > 0$ by a Brownian walker is distributed as[5] Schrödinger, 1915

$$f_t(t; \ell, \nu, \sigma) = \frac{\ell}{\sqrt{2\pi}\sigma}\, t^{-3/2}\, \exp\left[-\frac{(\ell - \nu t)^2}{2\sigma^2 t}\right] . \tag{2.43}$$

[4] To address this issue, Bianchi, Percival and Bel, 2016 truncate the σ distribution at zero and renormalise it to account for the probability in the Gaussian tail with negative support.

[5] In cosmology, this PDF has been used by Bond, Cole et al., 1991 to solve the cloud-in-cloud problem in the excursion-set model for the halo mass function.

When expressed in terms of the parameters $\mu = \ell/\nu$ and $\gamma = \ell^2/\sigma^2$, this equation defines the 'inverse Gaussian distribution' (see e.g. Chhikara and Folks, 1989; Seshadri, 1999, for a comprehensive review of its properties),

$$\mathcal{I}_t(t;\mu,\gamma) = \left(\frac{\gamma}{2\pi}\right)^{1/2} t^{-3/2} \exp\left[-\frac{\gamma\,(t-\mu)^2}{2\mu^2 t}\right] . \tag{2.44}$$

This PDF provides a classic model for non-negative, unimodal and positively skewed data and is widely employed to perform lifetime and survival studies in ecology, engineering, finance, law and medicine. The mean of the distribution coincides with the location parameter μ, while the variance (μ^3/γ), skewness ($3\sqrt{\mu/\gamma}$) and kurtosis ($15\mu/\gamma$) also depend on the scale parameter γ. The name inverse Gaussian was coined by Tweedie, 1956 and only refers to the fact that, while the Gaussian distribution describes the distribution of x at fixed t, $\mathcal{I}_t$ gives the PDF of the time at which the particles first cross a fixed position.

Generalised inverse Gaussian distribution

In the 1940s and 1950s, a larger family of unimodal PDFs with positive support was introduced. Since this class includes the inverse Gaussian distribution as a special case, it now goes under the name of the 'generalised inverse Gaussian distribution' (Jørgensen, 1982). The corresponding PDF for the random variable $t > 0$ is

$$\mathcal{G}_t(t;\lambda,\chi,\psi) = \frac{(\psi/\chi)^{\lambda/2}}{2\,K_\lambda(\sqrt{\psi\chi})}\, t^{\lambda-1} \exp\left[-\frac{1}{2}\left(\psi t + \frac{\chi}{t}\right)\right] , \tag{2.45}$$

where $\lambda \in \mathbb{R}$, $\chi \in \mathbb{R}_{>0}$, $\psi \in \mathbb{R}_{>0}$ and K_λ is the modified Bessel function of the second kind with order λ (Abramowitz and Stegun, 1972). For $\lambda = -1/2$, $\psi = \gamma/\mu^2$ and $\chi = \gamma$, equation (2.45) reduces to the inverse Gaussian distribution given in equation (2.44). The generalised inverse Gaussian distribution can be interpreted as the distribution of the first passage time or, depending on the sign of λ, the last exit time of more complicated diffusion processes than Brownian motion (Vallois, 1991). Note that, for large values of t, $\mathcal{G}_t$ has a thin tail $\propto t^{\lambda-1}\exp(-\psi t/2)$. Another interesting property is that, if t follows $\mathcal{G}_t(t;\lambda,\chi,\psi)$, then t^{-1} follows $\mathcal{G}_{t^{-1}}(t^{-1};-\lambda,\psi,\chi)$. In analogy with $\mathcal{I}_t$, the generalised inverse Gaussian distribution finds many direct applications in risk assessment and queue modelling. Moreover, it is commonly used as a mixing distribution whenever there is the need for skewed weighting. This practice was initiated by Sichel, 1974 who used mixtures of Poisson distributions to model the distribution of sentence lengths and word frequencies.

Normal variance-mean mixtures

Let us return to the Wiener process with drift we introduced in Section 2.5.1. This time, however, we assume that the Brownian particles start from $x = \alpha \in \mathbb{R}$ at $t = 0$. At a given time $t > 0$, the position of a random Brownian walker is then $x = \alpha + \nu t + \sigma\sqrt{t}\,g$ where g is a Gaussian random variable with zero mean and unit variance. Let us now introduce a second random variable $p > 0$ which is independent of g and follows a generic distribution $\mathcal{P}_p$. We use p to pick random times at which we sample the positions of the Brownian particles. This leads us to consider the random

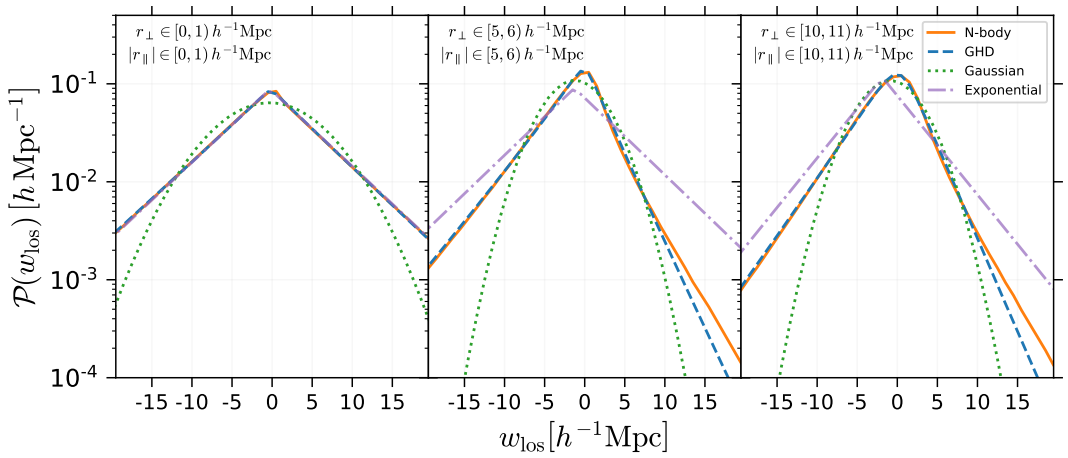

Figure 2.10: The los pairwise velocity distribution for the DM particles in the W0 simulation at $z = 0$ (solid) is compared with the best-fitting GH (dashed), exponential (dot-dashed) and Gaussian (dotted) approximations for three different pair-separation distances in real space.

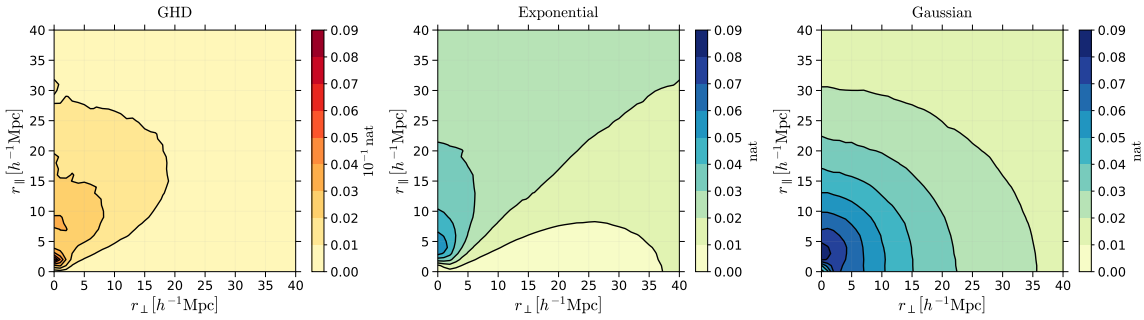

Figure 2.11: KL divergence for the GHD (left), exponential (middle) and Gaussian (right) best-fitting functions with respect to the los pairwise velocity distribution measured in the simulation. The reported values are expressed in natural units of information. Note that the color bar in the left panel is compressed by a factor of 10 compared with the middle and right panel.

variable $x = \alpha + \beta p + \sigma\sqrt{p}\,g$ which is a non-linear combination of g and p. Its PDF,

$$\mathcal{P}_x(x) = \mathcal{N}_x(x; \alpha + \beta\, p, \sigma^2\, p) \circ \mathcal{P}_p(p)\ , \tag{2.46}$$

is called a normal variance-mean mixture (Barndorff-Nielsen, Kent and Sorensen, 1982). A theorem shows that if p is unimodal then so is x (Yu, 2011).

The generalised hyperbolic distribution

A Gaussian PDF plotted on a semi-logarithmic graph describes a parabola. Although the frequency distribution of many empirical phenomena shows this property, there exist cases in which an hyperbola provides a much better description than a parabola due to the presence of exponential tails. A classic example is the log-size distribution of sand grains in natural aeolian deposits (Bagnold, 1941) and

many others arise particularly in finance. The name 'hyperbolic distributions' has been coined to designate this class of probability densities. The very first analytical example of such a PDF was derived in physics by calculating the distribution of particle velocities in an ideal relativistic gas (Jüttner, 1911).

The GHD is a larger family of PDFs that includes the hyperbolic distributions as a particular case. It was introduced by Barndorff-Nielsen, 1977 in order to model the log-size distribution of sand grains and is defined as a normal variance-mean mixture in which $\sigma = 1$ and $\mathcal{P}_p(p) = \mathcal{G}_p(p; \lambda, \delta^2, \alpha^2 - \beta^2)$. Its PDF takes the form (Prause, 1999)

$$\begin{aligned} \mathcal{H}_x(x; \alpha, \beta, \delta, \lambda, \mu) = \mathcal{N}_x(x; \mu + \beta\, p, p) \circ \mathcal{G}_p(p; \lambda, \delta^2, \sqrt{\alpha^2 - \beta^2}) = \\ C \left[\delta^2 + (x-\mu)^2\right]^{\frac{\lambda - 1/2}{2}} e^{\beta(x-\mu)}\, K_{\lambda - \frac{1}{2}}\left(\alpha \sqrt{\delta^2 + (x-\mu)^2}\right) , \end{aligned} \tag{2.47}$$

with normalisation constant

$$C = \frac{\left(\alpha^2 - \beta^2\right)^{\frac{\lambda}{2}}}{\sqrt{2\pi}\, \alpha^{\lambda - 1/2}\, \delta^{\lambda}\, K_{\lambda}\left[\delta \sqrt{\alpha^2 - \beta^2}\right]} . \tag{2.48}$$

The domain of variation of the parameters is

$$\begin{aligned} &\delta \geq 0, \;\; |\beta| < \alpha, \quad \text{if } \lambda > 0 , \\ &\delta > 0, \;\; |\beta| < \alpha, \quad \text{if } \lambda = 0 , \\ &\delta > 0, \;\; |\beta| \leq \alpha, \quad \text{if } \lambda < 0 . \end{aligned} \tag{2.49}$$

It is not easy to isolate the impact of each of them and several alternative parameterizations of the GHD have been introduced to alleviate this problem. Broadly speaking, λ defines various subclasses and influences the tails, α modifies the shape (i.e. variance and kurtosis), β the skewness, δ the scale and μ shifts the mean value. A convenient property of the GHD is that it reduces to several named distributions in the appropriate limit. For example, it gives the hyperbolic distribution for $\lambda = 1$ and becomes a Gaussian distribution with variance δ/α when both α and δ tend to infinity (Hammerstein, 2011).

The GHD shows semi-heavy tails (Barndorff-Nielsen and Blaesild, 1981),

$$\mathcal{H}_x \sim |x|^{\lambda - 1} \exp(-\alpha|x| + \beta x) \quad \text{as} \quad x \to \pm\infty , \tag{2.50}$$

and all its moments exist. The moment generating function is

$$M(x) = e^{\mu x} \left[\frac{\alpha^2 - \beta^2}{\alpha^2 - (\beta + x)^2}\right]^{\lambda/2} \frac{K_{\lambda}\left(\delta \sqrt{\alpha^2 - (\beta + x)^2}\right)}{K_{\lambda}\left(\delta \sqrt{\alpha^2 - \beta^2}\right)} , \tag{2.51}$$

with $|\beta + x| < \alpha$ which follows from equation (2.49). Explicit expressions for the first four moments and cumulants are given in Barndorff-Nielsen and Blaesild, 1981.

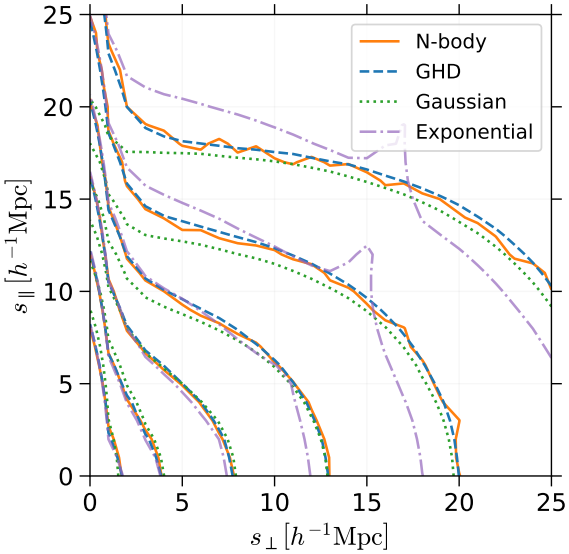

Figure 2.12: The redshift-space correlation function ξ_s for the particles in our N-body simulations (solid) is compared with the outcome of the streaming model obtained by fitting either a GHD (dashed), a Gaussian distribution (dotted) or an exponential (dash-dotted) to $\mathcal{P}_{w_\mathrm{los}}(w_\mathrm{los}|\mathbf{r})$.

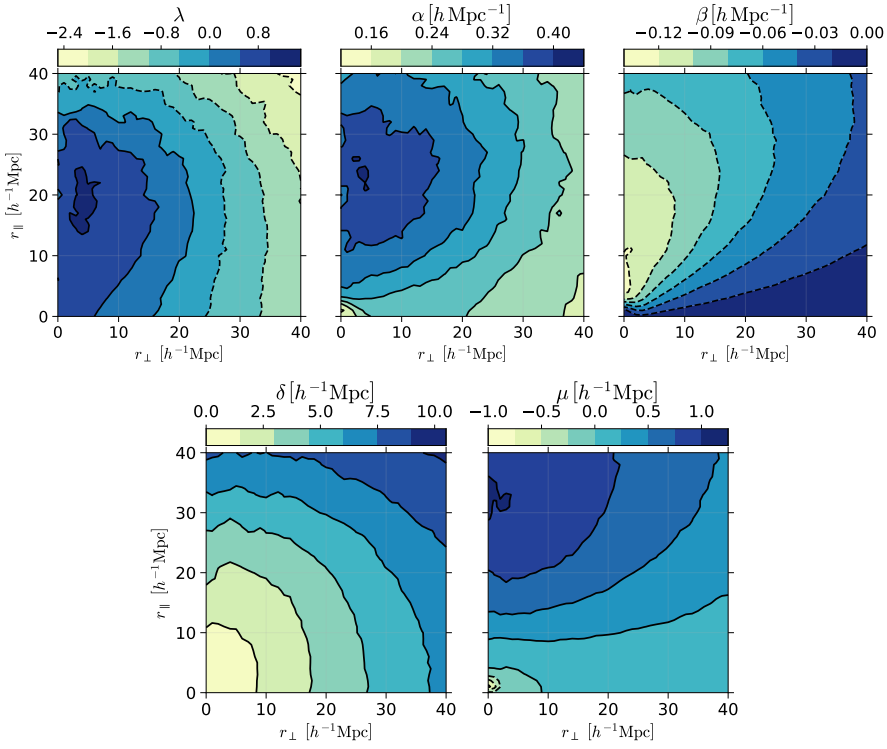

Figure 2.13: Best-fitting parameters of the GHD as a function of $r_\parallel$ and $r_\perp$.

2.5.2 Application to pairwise velocities

DM particles

In Fig. 2.10, we show that the GHD (dashed line) provides a very good fit to the histogram of $w_{\rm los}$ extracted from the W0 simulation (solid line). The optimal values for the parameters have been determined assuming (symmetrised) Poisson errors (Gehrels, 1986) and using least-squares fitting with a Markov Chain Monte Carlo sampler (we have checked for a few separations that this method gives consistent results with a maximum-likelihood analysis which is time consuming given the huge number of particle pairs). Our results show that the GHD accurately describes $\mathcal{P}_{w_{\rm los}}$ around the mode and in the negative tail while it slightly underestimates the PDF in the positive tail. The improvement with respect to Gaussian fits (dotted lines) is dramatic as the normal distribution cannot match the exponential tails seen in the simulation. For very small spatial separations, the exponential distribution given in equation (2.30) also provides a very good fit (dot-dashed lines). However, the agreement with the simulation data rapidly decreases with increasing r as the model has the wrong shape around the mode of the distribution. A more quantitative analysis is performed in Fig. 2.11 where we compare the information loss associated with the GHD, exponential and Gaussian approximations. Shown is the Kullback-Leibler (KL) divergence between the actual PDF measured in the simulations and the three approximations as a function of the real-space separation of the pairs. This quantity provides a measure of goodness of fit. For the range of separation vectors shown in Fig. 2.11, the information loss associated with the Gaussian approximation is always at least one order of magnitude larger than for the GHD. This property persists also on larger scales. Similar conclusions can be drawn comparing the exponential and the GHD approximations, although, in this case, the fits are of similar quality at very small separations ($r_\parallel < 1\,h^{-1}$ Mpc and $r_\perp < 15\,h^{-1}$ Mpc). Note that the GHD compression is nearly lossless at all scales.

Finally, in Fig. 2.12 we show the redshift-space correlation function obtained with the streaming model by inserting the best-fitting GHD in equation (2.22) together with the real-space correlation function extracted from the simulation. Our results (dashed lines) provide an excellent description of the redshift-space correlation measured in the simulation (solid lines). For $s > 5\,h^{-1}$ Mpc, deviations are comparable with the Poisson error for $\xi_{\rm s}$ which is always between one and a few per cent. On smaller scales, where the Poisson error becomes substantially sub per cent, one starts noticing statistically significant deviations at a few per cent level (not visible in the plot). For comparison, we also show the results obtained using the Gaussian and exponential fits for $\mathcal{P}_{w_{\rm los}}$. The Gaussian model (dotted lines) shows large systematic deviations on small scales and matches the simulations (at the level of the Poisson errors) only for $s_\parallel > 20\,h^{-1}$ Mpc and $s_\perp > 5\,h^{-1}$ Mpc. The exponential model[6] (dot-dashed lines), on the other hand, is accurate only at small $s_\perp$.

The high fidelity of the GHD fit comes at the price of using five free parameters. Their marked scale dependence (see Fig. 2.13) represents a severe limitation for future practical applications that aim to interpret observational data. We note, however, that the best-fitting parameters at different $\mathbf{r}$ tightly cluster along a flattened sequence in five-dimensional space. By applying a principal component analysis to the standardised variables, we find that the first three components account for 99.8 per cent of the variance. We thus fit again the distribution of $w_{\rm los}$ in the simulation using only three free

[6] The features that are noticeable in the contour map of $\xi_{\rm s}$ at $s_\parallel \simeq s_\perp$ are caused by discontinuities in $\bar{w}_\parallel$ and σ_{12} as a function of $r_\parallel$ and $r_\perp$. In fact, the posterior probability density of these parameters is bimodal for a range of real-space separations and we selected the peak with the highest integrated probability to draw the dot-dashed lines in Fig. 2.12.

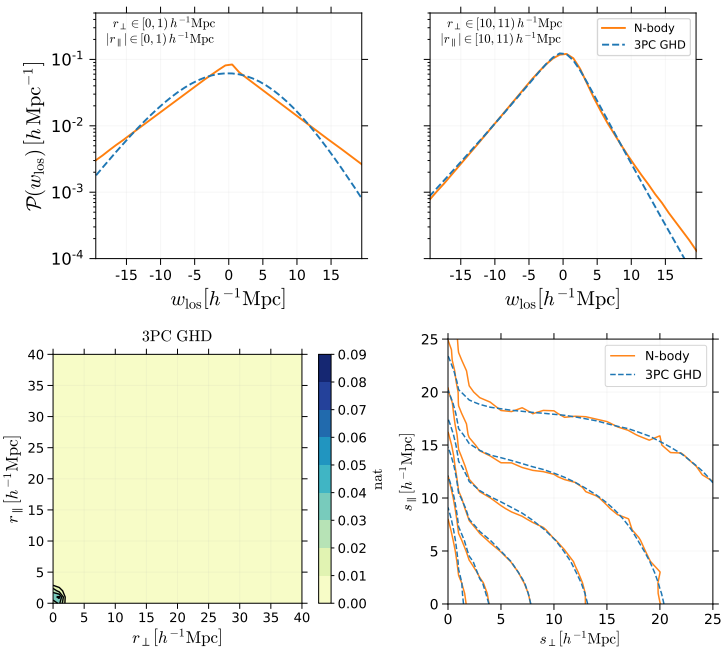

Figure 2.14: As in Figs. 2.10, 2.11 and 2.12 but for a GHD with only 3 degrees of freedom that identify the position of the model parameters within the volume spanned by the first 3 principal components.

parameters that denote the position of $\alpha, \beta, \delta, \lambda$ and μ within the space spanned by the first three principal components. In Fig. 2.14, we show the quality of the best-fitting functions as well as the corresponding $\xi_{\rm s}$ obtained by inserting them into equation (2.22). The three-parameter GHD still outperforms the Gaussian approximation at all scales. This requirement can be relaxed at larger scales where $\mathcal{P}_{w_{\rm los}}$ assumes a simpler shape. Fig. 2.15 shows that a two-parameter GHD obtained through PCA for larger scales provides an excellent fit that better describes the tails of the distribution with respect to the Gaussian approximation at all spatial separations. Note that even the integrand of the streaming equation is impeccably reproduced in this case.

DM haloes

DM haloes are biased tracers of the matter distributions and, as discussed in Section 2.4.2, are also characterized by a different pairwise-velocity PDF which presents less prominent tails than for the matter. In fact, haloes are not subject to the Finger-of-God effect and have a substantially smaller pairwise velocity dispersion, especially at small separations. In Fig. 2.16, we show that the GHD provides an excellent fit to the halo pairwise velocity distribution and, also in this case, outperforms the Gaussian approximation.

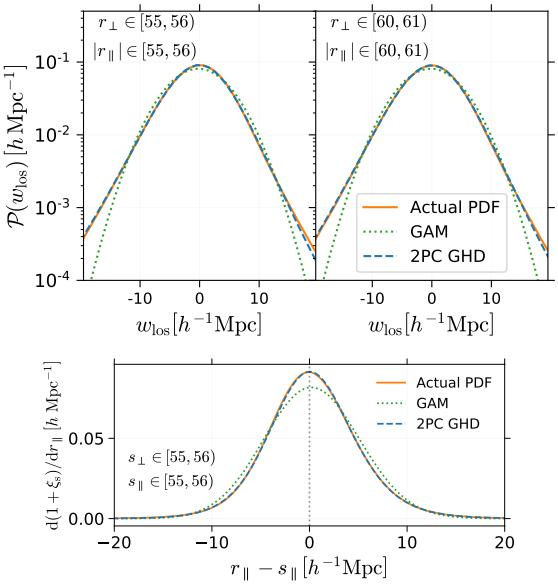

Figure 2.15: A simplified GHD model for $\mathcal{P}_{w_{\rm los}}$ in which the number of free parameters is reduced to 2 through PCA (2PC GHD, dashed) provides an excellent description of the N-body data (solid) on large scales and vastly outperforms the Gaussian approximation (dotted). In the top panel, we directly compare data and best-fit models for the pairwise-velocity PDF (as in Fig. 2.10 but for larger pair separations given in units of h^{-1} Mpc). In the bottom panel, we show the corresponding integrand of the streaming equation, as in Fig. 2.4.

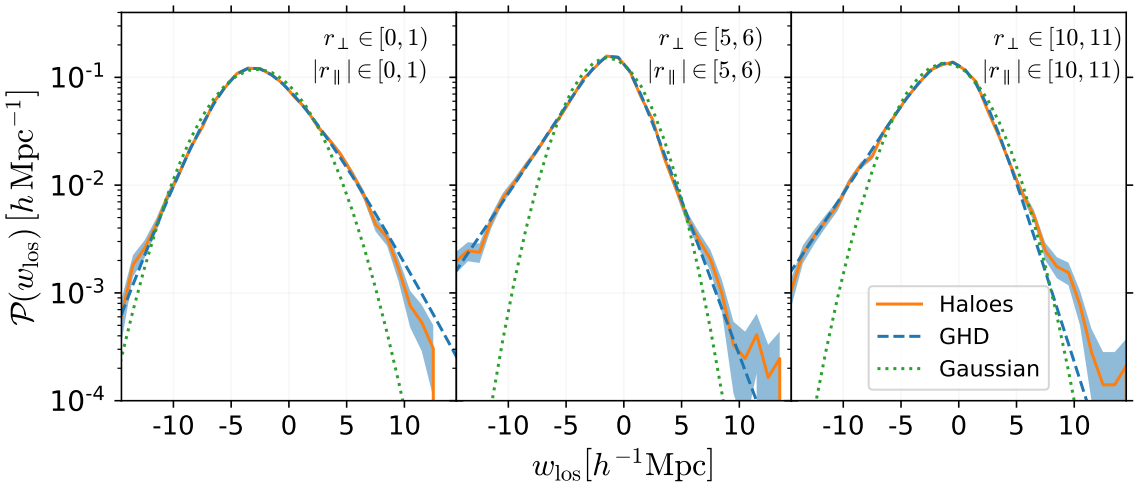

Figure 2.16: The los pairwise velocity distribution for the DM haloes identified in the W0 simulation at $z = 0$ (solid line with shaded error) is compared with the best-fitting GH (dashed) and Gaussian (dotted) approximations for diffferent real-space pair separations expressed in $h^{-1}{\rm Mpc}$.

2.5.3 Discussion

Comparison with previous work

The GHD is a mixture of Gaussians analogous to that introduced in Bianchi, Chiesa and Guzzo, 2015, although with a very different mixing distribution. It is thus interesting to highlight similarities and differences between the two approaches. In both cases, skewness is generated by the correlation between the mean and the variance of the constituent Gaussian distributions. However, the two models achieve this differently. In Bianchi, Chiesa and Guzzo, 2015, μ and σ are Gaussian random variables and their correlation is a free parameter. The GHD instead originates from the deterministic relation $\mu = \alpha + \beta\sigma^2$. Additional skewness appears in the GHD because the mixing distribution $\mathcal{G}$ is itself skewed. This illustrates why the GHD can accommodate the large skewness measured in N-body simulations at small r while the model by Bianchi, Chiesa and Guzzo, 2015 cannot (see Bianchi, Percival and Bel, 2016).

Another difference between the two approaches lies in the support of the mixing distribution. Although the rms value σ is by definition non-negative, Bianchi, Chiesa and Guzzo, 2015 use a mixing function with support on $\mathbb{R}^2$ for μ and σ. The mixing integral therefore extends over unphysical regions where $\sigma < 0$. A convenient fix is to truncate the Gaussian mixing distribution at $\sigma = 0$ (and renormalise it) as proposed in Bianchi, Percival and Bel, 2016. On the other hand, the GHD is based on a non-Gaussian mixing distribution with positive support for σ^2. In brief, while Bianchi, Percival and Bel, 2016 use a mixture of (slightly) non-Gaussian distributions with (truncated) Gaussian mixing, we use a mixture of normals with a strongly non-Gaussian mixing distribution.

Our approach offers multiple benefits: i) the GHD has long been studied and its mathematical properties are well known; ii) it has an analytical expression with several different parameterisations; iii) its moment generating function is analytical and expressions are available for its first four cumulants; iv) it reduces to the Gaussian distribution in some limit; v) optimised techniques have been developed for estimating its parameters given a set of data; vi) packages in the most popular computer languages are available for its efficient evaluation and also for the estimation of its parameters.

Cosmology dependence

Current cosmic-microwave-background experiments and large-scale-structure studies have set tight constraints on the cosmological parameters of the ΛCDM model. One open question is whether the pairwise velocity PDF changes significantly when the underlying cosmological model is varied within the currently allowed region of parameter space. We investigate this issue in Fig. 2.17 where we compare the pairwise velocity PDFs at $z = 0$ for the DM particles extracted from the 6 simulations introduced in Section 2.1. Switching from the WMAP to the Planck cosmology or considering non-Gaussian initial fluctuations (even at a level that violates current observational limits) only introduces minimal changes in $\mathcal{P}_{w_{\rm los}}$ at all separation vectors. Minute differences are noticeable only in the high-velocity tails. This is good news as it means that it should be possible to parameterize the scale-dependence of the PDF in a cosmology-independent way so that to facilitate practical applications of the GHD model.

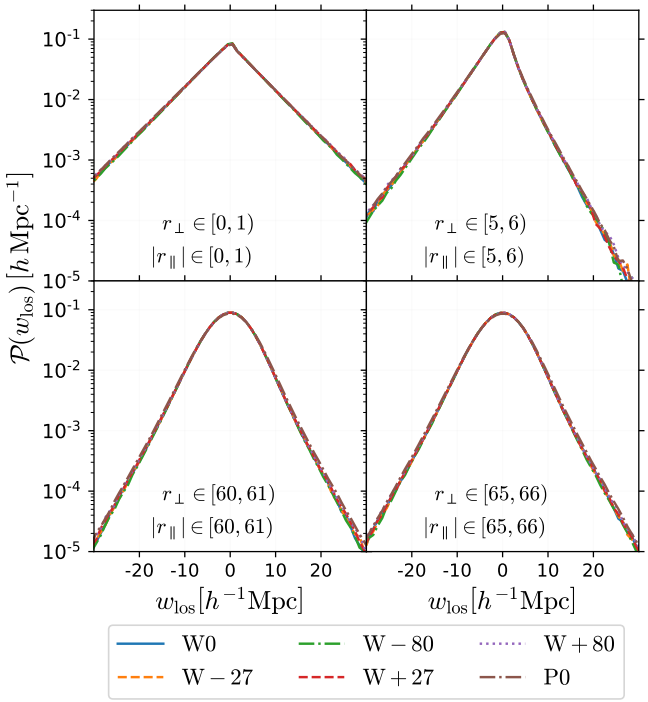

Figure 2.17: The los pairwise velocity distribution measured at $z = 0$ for the DM particles in the six cosmological models introduced in Table 2.1. Spatial separations are given in units of $h^{-1}\mathrm{Mpc}$.

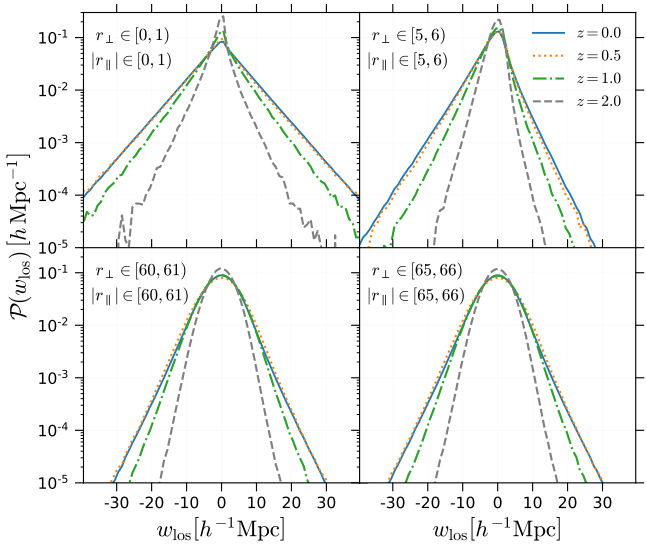

Figure 2.18: Redshift evolution of the los pairwise velocity distribution for the DM particles of the W0 simulation. Real-space separations are given in units of $h^{-1}\mathrm{Mpc}$.

Redshift evolution

The pairwise-velocity PDF for the DM particles reflects the non-linear growth of the large-scale structure of the Universe and, therefore, evolves with time. This is shown in Fig. 2.18, where we use the W0 simulation to plot $\mathcal{P}_{w_{\rm los}}$ for various real-space separations at four different epochs. At $z = 2$, the PDF already exhibits non-Gaussian features including asymmetry around the mode. However, the PDF is much more strongly peaked and presents less prominent exponential tails than at $z = 0$. In fact, only rare massive haloes are resolved at early times and the velocity PDF is dominated by field-field pairs. As time goes by, more and more haloes above the mass-resolution limit form and the velocity PDF develops fatter tails. It is worth stressing that almost no evolution is noticeable between $z = 0.5$ and $z = 0$. This is a consequence of the fact that the energy budget of the universe becomes dominated by the cosmological constant and further development of structure is inhibited. Combined with the results of Section 2.5.3, this finding implies that, for $z \lesssim 0.5$, it should be possible to define a cosmology- and redshift-independent parameterization of the pairwise-velocity PDF, at least for the DM particles.

DM vs galaxies

The ultimate application of the streaming model is the interpretation of the clustering signal extracted for galaxy redshift surveys. However, our study (like many others before) focusses on the analysis of simulated DM particles and haloes. The advantage of using the simulation particles is that they offer a huge statistical sample. On the other hand, the PDF of their pairwise velocities shows stronger exponential tails with respect to haloes due to the broadening generated by virial motions and spikier peaks due to diffuse matter (see Fig. 2.8). In a sense, a galaxy sample is expected to show intermediate properties between halo and particle datasets. A pure sample of central galaxies will closely look like a halo sample while adding more and more satellites will progressively drive the PDF towards the results for simulation particles. It is long known that galaxy clustering in redshift space is well described by the streaming model assuming an exponential $\mathcal{P}_{w_{\rm los}}$ on very small scales and a Gaussian one on very large scales. Since the GHD is of very general form and reduces to these limits for particular combinations of its parameters, we are confident that our analysis can be straightforwardly generalised to galaxies. We will investigate this issue in our future work.

2.6 Summary

The galaxy 2-point correlation function in redshift space depends on the orientation of the pair-separation vector with respect to the los. This anisotropy encodes information about the velocities arising from gravitational instability. On large scales, where linear perturbation theory applies, RSD allow for a measurement of the growth rate of structure. Combining estimates at different redshifts help differentiate dark energy models based on General Relativity from modified gravity as the cause of the accelerating Universe.

Modifications to the theory of gravity generally introduce extra degrees of freedom whose effect (the so-called fifth force) must be suppressed by some screening mechanism on scales where General Relativity is well tested. Such constraint implies that characteristic signatures will be imprinted on intermediate cosmological scales. In fact, the screening mechanism is expected to affect the non-linear clustering and the velocities of tracers of the large-scale structure. Testing these predictions provides a

strong motivation to extend the analysis of galaxy clustering to smaller scales than currently done in cosmological studies.

Realising this program in practice requires, however, a number of tools. Among them, robust theoretical predictions for the modified theories of gravity together with an accurate (and, possibly, non-perturbative) description of RSD. In this paper, we focussed on the latter issue. In particular, we discussed the classical streaming model for RSD and how its implementation can be improved to get accurate predictions at non-linear scales. Our main results can be summarised as follows.

In Section 2.3, starting from the one- and two-particle phase-space densities, we derived the governing equations of the model. For ordered pairs, we obtained equation (2.14) which coincides with the standard equation discussed in the literature. Our result is exact and holds true also in the case of multi streaming thanks to our particle-based approach. The correct solution for unordered pairs has been given in equation (2.22). The modifications with respect to equation (2.14) account for the pairs that reverse their los ordering between real and redshift space. These swaps occur more frequently for pairs with small spatial separations.

After briefly reviewing the history of the streaming model and of its applications, we investigated the limitations of using the Gaussian ansatz for the pairwise-velocity PDF. In agreement with previous studies, we showed that this approximation fails to reproduce the outcome of N-body simulations for redshift-space separations $s \lesssim 20\,h^{-1}$Mpc while it achieves percent level accuracy on ξ_s on substantially larger scales. Our analysis revealed, however, that a Gaussian PDF never manages to reproduce the integrand of the streaming equation to the same level of accuracy. The success of the GSM on large scales, therefore, originates from fortuitous cancellations between the contributions of the peak and the wings in the integrand of the streaming equation (see Fig. 2.4).

In Section 2.4, we used a high-resolution N-body simulation to investigate how the PDF of the los component of the pairwise-velocity, $w_\parallel$, depends on the pair separation vector for both DM particles and haloes. The first four cumulants of the PDF show a complex pattern (Fig. 2.5) that can be understood in terms of a few isotropic components and the angle that the pair separation forms with the los. We derived a general relation between the cumulants of $w_\parallel$ and those of the radial and transverse pairwise velocities, equation (2.37). We then studied the scale-dependence of the isotropic components in the simulation (Fig. 2.6) and measured the pairwise-velocity bias of the DM haloes (Fig. 2.7). Additionally, we dissected the pairwise-velocity PDF for the DM and showed that the tails are generated by particles in massive haloes while the region around the mode is dominated by field particles (Figs. 2.8 and 2.9).

Finally, in Section 2.5, we proposed an analytical fitting function for the pairwise-velocity distribution and demonstrated that it provides an excellent description of numerical data. We first introduced the mathematical background of mixtures and then described the properties of the GHD, a unimodal PDF with exponential tails. Comparing with N-body simulations, we showed that the GHD is able to approximate the PDF of the los pairwise velocity at all scales (for both DM particles and haloes) with minimal information loss compared to the common exponential and Gaussian fits (Figs. 2.10, 2.11, and 2.12). The main drawback to using the GHD in future practical applications is that it depends on 5 tunable parameters. In fact, fixing their values to best fit the N-body data gives rise to non-trivial scale dependencies (Fig. 2.13). However, the best-fitting values are strongly correlated and tend to populate a lower-dimensional sequence in 5-dimensional parameter space. Using principal-component analysis to exploit the correlations, we managed to reduce the complexity of the model while still providing a remarkable fit to ξ_s. We found that 2 parameters are enough on large scales ($s > 70\,h^{-1}$ Mpc) while at least 3 are needed on smaller scales. In this case, even the integrand of the streaming equation is

accurately reproduced by the model (Fig. 2.15).

Intriguingly, we found that the pairwise-velocity PDF for the DM at $z = 0$ shows only minimal changes when the underlying cosmological parameters are varied within the current constraints for the ΛCDM model (Fig. 2.17). Moreover, it does not show any noticeable time evolution for redshifts $z \lesssim 0.5$ (Fig. 2.18). All this suggests that, for low-redshift tracers, it should be possible to find a cosmology- and redshift-independent parameterization for the PDF of their pairwise velocities as a function of the separation vector. This would greatly simplify the implementation of the GHD model for studying anisotropic galaxy clustering. We will investigate the applicability of these findings to forthcoming data in our future work.

2.A Appendix

2.A.1 Reversed pairs

In Fig. 2.19, we quantify the importance of pair reversals for the two-point correlation function in redshift space. After measuring $\xi(r)$ and $\mathcal{P}_{w_{\rm los}}$ in our simulation, we apply equation (2.22) and obtain the solid contour levels for ξ_s that nicely match those shown in the right-hand panel of Fig. 2.1. The dashed contours, instead, are computed integrating over the positive values of $r_\parallel$ only, which corresponds to neglecting the reversed pairs. Not only this incomplete model underestimates $\xi_{\rm s}$ by a factor of two in the FoG regime ($s_\perp < 2\,h^{-1}$ Mpc and $s_\parallel \gg s_\perp$ where reversed pairs are as many as the preserved ones), but also severely suppresses the redshift-space correlation whenever $s_\parallel \ll s_\perp$. The reversed pairs thus give an important contribution on a vast range of redshift-space separations that extend well beyond the typical size of DM haloes.

It is also interesting to explore what would happen if one would naively replace $\mathcal{P}_{w_\parallel}$ with $\mathcal{P}_{w_{\rm los}}$ in equation (2.14) or, equivalently, drop the sgn function in equation (2.22). The corresponding result for $\xi_{\rm s}$ is shown with dotted lines in Fig. 2.19 and it underestimates the actual correlation function on many scales although less severely than in the previous case. To further investigate the origin of the differences, in the top panel of Fig. 2.20, we consider a narrow range of redshift-space separations ($s_\parallel \in [5,6)\,h^{-1}$Mpc and $s_\perp \in [2,3)\,h^{-1}$Mpc) and plot the integrand of equation (2.22) as a function of $r_\parallel$ (solid line). For comparison, we also indicate with a dashed line the integrand obtained neglecting the sgn function in the argument of $\mathcal{P}_{w_{\rm los}}$ for $r_\parallel < 0$. Although the reversed pairs are taken into account in the latter case, they are miscounted which leads to the underestimation of $\xi_{\rm s}$.

Note that the correct function $\mathrm{d}(1+\xi_{\rm s})/\,\mathrm{d}r_\parallel$ is discontinous at $r_\parallel = 0$. This feature originates from the function $\mathcal{P}_{w_{\rm los}}[(s_\parallel - r_\parallel)\,\mathrm{sgn}(r_\parallel) \mid \mathbf{r}]$ which is plotted in the middle panel of Fig. 2.20: the factor $\mathrm{sgn}(r_\parallel)$ makes sure that the (continuous but asymmetric) velocity PDF is sampled at $w_{\rm los} = s_\parallel - r_\parallel$ for $r_\parallel \to 0^+$ and at $w_{\rm los} = r_\parallel - s_\parallel$ for $r_\parallel \to 0^-$. Also note that $\mathcal{P}_{w_{\rm los}}$ presents a prominent peak around $r_\parallel \simeq s_\parallel$ corresponding to pairs with relatively small relative los velocity. The enhancement of the region around $r_\parallel \sim 0$ in the full integrand is due to the term $1 + \xi(r)$ which is plotted in the bottom panel of the figure. In simple words, real-space clustering boosts the contribution from close pairs with large pairwise los velocity.

It is worth mentioning that, for much larger redshift-space separations (e.g. $s_\parallel \gg 20\,h^{-1}$Mpc and $s_\perp \gg 20\,h^{-1}$Mpc), the peak around $r_\parallel \approx 0$ is suppressed and the impact of the reversed pairs becomes much less important. In this case, neglecting the sgn function in equation (2.22) or using $\mathcal{P}_{w_{\rm los}}$ in equation (2.14) generates only small errors.

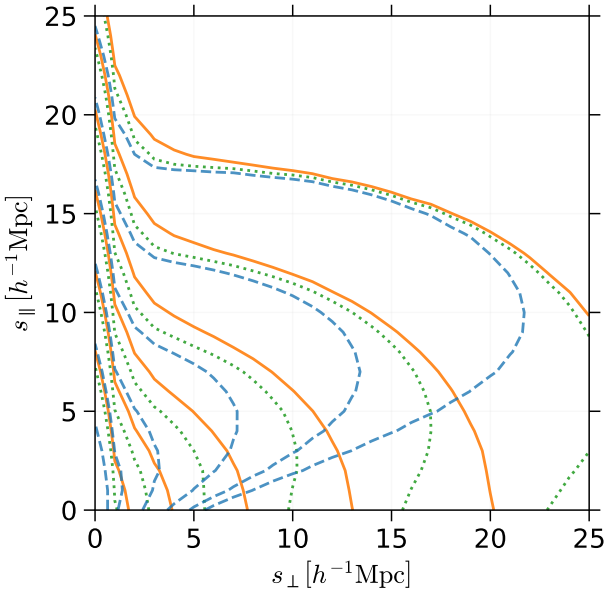

Figure 2.19: Impact of the reversed pairs on ξ_s. The solid lines show the contour levels obtained using equation (2.22) which is exact for ordered pairs. In this case, the correlation function nicely matches the measurements presented in Fig. 2.1. This result is compared with two approximations that do not properly account for the reversed pairs. The dashed lines only considers the region with $r_\parallel > 0$ in equation (2.22) and thus completely disregards the swapped pairs. The dotted lines, on the other hand, are obtained by replacing $\mathcal{P}_{w_\parallel}$ with $\mathcal{P}_{w_\mathrm{los}}$ in equation (2.14) which improperly weighs the reversed pairs.

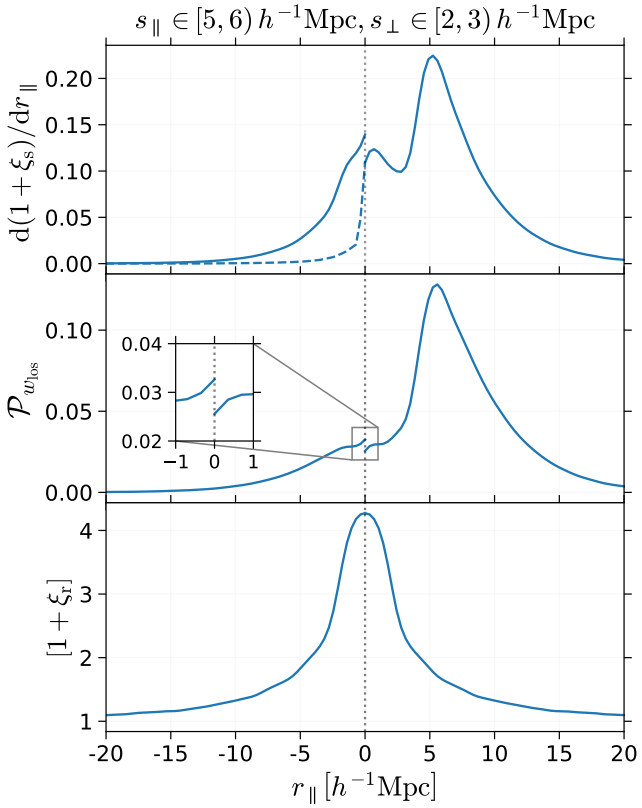

Figure 2.20: Top: The solid line shows the function $\mathrm{d}(1+\xi_\mathrm{s})/\,\mathrm{d}r_\parallel$ – i.e. the integrand in equation (2.22) – for a narrow range of redshift-space separations indicated above the plot. The dashed line for $r_\parallel < 0$ shows the effect of removing the sgn function from the argument of the velocity PDF in equation (2.22). Note that this severely miscounts the reversed pairs ultimately leading to an underestimate of ξ_s. Middle: The contribution to the integrand due to the pairwise-velocity PDF, $\mathcal{P}_{w_\mathrm{los}}[(s_\parallel - r_\parallel)\,\mathrm{sgn}(r_\parallel) \mid \mathbf{r}]$, is plotted as a function of $r_\parallel$. Bottom: The contribution to the integrand due to real-space clustering, $1+\xi(r)$, is shown as a function of $r_\parallel$.

CHAPTER 3

Three-point redshift-space correlation function

Maps of the large-scale structure of the Universe obtained from galaxy redshift surveys suffer from the so-called redshift-space distortions (RSD) generated by galaxy peculiar velocities (Jackson, 1972; Sargent and Turner, 1977). RSD break the isotropy of galaxy N-point statistics by introducing an angular dependence with respect to the direction of the line of sight (los) (Kaiser, 1987; Hamilton, 1998). The degree of anisotropy depends on the growth rate of cosmic structure and can thus be used to probe dark energy and test gravity theories. Achieving this goal, however, requires modelling daunting non-linear and non-perturbative physics as motions within virialised galaxy clusters alter galaxy statistics on significantly large scales.

The introduction of the streaming model for the 2-point correlation function (Peebles, 1980) represents a key milestone in this development. The basic idea is to compute the distorted anisotropic two-point correlation function (in 'redshift space') by an integral transformation of the underlying isotropic correlation function (in 'real space') combined with the distribution function of the relative los velocities of galaxy pairs. However, since the moments of this 'pairwise velocity distribution function' (PVD) are strongly scale dependent and difficult to predict from first principles, the streaming model has been often considered as a rather impractical tool to use for cosmological inferences (although it is exact in the distant-observer approximation). Assuming that the PVD is Gaussian for large spatial separations and that its mean and variance can be evaluated using perturbation theory formed a successful step forward in this direction (Fisher, 1995; B. A. Reid and M. White, 2011; Carlson, B. Reid and M. White, 2013; M. White, B. Reid et al., 2015; Vlah, Castorina and M. White, 2016). This 'Gaussian streaming model' has been successfully applied to galaxy redshift surveys (B. A. Reid, Samushia et al., 2012; Samushia et al., 2014; Alam, Ho et al., 2015; Chuang, Pellejero-Ibanez et al., 2017; Satpathy et al., 2017). In a parallel line of research, several authors have discussed how to go beyond the Gaussian approximation by incorporating higher-order cumulants of the PVD (Bianchi, Chiesa and Guzzo, 2015; Uhlemann, Kopp and Haugg, 2015; Bianchi, Percival and Bel, 2016; Kuruvilla and Porciani, 2018).

In this paper, we derive an exact streaming model for generic n-point correlation functions (nPCFs) with $n \geq 2$. In full analogy with the 2-point case, we find that the n-point correlation in redshift space is given by an integral transformation of its real-space counterpart multiplied by the multivariate distribution of the relative los velocities between $n-1$ galaxy pairs in a n-tuple. After studying the properties of this distribution for triplets of dark-matter particles in a large N-body simulation, we formulate a Gaussian streaming model for the 3PCF and test its performance against the simulation.

Measurements of the 3PCF have a long history that reflects the development of galaxy surveys. Pioneering studies, dating back to the 1970s, were based on a few thousand galaxy positions on the sky (Peebles and Groth, 1975; Groth and Peebles, 1977; Peebles, 1981). Early redshift surveys provided samples containing a few hundred objects (Bean et al., 1983; Efstathiou and Jedrzejewski, 1984; Hale-Sutton et al., 1989). A measurement with much larger signal-to-noise ratio was performed using nearly 20,000 galaxies from the Las Campanas Redshift Survey (Jing and Börner, 1998). Eventually, in the early 2000s, the advent of multi-fiber spectrographs provided homogeneous samples with 10^{5-6} galaxies at low redshift. The 3PCF was measured from the Two-Degree Field Galaxy Redshift Survey (Jing and Börner, 2004; Y. Wang et al., 2004; Gaztañaga, Norberg et al., 2005), different generations of the Sloan Digital Sky Survey (Kayo et al., 2004; Nichol et al., 2006; Ross, Brunner and Myers, 2006; Kulkarni et al., 2007; Gaztañaga, Cabré et al., 2009; McBride et al., 2011; F. Marıén, 2011; Guo, C. Li et al., 2014; Guo, Zheng et al., 2015; Slepian, Eisenstein et al., 2017), and the WiggleZ Dark Energy Survey (F. A. Marıén et al., 2013). Recently, it was also possible to extend the analysis at redshifts $0.5 < z < 1$ by using nearly 50,000 galaxies from the VIMOS Public Extragalactic Redshift Survey (Moresco, Marulli, Moscardini et al., 2017).

In spite of this impressive progress, estimates of 3-point statistics on large scales still suffer from systematic shifts generated by rare statistical fluctuations, meaning that substantially larger volumes need to be covered in order to obtain unbiased measurements, e.g. (Nichol et al., 2006). Fortunately, dark-energy science is providing a strong motivation for building such unprecedentedly large samples. This led the community to develop and build dedicated facilities like the Dark Energy Spectroscopic Instrument (DESI, Levi et al., 2013), the EUCLID mission (Amendola et al., 2013), the Wide-Field Infrared Survey Telescope (WFIRST, D. Spergel et al., 2013), the Prime Focus Spectrograph (PFS, Takada et al., 2014), the Large Synoptic Survey Telescope (LSST, LSST Science Collaboration et al., 2009) and the Spectro-Photometer for the History of the Universe, Epoch of Reionization, and Ices Explorer (SPHEREX, Dore et al., 2014).

Several authors have recently highlighted that combining two- and three-point clustering statistics with data of this calibre will ultimately lead to a sizeable information gain about the cosmological parameters (Sefusatti, Crocce et al., 2006; Gil-Marıén, Noreña et al., 2015; Gil-Marıén, Percival et al., 2017; Karagiannis et al., 2018; Yankelevich and Porciani, 2019; Chudaykin and Ivanov, 2019). In particular, 3-point clustering statistics (either in configuration or Fourier space) are expected to: i) remove the degeneracy between the amplitude of dark-matter perturbations and the galaxy linear bias coefficient that plagues 2-point statistics (Fry, 1994; Frieman and Gaztanaga, 1994; Matarrese, Verde and Heavens, 1997) and constrain the linear growth rate of matter fluctuations (Hoffmann, Bel et al., 2015); ii) provide an accurate determination of galaxy biasing (Gil-Marıén, Noreña et al., 2015; Yankelevich and Porciani, 2019); iii) constrain the level of primordial non Gaussianity (Scoccimarro, Sefusatti and Zaldarriaga, 2004; Sefusatti and Komatsu, 2007; Giannantonio and Porciani, 2010; Tellarini et al., 2016; Karagiannis et al., 2018); iv) help distinguish between alternative models like coupled dark-energy cosmologies (Moresco, Marulli, Baldi et al., 2014); v) constrain neutrino masses.

In order to keep these promises and fully exploit the forthcoming data, it is essential to make fast progress from the theoretical point of view as well. Historically, most models of the 3PCF were based on the basic 'hierarchical clustering' ansatz (Peebles, 1980) or on the phenomenological halo model (Y. Wang et al., 2004; Guo, Zheng et al., 2015). It is only recently that more quantitative techniques have received increased attention. For instance, perturbation theory has been used to compute a model for the 3PCF in redshift space (Slepian and Eisenstein, 2017) in analogy with previous results obtained in Fourier space (Scoccimarro, Couchman and Frieman, 1999). Our work provides a framework

for further developing this line of research along a path that was already very successful for 2-point statistics.

The paper is organised as follows. In section 3.1, we review the basic concepts of RSD and derive the fundamental equations of the generalised streaming model for the nPCF. This first part is very general and technical. We then focus on applications of the theory to the 3PCF. With this goal in mind, in section 3.2, we use an N-body simulation and perturbation theory to study the properties of the bivariate distribution of the relative los velocities between particle pairs in a triplet. Motivated by the resuls, in section 3.3, we formulate the 3-point Gaussian streaming model and test it against the simulation. Finally, we summarise our results in section 3.4.

3.1 The streaming model

We start with a note. Busy readers who want to focus on applications of the theory to the 3PCF may want to skip large parts of this section on first reading but will want to read sections 3.2, 3.3 and 3.4 in their entirety. To help them scan for desired information and skip those parts that are more conceptual, we recommend familiarising themselves with section 3.1.1, equation (3.14), the short sentence following equation (3.16) that provides a definition in words of the functions we denote by $\mathcal{P}^{(n)}_{\boldsymbol{w}_\parallel}$, and the beginning of section 3.1.4 until equation (3.21).

3.1.1 Redshift-space distortions

The distance to a galaxy, quasar or galaxy cluster is generally estimated starting from the observed redshift of spectral lines in its electromagnetic spectrum. This conversion assumes an unperturbed Friedmann model of the Universe with instantaneous expansion factor a and thus a perfect Hubble flow with instantaneous Hubble parameter H. Therefore, this distance estimate is never exact with actual data due to the presence of peculiar velocities. In the distant-observer (or plane-parallel) approximation (Hamilton, 1998), a single los direction $\hat{\boldsymbol{s}}$ can be defined for all objects. Hence, the actual comoving distance $\boldsymbol{x}$ and the redshift-based estimate $\boldsymbol{x}_\mathrm{s}$ satisfy the relation

$$\boldsymbol{x}_\mathrm{s} = \boldsymbol{x} + (\boldsymbol{v}\cdot\hat{\boldsymbol{s}})\,\hat{\boldsymbol{s}}\,. \tag{3.1}$$

where $\boldsymbol{v}$ denotes the peculiar velocity $\boldsymbol{u}$ divided by the factor aH. The locations described by the coordinates $\boldsymbol{x}_\mathrm{s}$ and $\boldsymbol{x}$ are commonly referred to as the 'redshift space' and the 'real space' position, respectively. Consider two tracers of the large-scale structure with real-space separation $\boldsymbol{r}_{12} = \boldsymbol{x}_2 - \boldsymbol{x}_1$. Their redshift-space separation along the los is then

$$s_{12\parallel} = (\boldsymbol{x}_{\mathrm{s}_2} - \boldsymbol{x}_{\mathrm{s}_1})\cdot\hat{\boldsymbol{s}} = r_{12\parallel} + w_{12\parallel}\,, \tag{3.2}$$

where $r_{12\parallel} = \boldsymbol{r}_{12}\cdot\hat{\boldsymbol{s}}$ and $w_{12\parallel} = (\boldsymbol{v}_2 - \boldsymbol{v}_1)\cdot\hat{\boldsymbol{s}}$. On the other hand, in the perpendicular plane, the real- and redshift-space separations coincide, i.e. $\boldsymbol{s}_{12\perp} = \boldsymbol{r}_{12\perp}$.

3.1.2 Phase-space densities and correlation functions

Let us consider a system consisting of N particles in 3-dimensional space. At any instant of time, each particle is characterised by its comoving position $\boldsymbol{x}_i$ and the (rescaled) peculiar velocity $\boldsymbol{v}_i$ (with

$1 \leq i \leq N$). We introduce the n-particle phase-space densities (Yvon, 1935; Huang, 1987; Kardar, 2007)

$$f_n(\boldsymbol{x}_{\mathrm{A}_1}, \ldots, \boldsymbol{x}_{\mathrm{A}_n}, \boldsymbol{v}_{\mathrm{A}_1}, \ldots, \boldsymbol{v}_{\mathrm{A}_n}) = \sum_{i_1=1}^{N} \sum_{i_2 \neq i_1} \cdots \sum_{i_n \neq i_1, \ldots, i_{n-1}} \left\langle \delta_{\mathrm{D}}^{(3)}(\boldsymbol{x}_{\mathrm{A}_1} - \boldsymbol{x}_{i_1}) \ldots \delta_{\mathrm{D}}^{(3)}(\boldsymbol{x}_{\mathrm{A}_n} - \boldsymbol{x}_{i_n}) \, \delta_{\mathrm{D}}^{(3)}(\boldsymbol{v}_{\mathrm{A}_1} - \boldsymbol{v}_{i_1}) \ldots \delta_{\mathrm{D}}^{(3)}(\boldsymbol{v}_{\mathrm{A}_n} - \boldsymbol{v}_{i_n}) \right\rangle , \tag{3.3}$$

where $\delta_{\mathrm{D}}^{(n)}$ is the Dirac delta distribution in $\mathbb{R}^n$ and the brackets denote averaging over an ensemble of realisations. Before we proceed, let us clarify our notation. The symbols $\boldsymbol{x}_{\mathrm{A}_i} \in \mathbb{R}^3$ and $\boldsymbol{v}_{\mathrm{A}_i} \in \mathbb{R}^3$ denote the independent variables of the f_n functions. On the other hand, as we have already mentioned, $\boldsymbol{x}_{i_j}$ and $\boldsymbol{v}_{i_j}$ indicate the position and velocity of the i_j^{th} particle. The indices $\{i_1, \ldots, i_n\}$ specify a set of n different particles and the sums run over all possible n-tuples that can be formed with N particles. Note that f_n is normalised to the total number of ordered n-tuples of particles: $\int f_n \, \mathrm{d}\boldsymbol{x}_{\mathrm{A}_1} \ldots \mathrm{d}\boldsymbol{x}_{\mathrm{A}_n} \, \mathrm{d}\boldsymbol{v}_{\mathrm{A}_1} \ldots \mathrm{d}\boldsymbol{v}_{\mathrm{A}_n} = N!/(N-n)!$. Assuming statistical isotropy and homogeneity as well as that $N \to \infty$, it follows that $f_1 = \bar{n} \, \mathcal{P}_{\boldsymbol{v}}^{(1)}$ where $\bar{n}$ denotes the mean particle number density per unit volume and $\mathcal{P}_{\boldsymbol{v}}^{(1)}$ is the probability density function (PDF) of peculiar velocities that can only depend on v^2 and is normalised such that $4\pi \int \mathcal{P}_{\boldsymbol{v}}^{(1)} \, v^2 \, \mathrm{d}v = 1$ (Kuruvilla and Porciani, 2018). Under the same assumptions, the n-point spatial correlation function of the particles in configuration space ($n \geq 2$) can be expressed as

$$\mathcal{F}_n = \frac{\int f_n \, \mathrm{d}\boldsymbol{v}_{\mathrm{A}_1} \ldots \mathrm{d}\boldsymbol{v}_{\mathrm{A}_n}}{\left(\int f_1 \, \mathrm{d}\boldsymbol{v} \right)^n} = \frac{1}{\bar{n}^n} \int f_n \, \mathrm{d}\boldsymbol{v}_{\mathrm{A}_1} \ldots \mathrm{d}\boldsymbol{v}_{\mathrm{A}_n} , \tag{3.4}$$

where we did not write explicitly the arguments of the correlation functions to simplify notation. The irreducible (or connected) spatial n-point correlation functions can be expressed in terms of the $\mathcal{F}_n$. For instance, $\mathcal{F}_2$ and the 2-point connected function ξ satisfy the relation

$$\mathcal{F}_2(r) = 1 + \xi(r) , \tag{3.5}$$

where $r = |\boldsymbol{x}_{\mathrm{A}_2} - \boldsymbol{x}_{\mathrm{A}_1}|$ denotes the comoving separation between the points at which the functions are evaluated. Similarly, $\mathcal{F}_3$ is related to the 3-point connected function ζ by

$$\mathcal{F}_3(r_{12}, r_{23}, r_{31}) = 1 + \xi(r_{12}) + \xi(r_{23}) + \xi(r_{31}) + \zeta(r_{12}, r_{23}, r_{31}) , \tag{3.6}$$

where the different $r_{ij} = |\boldsymbol{x}_{\mathrm{A}j} - \boldsymbol{x}_{\mathrm{A}i}|$ indicate the comoving separations between pairs of points in a triplet.

Analogous considerations apply in redshift space, where we can introduce the n-particle phase-space densities g_n and the n-point spatial correlation functions

$$\mathcal{G}_n = \frac{\int g_n \, \mathrm{d}\boldsymbol{v}_{\mathrm{A}_1} \dots \mathrm{d}\boldsymbol{v}_{\mathrm{A}_n}}{\left(\int g_1 \, \mathrm{d}\boldsymbol{v}\right)^n} = \frac{1}{\bar{n}^n} \int g_n \, \mathrm{d}\boldsymbol{v}_{\mathrm{A}_1} \dots \mathrm{d}\boldsymbol{v}_{\mathrm{A}_n} \, . \tag{3.7}$$

Since redshift-space distortions appear along the line of sight, these functions are not isotropic. However, due to the invariance under rotations along the los, $\mathcal{G}_2$ and ξ_s only depend on the modulus of $\boldsymbol{s}_\perp$:

$$\mathcal{G}_2(s_\parallel, s_\perp) = 1 + \xi_\mathrm{s}(s_\parallel, s_\perp) \, . \tag{3.8}$$

Similarly, we can write

$$\mathcal{G}_3(\triangle_{123}) = 1 + \xi_\mathrm{s}(s_{12\parallel}, s_{12\perp}) + \xi_\mathrm{s}(s_{23\parallel}, s_{23\perp}) + \xi_\mathrm{s}(s_{31\parallel}, s_{31\perp}) + \zeta_\mathrm{s}(\triangle_{123}) \, , \tag{3.9}$$

although the compact notation above needs further explanation. First of all, there are multiple ways to parameterize the triangle $\triangle_{123} \equiv \{\boldsymbol{s}_{12}, \boldsymbol{s}_{23}, \boldsymbol{s}_{31}\}$. Since, by definition, $\boldsymbol{s}_{12} + \boldsymbol{s}_{23} + \boldsymbol{s}_{31} = 0$, picking two of the legs automatically determines the third one. For instance, we could write

$$\mathcal{G}_3(\boldsymbol{s}_{12}, \boldsymbol{s}_{23}) = 1 + \xi_\mathrm{s}(s_{12\parallel}, s_{12\perp}) + \xi_\mathrm{s}(s_{23\parallel}, s_{23\perp}) + \xi_\mathrm{s}(s_{31\parallel}, s_{31\perp}) + \zeta_\mathrm{s}(\boldsymbol{s}_{12}, \boldsymbol{s}_{23}) \, , \tag{3.10}$$

even though also this notation does not reflect the full picture. In fact, $\mathcal{G}_3$ and ζ_s only depend on $s_{12\parallel}, s_{12\perp}, s_{23\parallel}, s_{23\perp}$ and $\cos\theta_\perp = \hat{\boldsymbol{s}}_{12\perp} \cdot \hat{\boldsymbol{s}}_{23\perp}$. Since, $s_{31\perp}^2 = s_{12\perp}^2 + s_{23\perp}^2 + 2 s_{12\perp} s_{23\perp} \cos\theta_\perp$ and $s_{31\parallel} = -(s_{12\parallel} + s_{23\parallel})$, we can equivalently express the functional dependence of ζ_s in terms of five separations: $s_{12\perp}, s_{12\parallel}, s_{23\perp}, s_{23\parallel}$ and $s_{31\perp}$ (as we will do in sections 3.2.3 and 3.3). However, the 3PCFs $\mathcal{G}_3$ and ζ_s do not depend on the labelling of the vertices of $\triangle_{123}$, e.g. $\zeta_\mathrm{s}(\boldsymbol{s}_{12}, \boldsymbol{s}_{23}) = \zeta_\mathrm{s}(\boldsymbol{s}_{13}, \boldsymbol{s}_{32}) = \zeta_\mathrm{s}(\boldsymbol{s}_{21}, \boldsymbol{s}_{13}) = \zeta_\mathrm{s}(\boldsymbol{s}_{23}, \boldsymbol{s}_{31}) = \zeta_\mathrm{s}(\boldsymbol{s}_{31}, \boldsymbol{s}_{12}) = \zeta_\mathrm{s}(\boldsymbol{s}_{32}, \boldsymbol{s}_{21})$, whereas using $s_{12\perp}, s_{12\parallel}, s_{23\perp}, s_{23\parallel}$ and $s_{31\perp}$ associates different parameter sets to different labellings. For instance, in a measurement, a single triplet of points would contribute to six different triangular configurations thus introducing unnecessary covariances and repetitions. Fixing the labelling so that $s_{12} \geq s_{23} \geq s_{31}$ provides a simple solution to this issue (Yankelevich and Porciani, 2019) but we will not adopt this convention in this work.

3.1.3 The streaming model for the 2-point correlation function

In this section, we outline the original derivation of the streaming model for the 2PCF presented in Kuruvilla and Porciani, 2018. By definition, the phase-space distributions f_2 and g_2 differ only by the coordinate change in equation (3.2). We can thus combine equations (3.7) and (3.8) and write[1]

$$1 + \xi_\mathrm{s}(s_\parallel, s_\perp) = \frac{1}{\bar{n}^2} \int f_2(s_\parallel - w_\parallel, s_\perp, \boldsymbol{v}_\mathrm{A}, \boldsymbol{v}_\mathrm{B}) \, \delta_\mathrm{D}^{(1)}(w_\parallel - v_{\mathrm{B}\parallel} + v_{\mathrm{A}\parallel}) \, \mathrm{d}w_\parallel \, \mathrm{d}\boldsymbol{v}_\mathrm{A} \, \mathrm{d}\boldsymbol{v}_\mathrm{B} \, . \tag{3.11}$$

[1] To avoid the proliferation of subscripts, whenever possible (i.e. when we discuss explicit examples for the 2 and 3PCFs instead of the generic n-point case), we use the indices A, B, ... instead of $\mathrm{A}_1, \mathrm{A}_2, \dots$.

We now multiply the integrand in the right-hand side (rhs) of the last equation by the quantity

$$\frac{\bar{n}^2\left[1+\xi\left(\sqrt{(s_\parallel-w_\parallel)^2+s_\perp^2}\right)\right]}{\int f_2(s_\parallel-w_\parallel,s_\perp,\boldsymbol{v}_\mathrm{A},\boldsymbol{v}_\mathrm{B})\,\mathrm{d}\boldsymbol{v}_\mathrm{A}\,\mathrm{d}\boldsymbol{v}_\mathrm{B}}=\frac{\bar{n}^2\left\{1+\xi[r(s_\parallel,s_\perp,w_\parallel)]\right\}}{\int f_2[r_\parallel(s_\parallel,w_\parallel),r_\perp(s_\perp),\boldsymbol{v}_\mathrm{A},\boldsymbol{v}_\mathrm{B}]\,\mathrm{d}\boldsymbol{v}_\mathrm{A}\,\mathrm{d}\boldsymbol{v}_\mathrm{B}}\,, \tag{3.12}$$

(which is identically one) and define the pairwise-velocity PDF at fixed real-space separations $r_\parallel = s_\parallel - w_\parallel$ and $r_\perp = s_\perp$ as

$$\begin{aligned}\mathcal{P}^{(2)}_{w_\parallel}\left[w_\parallel|\boldsymbol{r}\left(s_\parallel,s_\perp,w_\parallel\right)\right]&=\frac{\int f_2(s_\parallel-w_\parallel,s_\perp,\boldsymbol{v}_\mathrm{A},\boldsymbol{v}_\mathrm{B})\,\delta_\mathrm{D}^{(1)}(w_\parallel-v_{\mathrm{B}\parallel}+v_{\mathrm{A}\parallel})\,\mathrm{d}\boldsymbol{v}_\mathrm{A}\,\mathrm{d}\boldsymbol{v}_\mathrm{B}}{\int f_2(s_\parallel-w_\parallel,s_\perp,\boldsymbol{v}_\mathrm{A},\boldsymbol{v}_\mathrm{B})\,\mathrm{d}\boldsymbol{v}_\mathrm{A}\,\mathrm{d}\boldsymbol{v}_\mathrm{B}}\\&=\frac{\int f_2(s_\parallel-w_\parallel,s_\perp,\boldsymbol{v}_\mathrm{A},\boldsymbol{v}_\mathrm{B})\,\delta_\mathrm{D}^{(1)}(w_\parallel-v_{\mathrm{B}\parallel}+v_{\mathrm{A}\parallel})\,\mathrm{d}\boldsymbol{v}_\mathrm{A}\,\mathrm{d}\boldsymbol{v}_\mathrm{B}}{\bar{n}^2\left[1+\xi\left(\sqrt{(s_\parallel-w_\parallel)^2+s_\perp^2}\right)\right]}\,.\end{aligned} \tag{3.13}$$

Equation (3.11) thus reduces to the fundamental equation of the streaming model

$$\begin{aligned}1+\xi_\mathrm{s}(s_\parallel,s_\perp)&=\int\left[1+\xi\left(\sqrt{(s_\parallel-w_\parallel)^2+s_\perp^2}\right)\right]\,\mathcal{P}^{(2)}_{w_\parallel}\left[w_\parallel|\boldsymbol{r}\left(s_\parallel,s_\perp,w_\parallel\right)\right]\,\mathrm{d}w_\parallel\\&=\int\left[1+\xi(\check{r})\right]\,\mathcal{P}^{(2)}_{w_\parallel}(s_\parallel-r_\parallel|\check{\boldsymbol{r}})\,\mathrm{d}r_\parallel\,.\end{aligned} \tag{3.14}$$

where a descending wedge symbol highlights variables that are derived and not independent.

3.1.4 The streaming model for the n-point correlation function

The reasoning above can be generalised to derive a streaming model for the nPCF. An ordered n-tuple of points is fully described by the position of one of them together with $n-1$ independent separation vectors.[2] Then, the n-point analogue of equation (3.11) is

$$\begin{aligned}\mathcal{G}_n=\frac{1}{\bar{n}^n}\int f_n(&s_{12\parallel}-w_{12\parallel},\ldots,s_{mn\parallel}-w_{mn\parallel},\boldsymbol{s}_{12\perp},\ldots,\boldsymbol{s}_{mn\perp},\boldsymbol{v}_{\mathrm{A}_1},\ldots,\boldsymbol{v}_{\mathrm{A}_n})\\&\delta_\mathrm{D}^{(1)}(w_{12\parallel}-v_{\mathrm{A}_2\parallel}+v_{\mathrm{A}_1\parallel})\ldots\delta_\mathrm{D}^{(1)}(w_{mn\parallel}-v_{\mathrm{A}_n\parallel}+v_{\mathrm{A}_m\parallel})\,\mathrm{d}w_{12\parallel}\ldots\mathrm{d}w_{mn\parallel}\,\mathrm{d}\boldsymbol{v}_{\mathrm{A}_1}\ldots\mathrm{d}\boldsymbol{v}_{\mathrm{A}_n}\,,\end{aligned} \tag{3.15}$$

where the subscript m is a short for the index $n-1$. We now multiply and divide the integrand in the rhs of equation (3.15) by $\bar{n}^n\,\mathcal{F}_n/\int f_n\,\mathrm{d}\boldsymbol{v}_{\mathrm{A}_1}\ldots\mathrm{d}\boldsymbol{v}_{\mathrm{A}_n}$ (which is identically one) and define

$$\mathcal{P}^{(n)}_{\boldsymbol{w}_\parallel}=\frac{\int f_n\,\delta_\mathrm{D}^{(1)}(w_{12\parallel}-v_{\mathrm{A}_2\parallel}+v_{\mathrm{A}_1\parallel})\ldots\delta_\mathrm{D}^{(1)}(w_{mn\parallel}-v_{\mathrm{A}_n\parallel}+v_{\mathrm{A}_m\parallel})\,\mathrm{d}\boldsymbol{v}_{\mathrm{A}_1}\ldots\mathrm{d}\boldsymbol{v}_{\mathrm{A}_n}}{\bar{n}^n\,\mathcal{F}_n}\,, \tag{3.16}$$

[2] Convenient choices could be either the 'star rays' $\boldsymbol{r}_{12},\boldsymbol{r}_{13},\ldots,\boldsymbol{r}_{1n}$ computed with respect to one of the points or the 'polygon sides' $\boldsymbol{r}_{12},\boldsymbol{r}_{23},\ldots,\boldsymbol{r}_{(n-1)n}$ computed between points with consecutive labels. We adopt this second option.

where f_n has the same functional dependencies as in equation (3.15). This is the joint PDF of the $n-1$ relative pairwise (i.e. for unordered 2-subsets of points) los velocities that fully determine the redshift-space distortions for a fixed n-tuple configuration in real space (bear in mind that $w_{n1\parallel} = -w_{12\parallel} - \cdots - w_{mn\parallel}$). It follows immediately from the definition above that $\mathcal{P}^{(n)}_{\boldsymbol{w}_\parallel}$ is symmetric under particle exchange and parity transformations. By combining equations (3.15) and (3.16) we obtain the streaming model for n-point statistics

$$\mathcal{G}_n = \int \mathcal{F}_n \, \mathcal{P}^{(n)}_{\boldsymbol{w}_\parallel} \, \mathrm{d}w_{12\parallel} \ldots \mathrm{d}w_{mn\parallel} \,, \tag{3.17}$$

which is one of the central results of this paper. Note that equation (3.17) is exact under the distant-observer approximation and the assumption of statistical homogeneity and isotropy in real space. For dark matter, our particle-based approach holds true even in multi-stream regions and fully accounts for density-velocity correlations. At the same time, the n-point streaming model obtained above applies to any population of tracers of the large-scale structure (e.g. galaxies or their host dark-matter halos) without making any assumptions regarding their interactions.

Application to the 3-point correlation function

The main focus of this paper is 3-point statistics. We therefore give a closer look at the streaming model for the 3PCF. After setting $n = 3$, equation (3.17) gives

$$\begin{aligned}
&1 + \xi_\mathrm{s}(s_{12\parallel}, s_{12\perp}) + \xi_\mathrm{s}(s_{23\parallel}, s_{23\perp}) + \xi_\mathrm{s}(\check{s}_{31\parallel}, s_{31\perp}) + \zeta_\mathrm{s}(\boldsymbol{s}_{12}, \boldsymbol{s}_{23}) \\
&\quad = \int \left[1 + \xi(\check{r}_{12}) + \xi(\check{r}_{23}) + \xi(\check{r}_{31}) + \zeta(\check{r}_{12}, \check{r}_{23}, \check{r}_{31})\right] \\
&\qquad\qquad \mathcal{P}^{(3)}_{\boldsymbol{w}_\parallel}\left[w_{12\parallel}, w_{23\parallel} \middle| \check{\boldsymbol{r}}_{12}(\boldsymbol{s}_{12}, w_{12\parallel}), \check{\boldsymbol{r}}_{23}(\boldsymbol{s}_{23}, w_{23\parallel})\right] \, \mathrm{d}w_{12\parallel} \, \mathrm{d}w_{23\parallel} \qquad (3.18) \\
&\quad = \int \left[1 + \xi(\check{r}_{12}) + \xi(\check{r}_{23}) + \xi(\check{r}_{31}) + \zeta(\check{r}_{12}, \check{r}_{23}, \check{r}_{31})\right] \\
&\qquad\qquad \mathcal{P}^{(3)}_{\boldsymbol{w}_\parallel}\left(s_{12\parallel} - r_{12\parallel}, s_{23\parallel} - r_{23\parallel} \middle| \check{\boldsymbol{r}}_{12}, \check{\boldsymbol{r}}_{23}\right) \, \mathrm{d}r_{12\parallel} \, \mathrm{d}r_{23\parallel} \,. \qquad (3.19)
\end{aligned}$$

where $s_{31\parallel}$ and $s_{31\perp}$ have been defined in the text following equation (3.9) and for the derived variables we have $\check{r}_{12} = \left[(s_{12\parallel} - w_{12\parallel})^2 + s^2_{12\perp}\right]^{1/2} = (r^2_{12\parallel} + s^2_{12\perp})^{1/2}$, $\check{r}_{23} = \left[(s_{23\parallel} - w_{23\parallel})^2 + s^2_{23\perp}\right]^{1/2} = (r^2_{23\parallel} + s^2_{23\perp})^{1/2}$ and $\check{r}_{31} = \left[(-s_{12\parallel} - s_{23\parallel} + w_{12\parallel} + w_{23\parallel})^2 + s^2_{31\perp}\right]^{1/2} = \left[(-r_{12\parallel} - r_{23\parallel})^2 + s^2_{31\perp}\right]^{1/2}$.

We can now use the streaming model for the 2PCF to replace all appearances of ξ_s and write an

equation for the connected 3PCF in redshift space:

$$
\begin{aligned}
-2+\zeta_{\rm s}(\boldsymbol{s}_{12},\boldsymbol{s}_{23}) &= -\int [1+\xi(\check{r}_{12})]\ \mathcal{P}^{(2)}_{w_{12\parallel}}(w_{12\parallel}|\check{\boldsymbol{r}}_{12})\,{\rm d}w_{12\parallel} \\
&\quad -\int [1+\xi(\check{r}_{23})]\ \mathcal{P}^{(2)}_{w_{23\parallel}}(w_{23\parallel}|\check{\boldsymbol{r}}_{23})\,{\rm d}w_{23\parallel} - \int [1+\xi(\check{r}_{31})]\ \mathcal{P}^{(2)}_{w_{31\parallel}}(w_{31\parallel}|\check{\boldsymbol{r}}_{31})\,{\rm d}w_{31\parallel} \qquad (3.20)\\
&\quad +\int [1+\xi(\check{r}_{12})+\xi(\check{r}_{23})+\xi(\check{r}_{31})+\zeta(\check{r}_{12},\check{r}_{23},\check{r}_{31})]\ \mathcal{P}^{(3)}_{\boldsymbol{w}_\parallel}(w_{12\parallel},w_{23\parallel}|\check{\boldsymbol{r}}_{12},\check{\boldsymbol{r}}_{23})\,{\rm d}w_{12\parallel}\,{\rm d}w_{23\parallel} \\
&= -\int [1+\xi(\check{r}_{12})]\mathcal{P}^{(2)}_{w_{12\parallel}}(s_{12\parallel}-r_{12\parallel}|\,\check{\boldsymbol{r}}_{12})\,{\rm d}r_{12\parallel} - \int [1+\xi(\check{r}_{23})]\mathcal{P}^{(2)}_{w_{23\parallel}}(s_{23\parallel}-r_{23\parallel}|\,\check{\boldsymbol{r}}_{23})\,{\rm d}r_{23\parallel} \\
&\quad -\int [1+\xi(\check{r}_{31})]\mathcal{P}^{(2)}_{w_{31\parallel}}(s_{31\parallel}-r_{31\parallel}|\,\check{\boldsymbol{r}}_{31})\,{\rm d}r_{31\parallel} + \int [1+\xi(\check{r}_{12})+\xi(\check{r}_{23})+\xi(\check{r}_{31}) \\
&\qquad +\zeta(\check{r}_{12},\check{r}_{23},\check{r}_{31})]\,\mathcal{P}^{(3)}_{\boldsymbol{w}_\parallel}\left(s_{12\parallel}-r_{12\parallel},s_{23\parallel}-r_{23\parallel}|\,\check{\boldsymbol{r}}_{12},\check{\boldsymbol{r}}_{23}\right)\,{\rm d}r_{12\parallel}\,{\rm d}r_{23\parallel}\ . \qquad (3.21)
\end{aligned}
$$

Since $\xi(\check{r}_{12})$ does not depend on $w_{23\parallel}$, $\xi(\check{r}_{23})$ does not depend on $w_{12\parallel}$, and the term $\xi(\check{r}_{31})$ in the last row is a function of $t_\parallel=-w_{12}-w_{23}$ but does not depend on $p_\parallel=w_{12\parallel}-w_{23\parallel}$, we can write

$$
\begin{aligned}
&-2+\zeta_{\rm s}(\boldsymbol{s}_{12},\boldsymbol{s}_{23}) = \\
&\quad \int [-2+\zeta(\check{r}_{12},\check{r}_{23},\check{r}_{31})]\ \mathcal{P}^{(3)}_{\boldsymbol{w}_\parallel}(w_{12\parallel},w_{23\parallel}|\check{\boldsymbol{r}}_{12},\check{\boldsymbol{r}}_{23})\,{\rm d}w_{12\parallel}\,{\rm d}w_{23\parallel} \\
&\quad +\int [1+\xi(\check{r}_{12})]\left[\int \mathcal{P}^{(3)}_{\boldsymbol{w}_\parallel}(w_{12\parallel},w_{23\parallel}|\check{\boldsymbol{r}}_{12},\check{\boldsymbol{r}}_{23})\,{\rm d}w_{23\parallel} - \mathcal{P}^{(2)}_{w_{12\parallel}}(w_{12\parallel}|\check{\boldsymbol{r}}_{12})\right]\,{\rm d}w_{12\parallel} \\
&\quad +\int [1+\xi(\check{r}_{23})]\left[\int \mathcal{P}^{(3)}_{\boldsymbol{w}_\parallel}(w_{12\parallel},w_{23\parallel}|\check{\boldsymbol{r}}_{12},\check{\boldsymbol{r}}_{23})\,{\rm d}w_{12\parallel} - \mathcal{P}^{(2)}_{w_{23\parallel}}(w_{23\parallel}|\check{\boldsymbol{r}}_{23})\right]\,{\rm d}w_{23\parallel} \qquad (3.22)\\
&\quad +\int [1+\xi(\check{r}_{31})]\left[\frac{1}{2}\int \mathcal{P}^{(3)}_{\boldsymbol{w}_\parallel}\left(\frac{-t_\parallel+p_\parallel}{2},\frac{-t_\parallel-p_\parallel}{2}|\check{\boldsymbol{r}}_{12},\check{\boldsymbol{r}}_{23}\right)\,{\rm d}p_\parallel - \mathcal{P}^{(2)}_{t_\parallel}(t_\parallel|\check{\boldsymbol{r}}_{31})\right]\,{\rm d}t_\parallel\ ,
\end{aligned}
$$

where we have changed the integration variables from $w_{12\parallel}$ and $w_{23\parallel}$ to $t_\parallel$ and $p_\parallel$ in the last line. The asymmetry of this term reflects the fact that we have picked $w_{12\parallel}$ and $w_{23\parallel}$ as the independent variables for $\mathcal{P}^{(3)}_{\boldsymbol{w}_\parallel}$.

3.1.5 The streaming model for the connected correlation functions

The procedure discussed above can be iterated to write down the streaming model for the connected nPCFs. The course of action consists of three basic steps: (i) start by writing down equation (3.17); (ii) express $\mathcal{G}_n$ and $\mathcal{F}_n$ in terms of the connected functions of order 2 to n; (iii) recursively apply the streaming model for the connected functions of order $n-1$ to 2.

We now derive an alternative formulation of the streaming model that only involves connected correlation functions. In order to facilitate understanding, we first discuss 2-point statistics and then generalise the derivation to n-point correlations.

2-point statistics

Our starting point is the introduction of the connected 2-point phase-space density $f_2^{(c)} = f_2 - f_1 f_1$. The corresponding quantity in redshift-space is

$$g_2^{(c)} = \int f_2^{(c)}\, \delta_{\rm D}^{(1)}(w_\parallel - v_{{\rm B}\parallel} + v_{{\rm A}\parallel})\, {\rm d}w_\parallel \,, \tag{3.23}$$

so that the 2PCF

$$\xi_{\rm s}(s_\parallel, s_\perp) = \frac{1}{\bar{n}^2} \int g_2^{(c)}\, {\rm d}\boldsymbol{v}_{\rm A}\, {\rm d}\boldsymbol{v}_{\rm B} = \frac{1}{\bar{n}^2} \int f_2^{(c)}\; \delta_{\rm D}^{(1)}(w_\parallel - v_{{\rm B}\parallel} + v_{{\rm A}\parallel})\, {\rm d}\boldsymbol{v}_{\rm A}\, {\rm d}\boldsymbol{v}_{\rm B} \,. \tag{3.24}$$

We then multiply the integrand on the rhs by $\bar{n}^2\xi / \int f_2^{(c)}\, {\rm d}\boldsymbol{v}_{\rm A}\, {\rm d}\boldsymbol{v}_{\rm B}$ which is always identical to one. By rearranging the terms, we obtain

$$\xi_{\rm s}(s_\parallel, s_\perp) = \int \xi\left[\sqrt{(s_\parallel - w_\parallel)^2 + s_\perp^2}\right]\, \mathcal{C}_{w_\parallel}^{(2)}\left[w_\parallel | \check{\boldsymbol{r}}\left(s_\parallel, s_\perp, w_\parallel\right)\right]\, {\rm d}w_\parallel \,, \tag{3.25}$$

with

$$\mathcal{C}^{(2)} = \frac{\displaystyle\int f_2^{(c)}\, \delta_{\rm D}^{(1)}(w_\parallel - v_{{\rm B}\parallel} + v_{{\rm A}\parallel})\, {\rm d}\boldsymbol{v}_{\rm A}\, {\rm d}\boldsymbol{v}_{\rm B}}{\displaystyle\int f_2^{(c)}\, {\rm d}\boldsymbol{v}_{\rm A}\, {\rm d}\boldsymbol{v}_{\rm B}} = \frac{\displaystyle\int f_2^{(c)}\, \delta_{\rm D}^{(1)}(w_\parallel - v_{{\rm B}\parallel} + v_{{\rm A}\parallel})\, {\rm d}\boldsymbol{v}_{\rm A}\, {\rm d}\boldsymbol{v}_{\rm B}}{\bar{n}^2\, \xi} \,. \tag{3.26}$$

Equation (3.25) embodies the streaming model for the connected part of the 2PCF. Here $\mathcal{C}^{(2)}$ accounts for the relative los velocity between particles forming 'correlated pairs'. In order to better grasp its meaning, we replace $f_2^{(c)} = f_2 - f_1\, f_1$ in equation (3.26) and express $\mathcal{C}^{(2)}$ in terms of $\mathcal{P}_{w_\parallel}^{(2)}$ to obtain

$$\mathcal{C}^{(2)} = \frac{(1+\xi)\, \mathcal{P}_{w_\parallel}^{(2)} - \mathcal{R}_{w_\parallel}^{(2)}}{\xi} \,, \tag{3.27}$$

with

$$\begin{aligned} \mathcal{R}_{w_\parallel}^{(2)} &= \frac{\displaystyle\int f_1\, f_1\, \delta_{\rm D}^{(1)}(w_\parallel - v_{{\rm B}\parallel} + v_{{\rm A}\parallel})\, {\rm d}\boldsymbol{v}_{\rm A}\, {\rm d}\boldsymbol{v}_{\rm B}}{\bar{n}^2} \\ &= \int \mathcal{P}_{\boldsymbol{v}_{\rm A}}^{(1)}\, \mathcal{P}_{\boldsymbol{v}_{\rm B}}^{(1)}\, \delta_{\rm D}^{(1)}(w_\parallel - v_{{\rm B}\parallel} + v_{{\rm A}\parallel})\, {\rm d}\boldsymbol{v}_{\rm A}\, {\rm d}\boldsymbol{v}_{\rm B} \,. \end{aligned} \tag{3.28}$$

As discussed in section 3.1.2, due to statistical homogeneity, $\mathcal{P}_{\boldsymbol{v}_{\rm A}}^{(1)}$ and $\mathcal{P}_{\boldsymbol{v}_{\rm B}}^{(1)}$ assume the same functional form. Let us denote by $\mathcal{P}_{v_\parallel}^{(1)}$ the PDF of the los velocity obtained marginalising $\mathcal{P}_{\boldsymbol{v}}^{(1)}$ over the two

perpendicular directions.[3] Then, equation (3.28) reduces to

$$\mathcal{R}^{(2)}_{w_\parallel}(w_\parallel) = \int \mathcal{P}^{(1)}_{v_\parallel}(v_{\mathrm{A}\parallel})\, \mathcal{P}^{(1)}_{v_\parallel}(w_\parallel + v_{\mathrm{A}\parallel})\, \mathrm{d}v_{\mathrm{A}\parallel} \,. \tag{3.29}$$

While $\mathcal{P}^{(2)}_{w_\parallel}$ gives the PDF of the relative los velocity between particles in all pairs with a given real-space separation, $\mathcal{R}^{(2)}_{w_\parallel}$ is the distribution of $w_\parallel$ generated by sampling (allowing repetitions) two particles at random irrespective of their separation. This provides an operational way to compute $\mathcal{C}^{(2)}$ from simulations. Note that, although $\int \mathcal{C}^{(2)}\, \mathrm{d}w_\parallel = 1$, $\mathcal{C}^{(2)}$ is not a PDF (this is why we do not write the subscript $w_\parallel$ for it) and can assume negative values. In brief, this function quantifies the excess (or defect) probability to get pairs with a given $w_\parallel$ with respect to random.

By substituting equation (3.27) into equation (3.25) we get

$$\xi_{\mathrm{s}}(s_\parallel, s_\perp) = \int [1 + \xi(\check{r})]\, \mathcal{P}^{(2)}_{w_\parallel}(w_\parallel|\check{\boldsymbol{r}})\, \mathrm{d}w_\parallel - \int \mathcal{R}^{(2)}_{w_\parallel}(w_\parallel)\, \mathrm{d}w_\parallel \,, \tag{3.30}$$

and, after integrating over $w_\parallel$, it is obvious that the second term is identically equal to one and that equation (3.25) is equivalent to the classic streaming model.

3-point statistics

The reasoning above can be generalised to n-point statistics. After repeating the same basic steps, we obtain

$$\mathcal{G}^{(c)}_n = \int \mathcal{F}^{(c)}_n\, \mathcal{C}^{(n)}(w_{12\parallel}, \ldots, w_{mn\parallel})\, \mathrm{d}w_{12\parallel} \ldots \mathrm{d}w_{mn\parallel} \,, \tag{3.31}$$

where

$$\mathcal{C}^{(n)} = \frac{\displaystyle\int f^{(c)}_n\, \delta^{(1)}_{\mathrm{D}}(w_{12\parallel} - v_{\mathrm{A}_2\parallel} + v_{\mathrm{A}_1\parallel}) \ldots \delta^{(1)}_{\mathrm{D}}(w_{mn\parallel} - v_{\mathrm{A}_n\parallel} + v_{\mathrm{A}_m\parallel})\, \mathrm{d}\boldsymbol{v}_{\mathrm{A}_1} \ldots \mathrm{d}\boldsymbol{v}_{\mathrm{A}_n}}{\bar{n}^n\, \mathcal{F}^{(c)}_n} \,. \tag{3.32}$$

In particular, for $n = 3$, we have

$$\zeta_{\mathrm{s}}(\boldsymbol{s}_{12}, \boldsymbol{s}_{23}) = \int \zeta(\check{r}_{12}, \check{r}_{23}, \check{r}_{31})\, \mathcal{C}^{(3)}(w_{12\parallel}, w_{23\parallel}|\check{\boldsymbol{r}}_{12}, \check{\boldsymbol{r}}_{23})\, \mathrm{d}w_{12\parallel}\, \mathrm{d}w_{23\parallel} \,, \tag{3.33}$$

where

$$\mathcal{C}^{(3)} = \frac{\displaystyle\int f^{(c)}_3\, \delta^{(1)}_{\mathrm{D}}(w_{12\parallel} - v_{\mathrm{B}\parallel} + v_{\mathrm{A}\parallel})\, \delta^{(1)}_{\mathrm{D}}(w_{23\parallel} - v_{\mathrm{C}\parallel} + v_{\mathrm{B}\parallel})\, \mathrm{d}\boldsymbol{v}_{\mathrm{A}}\, \mathrm{d}\boldsymbol{v}_{\mathrm{B}}\, \mathrm{d}\boldsymbol{v}_{\mathrm{C}}}{\bar{n}^3\, \zeta} \,. \tag{3.34}$$

[3] Because of statistical isotropy, the PDF of the velocity components parallel to any axis must assume the same form.

Since $f_3^{(c)} = f_3 - (f_2^{(c)}\, f_1 + \text{symm.}) - f_1\, f_1\, f_1$ and $f_2^{(c)} = f_2 - f_1\, f_1$, it follows that $f_3^{(c)} = f_3 - (f_2\, f_1 + \text{symm.}) + 2\, f_1\, f_1\, f_1$. It is thus convenient to re-write $\mathcal{C}^{(3)}$ as

$$\mathcal{C}^{(3)} = \frac{[1 + \xi_{12} + \xi_{23} + \xi_{31} + \zeta]\ \mathcal{P}^{(3)}_{\boldsymbol{w}_\parallel} - \Big[(1+\xi_{12})\, \mathcal{Q}^{(3\mathrm{AB})}_{\boldsymbol{w}_\parallel} + \text{symm.}\Big] + 2\, \mathcal{R}^{(3)}_{\boldsymbol{w}_\parallel}}{\zeta} \,. \tag{3.35}$$

where we have used ξ_{ij} as a short for $\xi(r_{ij})$ and the PDFs $\mathcal{Q}^{(3\mathrm{AB})}_{\boldsymbol{w}_\parallel}$ and $\mathcal{R}_{\boldsymbol{w}_\parallel}$ are defined as:

$$\begin{aligned}
\mathcal{Q}^{(3\mathrm{AB})}_{\boldsymbol{w}_\parallel} &= \frac{\displaystyle\int f_2(\mathrm{A},\mathrm{B})\, f_1(\mathrm{C})\, \delta_{\mathrm{D}}^{(1)}(w_{12\parallel} - v_{\mathrm{B}\parallel} + v_{\mathrm{A}\parallel})\, \delta_{\mathrm{D}}^{(1)}(w_{23\parallel} - v_{\mathrm{C}\parallel} + v_{\mathrm{B}\parallel})\, \mathrm{d}\boldsymbol{v}_\mathrm{A}\, \mathrm{d}\boldsymbol{v}_\mathrm{B}\, \mathrm{d}\boldsymbol{v}_\mathrm{C}}{\bar{n}^3\, \xi_{12}} \\
&= \int G(v_{\mathrm{A}\parallel}, v_{\mathrm{A}\parallel} + w_{12}|\boldsymbol{r}_{12})\, \mathcal{P}^{(1)}_{v_\parallel}(v_{\mathrm{A}\parallel} + w_{12\parallel} + w_{23\parallel})\, \mathrm{d}v_{\mathrm{A}\parallel} \,,
\end{aligned} \tag{3.36}$$

(the function G is defined such that $\mathcal{P}^{(2)}_{w_\parallel}(w_{12}|\boldsymbol{r}_{12}) = \int G(v_{\mathrm{A}\parallel}, v_{\mathrm{A}\parallel} + w_{12}|\boldsymbol{r}_{12})\, \mathrm{d}v_{\mathrm{A}\parallel}$) and

$$\begin{aligned}
\mathcal{R}^{(3)}_{\boldsymbol{w}_\parallel} &= \frac{\displaystyle\int f_1(\mathrm{A})\, f_1(\mathrm{B})\, f_1(\mathrm{C})\, \delta_{\mathrm{D}}^{(1)}(w_{12\parallel} - v_{\mathrm{B}\parallel} + v_{\mathrm{A}\parallel})\, \delta_{\mathrm{D}}^{(1)}(w_{23\parallel} - v_{\mathrm{C}\parallel} + v_{\mathrm{B}\parallel})\, \mathrm{d}\boldsymbol{v}_\mathrm{A}\, \mathrm{d}\boldsymbol{v}_\mathrm{B}\, \mathrm{d}\boldsymbol{v}_\mathrm{C}}{\bar{n}^3} \\
&= \int \mathcal{P}^{(1)}_{\boldsymbol{v}_\mathrm{A}}\, \mathcal{P}^{(1)}_{\boldsymbol{v}_\mathrm{B}}\, \mathcal{P}^{(1)}_{\boldsymbol{v}_\mathrm{C}}\, \delta_{\mathrm{D}}^{(1)}(w_{12\parallel} - v_{\mathrm{B}\parallel} + v_{\mathrm{A}\parallel})\, \delta_{\mathrm{D}}^{(1)}(w_{23\parallel} - v_{\mathrm{C}\parallel} + v_{\mathrm{B}\parallel})\, \mathrm{d}\boldsymbol{v}_\mathrm{A}\, \mathrm{d}\boldsymbol{v}_\mathrm{B}\, \mathrm{d}\boldsymbol{v}_\mathrm{C} \\
&= \int \mathcal{P}^{(1)}_{v_\parallel}(v_{\mathrm{A}\parallel})\, \mathcal{P}^{(1)}_{v_\parallel}(v_{\mathrm{A}\parallel} + w_{12\parallel})\, \mathcal{P}^{(1)}_{v_\parallel}(v_{\mathrm{A}\parallel} + w_{12\parallel} + w_{23\parallel})\, \mathrm{d}v_{\mathrm{A}\parallel} \,.
\end{aligned} \tag{3.37}$$

In full analogy with the 2-point case, equation (3.34) provides an operational way to compute $\mathcal{C}^{(3)}$ in practice. The first term on the rhs is proportional to $\mathcal{P}^{(3)}_{\boldsymbol{w}_\parallel}$ and thus represents the (rescaled) bivariate distribution of the relative los velocities in actual triplets of particles. The next three terms are proportional to $\mathcal{Q}^{(3ij)}_{\boldsymbol{w}_\parallel}$ i.e. to the bivariate distribution of the relative los velocities in triplets that are formed by an actual pair of particles with a fixed separation $\boldsymbol{r}_{ij}$ and a third particle which is randomly selected (irrespective from its actual position). Finally, the last term accounts for the contribution of fully random triplets. Note that, by definition, $\int \mathcal{C}^{(3)}(w_{12\parallel}, w_{23\parallel}|\boldsymbol{r}_{12}, \boldsymbol{r}_{23})\, \mathrm{d}w_{12\parallel}\, \mathrm{d}w_{23\parallel} = 1$. Substituting equation (3.35) into (3.33) and taking into account that $\int \mathcal{R}^{(3)}_{\boldsymbol{w}_\parallel}\, \mathrm{d}w_{12\parallel}\, \mathrm{d}w_{23\parallel} = 1$ gives back equation (3.20)

3.1.6 Collisionless systems

So far we have considered the most general and complete description of an N-body system and our equations are exact. However, great simplifications are possible in particular cases. For instance, systems composed by very many particles interacting exclusively through long-range forces are conveniently described by kinetic equations of the Jeans-Vlasov type. This corresponds to neglecting two-body and higher-order velocity correlations, i.e. to assuming that

$$f_n(\boldsymbol{x}_{\mathrm{A}_1}, \ldots, \boldsymbol{x}_{\mathrm{A}_n}, \boldsymbol{v}_{\mathrm{A}_1}, \ldots, \boldsymbol{v}_{\mathrm{A}_n}) \propto \Big\langle \prod_{j=1}^{n} \bar{f}(\boldsymbol{x}_{\mathrm{A}_j}, \boldsymbol{v}_{\mathrm{A}_j}) \Big\rangle \,, \tag{3.38}$$

where $\bar{f}$ denotes the macroscopic coarse-grained phase-space density that satisfies Vlasov equation. The approximation holds true for time scales comparable to the collision time. Since dark-matter particles form a collisionless system for the entire life of the Universe, equation (3.38) is often implicitly assumed in the cosmological literature. In order to compare our results with previous work, we recast our equations in terms of $\bar{f}$. After introducing the mass density contrast $\delta(\boldsymbol{x})$, in the single-stream regime, we can write $\bar{f}(\boldsymbol{x},\boldsymbol{v}) = \bar{n}\,[1+\delta(\boldsymbol{x})]\,\delta_{\mathrm{D}}^{(3)}[\boldsymbol{v}-\mathsf{v}(\boldsymbol{x})]$ (where $\mathsf{v}(\boldsymbol{x})$ denotes the continuous velocity field), while $\bar{f}(\boldsymbol{x},\boldsymbol{v}) = \bar{n}\,[1+\delta(\boldsymbol{x})]\,F_{\boldsymbol{v}}(\boldsymbol{x},\boldsymbol{v})$ with $\int F_{\boldsymbol{v}}(\boldsymbol{x},\boldsymbol{v})\,\mathrm{d}\boldsymbol{v} = 1$ in the multi-stream case. Therefore,[4]

$$\mathcal{P}_{w_\parallel}^{(2)}(w_{12\parallel}|\boldsymbol{x}_2-\boldsymbol{x}_1) = \frac{\langle[1+\delta(\boldsymbol{x}_1)]\,[1+\delta(\boldsymbol{x}_2)]\,\mathcal{K}^{(2)}(w_{12\parallel},\boldsymbol{x}_1,\boldsymbol{x}_2)\rangle}{1+\xi(r)}\,, \tag{3.39}$$

where[5]

$$\mathcal{K}^{(2)}(w_{12\parallel},\boldsymbol{x}_1,\boldsymbol{x}_2) = \int F_{\boldsymbol{v}_1}(\boldsymbol{x}_1,\boldsymbol{v}_1)\,F_{\boldsymbol{v}_2}(\boldsymbol{x}_2,\boldsymbol{v}_2)\,\delta_{\mathrm{D}}^{(1)}(w_{12\parallel}-v_{2\parallel}+v_{1\parallel})\,\mathrm{d}\boldsymbol{v}_1\,\mathrm{d}\boldsymbol{v}_2\,. \tag{3.40}$$

which, in the single-stream regime, reduces to $\mathcal{K}^{(2)}(w_{12\parallel},\boldsymbol{x}_1,\boldsymbol{x}_2) = \delta_{\mathrm{D}}^{(1)}[w_{12\parallel}-v_\parallel(\boldsymbol{x}_2)+v_\parallel(\boldsymbol{x}_1)]$. By Fourier transforming $\mathcal{K}^{(2)}$, we obtain the characteristic function

$$\widetilde{\mathcal{P}}_{w_\parallel}^{(2)}(k|\boldsymbol{x}_2-\boldsymbol{x}_1) = \frac{\langle[1+\delta(\boldsymbol{x}_1)]\,[1+\delta(\boldsymbol{x}_2)]\,\widetilde{\mathcal{K}}^{(2)}(k,\boldsymbol{x}_1,\boldsymbol{x}_2)\rangle}{1+\xi(r)}\,, \tag{3.41}$$

with

$$\widetilde{\mathcal{K}}^{(2)}(k,\boldsymbol{x}_1,\boldsymbol{x}_2) = \int F_{\boldsymbol{v}_1}(\boldsymbol{x}_1,\boldsymbol{v}_1)\,F_{\boldsymbol{v}_2}(\boldsymbol{x}_2,\boldsymbol{v}_2)\,e^{ik(v_{\mathrm{A}_2\parallel}+v_{\mathrm{A}_1\parallel})}\,\mathrm{d}\boldsymbol{v}_1\,\mathrm{d}\boldsymbol{v}_2\,. \tag{3.42}$$

The pairwise-velocity distribution is therefore fully determined by the so-called[6] 'moment generating function' (which is actually a characteristic function)

$$1+\mathcal{M}(J,\boldsymbol{x}_2-\boldsymbol{x}_1) = \langle[1+\delta(\boldsymbol{x}_1)]\,[1+\delta(\boldsymbol{x}_2)]\,\widetilde{\mathcal{K}}^{(2)}(J,\boldsymbol{x}_1,\boldsymbol{x}_2)\rangle\,. \tag{3.43}$$

The streaming model for the 2PCF can be derived by applying a cumulant expansion to it, i.e. by expanding $\ln[1+\mathcal{M}(J,\boldsymbol{x}_2-\boldsymbol{x}_1)]$ in J (Scoccimarro, 2004; Vlah and M. White, 2019). This approach has been generalised to 3-point statistics in Vlah and M. White, 2019. Their equation 7.7 provides the Fourier-space version of the streaming model. Compared to our equation (3.20) in real space, their expression is missing several terms. This difference stems from the incorrect assumption that the Fourier transform of $\langle[1+\delta(\boldsymbol{x}_1)]\,[1+\delta(\boldsymbol{x}_2)]\,[1+\delta(\boldsymbol{x}_3)]\rangle$ gives the bispectrum, i.e. the full 3PCF

[4] To simplify the notation, from now on we use the symbols $\boldsymbol{x}_i$ and $\boldsymbol{v}_i$ to indicate generic positions and velocities. This differs from section 3.1.2 where we used the same symbols to indicate the location and velocity of the i^{th} particle.

[5] In the full solution, the term $F_{\boldsymbol{v}_1}F_{\boldsymbol{v}_2}$ should be replaced with $F_{\boldsymbol{v}_1}F_{\boldsymbol{v}_2}+G_{\boldsymbol{v}_1,\boldsymbol{v}_2}$ where the function $G_{\boldsymbol{v}_1,\boldsymbol{v}_2}$ accounts for velocity correlations.

[6] With an abuse of notation due to the fact that it was originally derived assuming a single-stream fluid (Scoccimarro, 2004), equation (3.43) is usually written as $1+\mathcal{M}(J,\boldsymbol{x}_2-\boldsymbol{x}_1) = \langle[1+\delta(\boldsymbol{x}_1)]\,[1+\delta(\boldsymbol{x}_2)]\,e^{iJv_{21\parallel}}\rangle$ (e.g. Vlah and M. White, 2019).

has been replaced with its connected part in Vlah and M. White, 2019. Note that,

$$\mathcal{P}^{(3)}_{\boldsymbol{w}_\parallel}(w_{12\parallel}, w_{23\parallel}|\boldsymbol{r}_{12}, \boldsymbol{r}_{23}) = \frac{\langle [1+\delta(\boldsymbol{x}_1)]\,[1+\delta(\boldsymbol{x}_2)]\,[1+\delta(\boldsymbol{x}_3)]\,\mathcal{K}^{(3)}(w_{12\parallel}, w_{23\parallel}, \boldsymbol{x}_1, \boldsymbol{x}_2, \boldsymbol{x}_3)\rangle}{1+\xi(r_{12})+\xi(r_{23})+\xi(r_{31})+\zeta(r_{12}, r_{23}, r_{31})}\,, \tag{3.44}$$

where

$$\mathcal{K}^{(3)}(w_{12\parallel}, w_{23\parallel}, \boldsymbol{x}_1, \boldsymbol{x}_2, \boldsymbol{x}_3) = \int F_{\boldsymbol{v}_1}(\boldsymbol{x}_1, \boldsymbol{v}_1)\, F_{\boldsymbol{v}_2}(\boldsymbol{x}_2, \boldsymbol{v}_2)\, F_{\boldsymbol{v}_3}(\boldsymbol{x}_3, \boldsymbol{v}_3)\, \delta^{(1)}_{\rm D}(w_{12\parallel} - v_{2\parallel} + v_{1\parallel})$$
$$\delta^{(1)}_{\rm D}(w_{23\parallel} - v_{3\parallel} + v_{2\parallel})\, \mathrm{d}\boldsymbol{v}_1\, \mathrm{d}\boldsymbol{v}_2\, \mathrm{d}\boldsymbol{v}_3\,. \tag{3.45}$$

By direct integration, we find that

$$\int \mathcal{K}^{(3)}(w_{12\parallel}, w_{23\parallel}, \boldsymbol{x}_1, \boldsymbol{x}_2, \boldsymbol{x}_3)\, \mathrm{d}w_{12\parallel}\, \mathrm{d}\boldsymbol{v}_3 = \mathcal{K}^{(2)}(w_{12\parallel}, \boldsymbol{x}_1, \boldsymbol{x}_2)\,, \tag{3.46}$$

and

$$\int \mathcal{P}^{(3)}_{\boldsymbol{w}_\parallel}(w_\parallel, q_\parallel|\boldsymbol{r}_{12}, \boldsymbol{r}_{23})\, \mathrm{d}q_\parallel - \mathcal{P}^{(2)}_{w_\parallel}(w_\parallel|\boldsymbol{r}_{12}) = \tag{3.47}$$
$$\left\langle \left\{ \frac{[1+\delta(\boldsymbol{x}_1)]\,[1+\delta(\boldsymbol{x}_2)]\,[1+\delta(\boldsymbol{x}_3)]}{1+\xi(r_{12})+\xi(r_{23})+\xi(r_{31})+\zeta(r_{12}, r_{23}, r_{31})} - \frac{[1+\delta(\boldsymbol{x}_1)]\,[1+\delta(\boldsymbol{x}_2)]}{1+\xi(r_{12})} \right\} \mathcal{K}^{(2)}(w_{12\parallel}, \boldsymbol{x}_1, \boldsymbol{x}_2) \right\rangle\,,$$

which gives the difference between the triplet weighted and the pair weighted averages of the function $\mathcal{K}^{(2)}(w_{12\parallel}, \boldsymbol{x}_1, \boldsymbol{x}_2)$ and does not necessarily vanish.

3.2 The joint distribution of pairwise velocities in a triplet

The joint distribution of pairwise los velocities for a given triangle in configuration space, $\mathcal{P}^{(3)}_{\boldsymbol{w}_\parallel}(w_{12\parallel}, w_{23\parallel}|\boldsymbol{r}_{12}, \boldsymbol{r}_{23}) \equiv \mathcal{P}^{(3)}_{\boldsymbol{w}_\parallel}(w_{12\parallel}, w_{23\parallel}|\triangle_{123})$, is a central quantity in the streaming model for the 3PCF. In this section, we use a large N-body simulation and perturbative techniques to study its properties.

3.2.1 N-body simulation

We use the public code GADGET-2 (Springel, 2005) to simulate the formation of the large-scale structure of the Universe within a periodic cubic box with a side of 1.2 h^{-1}Gpc. We assume the base ΛCDM model that provides the best fit to the 2015 power spectra determined by the PLANCK satellite in combination with lensing reconstruction and external data (Planck Collaboration, Adam et al., 2016). In brief, the flat background is characterised by the density parameters $\Omega_{\rm m} = 0.3089$ (total matter), $\Omega_\Lambda = 0.6911$ (cosmological constant), $\Omega_{\rm b} = 0.0486$ (baryonic matter) and by the present-day value of the Hubble parameter of $H_0 \equiv H(z=0) = 100\,h\,\mathrm{km\,s^{-1}Mpc^{-1}}$ with $h = 0.6774$. The primordial spectral index of the density perturbations is $n_s = 0.9667$ and the linear rms fluctuation measured in spheres of 8 h^{-1}Mpc is $\sigma_8 = 0.8159$. The matter content of the simulation box is discretised into 1024^3 identical particles, each with a mass of $M_{\rm part} = 1.379 \times 10^{11}\,h^{-1}\mathrm{M}_\odot$. The input linear power spectrum of the matter perturbations is obtained using the Code for Anisotropies

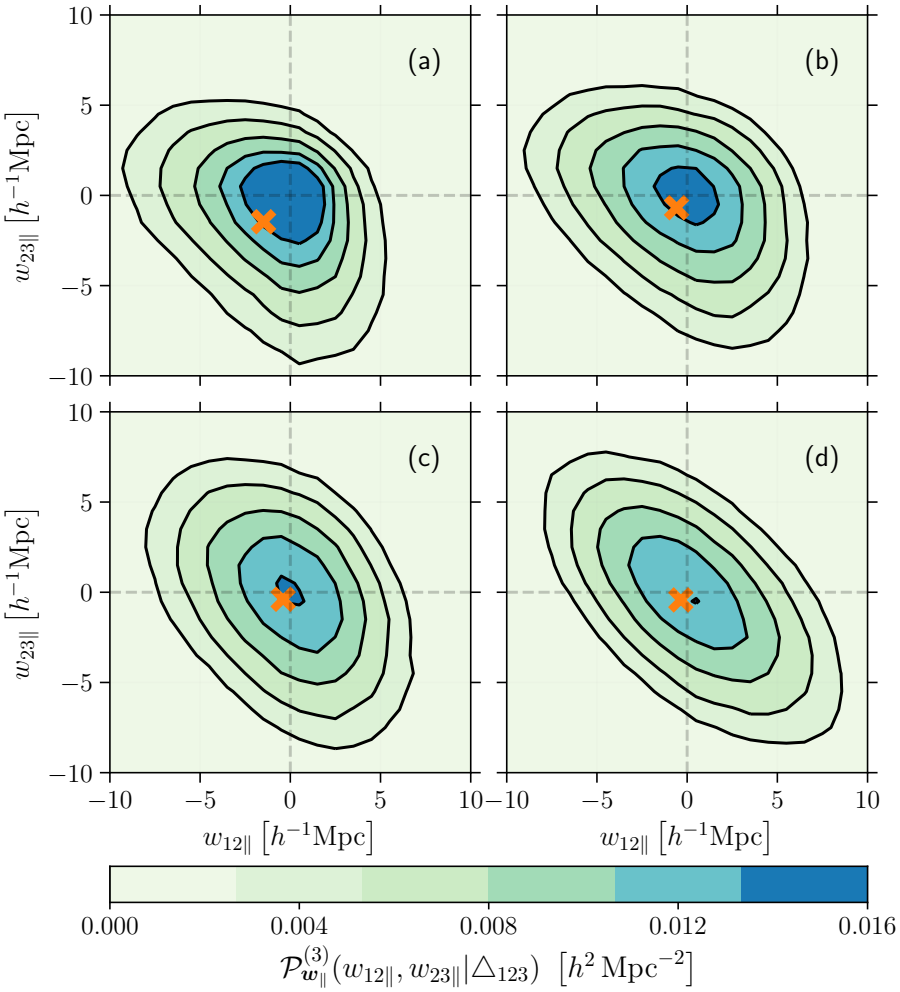

Figure 3.1: Contour levels for the joint probability distribution of the relative los velocities $w_{12\parallel}$ and $w_{23\parallel}$ extracted from our N-body simulation. The mean is indicated with a cross. The four panels correspond to different triangular configurations with $\{r_{12\parallel}, r_{12\perp}, r_{23\parallel}, r_{23\perp}, r_{31\perp}\}$ lying within ($5\,h^{-1}$Mpc wide) bins centred at $\{7.5, 7.5, 7.5, 7.5, 7.5\}_{(\mathrm{a})}$, $\{27.5, 17.5, 17.5, 17.5, 27.5\}_{(\mathrm{b})}$, $\{22.5, 32.5, 42.5, 32.5, 27.5\}_{(\mathrm{c})}$, $\{52.5, 47.5, 57.5, 42.5, 62.5\}_{(\mathrm{d})}$ in units of h^{-1} Mpc.

in the Microwave Background (CAMB[7], A. Lewis, Challinor and Lasenby, 2000). Gaussian initial conditions are generated at redshift $z = 50$ according to second-order Lagrangian perturbation theory using the MUSIC code (Hahn and Abel, 2011).

3.2.2 Basic properties of $\mathcal{P}^{(3)}_{\boldsymbol{w}_\parallel}(\boldsymbol{w_{12\parallel}}, \boldsymbol{w_{23\parallel}}|\triangle_{\mathbf{123}})$

We measure $\mathcal{P}^{(3)}_{\boldsymbol{w}_\parallel}(w_{12\parallel}, w_{23\parallel}|\triangle_{123})$ from the final output of our N-body simulation at $z = 0$. This is a demanding task as it requires identifying all particle triplets with a given $r_{12\parallel}, r_{12\perp}, r_{23\parallel}, r_{23\perp}$

[7] camb.info

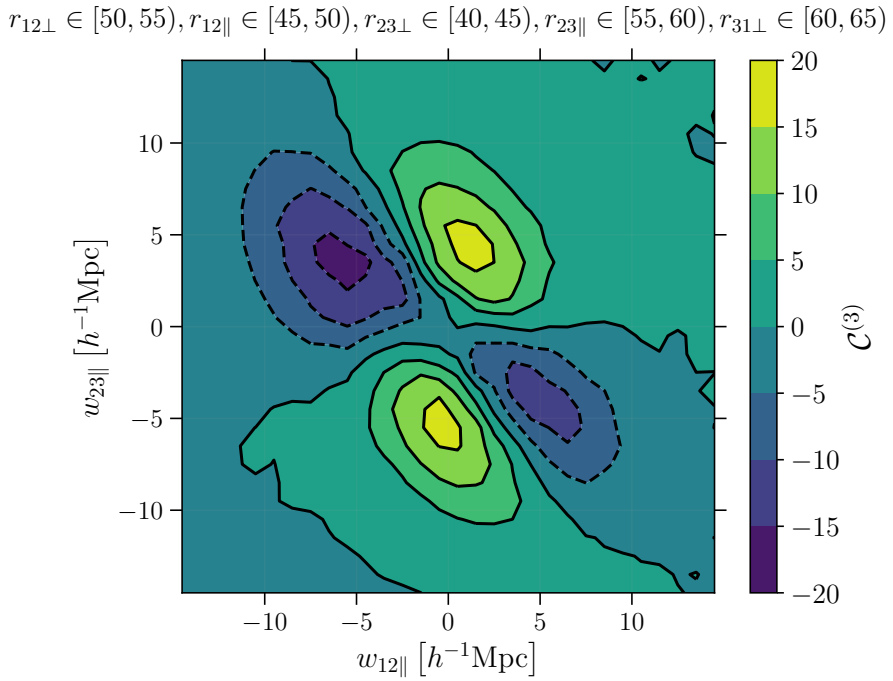

Figure 3.2: Contour levels for the function $\mathcal{C}^{(3)}(w_{12\parallel}, w_{23\parallel}|\triangle_{123})$ extracted from our N-body simulation by combining several PDFs as in equation (3.35). The side lengths that define the specific triangular configuration we consider are listed on top of the figure in units of $h^{-1}\mathrm{Mpc}$.

and $r_{31\perp}$. herefore, we consider a subsample of 100^3 randomly selected simulation particles. Four examples are shown in figure 3.1. Note that the distribution is always unimodal with a mode which is close to $(w_{12\parallel}, w_{23\parallel}) = (0, 0)$. On the other hand, the mean los pairwise velocities (indicated with a cross in the plot) are negative. In general, contour levels are not symmetric but tend to become elliptical for large separations. The pairwise velocities $w_{12\parallel}$ and $w_{23\parallel}$ anti-correlate on these scales due to the opposite sign of $v_{2\parallel}$ in their definition.

In figure 3.2, we show one example of the function $\mathcal{C}^{(3)}(w_{12\parallel}, w_{23\parallel}|\triangle_{123})$ for the same triangular configuration considered in the bottom-right panel of figure 3.1. As expected, $\mathcal{C}^{(3)}(w_{12\parallel}, w_{23\parallel}|\triangle_{123})$ is more complex than the corresponding $\mathcal{P}^{(3)}_{\boldsymbol{w}_\parallel}(w_{12\parallel}, w_{23\parallel}|\triangle_{123})$. The function $\mathcal{C}^{(3)}$ shows a typical quadrupolar structure with correlated steps in $w_{12\parallel}$ and $w_{23\parallel}$ giving a positive signal and anti-correlated ones producing a negative output value. Figures 3.1 and 3.2 suggest that $\mathcal{P}^{(3)}_{\boldsymbol{w}_\parallel}(w_{12\parallel}, w_{23\parallel}|\triangle_{123})$ is best suited for simple approximations in terms of analytical PDFs. We will pursue this phenomenological approach in section 3.3.

3.2.3 Moments of $\mathcal{P}^{(3)}_{\boldsymbol{w}_\parallel}(\boldsymbol{w_{12\parallel}}, \boldsymbol{w_{23\parallel}}|\triangle_{\mathbf{123}})$: perturbative predictions at leading order

In this section, we compute the first two moments of the joint distribution of $w_{12\parallel}$ and $w_{23\parallel}$ using standard perturbation theory at leading order (LO) and compare the results against our simulation.

Mean relative velocities between particle pairs in a triplet

Standard perturbation theory assumes that the matter content of the Universe is in the single-stream regime and, at any given time, describes it in terms of two continuous fields: the mass density contrast $\delta(\boldsymbol{x})$ and the peculiar velocity $\boldsymbol{u}(\boldsymbol{x})$. Linear perturbations in δ grow proportionally to the growth factor D while those in $\boldsymbol{u}$ grow proportionally to $aHfD$ with $f = \mathrm{d}\log D/\mathrm{d}\log a$. The Fourier transforms of the linear terms are related as

$$\tilde{\boldsymbol{u}}(\boldsymbol{k}) = aHf\,\frac{i\boldsymbol{k}}{k^2}\,\tilde{\delta}(\boldsymbol{k})\;. \tag{3.48}$$

To make equations shorter, we follow the notation introduced in sections 3.1.1 and 3.1.6 and describe peculiar velocities in terms of the vector field $\mathsf{v}(\boldsymbol{x}) = \boldsymbol{u}(\boldsymbol{x})/(aH)$, i.e. in terms of the comoving separation vector that gives rise to a Hubble velocity $\boldsymbol{u}$. However, we continue referring to v as a velocity.

Let us consider the mean pairwise (relative) velocity

$$\langle\boldsymbol{w}_{12}|\boldsymbol{r}_{12}\rangle_{\mathrm{p}} = \int \boldsymbol{w}_{12}\,\mathcal{P}^{(2)}_{\boldsymbol{w}_{12}}(\boldsymbol{w}_{12}|\boldsymbol{r}_{12})\,\mathrm{d}\boldsymbol{w}_{12}\,, \tag{3.49}$$

where the subscript p indicates a pair-weighted average, i.e. an average taken over all particle pairs with separation $\boldsymbol{r}_{12}$, and $\mathcal{P}^{(2)}_{\boldsymbol{w}_{12}}$ generalises equation (3.39) to the full vector $\boldsymbol{w}_{12}$. In the single-stream regime, since the number of particles at one location is proportional to $1+\delta$ (see section 3.1.6), we can write

$$\langle\boldsymbol{w}_{12}|\boldsymbol{r}_{12}\rangle_{\mathrm{p}} = \frac{\langle(1+\delta_1)(1+\delta_2)(\boldsymbol{v}_2-\boldsymbol{v}_1)\rangle}{\langle(1+\delta_1)(1+\delta_2)\rangle}\;, \tag{3.50}$$

where δ_i and $\boldsymbol{v}_i$ are short for $\delta(\boldsymbol{x}_i)$ and $\mathsf{v}(\boldsymbol{x}_i)$. At LO in the perturbations, $\langle\boldsymbol{w}_{12}|\boldsymbol{r}_{12}\rangle_{\mathrm{p}} \simeq \langle\delta_1\boldsymbol{v}_2\rangle - \langle\delta_2\boldsymbol{v}_1\rangle$ and, making use of equation (3.48), it is straightforward to show that

$$\langle\delta_1\boldsymbol{v}_2\rangle = -\frac{f}{2\pi^2}\,\hat{\boldsymbol{r}}_{12}\int_0^\infty k\,j_1(k\,r_{12})\,P(k)\,\mathrm{d}k\,, \tag{3.51}$$

where $j_1(x) = \sin(x)/x^2 - \cos(x)/x$, and $P(k)$ denotes the linear matter power spectrum. Putting everything together, one obtains (Fisher, 1995)

$$\langle\boldsymbol{w}_{12}|\boldsymbol{r}_{12}\rangle_{\mathrm{p}} \simeq -\frac{f}{\pi^2}\,\hat{\boldsymbol{r}}_{12}\int_0^\infty k\,j_1(k\,r_{12})\,P(k)\,\mathrm{d}k = \bar{w}(r_{12})\,\hat{\boldsymbol{r}}_{12}\,, \tag{3.52}$$

where the symbol $\simeq$ indicates that the expression has been truncated to LO. Note that, because of gravity, the particles in a pair approach each other on average, i.e. $\bar{w}(r_{12}) < 0$.

We now want to generalise this calculation to particle triplets with separations $\triangle_{123} = (\boldsymbol{r}_{12}, \boldsymbol{r}_{23}, \boldsymbol{r}_{31})$. In this case, there are three mean relative velocities to consider: $\langle\boldsymbol{w}_{12}|\triangle_{123}\rangle_{\mathrm{t}}$, $\langle\boldsymbol{w}_{23}|\triangle_{123}\rangle_{\mathrm{t}}$, and $\langle\boldsymbol{w}_{31}|\triangle_{123}\rangle_{\mathrm{t}}$ (the subscript t, here, denotes that averages are taken over all particle triplets with

separations $\triangle_{123}$). For instance, to LO in the perturbations,

$$\begin{aligned}\langle \boldsymbol{w}_{12}|\triangle_{123}\rangle_{\rm t} = & \quad \frac{\langle(1+\delta_1)(1+\delta_2)(1+\delta_3)(\boldsymbol{v}_2-\boldsymbol{v}_1)\rangle}{\langle(1+\delta_1)(1+\delta_2)(1+\delta_3)\rangle} \\ \simeq & \quad \langle\delta_1\boldsymbol{v}_2\rangle - \langle\delta_2\boldsymbol{v}_1\rangle + \langle\delta_3\boldsymbol{v}_2\rangle - \langle\delta_3\boldsymbol{v}_1\rangle \\ = & \quad \bar{w}(r_{12})\,\hat{\boldsymbol{r}}_{12} - \tfrac{1}{2}\left[\bar{w}(r_{23})\,\hat{\boldsymbol{r}}_{23} + \bar{w}(r_{31})\,\hat{\boldsymbol{r}}_{31}\right] . \end{aligned} \tag{3.53}$$

Note that the mean relative velocity between a particle pair in a triplet is not purely radial but has also a transverse component in the plane of the triangle defined by the particles. This is generated by the gravitational influence of the third particle on the pair. In order to separate the radial and transverse components, let us first denote by $\chi = \arccos(\hat{\boldsymbol{r}}_{12}\cdot\hat{\boldsymbol{r}}_{23})$ the (shortest) rotation angle from $\hat{\boldsymbol{r}}_{12}$ to $\hat{\boldsymbol{r}}_{23}$ around the normal vector $\boldsymbol{n} = \hat{\boldsymbol{r}}_{12}\times\hat{\boldsymbol{r}}_{23} = \hat{\boldsymbol{n}}\,\sin\chi$ (with $0\le\chi<\pi$ and $\sin\chi\ge 0$). We then build a right-handed Cartesian coordinate system with unit axes $\{\hat{\boldsymbol{r}}_{12},\hat{\boldsymbol{t}},\hat{\boldsymbol{n}}\}$ such that $\hat{\boldsymbol{t}} = \hat{\boldsymbol{n}}\times\hat{\boldsymbol{r}}_{12} = (\hat{\boldsymbol{r}}_{23} - \cos\chi\,\hat{\boldsymbol{r}}_{12})/\sin\chi$ (see also appendix A in Yankelevich and Porciani, 2019). By construction, $\hat{\boldsymbol{t}}$ lies in the plane of $\triangle_{123}$, is orthogonal to $\hat{\boldsymbol{r}}_{12}$, and always points towards the half-plane that contains point 3 with respect to the $\hat{\boldsymbol{r}}_{12}$ direction. Since $\boldsymbol{r}_{12}+\boldsymbol{r}_{23}+\boldsymbol{r}_{31}=0$, it follows that $\boldsymbol{r}_{31}\cdot\hat{\boldsymbol{r}}_{12} = -(r_{12}+r_{23}\,\cos\chi)$ and $\boldsymbol{r}_{31}\cdot\hat{\boldsymbol{t}} = -r_{23}\,\sin\chi$. We can thus decompose the mean relative velocity between a particle pair in a triplet into its radial and transverse components (by symmetry, there cannot be any component along $\hat{\boldsymbol{n}}$ as motions in the two vertical directions are equally likely)

$$\begin{aligned}\langle \boldsymbol{w}_{12}|\triangle_{123}\rangle_{\rm t} &= \langle \boldsymbol{w}_{12}\cdot\hat{\boldsymbol{r}}_{12}|\triangle_{123}\rangle_{\rm t}\,\hat{\boldsymbol{r}}_{12} + \langle \boldsymbol{w}_{12}\cdot\hat{\boldsymbol{t}}|\triangle_{123}\rangle_{\rm t}\,\hat{\boldsymbol{t}} \\ &= R_{12}(\triangle_{123})\,\hat{\boldsymbol{r}}_{12} + T_{12}(\triangle_{123})\,\hat{\boldsymbol{t}}\,, \end{aligned} \tag{3.54}$$

obtaining

$$R_{12}(\triangle_{123}) = \bar{w}(r_{12}) - \frac{1}{2}\left[\bar{w}(r_{23})\,\cos\chi - \bar{w}(r_{31})\,\frac{r_{12}+r_{23}\cos\chi}{\sqrt{r_{12}^2+r_{23}^2+2r_{12}r_{23}\cos\chi}}\right] , \tag{3.55}$$

$$T_{12}(\triangle_{123}) = -\frac{1}{2}\left[\bar{w}(r_{23}) - \bar{w}(r_{31})\,\frac{r_{23}}{\sqrt{r_{12}^2+r_{23}^2+2r_{12}r_{23}\cos\chi}}\right]\sin\chi\,, \tag{3.56}$$

where we have parameterized the shape of $\triangle_{123}$ in terms of r_{12}, r_{23} and χ (since $r_{31}^2 = r_{12}^2+r_{23}^2+2r_{12}r_{23}\cos\chi$ and $\sin\chi = \sqrt{1-\cos^2\chi}$ it is straightforward to use the three side lengths instead). Equations (3.55) and (3.56) describe how the presence of the third particle influences the mean radial velocity in a pair and gives rise to a transverse component. Depending on the exact geometrical configuration, $R_{12}(\triangle_{123})$ can be larger or smaller than $\bar{w}(r_{12})$ and $T_{12}(\triangle_{123})$ positive or negative. If $\boldsymbol{r}_{12}$ is the base of an isosceles triangle, for instance, then $R_{12} = \bar{w}(r_{12}) + \bar{w}(r_{23})(r_{12}/r_{31})/2$ and $T_{12}=0$. This reflects the fact that the 'gravitational pulls' due to the third particle add up to generate a larger relative velocity in the radial direction but exactly cancel out in the transverse one. For equilateral triangles, this reduces to $R_{12} = 3\bar{w}(r_{12})/2$ and $T_{12}=0$. Considering a degenerate triangle with $\chi = 0$ gives $R_{12} = \bar{w}(r_{12}) - [\bar{w}(r_{23}) - \bar{w}(r_{31})]/2$ and $T_{12}=0$. A note is in order here. Triangles with the same shape can have opposite orientations (intended as winding orders, i.e. signed areas of opposite signs) and both $\hat{\boldsymbol{t}}$ and $\hat{\boldsymbol{n}}$ flip sign if the winding order of $\triangle_{123}$ is switched

(e.g. by reflecting the triangle with respect to $\boldsymbol{r}_{12}$). It follows that, if one disregards orientation and takes the average among all triangles with given side lenghts, then the transverse part of the mean relative velocity between a particle pair in a triplet is a null vector as triangles with opposite winding orders give identical contributions in opposite directions. As stated in equation (3.54), with the term 'transverse component' we always refer to the projection along $\hat{\boldsymbol{t}}$ which does not vanish even when the average is taken irrespective of orientation.

The steps above can be repeated to decompose $\langle \boldsymbol{w}_{23}|\triangle_{123}\rangle_{\rm t}$ in its radial and transverse parts. In this case, we use a right-handed coordinate system with unit axes $\{\hat{\boldsymbol{r}}_{23}, \hat{\boldsymbol{t}}', \hat{\boldsymbol{n}}\}$ where $\hat{\boldsymbol{t}}' = \hat{\boldsymbol{n}} \times \hat{\boldsymbol{r}}_{23} = (-\hat{\boldsymbol{r}}_{12} + \cos\chi\, \hat{\boldsymbol{r}}_{23})/\sin\chi)$ and write $\langle \boldsymbol{w}_{23}|\triangle_{123}\rangle_{\rm t} = R_{23}(\triangle_{123})\, \hat{\boldsymbol{r}}_{23} + T_{23}(\triangle_{123})\, \hat{\boldsymbol{t}}'$. The resulting radial and transverse components are, respectively,

$$R_{23}(\triangle_{123}) = \bar{w}(r_{23}) - \frac{1}{2}\left[\bar{w}(r_{12})\,\cos\chi - \bar{w}(r_{31})\,\frac{r_{23} + r_{12}\cos\chi}{\sqrt{r_{12}^2 + r_{23}^2 + 2r_{12}r_{23}\cos\chi}}\right] , \tag{3.57}$$

$$T_{23}(\triangle_{123}) = \frac{1}{2}\left[\bar{w}(r_{12}) - \bar{w}(r_{31})\,\frac{r_{12}}{\sqrt{r_{12}^2 + r_{23}^2 + 2r_{12}r_{23}\cos\chi}}\right] \sin\chi\, . \tag{3.58}$$

In figures 3.3 and 3.4, we compare the perturbative results at LO for R_{12}, R_{23}, T_{12} and T_{23} against measurements from the simulation introduced in section 3.2.1. We consider triangular configurations $\triangle_{123}$ with different shapes and sizes (but we always average over winding order). In the top set of panels, we look at triangles with relatively large values of r_{12} and r_{23}. Here, $r_{12} \in [80, 85)\, h^{-1}{\rm Mpc}$ and each sub panel corresponds to a different narrow range for r_{23} as indicated by the labels. Results are plotted as a function of r_{31} (i.e. by varying χ). It is remarkable to see that the theoretical predictions match very well the measurements from the simulation for these large triangles. In the bottom set of panels, we consider smaller triangles with $r_{12} \in [20, 25)\, h^{-1}{\rm Mpc}$ and also smaller values for r_{23}. Also in this case, the LO predictions are quite accurate although to a lesser degree than in the top panel. We conclude that the perturbative calculations are a reliable tool to compute the mean relative velocity for triangular configurations with scales $r \gtrsim 20\, h^{-1}{\rm Mpc}$).

Dispersion of relative velocities between particle pairs in a triplet

The second moment of the pairwise velocity

$$\langle \boldsymbol{w}_{12}\, \boldsymbol{w}_{12}|\boldsymbol{r}_{12}\rangle_{\rm p} = \frac{\langle (1+\delta_1)(1+\delta_2)(\boldsymbol{v}_2 - \boldsymbol{v}_1)(\boldsymbol{v}_2 - \boldsymbol{v}_1)\rangle}{\langle (1+\delta_1)(1+\delta_2)\rangle} \tag{3.59}$$

is a dyadic tensor which, to LO in the perturbations, reduces to

$$\langle \boldsymbol{w}_{12}\, \boldsymbol{w}_{12}|\boldsymbol{r}_{12}\rangle_{\rm p} \simeq \langle \boldsymbol{v}_2\boldsymbol{v}_2\rangle - \langle \boldsymbol{v}_2\boldsymbol{v}_1\rangle - \langle \boldsymbol{v}_1\boldsymbol{v}_2\rangle + \langle \boldsymbol{v}_1\boldsymbol{v}_1\rangle\, . \tag{3.60}$$

Two-point correlations between linear velocity fields are conveniently written as (Gorski, 1988)

$$\langle v_{1i}\, v_{2j}\rangle \simeq \psi_p(r_{12})\, \delta_{ij} + [\psi_r(r_{12}) - \psi_p(r_{12})]\, \hat{r}_{12i}\, \hat{r}_{12j}\, , \tag{3.61}$$

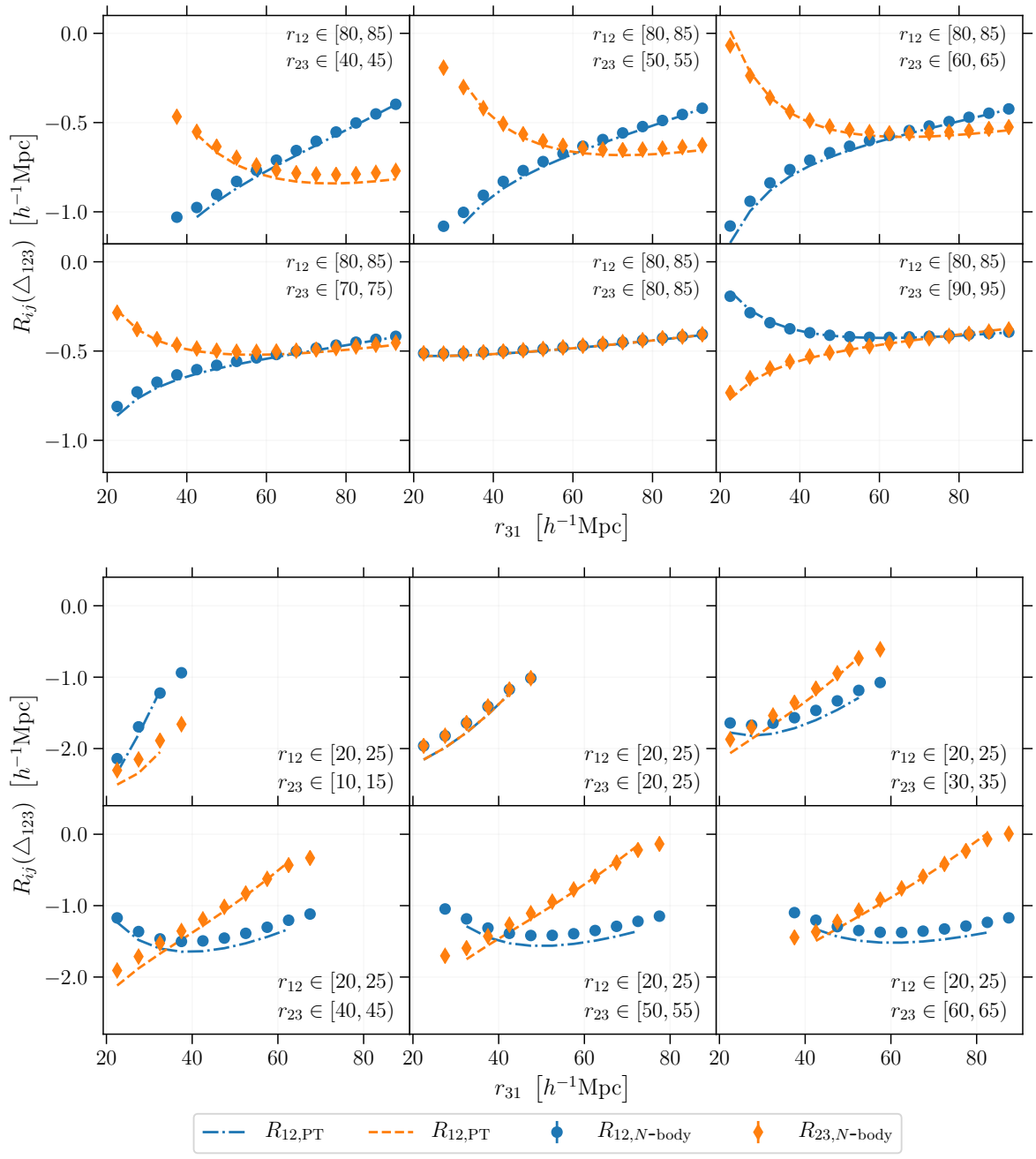

Figure 3.3: The radial component of the mean relative velocity between particle pairs in a triplet for different triangular configurations. Symbols with error bars denote measurements from our N-body simulation while the smooth curves show the predictions from the perturbative calculations at LO derived in section 3.2.3. The labels give the particle separations r_{12} and r_{23} in units of $h^{-1}\mathrm{Mpc}$.

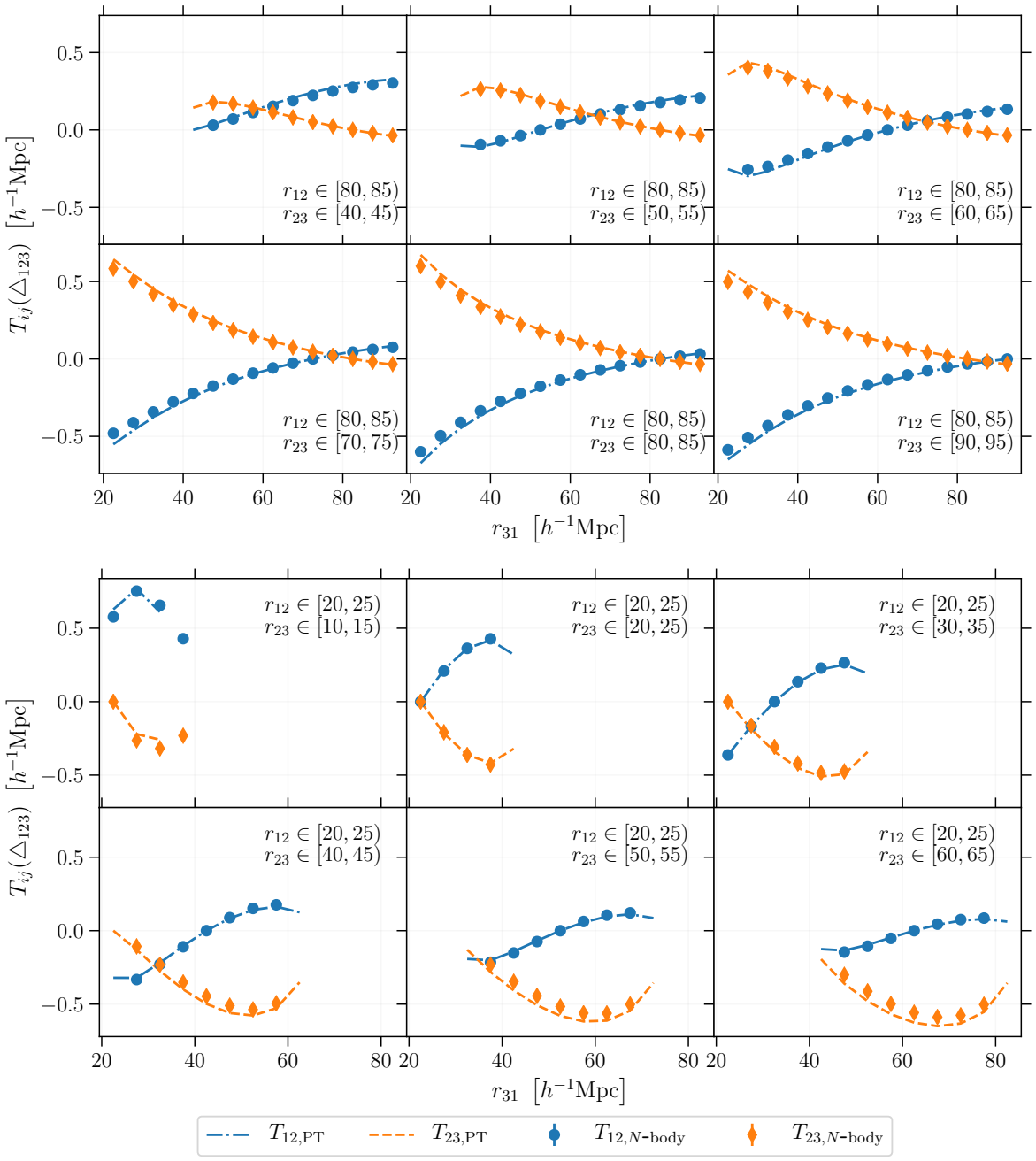

Figure 3.4: As in figure 3.3 but for the transverse component.

where the indices i and j denote the Cartesian components of the velocities (i.e. they run from 1 to 3), δ_{ij} is the Kronecker symbol, and ψ_r and ψ_p are the radial and transverse correlation functions defined as

$$\psi_r(r_{12}) = \frac{f^2}{2\pi^2}\int_0^\infty \left[j_0(k\,r_{12}) - 2\,\frac{j_1(k\,r_{12})}{k\,r_{12}}\right] P(k)\,\mathrm{d}k\ , \tag{3.62}$$

$$\psi_p(r_{12}) = \frac{f^2}{2\pi^2}\int_0^\infty \frac{j_1(k\,r_{12})}{k\,r_{12}}\,P(k)\,\mathrm{d}k\ , \tag{3.63}$$

with $j_0(x) = \sin(x)/x$. Note that, when $r_{12} \to 0$, $\psi_p \to \sigma_v^2$ and $\psi_r \to \sigma_v^2$ where

$$\sigma_v^2 = \frac{f^2}{6\pi^2}\int_0^\infty P(k)\,\mathrm{d}k \tag{3.64}$$

is the one-dimensional linear velocity dispersion, i.e. $\sigma_v^2 = \langle v_i^2\rangle$. Therefore, the velocity dispersion tensor at zero lag is isotropic

$$\langle v_{1i}\,v_{1j}\rangle = \langle v_{2i}\,v_{2j}\rangle = \sigma_v^2\,\delta_{ij}\ . \tag{3.65}$$

It follows that

$$\langle w_{12i}\,w_{12j}|\boldsymbol{r}_{12}\rangle_\mathrm{p} \simeq 2\left[\sigma_v^2 - \psi_p(r_{12})\right]\,\delta_{ij} - 2\left[\psi_r(r_{12}) - \psi_p(r_{12})\right]\,\hat{r}_{12i}\,\hat{r}_{12j}\ . \tag{3.66}$$

In other words, the second moments of the radial component is

$$\langle(\boldsymbol{w}_{12}\cdot\hat{\boldsymbol{r}}_{12})^2|\boldsymbol{r}_{12}\rangle_\mathrm{p} = 2\left[\sigma_v^2 - \psi_r(r_{12})\right]\ , \tag{3.67}$$

while for each of the perpendicular components (e.g. those along the unit vectors $\hat{\boldsymbol{n}}$ and $\hat{\boldsymbol{t}}$ introduced in section 3.2.3) we have

$$\frac{1}{2}\langle[\boldsymbol{w}_{12} - (\boldsymbol{w}_{12}\cdot\hat{\boldsymbol{r}}_{12})\hat{\boldsymbol{r}}_{12}]^2|\boldsymbol{r}_{12}\rangle_\mathrm{p} = 2\left[\sigma_v^2 - \psi_p(r_{12})\right]\ . \tag{3.68}$$

Moreover, the different Cartesian components are uncorrelated.

The calculations above can be easily extended to particle pairs in a triplet. In this case, we are interested in two types of combinations, e.g.

$$\langle\boldsymbol{w}_{12}\,\boldsymbol{w}_{12}|\triangle_{123}\rangle_\mathrm{t} = \frac{\langle(1+\delta_1)(1+\delta_2)(1+\delta_3)(\boldsymbol{v}_2-\boldsymbol{v}_1)(\boldsymbol{v}_2-\boldsymbol{v}_1)\rangle}{\langle(1+\delta_1)(1+\delta_2)(1+\delta_3)\rangle}\ , \tag{3.69}$$

and

$$\langle\boldsymbol{w}_{12}\,\boldsymbol{w}_{23}|\triangle_{123}\rangle_\mathrm{t} = \frac{\langle(1+\delta_1)(1+\delta_2)(1+\delta_3)(\boldsymbol{v}_2-\boldsymbol{v}_1)(\boldsymbol{v}_3-\boldsymbol{v}_2)\rangle}{\langle(1+\delta_1)(1+\delta_2)(1+\delta_3)\rangle}\ . \tag{3.70}$$

To LO in the perturbations, they reduce to

$$\langle\boldsymbol{w}_{12}\,\boldsymbol{w}_{12}|\triangle_{123}\rangle_\mathrm{t} \simeq \langle\boldsymbol{v}_2\boldsymbol{v}_2\rangle - \langle\boldsymbol{v}_2\boldsymbol{v}_1\rangle - \langle\boldsymbol{v}_1\boldsymbol{v}_2\rangle + \langle\boldsymbol{v}_1\boldsymbol{v}_1\rangle\ , \tag{3.71}$$

and

$$\langle \boldsymbol{w}_{12}\, \boldsymbol{w}_{23} | \triangle_{123} \rangle_{\mathrm{t}} \simeq \langle \boldsymbol{v}_2 \boldsymbol{v}_3 \rangle - \langle \boldsymbol{v}_2 \boldsymbol{v}_2 \rangle - \langle \boldsymbol{v}_1 \boldsymbol{v}_3 \rangle + \langle \boldsymbol{v}_1 \boldsymbol{v}_2 \rangle \,. \tag{3.72}$$

that have exactly the same structure as equation (3.61). Therefore, we conclude that

$$\langle w_{12i}\, w_{12j} | \triangle_{123} \rangle_{\mathrm{t}} \simeq 2 \left[\sigma_v^2 - \psi_p(r_{12}) \right] \delta_{ij} - 2 \left[\psi_r(r_{12}) - \psi_p(r_{12}) \right] \hat{r}_{12i}\, \hat{r}_{12j} \,, \tag{3.73}$$

and

$$\begin{aligned} \langle w_{12i}\, w_{23j} | \triangle_{123} \rangle_{\mathrm{t}} \simeq & \left[\psi_p(r_{12}) + \psi_p(r_{23}) - \psi_p(r_{31}) - \sigma_v^2 \right] \delta_{ij} \\ & + \left[\psi_r(r_{12}) - \psi_p(r_{12}) \right] \hat{r}_{12i}\, \hat{r}_{12j} \\ & + \left[\psi_r(r_{23}) - \psi_p(r_{23}) \right] \hat{r}_{23i}\, \hat{r}_{23j} \\ & - \left[\psi_r(r_{31}) - \psi_p(r_{31}) \right] \hat{r}_{31i}\, \hat{r}_{31j} \,. \end{aligned} \tag{3.74}$$

In figure 3.5, we compare some of these perturbative results to measurements performed in our numerical simulation. Shown are the second moments of the radial (top panel) and transverse (bottom panel) components of the relative velocity between particle pairs in a triplet. Symbols with error bars display the N-body measurements while the constant lines indicate the theoretical results to LO, i.e,

$$S_{12}(\triangle_{123}) = \langle (\boldsymbol{w}_{12} \cdot \hat{\boldsymbol{r}}_{12})^2 | \triangle_{123} \rangle_{\mathrm{t}} = 2 \left[\sigma_v^2 - \psi_r(r_{12}) \right] \,, \tag{3.75}$$

$$E_{12}(\triangle_{123}) = \langle (\boldsymbol{w}_{12} \cdot \hat{\boldsymbol{t}})^2 | \triangle_{123} \rangle_{\mathrm{t}} = 2 \left[\sigma_v^2 - \psi_p(r_{12}) \right] \,, \tag{3.76}$$

and the corresponding results for $\boldsymbol{w}_{23}$. The first thing worth mentioning is that the second moments are generally much larger than the mean values shown in figures. 3.3 and 3.4. The model, however, does not account for all the dispersion around the mean. In fact, as previously noted in the literature (B. A. Reid and M. White, 2011; L. Wang, B. Reid and M. White, 2014; Uhlemann, Kopp and Haugg, 2015), the prediction for σ_v^2 given in equation (3.64) is not very accurate. Being a zero-lag correlation, σ_v^2 is influenced by small-scale, non-perturbative physics. Adding a constant offset to equations (3.75) and (3.76) is a common fix that has been found to reproduce simulations well. We follow this approach and add a constant C to σ_v^2 so that to match the measurements for the largest triangles we consider (i.e. the rightmost points in the bottom-right sub panels). This way, we find consistent offset values ($C \simeq 4.8\, h^{-2}\mathrm{Mpc}^2$ within 1%) for the dispersions in the radial and transverse components as well as in the pairwise velocity. Keeping this shift fixed, we find that the theoretical predictions are able to reproduce the measurements from the simulation quite well for the largest triangles. However, the level of agreement drops off rapidly when lower separation scales are considered.

Projection along the line of sight

The los component of the relative velocities between particle pairs in a triplet depends on the relative orientation of $\triangle_{123}$ with respect to the los (see Appendix A in Yankelevich and Porciani, 2019 for a detailed discussion). We set up a spherical coordinate system with $\hat{\boldsymbol{r}}_{12}$ as the polar axis and use $\theta = \arccos(\hat{\boldsymbol{r}}_{12} \cdot \hat{\boldsymbol{s}})$ as the polar angle ($0 \leq \theta < \pi$). We also define the azimuthal angle ϕ ($0 \leq \phi < 2\pi$) as the angle between $\hat{\boldsymbol{n}}$ and the projection of $\hat{\boldsymbol{s}}$ on to the plane perpendicular to $\hat{\boldsymbol{r}}_{12}$

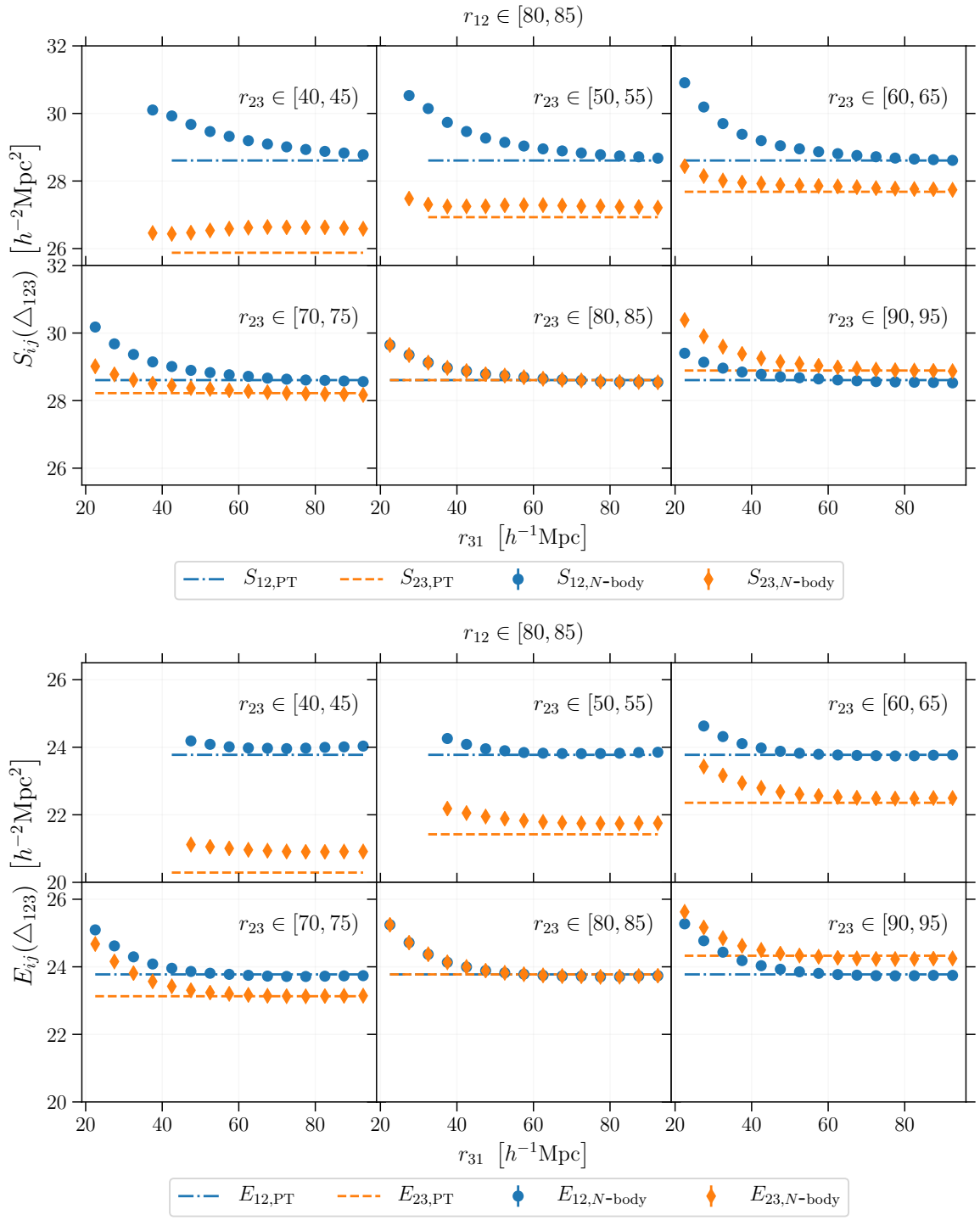

Figure 3.5: As in the top panel of figure 3.3 but for the second moment of the radial (top) and transverse (bottom) components of the relative velocity between particle pairs in a triplet. Note that a constant offset has been added to the theoretical predctions as described at the end of section 3.2.3.

so that $\cos\phi = 0$ whenever $\hat{\boldsymbol{s}}$ lies in the plane of the triangle. It follows that $\hat{\boldsymbol{t}} \cdot \hat{\boldsymbol{s}} = \sin\theta \sin\phi$, $\hat{\boldsymbol{n}} \cdot \hat{\boldsymbol{s}} = \sin\theta \cos\phi$, and $\hat{\boldsymbol{t}}' \cdot \hat{\boldsymbol{s}} = -\cos\theta \sin\chi + \sin\theta \sin\phi \cos\chi$. For the scalar products between the different pairwise separation vectors and the los direction, one thus finds (Scoccimarro, Couchman and Frieman, 1999; Yankelevich and Porciani, 2019),

$$\mu_{12} = \hat{\boldsymbol{r}}_{12} \cdot \hat{\boldsymbol{s}} = \frac{r_{12\parallel}}{r_{12}} = \cos\theta \;, \tag{3.77}$$

$$\mu_{23} = \hat{\boldsymbol{r}}_{23} \cdot \hat{\boldsymbol{s}} = \frac{r_{23\parallel}}{r_{23}} = \cos\theta \cos\chi + \sin\theta \sin\phi \sin\chi \;, \tag{3.78}$$

$$\mu_{31} = \hat{\boldsymbol{r}}_{31} \cdot \hat{\boldsymbol{s}} = \frac{-(r_{12\parallel} + r_{23\parallel})}{r_{31}} = -\frac{r_{12}}{r_{31}}\mu_{12} - \frac{r_{23}}{r_{31}}\mu_{23} \;. \tag{3.79}$$

Note that by flipping the winding order of $\triangle_{123}$ for a fixed los direction, $\cos\theta$ stays the same while both $\sin\phi$ and $\cos\phi$ change sign (i.e. $\phi \to \pi + \phi \mod 2\pi$) as $\hat{\boldsymbol{t}}$ and $\hat{\boldsymbol{n}}$ flip.

Combining equations (3.77), (3.78) and (3.79) with the results obtained in section 3.2.3, we can eventually write the first and second moments for the projections of the relative velocities along the los, $w_{12\parallel}$ and $w_{23\parallel}$. In particular, equation (3.53) gives

$$\langle w_{12\parallel} | \triangle_{123} \rangle_{\mathrm{t}} \simeq \bar{w}(r_{12})\, \mu_{12} - \frac{1}{2}\left[\bar{w}(r_{23})\, \mu_{23} + \bar{w}(r_{31})\, \mu_{31}\right] \;. \tag{3.80}$$

The very same expression can be derived from equation (3.54) and written as

$$\langle w_{12\parallel} | \triangle_{123} \rangle_{\mathrm{t}} \simeq R_{12}(\triangle_{123})\, \cos\theta + T_{12}(\triangle_{123})\, \sin\theta \sin\phi \;. \tag{3.81}$$

Similarly, we have

$$\langle w_{23\parallel} | \triangle_{123} \rangle_{\mathrm{t}} \simeq \bar{w}(r_{23})\, \mu_{23} - \frac{1}{2}\left[\bar{w}(r_{12})\, \mu_{12} + \bar{w}(r_{31})\, \mu_{31}\right] \;, \tag{3.82}$$

and

$$\langle w_{23\parallel} | \triangle_{123} \rangle_{\mathrm{t}} \simeq R_{23}(\triangle_{123})\, \mu_{23} + T_{23}(\triangle_{123})\, (-\cos\theta \sin\chi + \sin\theta \sin\phi \cos\chi) \;. \tag{3.83}$$

Moreover, from equation (3.73) we derive

$$\begin{aligned} \langle w_{12\parallel}^2 | \triangle_{123} \rangle_{\mathrm{t}} &\simeq 2\left[\sigma_v^2 - \psi_p(r_{12})\right] - 2\left[\psi_r(r_{12}) - \psi_p(r_{12})\right]\, \mu_{12}^2 \\ &= 2\left[\sigma_v^2 - \psi_\parallel(r_{12})\right] \;, \end{aligned} \tag{3.84}$$

with $\psi_\parallel(r_{12}) = \mu_{12}^2\, \psi_r(r_{12}) + (1 - \mu_{12}^2)\, \psi_p(r_{12})$. The corresponding expression for $\langle w_{23\parallel}^2 | \triangle_{123} \rangle_{\mathrm{t}}$ is

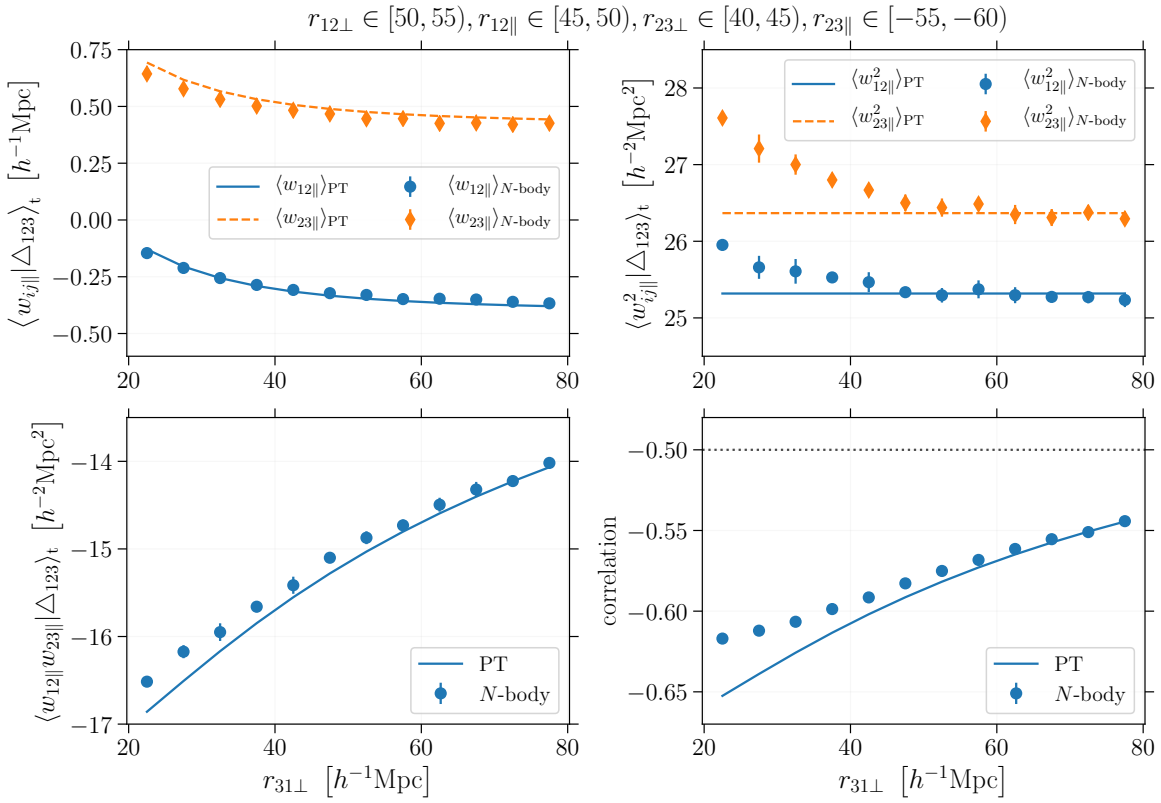

Figure 3.6: Moments of the relative los velocities between particle pairs in a triplet, $w_{12\parallel}$ and $w_{23\parallel}$. The mean values (top left), the second moments (top right), the second cross moment (bottom left), and the linear correlation coefficient (bottom right) are plotted for different triangular configurations $\triangle_{123}$. Symbols with error bars denote measurements from our N-body simulation while the smooth curves show the predictions from the perturbative calculations at LO derived in section 3.2.3. The labels give the particle separations in units of $h^{-1}\mathrm{Mpc}$.

obtained by replacing r_{12} with r_{23} in equation (3.84). Finally, equation (3.74) implies

$$\begin{aligned}\langle w_{12\parallel}\, w_{23\parallel} | \triangle_{123} \rangle_t \simeq & \Big[\psi_p(r_{12}) + \psi_p(r_{23}) - \psi_p(r_{31}) - \sigma_v^2\Big] \\ & + \big[\psi_r(r_{12}) - \psi_p(r_{12})\big]\ \mu_{12}^2 \\ & + \big[\psi_r(r_{23}) - \psi_p(r_{23})\big]\ \mu_{23}^2 \\ & - \big[\psi_r(r_{31}) - \psi_p(r_{31})\big]\ \mu_{31}^2 \\ = & \ \psi_\parallel(r_{12}) + \psi_\parallel(r_{23}) - \psi_\parallel(r_{31}) - \sigma_v^2 \ . \end{aligned} \tag{3.85}$$

We compare these results with measurements from the simulation in figure 3.6. In this case, we bin

our data based on the variables:

$$
\begin{aligned}
r_{12\parallel} &= r_{12}\,\cos\theta\ , \\
r_{12\perp} &= r_{12}\,|\sin\theta|\ , \\
r_{23\parallel} &= r_{23}\,(\cos\theta\cos\chi+\sin\theta\sin\phi\sin\chi)\ , \\
r_{23\perp} &= r_{23}\,[1-(\cos\theta\cos\chi+\sin\theta\sin\phi\sin\chi)^2]^{1/2}\ , \\
r_{31\perp} &= \left\{r_{12}^2+r_{23}^2+2r_{12}r_{23}\cos\chi-[r_{12}\cos\theta+r_{23}\,(\cos\theta\cos\chi+\sin\theta\sin\phi\sin\chi)]^2\right\}^{1/2}\ ,
\end{aligned}
\tag{3.86}
$$

(note that triangles with the same shape but opposite winding orders correspond to different sets of these variables). Results are plotted as a function of $r_{31\perp}$ by keeping the remaining four variables that define a triangular configuration fixed. The top-left panel shows $\langle w_{12\parallel}|\triangle_{123}\rangle_{\rm t}$ and $\langle w_{23\parallel}|\triangle_{123}\rangle_{\rm t}$. Here, the theoretical predictions are in very good agreement with the numerical data confirming the results presented in figures 3.3 and 3.4. The top-right panel displays $\langle w_{12\parallel}^2|\triangle_{123}\rangle_{\rm t}$ and $\langle w_{23\parallel}^2|\triangle_{123}\rangle_{\rm t}$ while the bottom-left panel shows $\langle w_{12\parallel}\,w_{23\parallel}|\triangle_{123}\rangle_{\rm t}$. Once adjusted for the offset discussed in section 3.2.3, the predictions for the second moments are excellent for $r_{31\perp}\gtrsim 50\,h^{-1}\,{\rm Mpc}$ but tend to slightly underestimate the N-body results by a few percent at smaller separations. Likewise, the model for the cross second moment always agrees to better than 3% with the simulation and gives better predictions when $r_{31\perp}$ is large. Note that the linear correlation coefficient between $w_{12\parallel}$ and $w_{23\parallel}$ (bottom-right panel) is always close to $-1/2$ as expected from drawing independent los velocities from $\mathcal{P}^{(1)}_{v_\parallel}$ at every vertex of $\triangle_{123}$ (see also figure 3.1 and the detailed discussion in section 3.3.4).

3.3 The 3-point Gaussian streaming model

3.3.1 Definitions

The streaming model for the 3PCF given in equation (3.18) is exact within the distant-observer approximation. However, it requires knowledge of the function $\mathcal{P}^{(3)}_{\boldsymbol{w}_\parallel}(w_{12\parallel},w_{23\parallel}|\triangle_{123})$ which is challenging to derive from first principles. In analogy to the literature on the 2-point correlation function, we propose the use of a scale-dependent bivariate Gaussian distribution to model $\mathcal{P}^{(3)}_{\boldsymbol{w}_\parallel}(w_{12\parallel},w_{23\parallel}|\triangle_{123})$. This choice is motivated by a number of considerations: i) For large inter-particle separations, the function $\mathcal{P}^{(3)}_{\boldsymbol{w}_\parallel}(w_{12\parallel},w_{23\parallel}|\triangle_{123})$ extracted from our simulation appears to be approximately Gaussian close to its peak (e.g. see the bottom right panel in figure 3.1); ii) Simplicity, as the Gaussian is the only probability density function that only requires two cumulants to be fully specified; iii) As shown in section 3.2.3, on large scales, we can accurately model the scale dependence of these cumulants by using perturbation theory at LO.

In the resulting phenomenological model, which we dub the '3-point Gaussian streaming model' (3ptGSM in short), the joint probability density function of $w_{12\parallel}$ and $w_{23\parallel}$ is given by a bivariate Gaussian distribution with mean values $m_1=\langle w_{12\parallel}|\triangle_{123}\rangle_{\rm t}$, $m_2=\langle w_{23\parallel}|\triangle_{123}\rangle_{\rm t}$ and covariance matrix with elements $C_{11}=\langle w_{12\parallel}^2|\triangle_{123}\rangle_{\rm t}-\langle w_{12\parallel}|\triangle_{123}\rangle_{\rm t}^2$, $C_{12}=C_{21}=\langle w_{12\parallel}\,w_{23\parallel}|\triangle_{123}\rangle_{\rm t}-\langle w_{12\parallel}|\triangle_{123}\rangle_{\rm t}\langle w_{23\parallel}|\triangle_{123}\rangle_{\rm t}$, $C_{22}=\langle w_{23\parallel}^2|\triangle_{123}\rangle_{\rm t}-\langle w_{23\parallel}|\triangle_{123}\rangle_{\rm t}^2$.

In what follows, we investigate the simplest possible implementation of the 3ptGSM based on the perturbative predictions at LO given in equations (3.80), (3.82), (3.84), and (3.85). In figure 3.7,

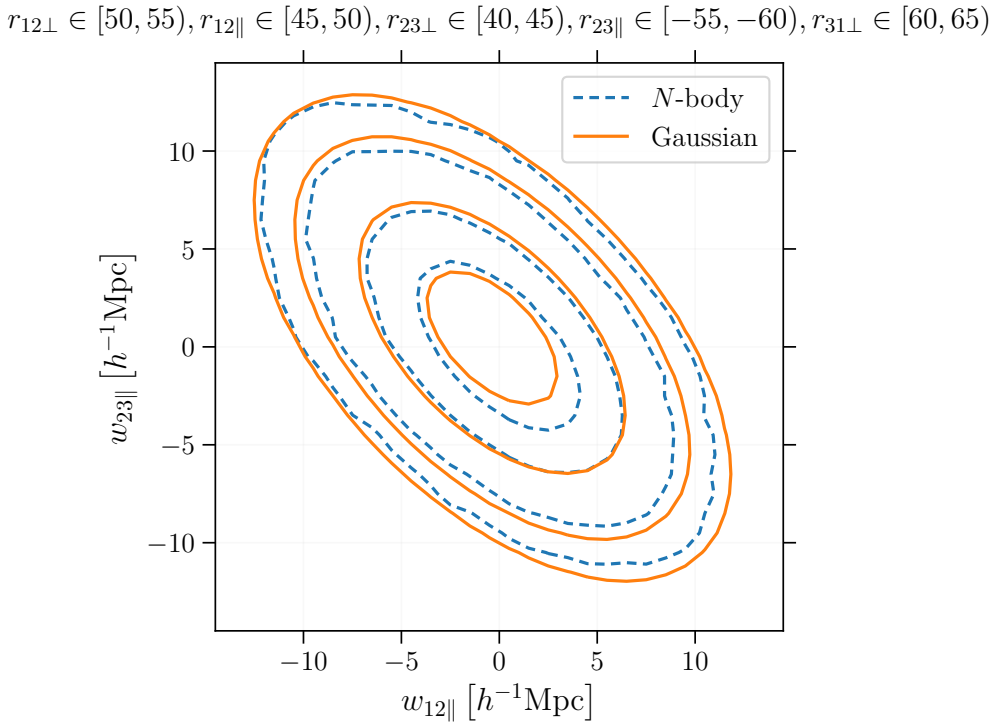

Figure 3.7: Contour levels of the joint PDF $\mathcal{P}^{(3)}_{\boldsymbol{w}_\parallel}(w_{12\parallel}, w_{23\parallel}|\triangle_{123})$ extracted from our N-body simulation (dashed) are compared with those of the Gaussian model (solid) with cumulants predicted from perturbation theory at LO. The triangular configuration we consider is specified in the label on top of the figure in units of $h^{-1}\mathrm{Mpc}$. Contours correspond to the levels $\{6, 3, 1, 0.4\} \times 10^{-3}$ with the values decreasing from inside to outside.

we compare the resulting PDF with that extracted from our simulation for a particular triangular configuration which is specified on top of the figure. To first approximation, the Gaussian model provides a very good description of the PDF. Looking into more details reveals that it slightly underestimates the probability density around the peak. The Kullback-Leibler (KL) and the Jensen-Shannon (JS) divergences[8] are 0.028 and 0.005 nats, respectively, indicating that the information loss associated with using the Gaussian approximation in place of the actual PDF is minimal. Similar values are obtained for different triangular configurations on large scales. However, the approximation clearly fails at smaller separations as is evident visually from figure 3.1. In this case, for the triangular configuration considered in the top-left panel, we find KL and JS divergences of 1.31 nats and 0.39 nats (the upper bound being $\ln(2) \simeq 0.69$ nats), respectively.

[8] The KL divergence is the expectation of the logarithmic difference between the actual distribution $\mathcal{P}$ and the approximating Gaussian $\mathcal{G}$: $D_{\mathrm{KL}}(\mathcal{P} \parallel \mathcal{G}) = \int_{\mathbb{R}^2} \mathcal{P}(\boldsymbol{x}) \ln[\mathcal{P}(\boldsymbol{x})/\mathcal{G}(\boldsymbol{x})]\, \mathrm{d}\boldsymbol{x}$. Since this statistic is not symmetric and is unbounded, it cannot be used to define the distance between two PDFs. However, starting from the KL divergence, a similarity measure between two PDFs which is symmetric was introduced in (Rao, 1987) and generalised in (Lin, 1991). This is known as the JS divergence (JSD) which is given as $\mathrm{JS}(\mathcal{P} \parallel \mathcal{G}) = [D_{\mathrm{KL}}(\mathcal{P} \parallel \mathcal{G}) + D_{\mathrm{KL}}(\mathcal{G} \parallel \mathcal{M})]/2$ where $\mathcal{M} = (\mathcal{P} + \mathcal{G})/2$. The JS divergence is bounded, $0 \leq \mathrm{JS} \leq \ln 2$, which makes the interpretation of its values easier. Additionally, the square root of the JS divergence is a pairwise distance metric.

3.3.2 3-point correlations in the N-body simulation

Our plan is to test the predictions of the 3ptGSM against our N-body simulation. In order to measure $\mathcal{G}_3$, we first generate catalogs of 'random' particles with uniform density within the simulation box and then use the 'natural' estimator DDD/RRR where the symbols DDD and RRR denote the normalised data-data-data and random-random-random triplet counts in a bin of triangular configurations, respectively (Peebles and Groth, 1975; Peebles, 1980). We characterize the shape and orientation of each triplet using the five-dimensional space $(s_{12\perp}, s_{12\parallel}, s_{23\perp}, s_{23\parallel}, s_{31\perp})$ and, for all separations, we use bins that are $5\,h^{-1}$ Mpc wide. To speed the calculation up, we analyse ten subsamples of 100^3 particles each randomly selected from the simulation. For each subsample, we employ five random catalogs containing 1.5×100^3 objects each to measure RRR. Our final estimates for $\mathcal{G}_3$ are obtained by averaging the partial results from the ten subsamples. Error bars are computed by resampling the measurements from the different subsamples with the bootstrap method. Since measuring the 3PCFs is very time consuming and perturbation theory is only expected to be accurate on large-enough scales, we consider a limited number of triangular configurations with fixed $s_{12\perp} \in [50, 55)\,h^{-1}$ Mpc and $s_{23\perp} \in [40, 45)\,h^{-1}$ Mpc. We vary $s_{12\parallel}$, $s_{23\parallel}$ in the range $[15, 65)\,h^{-1}$ Mpc and $s_{31\perp}$ between 25 and $80\,h^{-1}$ Mpc. We present some examples of our results in figure 3.8 and discuss them in detail in section 3.3.3.

We also measure the connected 3PCF using the Szapudi-Szalay estimator that we schematically write as $(D-R)(D-R)(D-R)/RRR$ (Szapudi and Szalay, 1998; Slepian and Eisenstein, 2015). We implement three versions of the estimator for the 3PCF obtained by binning the triplet counts in different ways.

1. To begin with, we consider the same binning scheme in five dimensions we have used to measure $\mathcal{G}_3$. This accounts for all the degrees of freedom in ζ_s but also provides relatively noisy estimates as the triplet counts are partitioned between many bins. We use the same data subsamples, random catalogs and separation ranges that have been described above for the full 3PCF. Results with their bootstrap standard errors are presented in figure 3.8 and discussed in section 3.3.3. We anticipate here that the final uncertainty of the individual estimates is comparable with the signal.

2. In order to measure the connected 3PCF in redshift space with a much higher signal-to-noise ratio, we average ζ_s over the orientation of $\triangle_{123}$ with respect to the line of sight (and the winding order) while keeping the shape of the triangle fixed. The resulting correlation function, $\bar{\zeta}_\mathrm{s}(s_{12}, s_{23}, s_{31})$, only depends on three variables. While the averaging procedure does not lead to any information loss in real space (as ζ is isotropic and $\bar{\zeta} = \zeta$), it obviously gives a lossy compression in redshift space. We use the Szapudi-Szalay method to measure $\bar{\zeta}_\mathrm{s}$ and ζ in our simulation after binning the triplet counts in terms of the leg lengths of $\triangle_{123}$ (once again we use bins that are $5\,h^{-1}$ Mpc wide). We apply the estimator to five of the subsamples introduced above. We eventually average the resulting 3PCF over the subsamples and compute bootstrap standard errors. These results are shown in figure 3.9 and discussed in section 3.3.3.

3. Finally, as an intermediate step between those discussed above, we combine narrow ($5\,h^{-1}$ Mpc wide) bins in s_{12}, s_{23}, and s_{31} with a few broad (0.5 wide) bins in μ_{12} and μ_{23}. This is similar to the 'clustering wedges' that have been used to characterize the 2PCF in redshift space (Kazin, Sánchez and Blanton, 2012; Sánchez et al., 2013). Note that changing sign to both μ_{12} and μ_{23} at

the same time does not affect the 3PCF as it is equivalent to reversing the sign of all the separation vectors that form the triangle $\triangle_{123}$ (see also section 3.2.2 in Yankelevich and Porciani, 2019). After summing up the triplet counts from pairs of corresponding bins under the transformation $(\mu_{12}, \mu_{23}) \to (-\mu_{12}, -\mu_{23})$, we end up considering eight wedges for each triangular shape. We denote the resulting correlation function with the symbol $\zeta_{\rm s}^{(ij)}(s_{12}, s_{23}, s_{31})$ where the index $i \in \{1, 2\}$ refers to the bins in $\mu_{12} \geq 0$ and the index $j \in \{1, 2, 3, 4\}$ maps to the bins in $-1 \leq \mu_{23} \leq 1$. We apply the estimator to five of the data subsamples described above. Examples of our results are shown in figure 3.10 and discussed in section 3.3.3.

3.3.3 Results for the 3-point correlation function

Full correlation function

We now solve equation (3.19) for the 3ptGSM. As input, we first use the real-space $\mathcal{F}_3$ evaluated at LO in perturbation theory. This means that we Fourier transform the linear matter spectrum to get ξ and neglect ζ (case A). In order to estimate the influence of higher-order terms, we repeat the calculation by also considering the LO expression for ζ as in Jing and Börner, 1997 (case B) although this is not fully consistent with the approximation we use for ξ as we do not consider one-loop corrections.[9] Finally, we account for non-linear evolution in the 2PCF by Fourier transforming the matter power spectrum given by the halo model (Mead et al., 2016) and also calculate ζ at LO (case C). As output, we obtain the redshift-space $\mathcal{G}_3$. In the left panels of figure 3.8, we compare the outcome of the 3ptGSM for different triangular configurations against measurements from our numerical simulation. Results are plotted as a function of $s_{31\perp}$ by keeping the remaining four variables that define a triangular configuration fixed. In the top panel, we consider a nearly isosceles triangle with $s_{12} \simeq s_{23} \simeq 71\,h^{-1}$ Mpc, $s_{12\parallel} \simeq 47.5\,h^{-1}$ Mpc (i.e. $\mu_1 \simeq 0.67$) and $s_{23\parallel} \simeq -57.5\,h^{-1}$ Mpc (i.e. $\mu_2 \simeq -0.80$) which corresponds to $s_{31\parallel} \simeq 10\,h^{-1}$ Mpc. By increasing $s_{31\perp}$, we change the shape of the triangle (i.e. increase s_{31} from 29 to $78\,h^{-1}$ Mpc or, equivalently, $\cos\chi$ from -0.92 to -0.4) and simultaneously reduce μ_3 from 0.34 to 0.13. For $s_{31\perp} \simeq 70\,h^{-1}$ Mpc, we obtain an equilateral configuration. On the other hand, in the bottom panel, we consider a scalene triangle with $s_{12} \simeq 55\,h^{-1}$ Mpc ($\mu_1 \simeq 0.32$) and $s_{23\parallel} \simeq 67.5\,h^{-1}$ Mpc ($\mu_2 \simeq -0.78$). In this case, we vary s_{31} from 44.5 to $85\,h^{-1}$ Mpc and μ_3 from 0.62 to 0.4. For $s_{31\perp} \simeq 42$ and $58\,h^{-1}$ Mpc, we obtain isosceles triangles. Overall, the model and the measurements show the same trends: the general agreement is rather good. The three different implementations of the model give very similar results and it is impossible to prefer one over the others based on our measurements.

Connected correlation function

We obtain predictions for the connected 3PCF $\zeta_{\rm s}$ using equation (3.21). We model the PDF of the pairwise velocities, $\mathcal{P}^{(2)}_{w_\parallel}(w_\parallel|\boldsymbol{r})$ with a Gaussian distribution whose moments are derived from equations (3.52) and (3.68) as well as (3.77), (3.78) and (3.79) for the los projections: $\langle w_{ij\parallel}|\boldsymbol{r}_{ij}\rangle_{\rm p} = \bar{w}(r_{ij})\,\mu_{ij}$ and $\langle w^2_{ij\parallel}|\boldsymbol{r}_{ij}\rangle_{\rm p} = 2[\sigma_v^2 - \psi_\parallel(r_{ij})]$. In the right panel of figure 3.8, we compare the results for $\zeta_{\rm s}$ with the data extracted from our simulation. Note that $\zeta_{\rm s}$ is very small on the scales we consider

[9] Since ζ is given by the ensemble average of the product of two mass overdensities evaluated at linear order and one at second order, we make sure that the final expression for ζ is properly symmetrized in the coordinates of the three points.

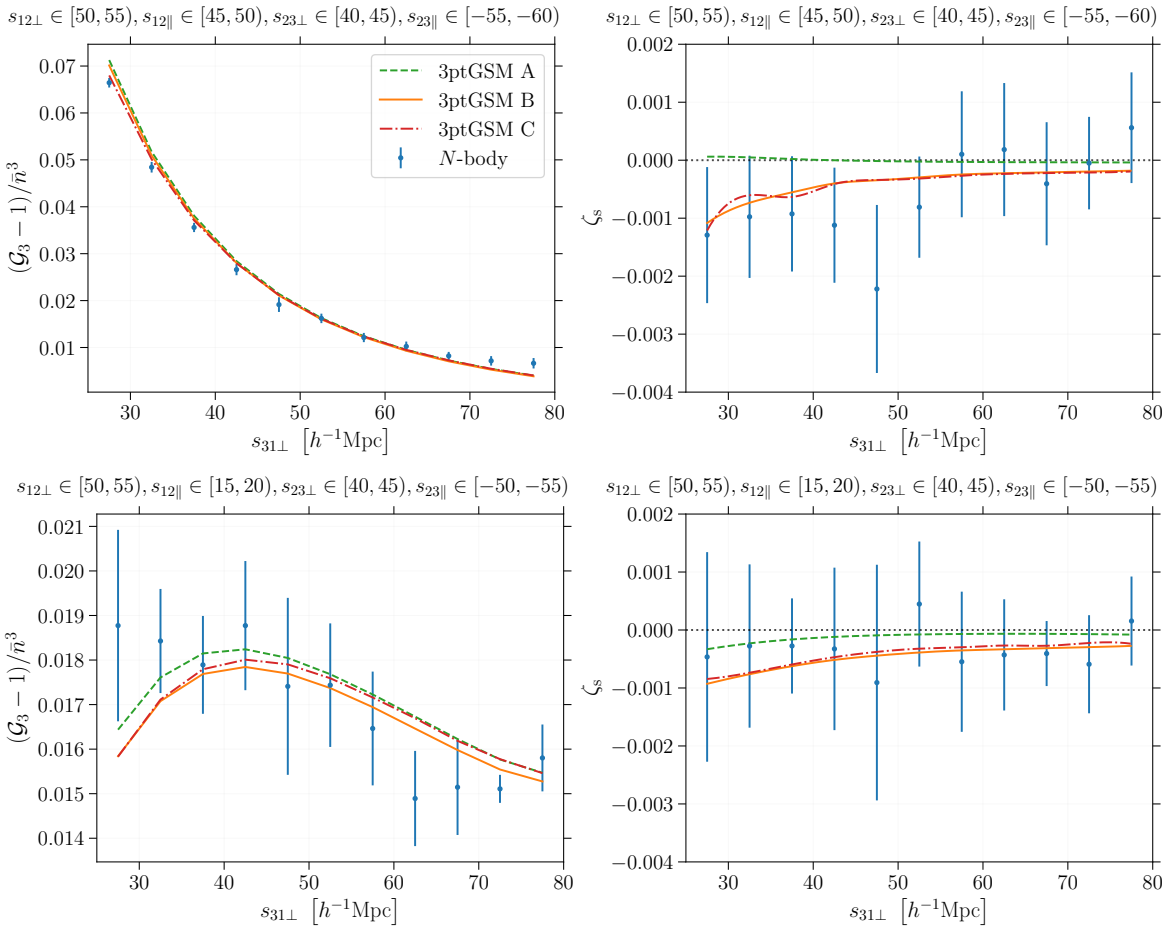

Figure 3.8: Left: Predictions from the 3ptGSM (lines) for the full redshift-space 3PCF $\mathcal{G}_3$ are compared with measurements from our N-body simulation (symbols with error bars). Three versions of the model are considered: case A uses as input the full 3PCF in real space $\mathcal{F}_3$ evaluated at LO in perturbation theory (dashed), case B also includes LO terms for ζ (solid), and case C combines the halo model for ξ with the perturbative model for ζ at LO. The redshift-space separations listed on top of the figures are given in units of $h^{-1}\mathrm{Mpc}$. Right: As in the left panel, but for the connected 3PCF in redshift space.

(remember that, in perturbation theory, $\zeta \sim \xi^2$) and our measurements are rather noisy due to the fact that estimating ζ_s requires binning the triplet counts in five dimensions. Anyway, the N-body results are in very good agreement with the predictions of the 3ptGSM for cases B and C and show the same behaviour as a function of $s_{31\perp}$.

Connected correlation function in real space

Feeding the 3ptGSM with an accurate input for ζ is a necessary prerequisite in order to properly test its capacity to model RSD. Therefore, in the left-panel of figure 3.9, we compare the real-space 3PCF obtained from the perturbative model at LO against the measurements in the simulation. We consider two narrow bins centred around $r_{12} = 37.5\,h^{-1}$ Mpc and $r_{23} = 62.5\,h^{-1}$ Mpc and vary r_{31} within

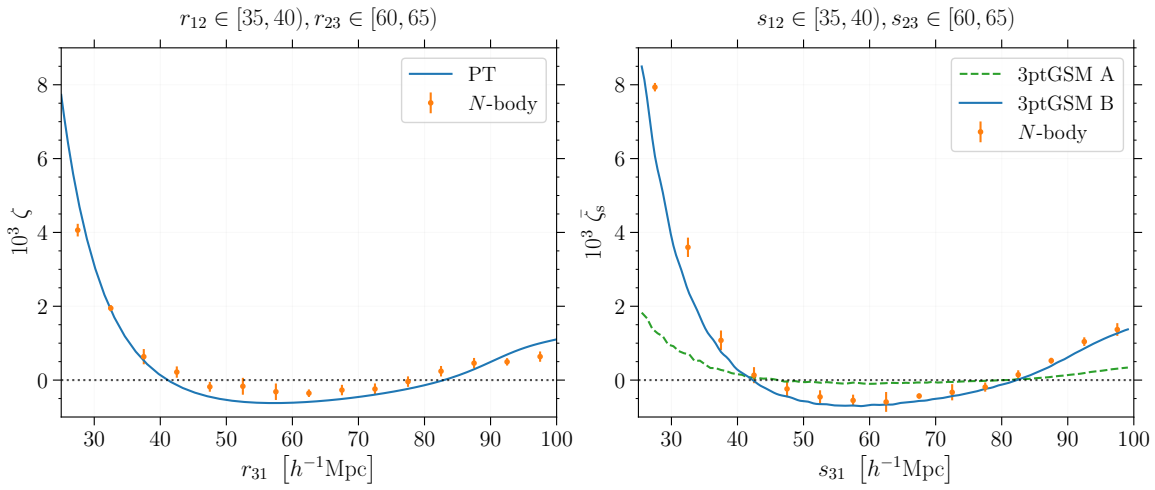

Figure 3.9: Left: The 3PCF in real space measured in the N-body simulation (symbols with error bars) is compared with the predictions from PT at LO (solid line) for a set of triangular configurations obtained by varying r_{31} while keeping r_{12} and r_{23} fixed (as indicated by the top labels that give separations in units of $h^{-1}\mathrm{Mpc}$). Right: As in the left panel but for the spherically-averaged 3PCF in redshift space, $\bar{\zeta}_\mathrm{s}$. In this case, the solid line indicates the predictions of the 3ptGSM.

the full range. Although the agreement is not perfect, we find that the model at LO is in the same ballpark as the simulation results. Overall, the model shows the same shape dependence of the data but relative deviations range typically between 20 and 50% and, obviously, become larger around the zero-crossing points. For larger triangles with sides $r_{12} \simeq 50\,h^{-1}$ Mpc and $r_{23} \simeq 100\,h^{-1}$ Mpc, the model appears to work better (see e.g. figure 11 in Fosalba et al., 2015) but ζ becomes very small and requires large simulated volumes for an accurate measurement. All these findings are consistent with other studies on the matter 3PCF (Jing and Börner, 1997; Barriga and Gaztañaga, 2002) and bispectrum (Scoccimarro and Couchman, 2001; Gil-Marıén, Wagner et al., 2012; McCullagh, Jeong and Szalay, 2016; Hoffmann, Gaztañaga et al., 2018; Takahashi et al., 2019).

Connected correlation function averaged over all orientations

In order to compute a theoretical prediction for the spherically-averaged $\bar{\zeta}_\mathrm{s}$, we use equation (3.21) to evaluate ζ_s with the 3ptGSM and calculate

$$\bar{\zeta}_\mathrm{s}(s_{12}, s_{23}, s_{31}) = \frac{\displaystyle\int \zeta_\mathrm{s}(\boldsymbol{s}_{12}, \boldsymbol{s}_{23})\, \delta_\mathrm{D}^{(1)}\left(s_{31} - \sqrt{s_{12}^2 + s_{23}^2 + 2 s_{12} s_{23}\, \hat{\boldsymbol{s}}_{12} \cdot \hat{\boldsymbol{s}}_{23}}\right) \mathrm{d}\hat{\boldsymbol{s}}_{12}\, \mathrm{d}\hat{\boldsymbol{s}}_{23}}{\displaystyle\int \delta_\mathrm{D}^{(1)}\left(s_{31} - \sqrt{s_{12}^2 + s_{23}^2 + 2 s_{12} s_{23}\, \hat{\boldsymbol{s}}_{12} \cdot \hat{\boldsymbol{s}}_{23}}\right) \mathrm{d}\hat{\boldsymbol{s}}_{12}\, \mathrm{d}\hat{\boldsymbol{s}}_{23}}\,, \tag{3.87}$$

where the integrals are performed by independently varying $\hat{\boldsymbol{s}}_{12}$ and $\hat{\boldsymbol{s}}_{23}$ over the unit sphere. Note that[10]

$$\begin{aligned}\bar{\zeta}_{\mathrm{s}}(s_{12}, s_{23}, s_{31}) &= \frac{\int \zeta_{\mathrm{s}}(\boldsymbol{s}_{12}, \boldsymbol{s}_{23})\, \delta_{\mathrm{D}}^{(1)}(s_{31} - \sqrt{s_{12}^2 + s_{23}^2 + 2 s_{12} s_{23}\, \hat{\boldsymbol{s}}_{12} \cdot \hat{\boldsymbol{s}}_{23}})\, \mathrm{d}\hat{\boldsymbol{s}}_{12}\, \mathrm{d}\hat{\boldsymbol{s}}_{23}}{8\pi^2 \int_{-1}^{+1} \delta_{\mathrm{D}}^{(1)}(s_{31} - \sqrt{s_{12}^2 + s_{23}^2 + 2 s_{12} s_{23}\, \cos\chi})\, \mathrm{d}\cos\chi} \\ &= \frac{\int \zeta_{\mathrm{s}}(\boldsymbol{s}_{12}, \boldsymbol{s}_{23})\, \delta_{\mathrm{D}}^{(1)}(s_{31} - \sqrt{s_{12}^2 + s_{23}^2 + 2 s_{12} s_{23}\, \hat{\boldsymbol{s}}_{12} \cdot \hat{\boldsymbol{s}}_{23}})\, \mathrm{d}\hat{\boldsymbol{s}}_{12}\, \mathrm{d}\hat{\boldsymbol{s}}_{23}}{8\pi^2\, \frac{s_{31}}{s_{12}\, s_{23}} \left[\Theta(s_{31} - |s_{12} - s_{23}|) - \Theta(s_{31} - s_{12} - s_{23})\right]}\,, \end{aligned} \tag{3.88}$$

where $\Theta(x)$ denotes the Heaviside step function. In practice, we use the Monte Carlo method to integrate the numerator and the denominator of equation (3.87) and average over $1\,h^{-1}$ Mpc wide bins for s_{31} at fixed s_{12} and s_{23}.

In the right panel of figure 3.9, we plot $\bar{\zeta}_{\mathrm{s}}$ as a function of s_{31} for the same triangular configurations we considered in real space. Shown are both the measurements from the simulation and the model predictions (excluding case C as it practically coincides with case B). Comparing the left and right panels reveals that RSD markedly enhance the clustering signal in the simulation, particularly for small r_{31}. The 3ptGSM nicely captures this trend. The agreement of our case B implementation with the simulation is rather good: the model nicely reproduces the dependence of $\bar{\zeta}_{\mathrm{s}}$ on s_{31} with typical systematic deviations at the 20% level.

Connected correlation function averaged over wedges

Model predictions for the wedge-averaged 3PCF are obtained using equation (3.21) in combination with

$$\bar{\zeta}_{\mathrm{s}}^{(ij)}(s_{12}, s_{23}, s_{31}) = \frac{\int \zeta_{\mathrm{s}}(\boldsymbol{s}_{12}, \boldsymbol{s}_{23})\, W^{(ij)}(\hat{\boldsymbol{s}}_{12} \cdot \hat{\boldsymbol{s}}, \hat{\boldsymbol{s}}_{23} \cdot \hat{\boldsymbol{s}})\, \mathrm{d}\hat{\boldsymbol{s}}_{12}\, \mathrm{d}\hat{\boldsymbol{s}}_{23}}{\int W^{(ij)}(\hat{\boldsymbol{s}}_{12} \cdot \hat{\boldsymbol{s}}, \hat{\boldsymbol{s}}_{23} \cdot \hat{\boldsymbol{s}})\, \mathrm{d}\hat{\boldsymbol{s}}_{12}\, \mathrm{d}\hat{\boldsymbol{s}}_{23}}\,, \tag{3.89}$$

where

$$W^{(ij)}(\mu_{12}, \mu_{23}) = \Pi_{\frac{i-1}{2}, \frac{i}{2}}(\mu_{12})\, \Pi_{\frac{j-3}{2}, \frac{j-2}{2}}(\mu_{23})\,, \tag{3.90}$$

and $\Pi_{a,b}(x) = \Theta(x-a) - \Theta(x-b)$ denotes the boxcar function. Once again we perform the integrals with the Monte Carlo method.

In figure 3.10, we compare the wedge-averaged correlation function $\zeta_{\mathrm{s}}^{(ij)}$ obtained from the 3ptGSM (case B) and from the simulation for the same triangular configurations considered in figure 3.9. The eight panels are organised as follows. The left and right columns correspond to $i = 1$ (i.e. $0 \leq \mu_{12} < 0.5$) and $i = 2$ (i.e. $0.5 \leq \mu_{12} \leq 1$), respectively. Rows, from top to bottom, refer to $j = 1$

[10] The scalar product $\hat{\boldsymbol{s}}_{12} \cdot \hat{\boldsymbol{s}}_{23}$ gives the component of $\hat{\boldsymbol{s}}_{23}$ along the direction of $\hat{\boldsymbol{s}}_{12}$. Since the two vectors are independent and uniformly distributed on the unit sphere, $\hat{\boldsymbol{s}}_{12} \cdot \hat{\boldsymbol{s}}_{23}$ is distributed as any projection along the coordinate axes, i.e. uniformly between -1 and 1.

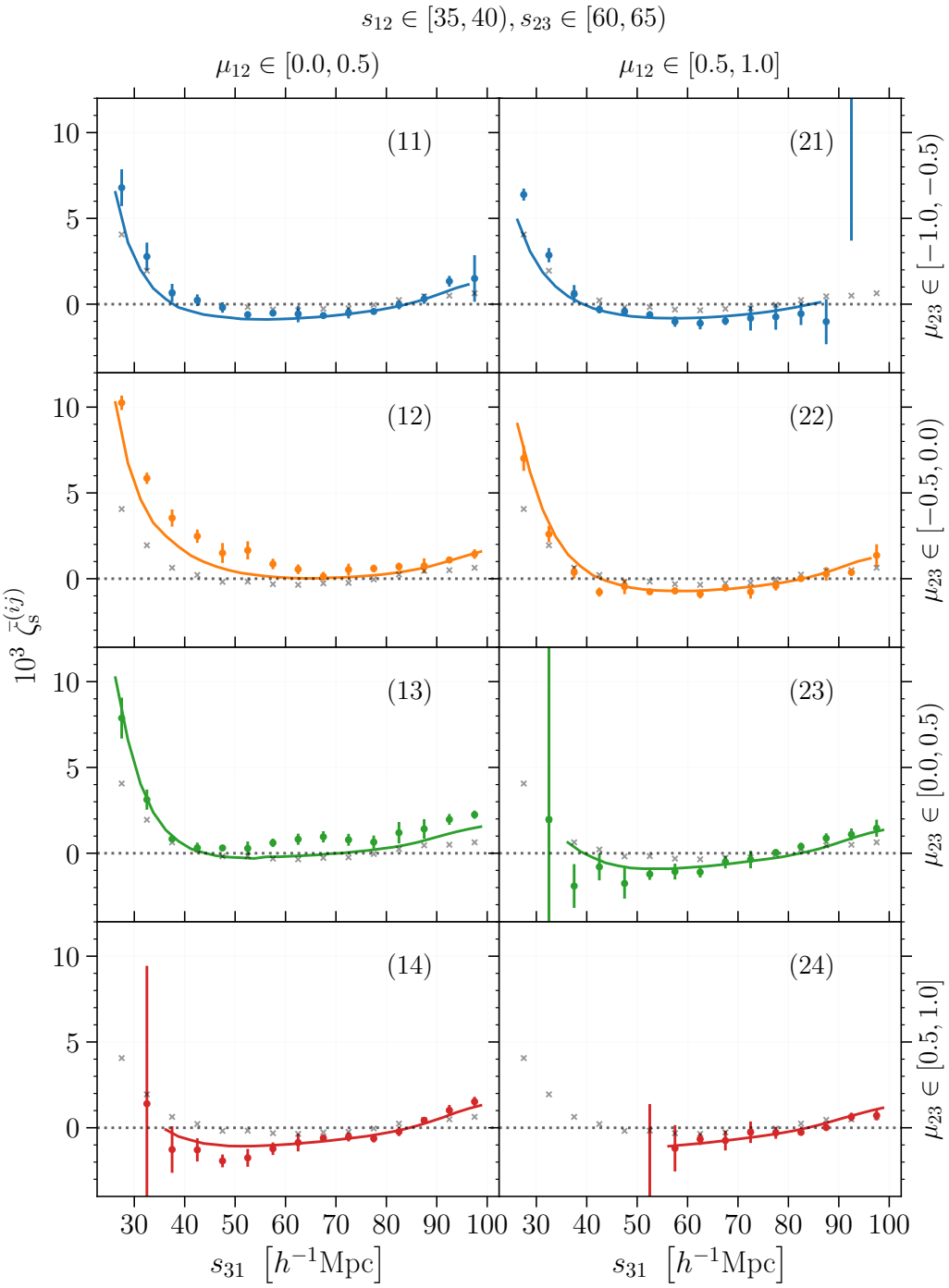

Figure 3.10: The wedge-averaged 3PCF measured in the simulation (symbols with error bars) is compared with the predictions of the 3ptGSM (solid lines). As a reference to help comparing the different panels, we also plot the real-space 3PCF extracted from the simulation (light $\times$ marks) and already shown in the left panel of figure 3.9. The side lengths of s_{12} and s_{23} are listed on top of the figure in units of $h^{-1}\mathrm{Mpc}$.

$(-1 \leq \mu_{23} < -0.5)$, $j = 2$ $(-0.5 \leq \mu_{23} < 0)$, $j = 3$ $(0 \leq \mu_{23} < 0.5)$ and $j = 4$ $(0.5 \leq \mu_{23} \leq 1)$. As a reference, in each panel we also show the real-space 3PCF measured in the simulation. The figure shows that RSD can enhance the 3PCF by a factor of a few (see, for instance, $\zeta_{\rm s}^{(14)}$, $\zeta_{\rm s}^{(21)}$, and $\zeta_{\rm s}^{(23)}$) as well as change its sign (as in $\zeta_{\rm s}^{(12)}$ and $\zeta_{\rm s}^{(13)}$). Independently of s_{31}, the 3ptGSM provides an excellent description of the numerical results for $\zeta_{\rm s}^{(24)}$, $\zeta_{\rm s}^{(23)}$ and $\zeta_{\rm s}^{(22)}$. In other cases, it works well only for large values of s_{31} (see $\zeta_{\rm s}^{(21)}$, $\zeta_{\rm s}^{(11)}$, $\zeta_{\rm s}^{(12)}$ and $\zeta_{\rm s}^{(14)}$). On the other hand, the model tends to underestimate the effect of RSD for $\zeta_{\rm s}^{(13)}$ even for large opening angles.

The main conclusion emerging from the analysis of figures 3.8, 3.9, and 3.10 is that our implementation of the 3ptGSM, although very simple, is already able to reproduce many features measured in the simulations. This very encouraging result motivates further work into building novel tools based on the 3ptGSM for modelling $\zeta_{\rm s}$ on large scales and analyse data from galaxy redshift surveys. As a first step in this direction, in the remainder of this paper, we analyse some key aspects of the 3ptGSM and discuss how the current implementation could be improved.

3.3.4 Discussion

Dissecting the 3ptGSM

Based on equations (3.20) and (3.22), whenever $\int \mathcal{P}^{(3)}_{\boldsymbol{w}_\parallel}(w_\parallel, q_\parallel|\boldsymbol{r}_{12}, \boldsymbol{r}_{23})\,{\rm d}q_\parallel \neq \mathcal{P}^{(2)}_{w_\parallel}(w_\parallel|\boldsymbol{r}_{12})$, RSD generate a non-vanishing connected 3PCF $\zeta_{\rm s}$ even when $\zeta = 0$. In the 3ptGSM, the marginalised distribution gives a Gaussian PDF with mean m_1 and variance C_{11}. On the other hand, $\mathcal{P}^{(2)}_{w_\parallel}$ is a Gaussian with mean $\langle w_{ij\parallel}|\boldsymbol{r}_{ij}\rangle_{\rm p}$ and variance $\langle w^2_{ij\parallel}|\boldsymbol{r}_{ij}\rangle_{\rm p} - \langle w_{ij\parallel}|\boldsymbol{r}_{ij}\rangle^2_{\rm p}$. Note that the mean values are slightly shifted and so are also the variances (although by an even smaller amount). It follows that the difference between the two PDFs does not identically vanish. In practice, however, the effect is very small. By considering, for example, the triangular configuration analysed in figure 3.7, we find that the mean $w_{12\parallel}$ is -0.36 and $-0.25\,h^{-1}{\rm Mpc}$ for the marginalised $\mathcal{P}^{(3)}_{\boldsymbol{w}_\parallel}$ and for $\mathcal{P}^{(2)}_{w_\parallel}$, respectively, while the standard deviation in $\simeq 4.67\,h^{-1}{\rm Mpc}$ for both. It follows that the term that multiplies $1 + \xi(r_{12})$ in equation (3.22) is at best of the order of 10^{-3} and switches sign as w_{12} grows past the mean value. This is shown in figure 3.11 where we also plot the difference between the PDFs estimated from the simulation. The 3ptGSM provides a reasonable approximation to the numerical results. The total contribution of terms like this one to $\zeta_{\rm s}$ is shown in the right panels of figures 3.8 and 3.9 as the result of our case A model. Note that it is always subdominant with respect to the contribution generated by ζ, at least for the configurations considered here. There is some evidence that the terms proportional to $1 + \xi$ in equation (3.22) might become more relevant at small scales where the mean relative velocities are not so small compared to the dispersion. For instance, they appear to give a $\sim 25\%$ contribution to $\bar{\zeta}_{\rm s}$ for the smallest values of s_{31} shown in figure 3.9. However, it is unclear whether such small scales can be robustly analysed with the 3ptGSM.

In figure 3.12, we plot the different terms that appear in the rhs of equation (3.20) using the same triangular configurations as in figure 3.8. The first thing to notice is that $\zeta_{\rm s}$ is obtained by subtracting two much larger numbers. This evidences the need for modelling $\mathcal{P}^{(2)}_{w_\parallel}$ and $\mathcal{P}^{(3)}_{\boldsymbol{w}_\parallel}$ in a consistent way. Also note that the integral $\int \mathcal{P}^{(3)}_{\boldsymbol{w}_\parallel}\,{\rm d}w_\parallel\,{\rm d}q_\parallel$ appearing in the last row of equation (3.20) is not identically equal to one as the conditional PDF needs to be evaluated considering different triangular configurations that reflect the running of the real-space parallel separations in the integral.

Although the Gaussian approximation for $\mathcal{P}^{(2)}_{w_\parallel}$ is not perfect, the Gaussian streaming model provides

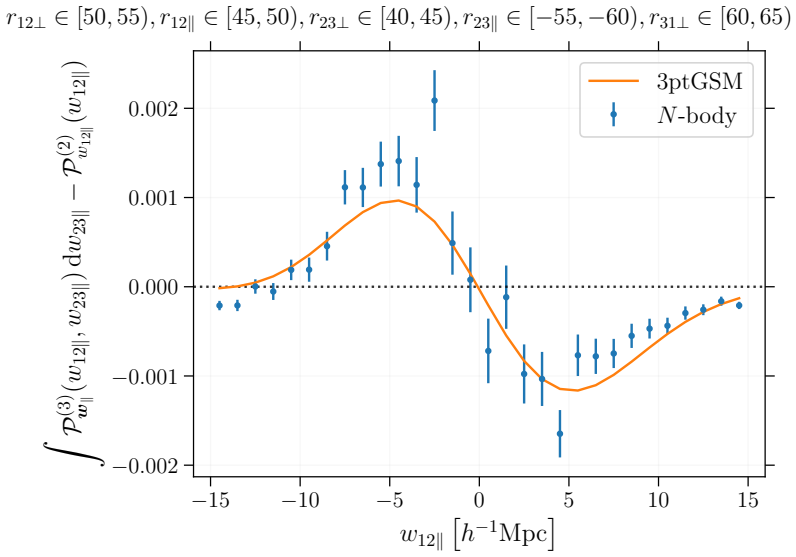

Figure 3.11: The difference of probability densities appearing in the rhs of equation (3.22). Symbols with error bars represent measurements from the N-body simulation while the dashed line shows the predictions of the 3ptGSM.

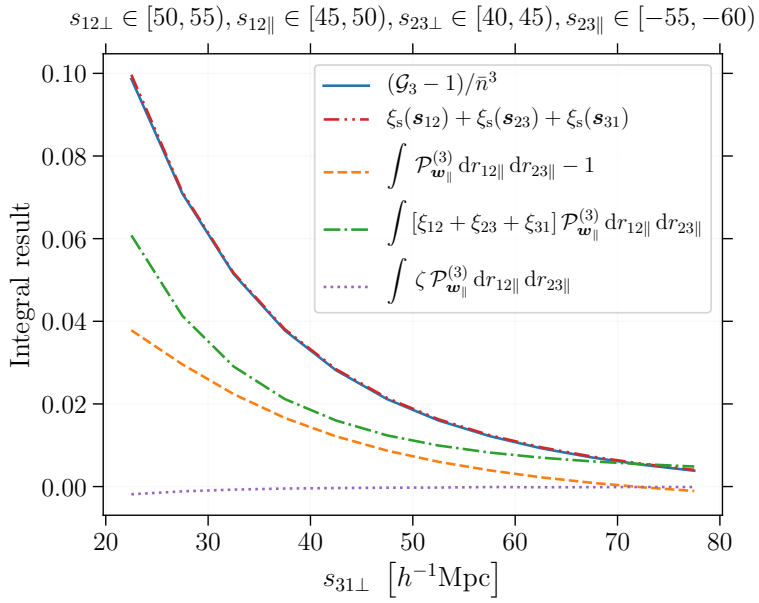

Figure 3.12: Partial contributions to the rhs of equation (3.21) in the 3ptGSM for the same triangular configurations displayed in the top row of figure 3.8 (particle separations are given on top of the figure in units of $h^{-1}\mathrm{Mpc}$). The solid curve represents the integral containing the full 3PCF in real space. The dash double dotted line (hardly distinguishable from the solid one) displays the sum of the three integrals containing the two-point correlation function. The connected 3PCF in redshift space is derived by subtracting the second contribution from the first. Note that the value of ζ_s is a small number obtained by subtracting two much larger numbers. The dashed, dash-dotted and dotted lines isolate the three sub-components of the solid curve. Namely, they show the part proportional to 1, ξ and ζ, respectively.

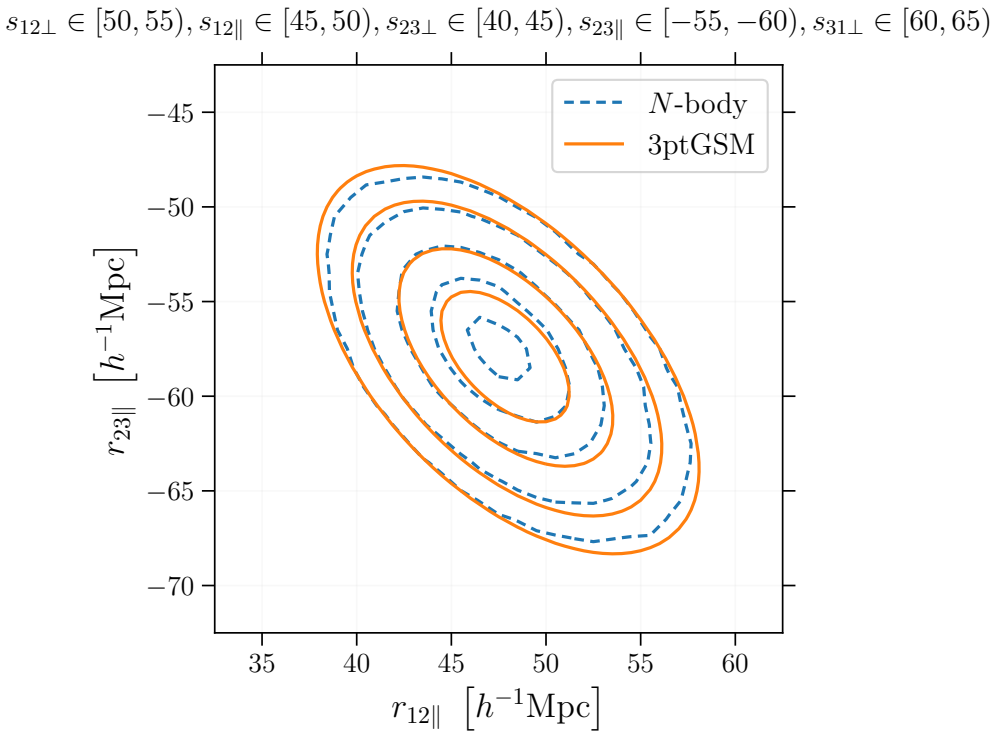

Figure 3.13: Contour levels of the integrand appearing in the rhs of equation (3.19) for one of the triangular configuration shown in figures 3.8 and 3.12 (particle separations are given on top of the figure in units of $h^{-1}\mathrm{Mpc}$). Solid and dashed lines correspond to the 3ptGSM and the N-body simulation, respectively. Contours correspond to the levels $\{8, 6, 4, 2, 1\} \times 10^{-3}$ with the values decreasing from inside to outside. Note that the predictions of the GSM do not reach the value 8×10^{-3}.

a very good description of ξ_s on large scales (e.g. B. A. Reid and M. White, 2011). This success originates from fortuitous cancellations between the contributions of the peak and the wings in the integrand of equation (3.14) (see figure 4 in Kuruvilla and Porciani, 2018). In figure 3.13, we show that the same phenomenon takes place in the 3ptGSM. Shown with solid lines are contour levels of the integrand appearing in the rhs of equation (3.21) for a configuration in which the 3ptGSM accurately reproduces the full 3PCF measured in the simulation. We extract the same quantity from the simulation by creating a bivariate histogram of $s_{ij\parallel} - w_{ij\parallel}$ for the particle triplets that form the same triangular configuration and making sure that its integral gives $\mathcal{G}_3$. The corresponding contour levels are plotted with dashed lines. From the figure, it is evident that the peak of the integrand in the 3ptGSM is underestimated and the tails are overestimated when compared to the numerical results. This provides motivation for improving the modelling of $\mathcal{P}^{(3)}_{\boldsymbol{w}_\parallel}$ along the lines that have been already used for the 2PCF (e.g. Bianchi, Chiesa and Guzzo, 2015; Uhlemann, Kopp and Haugg, 2015; Bianchi, Percival and Bel, 2016; Kuruvilla and Porciani, 2018).

Directions for future improvements

Overall, the simple version of the 3ptGSM we have implemented captures the main trends that can be observed in the simulation. However, there are some discrepancies. We identify a number of reasons for this partial agreement. First of all, the model we use for ζ needs to be substantially improved. As discussed above (left panel of figure 3.9) perturbation theory at LO only provides a sketchy description of the simulation data for the corresponding triangular configuration in real space (i.e. using $r_{12} = s_{12}$ and $r_{23} = s_{23}$). However, the situation is worse than that. In fact, the integral that gives $\zeta_{\rm s}(\triangle_{123})$ in the streaming model receives contributions from triangles with pairwise separations $r_{ij\parallel}$ and $r_{ij\perp}$ that differ by up to 40-50 h^{-1} Mpc from those that define $\triangle_{123}$. For some of them, the model for ζ at LO does not perform very well. Moreover, the second moments of the pairwise velocities predicted with standard perturbation theory at LO become progressively less accurate for squeezed triangles. One can notice this trend in some capacity already in the rightmost panels of figure 3.5 and in the top-right panel of figure 3.6: the model increasingly departs from the simulation results as r_{31} and $r_{31\perp}$ decrease. Since the double integral in equation (3.21) runs over all sorts of triangular configurations including some squeezed ones, this generates inaccuracies. As we have seen in section 3.3.4, the 3ptGSM prediction for $\zeta_{\rm s}$, which is of the order of ξ^2, is obtained from the subtraction of two much larger numbers of order ξ (this can also be noticed by comparing the left and right panels in figure 3.8). Therefore, relatively small errors in the terms that need to be subtracted can shift $\zeta_{\rm s}$ substantially. We thus expect that the 3ptGSM will considerably benefit from more sophisticated input models for ξ, ζ and the moments of the pairwise velocities as it has already happened at the 2-point level (Carlson, B. Reid and M. White, 2013; L. Wang, B. Reid and M. White, 2014; Vlah, Castorina and M. White, 2016). Implementing these improvements, however, clearly goes beyond the scope of this paper.

Connection with dispersion models for the bispectrum

Fourier transforming equation (3.14) provides an expression for the anisotropic power spectrum in redshift space, $P_{\rm s}(k_\parallel, k_\perp)$. If one is ready to assume, for simplicity, that $\mathcal{P}^{(2)}_{w_\parallel}(w_\parallel|\boldsymbol{r})$ does not depend on $\boldsymbol{r}$, the convolution theorem then gives $P_{\rm s}(k_\parallel, k_\perp) = S^{(2)}(k_\parallel)\, P(k_\parallel, k_\perp)$ with $S^{(2)}(k_\parallel)$ the Fourier transform of $\mathcal{P}^{(2)}_{w_\parallel}$. This situation occurs if $\mathcal{P}^{(2)}_{w_\parallel}(w_\parallel|\boldsymbol{r})$ is replaced by the scale-independent function $\mathcal{R}^{(2)}_{w_\parallel}(w_\parallel)$ we have introduced in equation (3.29). This defines the so-called 'dispersion model'. The basic underlying idea (originally proposed in Peacock, 1992) is to imagine that, due to highly non-linear physics taking place on small scales, the los velocity at each spatial location has a random component which is independently drawn from a distribution with variance σ_v^2 and the los relative velocities between two locations have thus a variance of $\sigma_{\rm p}^2 = 2\,\sigma_v^2$. Assuming that $\mathcal{P}^{(1)}_{v_\parallel}$ is well approximated by a zero-mean Gaussian with variance σ_v^2 gives $S^{(2)}(k_\parallel) = \exp(-k_\parallel^2\,\sigma_{\rm p}^2/2)$ which reduces to $S^{(2)}(k_\parallel) \simeq 1 - k_\parallel^2\,\sigma_{\rm p}^2/2$ on large scales.[11] This expression is commonly used to analyse survey and simulation data (e.g. Peacock and West, 1992; Park et al., 1994; Peacock and Dodds, 1994; Hawkins et al., 2003; Guzzo, Pierleoni et al., 2008; Beutler et al., 2012; Chuang and Y. Wang, 2013) and $\sigma_{\rm p}^2$ is treated as a free parameter.[12] The 'damping factor' $S^{(2)}(k_\parallel)$ thus accounts

[11] Note that, at quadratic order in the wavenumbers, Gaussian and Lorentzian damping functions coincide.

[12] For dark matter, the LO perturbative contribution to σ_v^2 is given in equation (3.64) but, as we have shown at the end of section 3.2.3, this does not accurately describe N-body data.

for the suppression of the clustering amplitude in redshift space due to incoherent relative motions along the los generated within collapsed structures (e.g. the 'finger-of-god' effect Jackson, 1972; Sargent and Turner, 1977).

We now use equation (3.21) to generalise the dispersion model to 3-point statistics. The 3PCF and the bispectrum $B(\boldsymbol{p},\boldsymbol{q},\boldsymbol{k})$ form a Fourier pair, i.e.

$$\begin{aligned}\zeta(\triangle_{123}) &= \langle\delta(\boldsymbol{x}_2)\,\delta(\boldsymbol{x}_2+\boldsymbol{r}_{21})\,\delta(\boldsymbol{x}_2+\boldsymbol{r}_{23})\rangle \\ &= \int B(\boldsymbol{p},\boldsymbol{q},-\boldsymbol{p}-\boldsymbol{q})\,e^{-i(\boldsymbol{p}\cdot\boldsymbol{r}_{21}+\boldsymbol{q}\cdot\boldsymbol{r}_{23})}\,\frac{\mathrm{d}^3p\,\mathrm{d}^3q}{(2\pi)^6}\,,\end{aligned} \tag{3.91}$$

(note that the correlation function is defined in terms of the 'star ray' separation $\boldsymbol{r}_{21}$ introduced in footnote 2 while we have always used $\boldsymbol{r}_{12}$ so far). Let us now consider the simplest possible case in which: (i) $\mathcal{P}^{(3)}_{\boldsymbol{w}_\parallel}$ does not depend on $\boldsymbol{r}_{21}$ and $\boldsymbol{r}_{23}$, (ii) the PDF of the pairwise velocities can be approximated by a Gaussian distribution with covariance matrix $\boldsymbol{\Sigma}$, and (iii) the contribution from the two-point terms in the rhs of equation (3.20) is subdominant (as discussed above). In this case, the convolution theorem gives

$$B_\mathrm{s}(\boldsymbol{p},\boldsymbol{q},-\boldsymbol{p}-\boldsymbol{q}) = S^{(3)}(p_\parallel,q_\parallel)\,B(\boldsymbol{p},\boldsymbol{q},-\boldsymbol{p}-\boldsymbol{q})\,, \tag{3.92}$$

with

$$\begin{aligned}S^{(3)}(p_\parallel,q_\parallel) &= \int \mathcal{P}^{(3)}_{\boldsymbol{w}_\parallel}(w_{21\parallel},w_{23\parallel}|\triangle_{123})\,e^{i(p_\parallel w_{21\parallel}+q_\parallel w_{23\parallel})}\,\mathrm{d}w_{21\parallel}\,\mathrm{d}w_{23\parallel} \\ &= \exp\left[-\frac{1}{2}(\Sigma_{11}\,p_\parallel^2+2\,\Sigma_{12}\,p_\parallel\,q_\parallel+\Sigma_{22}\,q_\parallel^2)\right]\,.\end{aligned} \tag{3.93}$$

However, the result must be invariant with respect to changing the pair of wavevectors we use to evaluate the damping factor, i.e. $S^{(3)}(p_\parallel,q_\parallel) = S^{(3)}(p_\parallel,-p_\parallel-q_\parallel) = S^{(3)}(-p_\parallel-q_\parallel,q_\parallel)$. It follows that the covariance matrix must have the form

$$\boldsymbol{\Sigma} = \sigma^2\begin{pmatrix}1 & 1/2\\ 1/2 & 1\end{pmatrix}\,, \tag{3.94}$$

with σ^2 a free parameter. For convenience, in this calculation we have used the variable $w_{21\parallel}$ while in the remainder of the paper we always dealt with $w_{12\parallel} = -w_{21\parallel}$. Therefore, equation (3.94) can be re-written in terms of the covariance matrix C we have introduced in section 3.3.1 as

$$\mathsf{C} = \sigma^2\begin{pmatrix}1 & -1/2\\ -1/2 & 1\end{pmatrix}\,. \tag{3.95}$$

It is reassuring to see that this result provides a zeroth-order approximation to the velocity statistics we measure in the N-body simulation as shown in the bottom-right panel of figure 3.1 and in figure 3.6. On large scales, the mean pairwise velocities are much smaller than their dispersions which are nearly scale independent. Moreover, the linear correlation coefficient between $w_{12\parallel}$ and $w_{23\parallel}$ is always close to $-1/2$.

Equation (3.95) has a simple and straightforward interpretation within the context of the dispersion

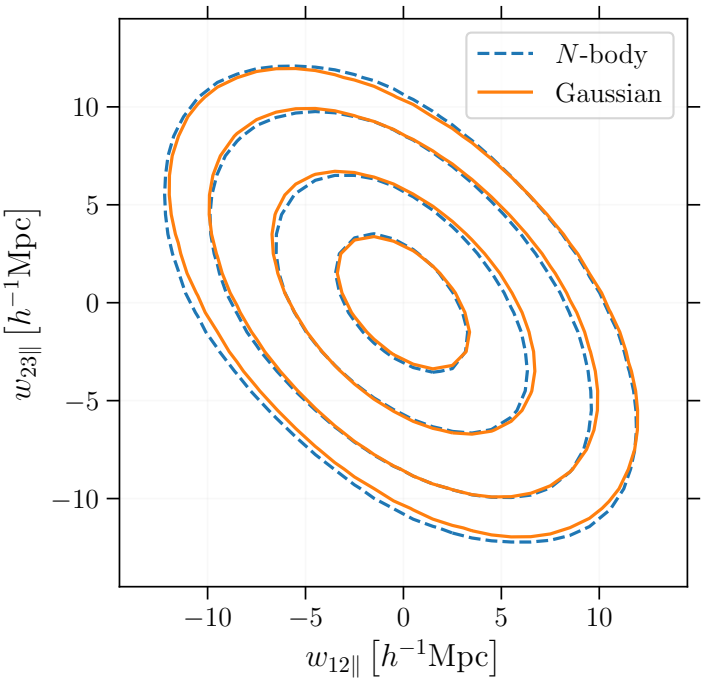

Figure 3.14: Contour levels of the scale-independent PDF $\mathcal{R}^{(3)}_{\boldsymbol{w}_\|}$, as given in equation (3.37). The dashed lines correspond to the direct measurement from the simulation while the solid lines represent a zero mean bivariate Gaussian with a covariance matrix of the same form as in equation (3.95) and $\sigma^2 = 24.2\,h^{-2}\mathrm{Mpc}^2$. Contours correspond to levels $\{6, 3, 1, 0.4\} \times 10^{-3}$ with the values decreasing from inside to outside.

model: if the los velocity at each location is independently drawn from a distribution with variance σ_v^2, then $\mathbf{C}$ is the covariance matrix of the velocity differences $w_{12\|}$ and $w_{23\|}$. The non-vanishing off-diagonal term comes from the fact that location number 2 appears in both pairs as evidenced in equation (3.72). Therefore, we can write that $\sigma^2 = \sigma_\mathrm{p}^2 = 2\,\sigma_v^2$. In other words, in full analogy with the 2-point case, the dispersion model is obtained by replacing $\mathcal{P}^{(3)}_{\boldsymbol{w}_\|}$ with the function $\mathcal{R}^{(3)}_{\boldsymbol{w}_\|}$ introduced in equation (3.37). While completing this work, we became aware that this line of reasoning was first pursued in Matsubara, 1994 to model the galaxy 3PCF on small scales. This publication also introduces a very rudimentary form of our equation (3.17) in which $\mathcal{R}^{(3)}_{\boldsymbol{w}_\|}$ appears instead of $\mathcal{P}^{(3)}_{\boldsymbol{w}_\|}$. In figure 3.14, we show that a Gaussian PDF provides an excellent approximation to $\mathcal{R}^{(3)}_{\boldsymbol{w}_\|}$.

In the literature on the bispectrum, the damping factor is generally written as a symmetric function of three wavenumbers, $\mathcal{F}(p_\|, q_\|, k_\|)$ with the condition $p_\| + q_\| + k_\| = 0$. Equations (3.93) and (3.95) say that $\mathcal{F}(p_\|, q_\|, -p_\| - q_\|) = S^{(3)}(p_\|, q_\|)$. There are multiple functional forms for $\mathcal{F}$ that satisfy this condition. For instance, we could obtain a valid $\mathcal{F}$ by applying a symmetrization method either to the function $S^{(3)}$ (i.e. $\mathcal{F}(p_\|, q_\|, k_\|) = [S^{(3)}(p_\|, q_\|) + S^{(3)}(p_\|, k_\|) + S^{(3)}(k_\|, q_\|)]/3$) or to the argument of the exponential function that appears in $S^{(3)}$ (i.e. $\mathcal{F}(p_\|, q_\|, k_\|) = \exp[-(2p_\|^2 + 2q_\|^2 + 2k_\|^2 + pq + kp + kq)\sigma^2/6]$). A simpler solution is found by further requiring that $\mathcal{F}$ only depends on the square of the wavenumbers which gives[13] $\mathcal{F}(p_\|, q_\|, k_\|) = \exp[-(p_\|^2 + q_\|^2 + k_\|^2)\,\sigma_\mathrm{p}^2/4] \simeq 1 - (p_\|^2 + q_\|^2 + k_\|^2)\,\sigma_\mathrm{p}^2/4$.

[13] This is the most commonly used ansatz and provides a reasonable fit to numerical simulations (e.g. Scoccimarro,

In brief, providing an expression for $\mathcal{F}$ is somewhat arbitrary. All what matters in practice is the function $S^{(3)}$.

3.4 Summary

We have derived, from first principles, the equations that relate the n-point correlation functions in real and redshift space. We have followed a particle-based approach using statistical-mechanics techniques based on the n-particle phase-space densities.[14] Our results are exact (within the distant-observer approximation) and completely independent of the nature of the tracers we consider and of their interactions. They generalise the so-called streaming model to n-point statistics. The theory is formulated more naturally in terms of the full n-point correlations. In this case, the redshift-space correlation function is obtained as an integral of its real-space counterpart times the joint PDF of $n-1$ relative los peculiar velocities. Equation (3.17) expresses this relation succinctly and the velocity PDF is defined in equation (3.16).

We have shown that it is possible to re-formulate the theory entirely in terms of connected correlation functions although the price to pay is a velocity term that is not a PDF (and can be negative) as well as a higher degree of abstractness. This result is expressed by equations (3.31) and (3.32).

In the second part of the paper, we have focused on 3-point statistics. First of all, by combining the streaming model for the 2PCF and the 3PCF, we have derived equation (3.21) which provides a computationally-friendly framework to calculate connected 3-point correlations in redshift space. A key ingredient appearing in this equation is the bivariate PDF for the los relative velocities between particles pairs in a triplet, $\mathcal{P}^{(3)}_{\boldsymbol{w}_\parallel}(w_{12\parallel}, w_{23\parallel}|\triangle_{123})$. Making use of a large N-body simulation, we have characterised the properties of this function for unbiased tracers of the matter-density field. Figures 3.1 and 3.7 show that the PDF is unimodal and, for large triangles, has a quasi-Gaussian peak. The dispersion of $w_{12\parallel}$ and $w_{23\parallel}$ is always much larger than the mean. Moreover, $w_{12\parallel}$ and $w_{23\parallel}$ tend to be anti-correlated, especially on large scales.

In section 3.2.3, we have derived theoretical predictions for the first two moments of $\boldsymbol{w}_{12}$ and $\boldsymbol{w}_{23}$ using standard perturbation theory at LO. Equation (3.53) shows that the mean relative velocity between a particle pair in a triplet is not purely radial but has also a transverse component in the plane of the triangle defined by the particles. Individual expressions for the different components are given in equations (3.54), (3.55) and (3.56). Figures 3.3 and 3.4 show that the LO predictions accurately match the simulation results from quasi-linear scales onward ($r_{ij} \gtrsim 20\,h^{-1}\mathrm{Mpc}$). Perturbative expressions for the second moments are given in equations (3.73) and (3.74). In this case, a constant offset needs to be added to the theoretical results (that neglect small-scale physics) in order to reproduce the simulations on large scales. Figure 3.5 shows that, after applying the correction, the model is accurate to better than a few per cent for separations $r_{ij} \gtrsim 50\,h^{-1}\mathrm{Mpc}$. In section 3.2.3, we have discussed the projection of the relative velocities along the los. Figure 3.6 shows that the perturbative predictions agree well with the simulation for triangles with legs $r_{ij} \gtrsim 50\,h^{-1}\mathrm{Mpc}$. Our results lay the groundwork for investigating 3-point statistics of the los pairwise velocities with future experiments based on the kinetic Sunyaev-Zel'dovich effect like the Simons Observatory (SO, P. Ade et al., 2019), CMB-S4 (Abazajian et al., 2016), CMB-HD (Sehgal, Aiola et al., 2019; Sehgal, Nguyen et al., 2019);

Couchman and Frieman, 1999; Hashimoto, Rasera and Taruya, 2017).

[14] In section 3.1.6, we have provided a dictionary to translate our formalism into the language used by many previous papers that discuss collisionless systems.

as well as with other peculiar-velocity surveys like the Taipan galaxy survey (Taipan, da Cunha et al., 2017) and the Widefield ASKAP L-band Legacy All-sky Blind Survey (WALLABY).

In section 3.3, we have introduced the 3ptGSM that brings together several elements of our study. This model is based on the exact equation (3.21) but phenomenologically approximates $\mathcal{P}^{(3)}_{\boldsymbol{w}_\parallel}(w_{12\parallel}, w_{23\parallel}|\triangle_{123})$ with a bivariate Gaussian distribution whose moments are computed using perturbative techniques (and offsetting the velocity dispersion with a constant so that to match its direct measurement in the simulation). We have then presented a simple practical implementation of the 3ptGSM by deriving all its ingredients (real-space clustering amplitudes and velocity statistics) from standard perturbation theory at LO. The comparison of the model predictions against the correlation function from the simulation performed in figures 3.8, 3.9 and 3.10 is very encouraging, in particular considering that the model has no free parameters.

The forthcoming generation of galaxy surveys will cover large-enough volumes to permit accurate measurements of the 3PCF on large scales. This achievement will inform us about galaxy formation, cosmology, neutrino masses, the nature of primordial perturbations, dark energy, and the gravity law. It is thus timely to create new theoretical tools that facilitate this endeavour. In this paper, we have developed a general framework for the analysis of RSDs in the n-point correlation functions. This pilot work sets the foundation for future developments including: (i) considering biased tracers of the matter-density field, (ii) extending our calculations to different flavours of PT (e.g. B. A. Reid and M. White, 2011; Carlson, B. Reid and M. White, 2013; Vlah, Castorina and M. White, 2016) for both real-space clustering and velocity statistics, and (iii) going beyond the Gaussian approximation for the PDF of the relative los velocities by introducing multivariate distributions with non-zero skewness and that are leptokurtic (e.g. Bianchi, Chiesa and Guzzo, 2015; Uhlemann, Kopp and Haugg, 2015; Bianchi, Percival and Bel, 2016; Kuruvilla and Porciani, 2018).

CHAPTER 4

Kinetic Sunyaev-Zeldovich effect

Current understanding of the cosmological model comes about from large-scale structure (LSS) probes using cosmic microwave background, galaxy distribution and gravitiational lensing surveys. Another probe which could enhance our understanding comes in the form of measuring peculiar velocity of the galaxies or galaxy clusters. For example, surveys focusing on peculiar velocities provide us with a complementary tool to test the current paradigm through measurements of the growth rate, f, which is given as the logarithmic derivative of the growth factor with respect to the scale factor. Different models of gravity predict different f, thus it becomes a tool to test the validity of general relativity (GR) as the correct theory of gravity on large scales.

Peculiar velocity measurement in redshift space can be done through two prominent ways. Firstly, direct measurements of the peculiar velocity can be done through redshifts and distances determined using scaling relations like the Tully-Fisher or the fundamental plane relation. These direct peculiar velocity surveys however lead to shallow surveys, thus offering an opportunity to probe the peculiar velocities of the nearby universe. Upcoming direct peculiar velocity measurement surveys like TAIPAN and WALLABY+WNSHS promises to be competitive as a cosmological probe for very low redshifts with the respect to current galaxy clustering surveys (e.g. Koda et al., 2014; Howlett, Staveley-Smith and Blake, 2017).

Another method to measure the peculiar velocity is through the kinematic Sunyaev-Zeldovich (kSZ) effect (Sunyaev and Zeldovich, 1970; Sunyaev and Zeldovich, 1972; Sunyaev and Zeldovich, 1980), in which CMB photons get scattered off free electrons which are in motion. This results in a Doppler shift, thus preserving the blackbody spectrum of the CMB. It is also one of the only known techniques through which we can measure the peculiar velocities of objects at cosmological distances. However the signal from kSZ effect is very weak, hence detection for individual objects has proven to be cumbersome. Current evidence of kSZ depends on the mean pairwise velocity quantity as it allows for stacking procedure which increases the statistical constraining power. First evidence of the kSZ effect through the pairwise mean velocity was detected by Hand et al., 2012 using the pairwise velocity estimator developed by Ferreira et al., 1999. Further evidence for the kSZ using pairwise velocities were shown in Planck Collaboration, P. A. R. Ade et al., 2016; Schaan et al., 2016; Soergel et al., 2016; De Bernardis et al., 2017; Y.-C. Li et al., 2017. One of the arguments for using the mean pairwise velocity is that on average the pairs would seem to move towards each other, rendering the mean pairwise velocity to be negative. This would be true only in the case when one considers the pairwise velocity distribution in real space, which is one of the main ingredient in modelling the redshift-space

distortions (e.g. Peebles, 1980; Fisher, 1995; Scoccimarro, 2004; Kuruvilla and Porciani, 2018). However in reality we probe the pairwise velocity in the redshift space. In the recent years, more focus has been placed on redshift-space peculiar velocity in the configuration space (Okumura et al., 2014; Sugiyama, Okumura and D. N. Spergel, 2016).

In this chapter, it is our aim to showcase the behaviour of pairwise and triple-wise velocity distribution in redshift space. Mean pairwise kSZ signal has been shown to have the potential to constrain neutrino masses (Mueller et al., 2015b), which could act as a complementary probe to the existing techniques. Pairwise velocities measured through kSZ can also be used to constrain dark energy and modified gravity, and would be competitive with the measurements from galaxy clustering surveys in future (see Bhattacharya and Kosowsky, 2008; Ma and Zhao, 2014; Mueller et al., 2015a; Alonso et al., 2016). This provides us the motivation that understanding the pairwise and triple-wise velocity distribution in redshift space is timely and necessary. The chapter is structured as follows. In section 4.1, we elaborate about the N-body simulation used in this work. In section 4.2, we introduce the pairwise velocity distribution in real space and redshift space. Further in section 4.2.1, we take a look into how the first four moments of the pairwise velocity distribution would look like in redshift space. An exploration of the redshift evolution of the pairwise velocity distribution is done in section 4.2.2 . We introduce the triple-wise velocity distribution in section 4.3, and its moments in section 4.3.1. We mitigate the optical depth degeneracy and introduce an bias-independent estimator in section 4.4. Finally in section 4.5 we provide our conclusions.

4.1 N-Body simulations

In our analysis, we make use of a N-body simulation ran using a lean version of GADGET-2 (Springel, Yoshida and S. D. M. White, 2001; Springel, 2005) that was labelled 1.0 in Pillepich, Porciani and Hahn, 2010. In brief, the simulation follows the formation of the large-scale structure from Gaussian initial conditions within a periodic cubic box with a side of 1.2 $h^{-1}\mathrm{Gpc}$. It assumes a flat ΛCDM cosmology with the best-fitting parameters determined by the five year analysis of the *WMAP* mission (Komatsu et al., 2009) and considers 1024^3 particles with a mass of $1.246 \times 10^{11} h^{-1}\mathrm{M}_\odot$ (see Pillepich et al. 2010 for further details).

4.2 Pairwise velocity distribution in redshift space

The distance of a cosmological object is simultaneously affected by both the homogeneous cosmic expansion with instantaneous scale factor a and Hubble parameter H, and its peculiar velocity. Thus we need to distinguish between the redshift-inferred distance of a galaxy $\boldsymbol{s}$ and its true comoving distance $\boldsymbol{x}$. In the distant-observer (or plane-parallel) approximation,

$$\boldsymbol{s} = \boldsymbol{x} + (\boldsymbol{v} \cdot \hat{\boldsymbol{z}})\, \hat{\boldsymbol{z}} \,, \tag{4.1}$$

where $\boldsymbol{v}$ denotes the peculiar velocity divided by the factor aH and $\hat{\boldsymbol{z}}$ denotes the los direction. The spurious displacement along the los distorts the clustering pattern of galaxies in redshift space from its actual configuration in real space.

$$s_\parallel = (\boldsymbol{s}_2 - \boldsymbol{s}_1) \cdot \hat{\boldsymbol{z}} = r_\parallel + w_\parallel \,, \tag{4.2}$$

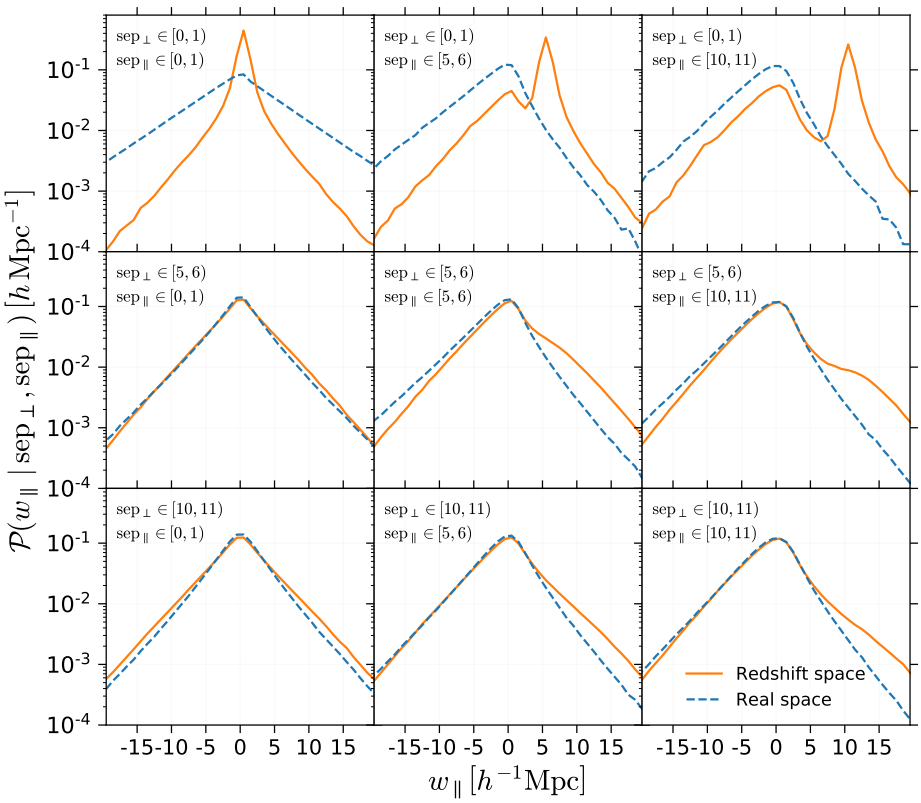

Figure 4.1: Line-of-sight pairwise velocity distribution in redshift space (solid lines) and real space (dashed lines). The pairwise velocity PDF in redshift space exhibits bimodal feature and deviates from the one in real space pairwise at the scales shown here. The units of the separations are given in $h^{-1}\mathrm{Mpc}$.

where $r_\parallel = \boldsymbol{r} \cdot \hat{\boldsymbol{z}}$ and $w_\parallel = (\boldsymbol{v}_2 - \boldsymbol{v}_1) \cdot \hat{\boldsymbol{z}}$, while the transverse separation remains unchanged, i.e.

$$\boldsymbol{s}_\perp = \boldsymbol{r}_\perp \ . \tag{4.3}$$

The pairwise velocity distribution function in redshift space, $\mathcal{P}_\mathrm{s}(w_\parallel \mid s_\perp, s_\parallel)$, can be written as

$$\mathcal{P}_\mathrm{s}(w_\parallel \mid s_\perp, s_\parallel) = \int_{-\infty}^{+\infty} \mathcal{P}_\mathrm{r}(w_\parallel \mid s_\perp, r_\parallel)\, \mathcal{P}(r_\parallel \mid s_\perp, s_\parallel)\, \mathrm{d}r_\parallel \,, \tag{4.4}$$

where $\mathcal{P}_\mathrm{r}(w_\parallel \mid s_\perp, r_\parallel)$ is the real space pairwise velocity distribution and $\mathcal{P}(r_\parallel \mid s_\perp, s_\parallel)$ is the real space separation distribution for a given redshift space separation. $\mathcal{P}(r_\parallel \mid s_\perp, s_\parallel)$ is what encompasses the RSD effect into the pairwise velocity distribution in redshift space and which we christen as the 'RSD transformation' distribution function. It tells us for pairs at given a redshift space separation, how they will be distributed in real space which is affected by the pairwise velocity as can be seen from equation (4.2). For pairs in redshift space with $s_\perp, s_\parallel \in \mathbb{R}_{\geq 0}$, $r_\parallel < 0$ implies pairs which have reversed their order in real space. As expected, it is more likely to find reversed pairs at smaller separations.

A bimodal feature for $\mathcal{P}_\mathrm{s}(w_\parallel \mid s_\perp, s_\parallel)$ (denoted by orange solid line) at small $s_\perp \in [0,1)\, h^{-1}\mathrm{Mpc}$

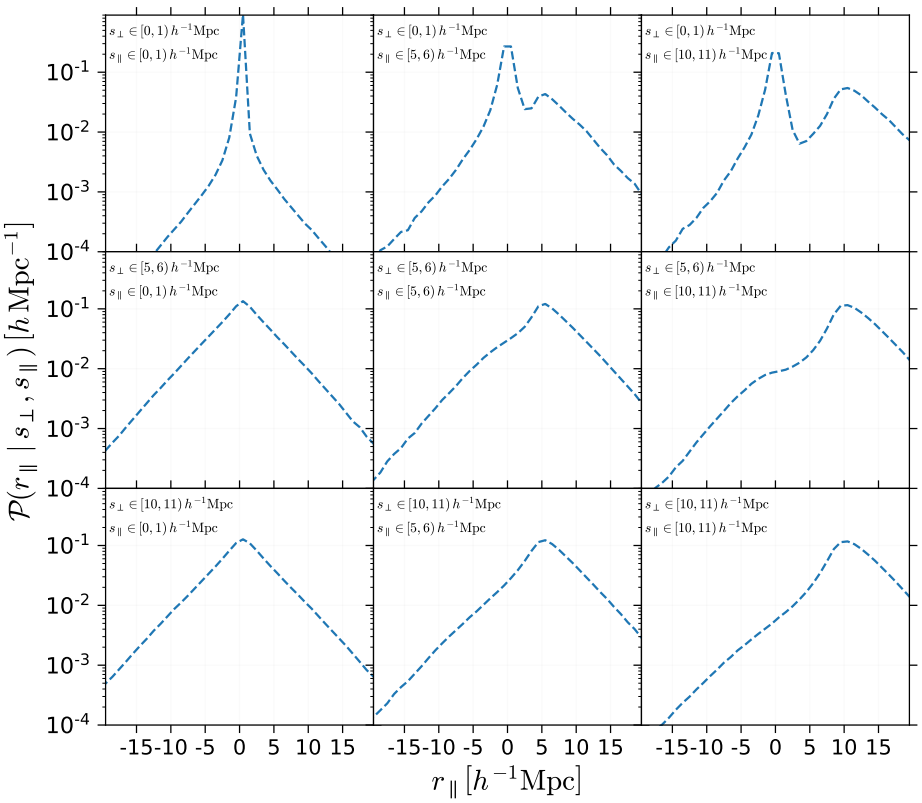

Figure 4.2: The RSD transformation distribution funciton which shows the real space separation distribution for pairs at a given redshift space separation. The pairs which have $r_\parallel < 0$ are the ones which have reversed their order compared to their redshift space counterpart. The RSD transformation distribution has the symmetry $\mathcal{P}(r_\parallel \mid s_\perp, s_\parallel) = \mathcal{P}(-r_\parallel \mid s_\perp, -s_\parallel)$.

and $s_\parallel > 1\,h^{-1}\mathrm{Mpc}$ pair separations can be clearly seen in Figure. 4.1. On first glance, we can see that the distributions are mostly different at the scales we have considered. However, in the left column which are for pairs having very minimal los separation but considerable transverse separation, they are similar. More interesting are the pairs which have a very small transverse pair separation but considerable los separation, the distribution in redshift space breaks the property of unimodality which is seen in the real space pairwise velocity distribution. This comes about from the bimodal behaviour of the 'RSD transformation' distribution function, $\mathcal{P}(r_\parallel \mid s_\perp, s_\parallel)$, at those scales as shown in figure 4.2. This feature comes about as a mixture of pairs having both high relative los velocity and low relative los velocities. The peak around $r_\parallel \simeq 0$ is generally formed by the pairs which have high pairwise velocity (resulting from the highly non-linear density field in which these pairs are embedded in). This peak contains mostly the pairs which partake in elongation of the structure along the los leading to the Finger-of-God (FoG) effect. The effect is maximal, unsurprisingly, for pairs having very low $s_\perp$ separation.

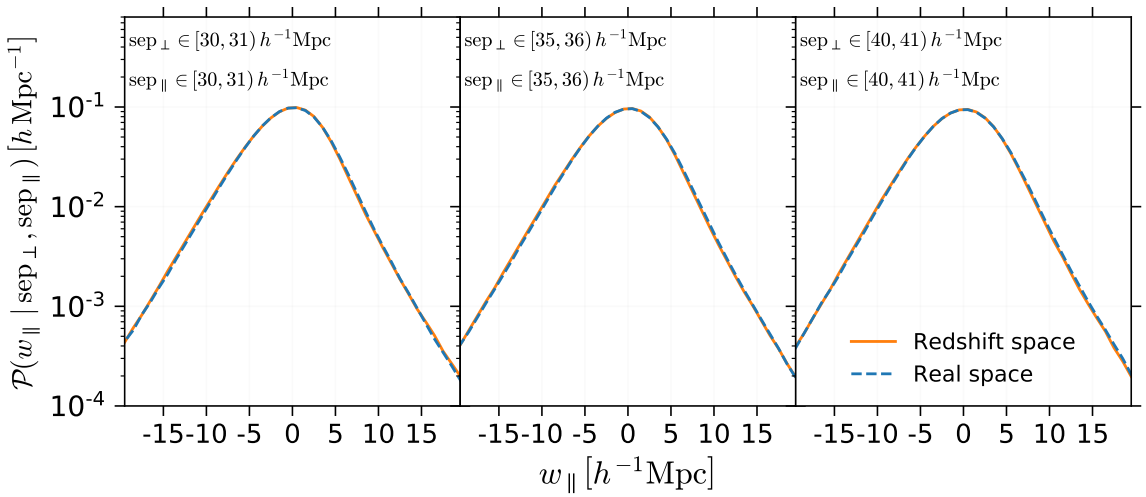

Figure 4.3: Line-of-sight pairwise velocity distribution in redshift space (solid lines) and real space (dashed lines). The pairwise velocity PDF in redshift space and the one in real space pairwise are essentially the same in large enough separations.

The distributions are symmetric under particle exchange or parity transformations

$$\mathcal{P}_\mathrm{r}(w_\parallel \mid s_\perp, r_\parallel) = \mathcal{P}_\mathrm{r}(-w_\parallel \mid s_\perp, -r_\parallel) \tag{4.5}$$

$$\mathcal{P}_\mathrm{s}(w_\parallel \mid s_\perp, s_\parallel) = \mathcal{P}_\mathrm{s}(-w_\parallel \mid s_\perp, -s_\parallel) \tag{4.6}$$

$$\mathcal{P}(r_\parallel \mid s_\perp, s_\parallel) = \mathcal{P}(-r_\parallel \mid s_\perp, -s_\parallel)\,. \tag{4.7}$$

In figure 4.3, we see that on large enough ($\geq 30\,h^{-1}\mathrm{Mpc}$) pair separation in both los and transverse scale, the velocity distributions are the same. This could be interpreted as the effect of RSD on pairwise velocity in redshift space as large on small scale pair separations and while being minuscule on quasi-linear scales and above.

4.2.1 Pairwise moments

One of the ways to quantify the distribution is by measuring its moments. As mentioned before, evidence for the kSZ effect is from measuring the first moment, i.e the mean. Figure 4.4 shows the 1D moments of the los pairwise velocity distribution. We show the first moment which is the 1D mean pairwise velocity (which is the quantity which is measured in pairwise kSZ). Here we compare with real space moments also. The mean pairwise velocity on redshift space undergoes sign inversion $\sim 25\,h^{-1}\mathrm{Mpc}$. This sign inversion of mean velocity in redshift space was first shown in Okumura et al., 2014. It is clear that for the higher moments, they are different from the real space moments for pair separations $< 40\,h^{-1}\mathrm{Mpc}$. Strikingly it can be seen that both the real space and redshift space distributions shows a leptkurtic behavior (i.e, kurtosis greater than that of a normal distribution which is 3). On very large scales, the even moments are the same. However the distribution depends on both the los and transverse pair separation. In figure 4.5, we illustrate the 2D scale dependence of the first four moments of the pairwise velocity in redshift space. On the left most panel, we

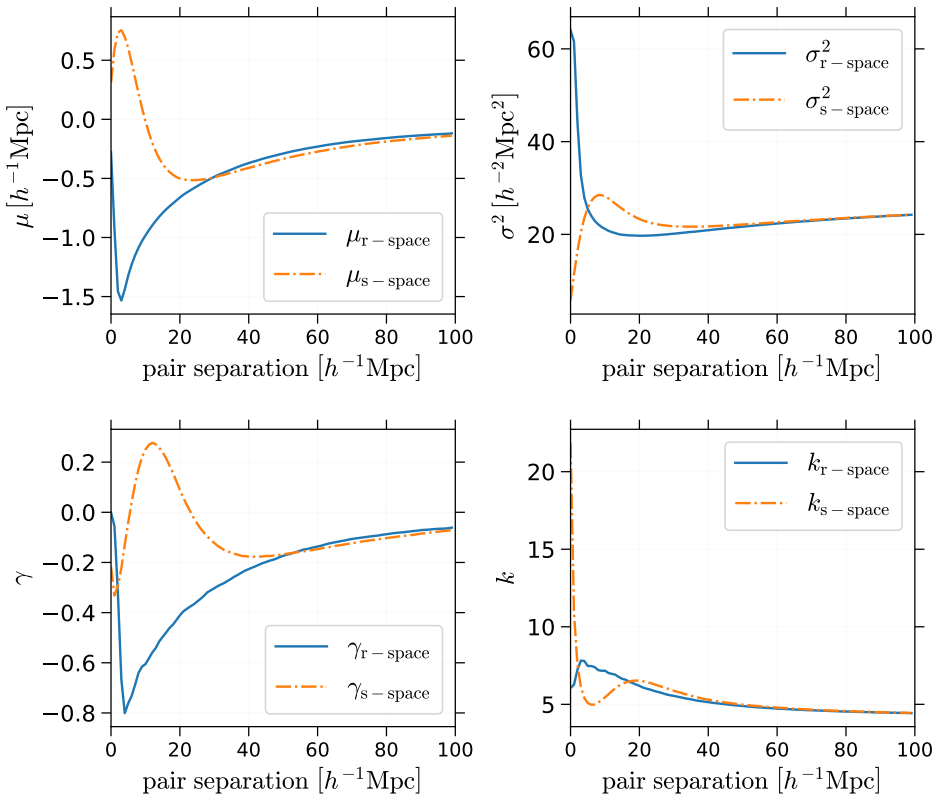

Figure 4.4: Moments of the relative line-of-sight velocity distribution in real space (solid lines) and redshift space (dash dotted lines) measured from the N-body simulation. The top row shows the mean (left) and the variance (right), while the bottom row illustrates the scale dependence of normalised higher order moments, namely the skewness (left) and the kurtosis (right).

show the mean pairwise velocity as function of parallel and perpendicular separation in redshift space. It is clear at very small scales, $s_\perp, s_\parallel \lesssim 8\,h^{-1}\mathrm{Mpc}$, the mean velocity is positive. This is not surprising considering the fact that the distribution at most of these scales show some degree of bimodality as shown in the earlier section, thus pushing the mean velocity to positive. This behaviour is different from the real space counterpart which at these scales are negative, implying on average the pairs are moving towards each other. The dispersion (second from left) shows that for very small $s_\perp \lesssim 3\,h^{-1}\mathrm{Mpc}$ as one moves from low to higher los separation the dispersion increases. On the second from right panel we see how the skewness behaves in redshift space. On account of the bimodality at small transverse separation, the distribution inherits a positive skewness at these scales. The kurtosis (right most) shows a valley feature at very small $s_\perp$ separations. This feature was also seen manifesting in the 1D kurtosis in figure 4.4. For comparison with the real space moments in 2D, we refer the reader to Kuruvilla and Porciani, 2018 which discusses about it in detail.

We consider the mean radial velocity in redshift space, $\langle w_r^{\mathrm{s}} \rangle$, and analytically predict it using linear

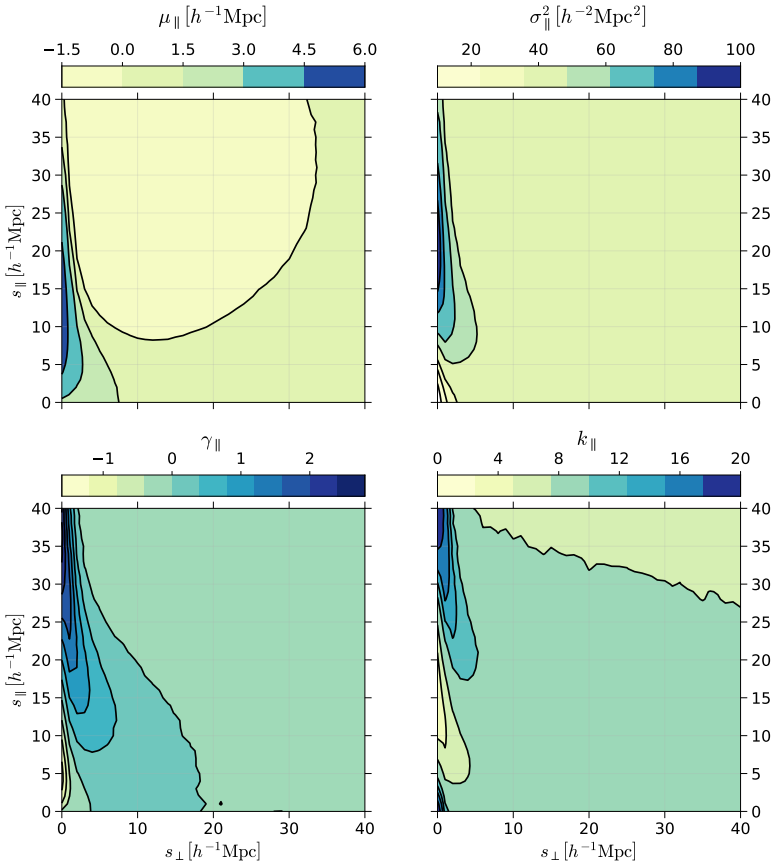

Figure 4.5: Moments of the relative line-of-sight velocity distribution in redshift space showcasing the 2D scale dependence. The mean and the dispersion are given by $\mu_\parallel$ and $\sigma^2_\parallel$ (left most and second from left panels). The higher normalised moments namely the skewness ($\gamma_\parallel$) and kurtosis ($k_\parallel$) are shown in second from the right and the right most panel respectively. The behaviour is markedly different from the real space counterparts.

theory

$$\begin{aligned}\langle w_r^{\mathrm{s}}(s)\rangle &= \frac{\langle(1+\delta_1^{\mathrm{s}})(1+\delta_2^{\mathrm{s}})(v_2-v_1)\rangle}{1+\xi_s(s)} \\ &= \frac{\displaystyle\int_0^1 \mathrm{d}\mu_\parallel\,(1+f\mu_\parallel^2)\,\langle w_r^{\mathrm{r}}(s)\rangle}{1+\dfrac{1}{2\pi^2}\displaystyle\int_0^1 \mathrm{d}\mu_\parallel \int_0^\infty \mathrm{d}k\,k^2 P(k)\,\frac{\sin(ks)}{ks}\,(1+f\mu_\parallel^2)^2} \\ &= \frac{\left(1+\dfrac{f}{3}\right)\langle w_r^{\mathrm{r}}(s)\rangle}{1+\left(1+\dfrac{2}{3}f+\dfrac{1}{5}f^2\right)\xi_{\mathrm{r}}(s)}\,,\end{aligned} \tag{4.8}$$

where δ^{s} is the density perturbation in redshift space, $\langle w_r^{\mathrm{r}}\rangle$ is the linear mean radial velocity in real

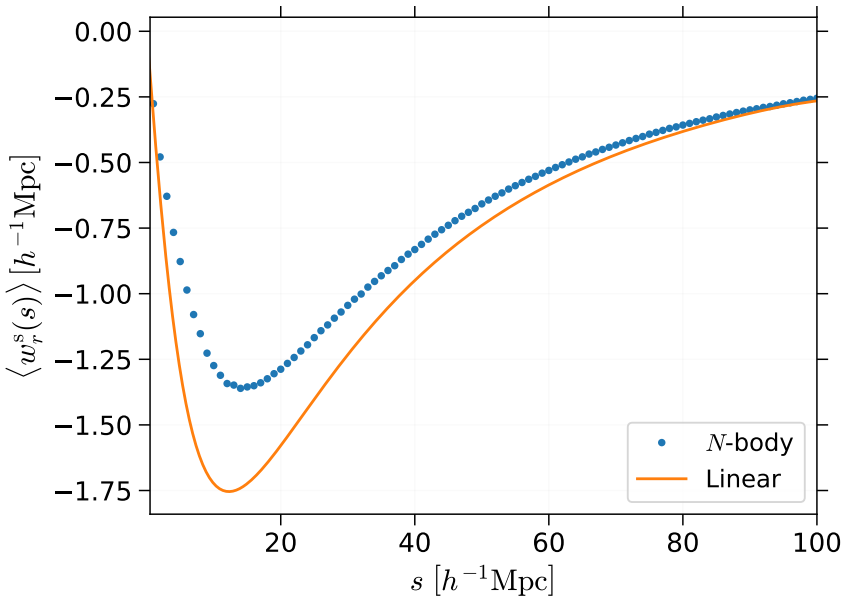

Figure 4.6: The mean radial pairwise velocity in redshift space measured from the DM simulation (blue dots). The analytical prediction from linear theory is shown in solid (orange) line.

space and $\mu_{\parallel} = k_{\parallel}/k$. In figure 4.6, we show the radial mean pairwise velocity measured from the simulation by solid (blue) points. The fidelity of linear theory prediction, equation (4.8), seems to hold only at $s \gtrsim 80\ h^{-1}$ Mpc. This could partially stem from the fact that the linear theory prediction for redshift space correlation function does not model the monopole accurately.

4.2.2 Redshift evolution

With the future planned surveys like the Simons Observatory (*SO*, P. Ade et al., 2019), *CMB-S4* type survey (Abazajian et al., 2016), and the proposed *CMB-HD* (Sehgal, Aiola et al., 2019; Sehgal, Nguyen et al., 2019), there will be precise measurements of kSZ effect over a range of redshift. This motivates us to take a look into how the velocity distribution evolves with redshift. It is shown in figure 4.7. It is clear as the redshift increases, the effect of RSD on the distribution decreases. At $z = 3$ given by dashed lines in the figure, the level of bimodality is very minimal compared to the lower redshift case. It should also be noted that the dispersion increases as function of the redshift, with minimal dispersion seen at $z = 3$ while the maximum dispersion at $z = 0$. Unsurprisingly even at different redshifts, it is clearly visible that the effect of RSD on the pairwise velocity is maximal for pairs which have minimal perpendicular separation between them.

4.3 Triple-wise velocity distribution in redshift space

In Chapter 3 we introduced the los triple-wise velocity distribution in real space and characterised several statistical properties of it. The underlying distribution which we can probe is however the one in redshift space. Thus we need to understand how RSD affects the three-point velocity statistics. The

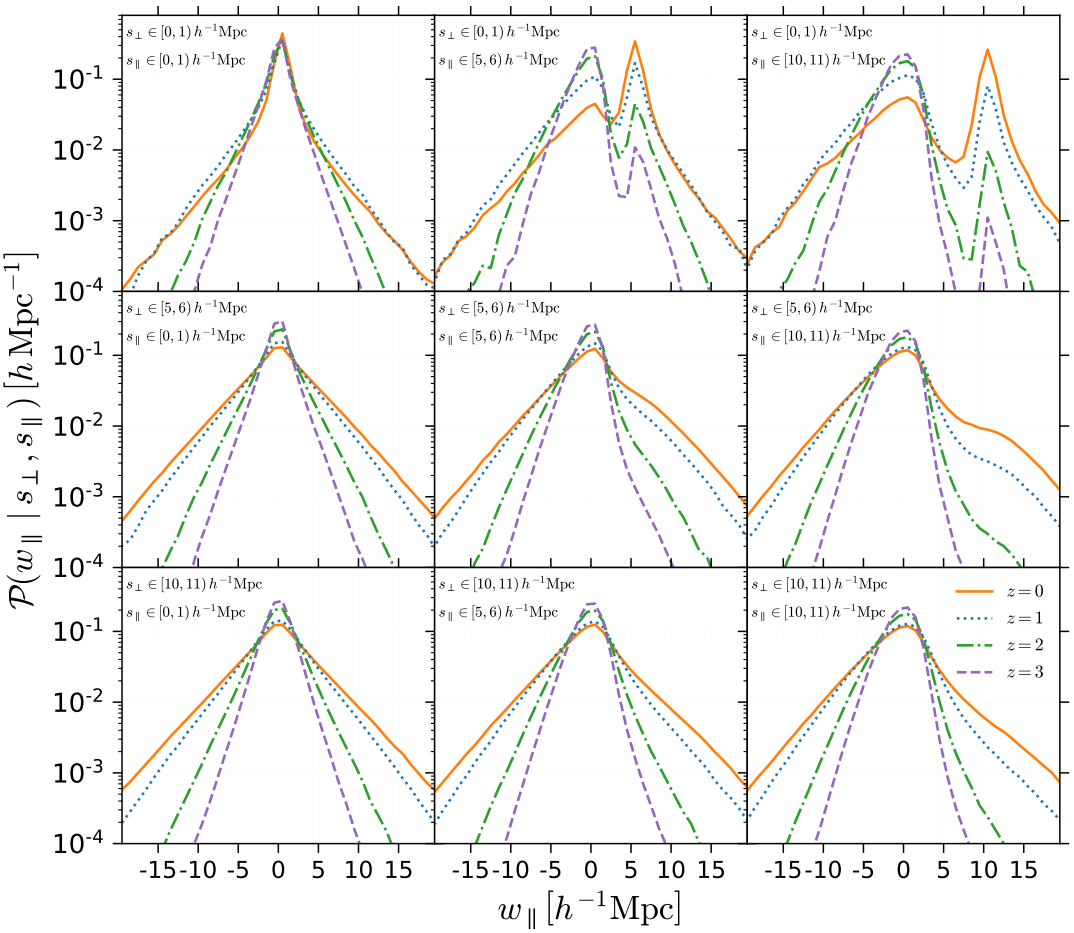

Figure 4.7: Line-of-sight pairwise velocity distribution in redshift space for different redshifts. The bimodality features (resulting from RSD) are prominent for lower redshifts.

corresponding los triple-wise PDF in redshift space $\mathcal{T}^{\mathrm{s}}(w_{12\parallel}, w_{23\parallel})$ can be written as

$$\mathcal{T}^{\mathrm{s}}(w_{12\parallel}, w_{23\parallel} \mid \boldsymbol{s}_{12}, \boldsymbol{s}_{23}, s_{31\perp}) = \int_{-\infty}^{+\infty} \mathcal{T}^{\mathrm{r}}(w_{12\parallel}, w_{23\parallel} \mid s_{12\perp}, r_{12\parallel}, s_{23\perp}, r_{23\parallel}, s_{31\perp}) \\ \mathcal{P}(r_{12\parallel}, r_{23\parallel} \mid s_{12\perp}, s_{12\parallel}, s_{23\perp}, s_{23\parallel}, s_{31\perp})\, \mathrm{d}r_{12\parallel}\, \mathrm{d}r_{23\parallel}\,, \tag{4.9}$$

where the superscript r and s denote the real- and redshift-space quantities respectively, $\mathcal{T}^{\mathrm{r}}(w_{12\parallel}, w_{23\parallel})$ is the los triple-wise velocity distribution in real space and $\mathcal{P}(r_{12\parallel}, r_{23\parallel} \mid s_{12\perp}, s_{12\parallel}, s_{23\perp}, s_{23\parallel}, s_{31\perp})$ is the three-point RSD transformation distribution function which details the effect of RSD on the triplet separation. In other words, it is the distribution of (unobserved) triplet separations in real space conditional on the observed triangular configuration in redshift space. Figure 4.8 shows this PDF for four such triplet configuration in redshift space which was directly measured from the simulation. To speed up the calculation, we randomly sample 100^3 DM particles and consider all the ordered

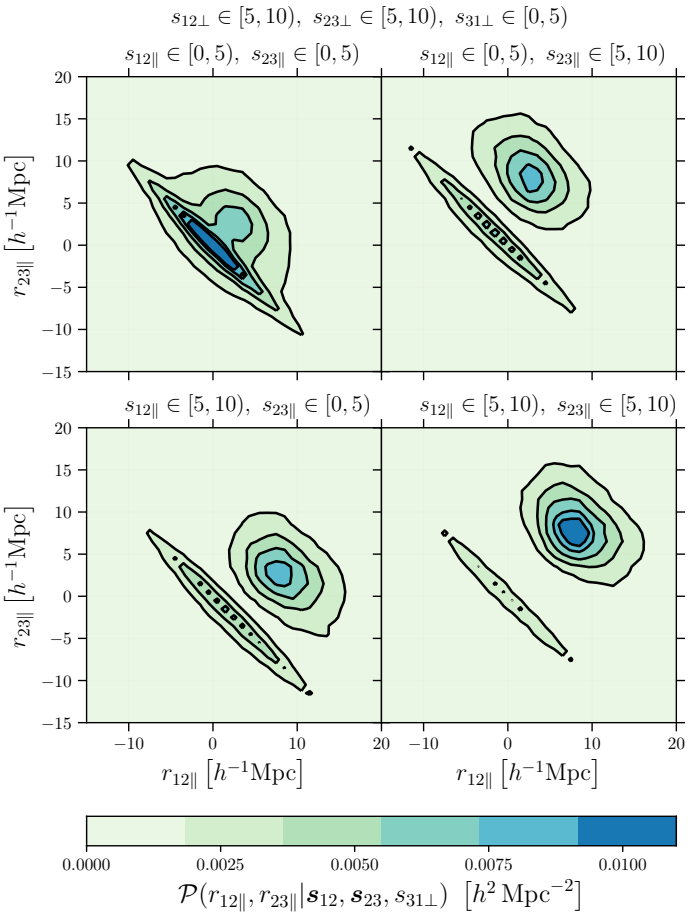

Figure 4.8: The RSD transformation distribution function in the case of three-point velocity statistics. We consider four triplet configuration, where we have kept the perpendicular separation in redshift-space fixed as mentioned on the very top of the figure. We let the parallel separation of 12 and 23 vary in each panel.

triplets between them. Each triplet is classified in 5 h^{-1} Mpc bin based on the values in five redshift space separation components of the triangular configuration. Ultimately, we build a two-dimensional histogram for $r_{12\parallel}$ and $r_{23\parallel}$ for each separation bin. One of the main features we see is the bimodal nature of this distribution function at these small scales. We chose these small triplet separations, with fixed perpendicular components ($s_{12\perp} \in [5,10), s_{23\perp} \in [5,10)$ and $s_{31\perp} \in [0,5)$ in units of h^{-1} Mpc), to highlight the effect of RSD. The different panels show the configuration where $s_{12\parallel}$ and $s_{23\parallel}$ are varied. In these panels, the bimodal peaks can be seen at $r_{12\parallel} = r_{23\parallel} \approx 0\,h^{-1}$ Mpc and $r_{12\parallel} \approx s_{12\parallel}$ and $r_{23\parallel} \approx s_{23\parallel}$. The peak around $0\,h^{-1}$ Mpc is the byproduct of the FoG effect, where $r_{12\parallel}, r_{23\parallel} \in \mathbb{R}_{<0}$ implies that they have flipped their position with respect to that in redshift space. In the top right panel, the contour lines around the peak at zero is skewed towards lower $r_{12\parallel}$. This can be understood from the fact that $s_{12\parallel} < s_{23\parallel}$ in that triangular configuration and it is more probable for the 12 component to have flipped their position in redshift space compared to that of the 23 pair. This behaviour is reversed in lower left panel where $s_{23\parallel} < s_{12\parallel}$, where the contour lines around zero is skewed towards lower $r_{23\parallel}$. The contour lines around the peak at $r_{12\parallel} \approx s_{12\parallel}$ and $r_{23\parallel} \approx s_{23\parallel}$

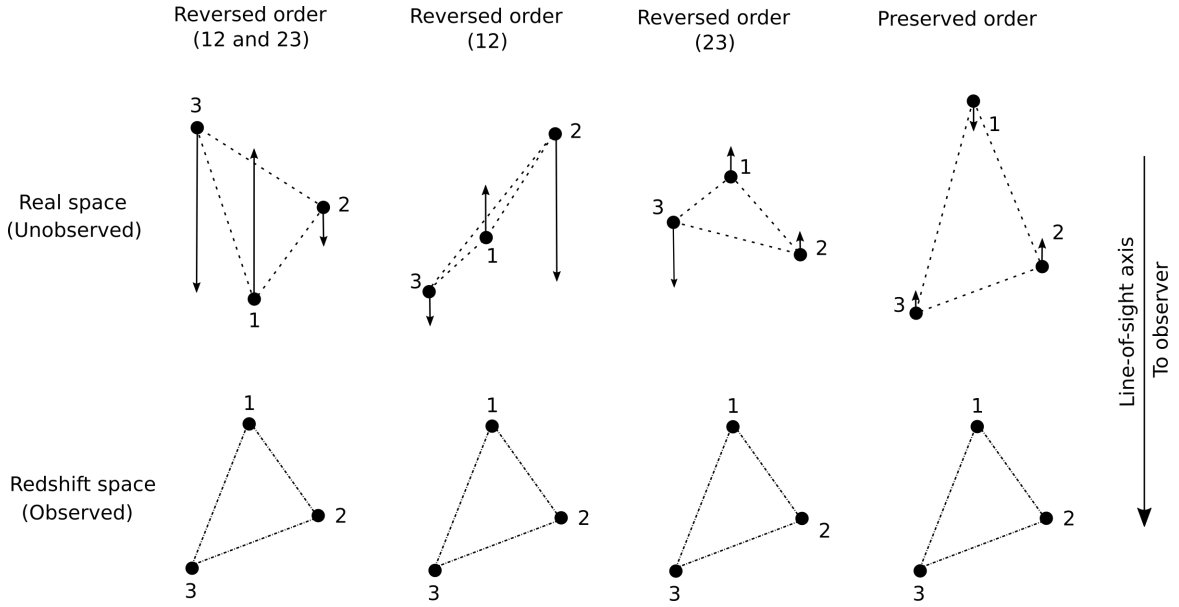

Figure 4.9: Schematic diagram illustrating how the relative infall velocities can change the triangular configuration of a triplet between real and redshift space. The vertical arrows represent the los component of the individual velocities. First three columns indicate the scenarios in which atleast one side of triangular configuration has reversed their order and the last column shows the scenario in which the triangular shape is preserved in going from real to redshift space.

corresponds to triplets having triplewise velocities close to zero, implying that these might be part of the large-scale coherent flow and can be seen as the linear effect of RSD on the triple-wise velocity. On the smallest triplet separation considered (top left panel), these effects are mixed together in such a way that it is difficult to isolate. However as the separations increase, this mixing and the effect from FoG (peak around 0) decreases. It is visually evident that the global maxima of the RSD distribution PDF, which corresponds to one of the mode, changes for each panel. In the top left panel the global maxima is at $r_{12\parallel} \in [-1, 0)\ h^{-1}$ Mpc and $r_{23\parallel} \in [0, 1)\ h^{-1}$ Mpc. On the top right, the global maxima are located at $r_{12\parallel} \in [3, 4)\ h^{-1}$ Mpc and $r_{23\parallel} \in [7, 8)\ h^{-1}$ Mpc. Similarly the modes are located close to the mean value of the redshift separation bin in the bottom left and right panel.

We show an illustration of the complex shape transformation a triplet can undergo going from real to redshift space in figure 4.9. The vertical arrows represent the los component of the individual velocities. We keep the triangular configuration fixed in the observed reference frame (redshift space) with $s_{12\parallel} > 0$ and $s_{23\parallel} > 0$. The first column from left corresponds to the case where both sides have reversed (flipped) their order in real space. The second and third column indicates the mapping where only one side has reversed their order. In these two scenario to get the triplet configuration in redshift space, it appears that in real space the triplets were in a configuration where one side is much larger than the other two sides. On larger separations, the fraction of triplets undergoing these transformations, as indicated in first three columns, would be low as they would require large triple-wise velocities. The fourth column indicates the situation in which shape is preserved in going from real to redshift space. At large separations, this would be the most probable transformation as indicated in figure 4.8 also.

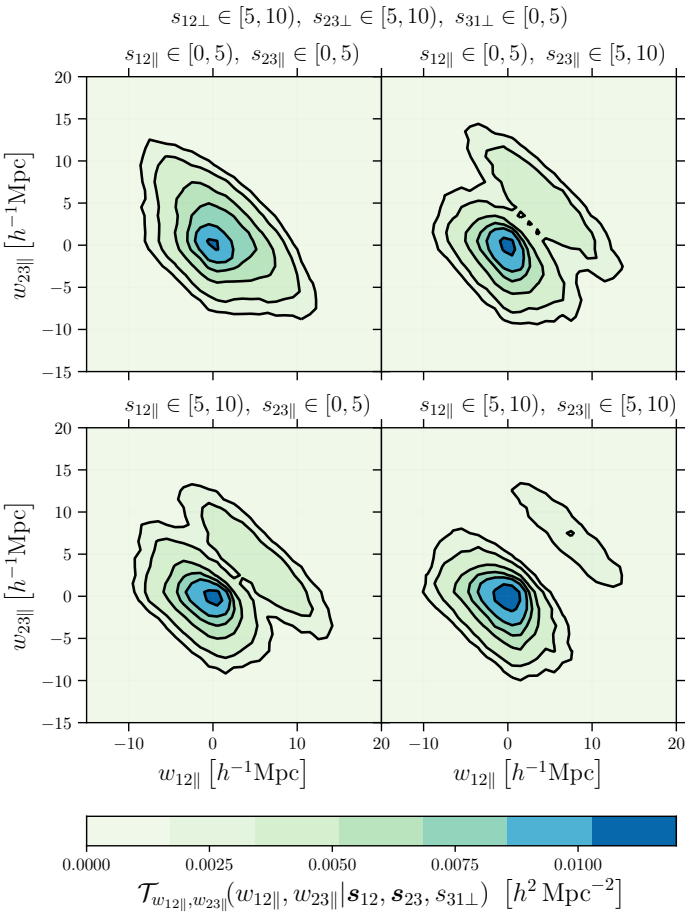

Figure 4.10: The matter triple-wise velocity distribution in redshift space. The perpendicular components are fixed for all the four panels. The peak around $s_{12\parallel} \approx w_{12\parallel}$ and $s_{23\parallel} \approx w_{23\parallel}$ denote the triplets which are affected by FoG.

Understanding how the triangular configurations can transform going from real to redshift space we can grasp the triple-wise PDF in redshift space which we show in figure 4.10. The configurations are shown to be same as in figure 4.8. We measure this bivariate PDF directly from the simulations, using velocity of the dark matter particles. The procedure is similar as for the RSD transformation PDF, where triplets are first binned in the five separation scales in redshift with a bin width of 5 h^{-1} Mpc and then we build a two-dimensional histogram of $w_{12\parallel}$ and $w_{23\parallel}$, with bin-width of 1 h^{-1} Mpc, for each separation bin. An important feature that can be seen is the bimodality of the PDF, barring for the configuration when $s_{12\parallel}, s_{23\parallel} \in [0,5)\,h^{-1}$ Mpc. The peak around $s_{12\parallel} \approx w_{12\parallel}$ and $s_{23\parallel} \approx w_{23\parallel}$ denotes the triplets which are affected by FoG and which might have flipped their positions in comparison to the real space configuration. As in the case of three-point RSD transformation PDF, the effect of FoG fades away as the triplet los separation increases and thus the amplitude of the second peak (around $s_{12\parallel} \approx w_{12\parallel}$ and $s_{23\parallel} \approx w_{23\parallel}$) decreases. This is expected as the non-linear RSD effects are most dominant at the small scale separations. We find that the global maxima is located between [-1,1) h^{-1} Mpc for both $w_{12\parallel}$ and $w_{23\parallel}$ in all the four panels. These PDFs are symmetric

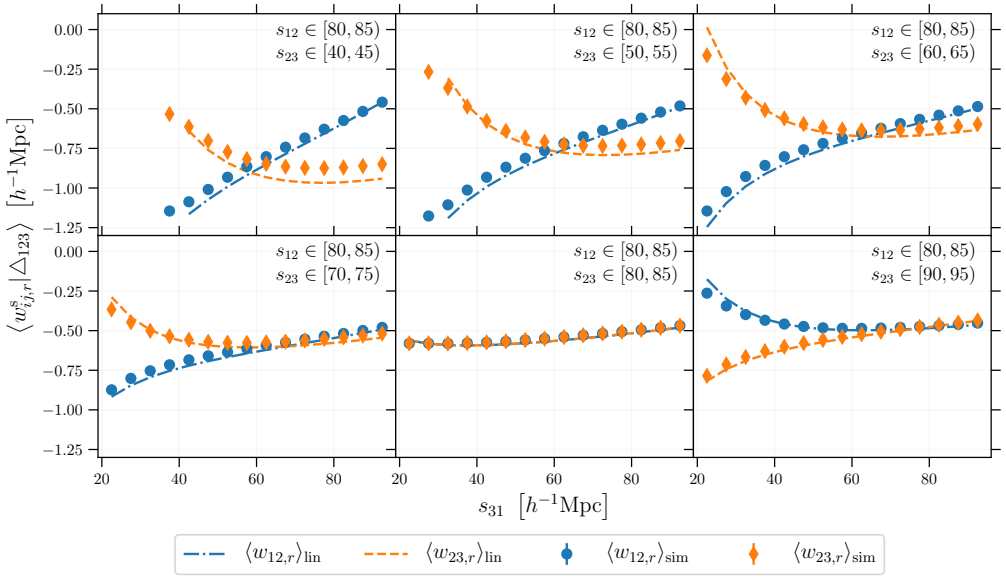

Figure 4.11: The mean three-point radial velocities in redshift space for different triangular configurations. For side 12, the measured mean velocity is shown using the circle (blue) points and the linear theory prediction is shown using the dot-dashed (blue) lines. In the case of side 23, the measured is denoted using diamonds (oranges), while the linear theory prediction using dashed (oranges) lines. The separations are given in units of h^{-1}Mpc.

under particle exchange or parity transformations,

$$\mathcal{T}^{\rm r}(w_{12\parallel}, w_{23\parallel} \mid \boldsymbol{s}_{12}, \boldsymbol{s}_{23}, s_{31\perp}) = \mathcal{T}^{\rm r}(-w_{12\parallel}, -w_{23\parallel} \mid -\boldsymbol{s}_{12}, -\boldsymbol{s}_{23}, s_{31\perp})\,, \tag{4.10}$$

$$\mathcal{P}(r_{12\parallel}, r_{23\parallel} \mid \boldsymbol{s}_{12}, \boldsymbol{s}_{23}, s_{31\perp}) = \mathcal{P}(-r_{12\parallel}, -r_{23\parallel} \mid -\boldsymbol{s}_{12}, -\boldsymbol{s}_{23}, s_{31\perp})\,, \tag{4.11}$$

$$\mathcal{T}^{\rm s}(w_{12\parallel}, w_{23\parallel} \mid \boldsymbol{s}_{12}, \boldsymbol{s}_{23}, s_{31\perp}) = \mathcal{T}^{\rm s}(-w_{12\parallel}, -w_{23\parallel} \mid -\boldsymbol{s}_{12}, -\boldsymbol{s}_{23}, s_{31\perp})\,. \tag{4.12}$$

4.3.1 Triple-wise moments

In this section, we try to predict the three-point velocity statistics using linear perturbation theory. We have already introduced the analytical prediction of real space mean triple-wise velocity in equations (3.55) and (3.57). We can define the linear theory prediction for redshift space mean velocities (denoted by superscript s),

$$\begin{aligned}\langle \boldsymbol{w}^{\rm s}_{12}(s_{12}|\triangle_{123})\rangle = \langle w^{\rm s}_{12}(s_{12}|\triangle_{123})\rangle \hat{\boldsymbol{s}}_{12} = & \quad \frac{\langle (1+\delta^{\rm s}_1)(1+\delta^{\rm s}_2)(1+\delta^{\rm s}_3)(\boldsymbol{v}_2 - \boldsymbol{v}_1)\rangle}{\langle (1+\delta^{\rm s}_1)(1+\delta^{\rm s}_2)(1+\delta^{\rm s}_3)\rangle} \\ \overset{\rm lin}{=} & \quad \frac{\langle \delta^{\rm s}_1 \boldsymbol{v}_2\rangle - \langle \delta^{\rm s}_2 \boldsymbol{v}_1\rangle + \langle \delta^{\rm s}_3 \boldsymbol{v}_2\rangle - \langle \delta^{\rm s}_3 \boldsymbol{v}_1\rangle}{1 + \xi_{\rm s}(s_{12}) + \xi_{\rm s}(s_{23}) + \xi_{\rm s}(s_{31})}\,.\end{aligned} \tag{4.13}$$

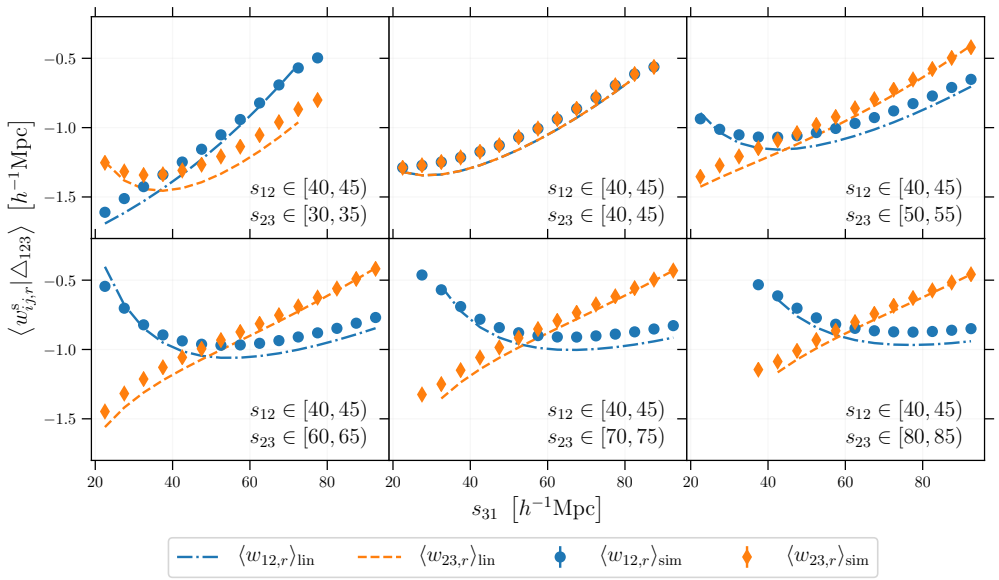

Figure 4.12: Same as figure 4.11 but for different and smaller triangular configurations in redshift space. For side 12, the measured mean velocity is shown using the (blue) circle points. In the case of side 23, the measurement from simulation is denoted using (orange) diamonds.

where $\triangle_{123}$ denotes the triangle with sides of length s_{12}, s_{23} and s_{31} in redshift space. The numerator in equation (4.13) can be written as

$$\langle \delta^{\mathrm{s}}_1 \boldsymbol{v}_2 \rangle - \langle \delta^{\mathrm{s}}_2 \boldsymbol{v}_1 \rangle + \langle \delta^{\mathrm{s}}_3 \boldsymbol{v}_2 \rangle - \langle \delta^{\mathrm{s}}_3 \boldsymbol{v}_1 \rangle = -\frac{aHf(f+3)}{3\pi^2} \Bigg[\hat{\boldsymbol{s}}_{12} \int_0^\infty \mathrm{d}k \, kP_{\mathrm{m}}(k) j_1(ks_{12}) + \frac{1}{2} \Bigg(\hat{\boldsymbol{s}}_{23} \int_0^\infty \mathrm{d}k \, kP_{\mathrm{m}}(k) j_1(ks_{23}) + \hat{\boldsymbol{s}}_{31} \int_0^\infty \mathrm{d}k \, kP_{\mathrm{m}}(k) j_1(ks_{31}) \Bigg) \Bigg] . \tag{4.14}$$

Projecting $\hat{\boldsymbol{s}}_{23}$ and $\hat{\boldsymbol{s}}_{31}$ along $\hat{\boldsymbol{s}}_{12}$, we get

$$\langle \delta^{\mathrm{s}}_1 \boldsymbol{v}_2 \rangle - \langle \delta^{\mathrm{s}}_2 \boldsymbol{v}_1 \rangle + \langle \delta^{\mathrm{s}}_3 \boldsymbol{v}_2 \rangle - \langle \delta^{\mathrm{s}}_3 \boldsymbol{v}_1 \rangle = -\frac{aHf(f+3)}{3\pi^2} \hat{\boldsymbol{s}}_{12} \Bigg[\int_0^\infty \mathrm{d}k \, kP_{\mathrm{m}}(k) j_1(ks_{12}) - \frac{1}{2} \Bigg(\cos\beta \int_0^\infty \mathrm{d}k \, kP_{\mathrm{m}}(k) j_1(ks_{23}) + \cos\alpha \int_0^\infty \mathrm{d}k \, kP_{\mathrm{m}}(k) j_1(ks_{31}) \Bigg) \Bigg] , \tag{4.15}$$

where β is the angle between the sides 12 and 23, where α is the angle between the sides 12 and 31. The angles α and β can be computed using the law of cosines. The linear mean radial triple-wise

velocity can then be written by substituting equation (4.15) into equation (4.13) as

$$\langle w_{12}^{\mathrm{s}}(s_{12}|\triangle_{123})\rangle \hat{\boldsymbol{s}}_{12} \overset{\mathrm{lin}}{=} \frac{-\frac{aHf(f+3)}{3\pi^2}\hat{\boldsymbol{s}}_{12}\left[\int_0^\infty \mathrm{d}k\, kP_{\mathrm{m}}(k)j_1(ks_{12}) + \frac{1}{2}\left(\cos\beta\int_0^\infty \mathrm{d}k\, kP_{\mathrm{m}}(k)j_1(ks_{23}) + \cos\alpha\int_0^\infty \mathrm{d}k\, kP_{\mathrm{m}}(k)j_1(ks_{31})\right)\right]}{1+\xi_{\mathrm{s}}(s_{12})+\xi_{\mathrm{s}}(s_{23})+\xi_{\mathrm{s}}(s_{31})} \tag{4.16}$$

Similarly the linear mean radial velocity of the second component is

$$\begin{aligned}\langle \boldsymbol{w}_{23}^{\mathrm{s}}(s_{23}|\triangle_{123})\rangle =& \frac{\langle(1+\delta_1^{\mathrm{s}})(1+\delta_2^{\mathrm{s}})(1+\delta_3^{\mathrm{s}})(\boldsymbol{v}_3-\boldsymbol{v}_2)\rangle}{\langle(1+\delta_1^{\mathrm{s}})(1+\delta_2^{\mathrm{s}})(1+\delta_3^{\mathrm{s}})\rangle} \\ & -\frac{aHf(f+3)}{3\pi^2}\hat{\boldsymbol{s}}_{23}\left[\int_0^\infty \mathrm{d}k\, kP_{\mathrm{m}}(k)j_1(ks_{23}) + \right. \\ & \left. \overset{\mathrm{lin}}{=} \frac{\frac{1}{2}\left(\cos\beta\int_0^\infty \mathrm{d}k\, kP_{\mathrm{m}}(k)j_1(ks_{12}) + \cos\gamma\int_0^\infty \mathrm{d}k\, kP_{\mathrm{m}}(k)j_1(ks_{31})\right)\right]}{1+\xi_{\mathrm{s}}(s_{12})+\xi_{\mathrm{s}}(s_{23})+\xi_{\mathrm{s}}(s_{31})}\,,\end{aligned} \tag{4.17}$$

where β is the angle between the sides 12 and 23, and γ is the angle between the sides 23 and 31. Thus from equations (4.16) and (4.17), it is evident that, similar to the case of real space triple-wise velocities, in redshift space also the mean triple-wise velocity are affected by the presence of the third point.

Figure 4.11 shows the comparison between the mean velocity measured from the simulations to that predicted from linear theory. In this figure, we fix s_{12} to have a magnitude $\in [80, 85)\, h^{-1}\mathrm{Mpc}$. In each subplot we however vary the length of side 23 and see in every subplot how the mean radial velocities varies as a function of the triangle's third leg. We can see that the predictions from linear theory fairs relatively well to that measured from the simulations at these quasi-linear scales. However the fidelity of the analytical prediction is not as good as in the case of real space prediction. When further compared to the real space counterpart in figure 3.3, the shape of the signal remains similar while the amplitude of the signal has changed. We probe even smaller separation scales in figure 4.12, where we see that at quasi-linear separations ($s \gtrsim 30\, h^{-1}\mathrm{Mpc}$) fidelity of the linear theory prediction decreases. Overall we see that mean radial velocity prediction from linear theory has an acceptable degree of accuracy when compared to the measured mean from the simulations at separations greater than $\sim 40\, h^{-1}\mathrm{Mpc}$. It was also measured and verified that the mean velocity of transverse components vanish due to statistical isotropy. It is also possible to predict the variance of triple-wise velocity in redshift space using linear theory,

$$\langle w_{12,r}^{2,\mathrm{s}}(s_{12}|\triangle_{123})\rangle \overset{\mathrm{lin}}{=} \frac{2[\sigma_v^2 - \Psi_{12,r}]}{1+\xi_{\mathrm{s}}(s_{12})+\xi_{\mathrm{s}}(s_{23})+\xi_{\mathrm{s}}(s_{31})}\,, \tag{4.18}$$

where σ_v^2 is the one-dimensional velocity dispersion and $\Psi_{12,r}$ is the radial component of the velocity correlation function for the pair 12. The only difference from its real space counterpart is the

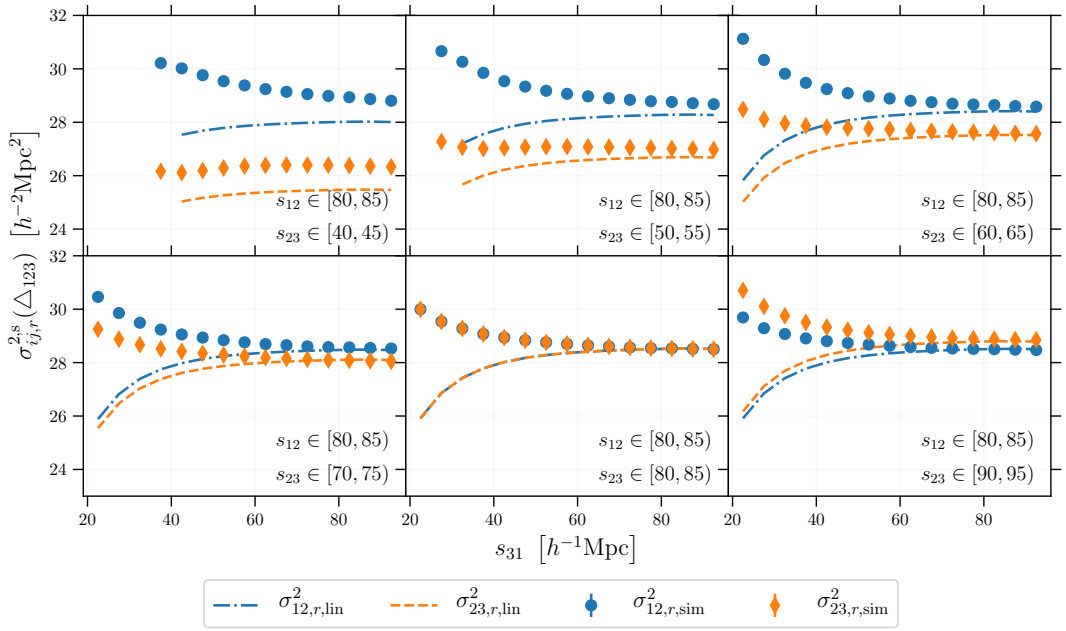

Figure 4.13: The three-point radial dispersion for different triangular configurations in redshift space, where $\sigma^2 \equiv \langle w^2 \rangle$. For side 12, the measured dispersion is shown using the circle points and the linear theory prediction is shown using the dot-dashed lines (both in blue color). In the case of side 23, the measured is denoted using diamonds, while the linear theory prediction using dashed lines (both in orange color). The separations are given in units of $h^{-1}\mathrm{Mpc}$. An offset of 9.59 $h^{-2}\mathrm{Mpc}^2$ was added to the linear theory prediction to match the measurement.

normalisation factor. Similarly the variance for the pair 23 can be written as

$$\langle w^{2,\mathrm{s}}_{23,r}(s_{23}|\triangle_{123})\rangle \overset{\mathrm{lin}}{=} \frac{2[\sigma_v^2 - \Psi_{23,r}]}{1 + \xi_{\mathrm{s}}(s_{12}) + \xi_{\mathrm{s}}(s_{23}) + \xi_{\mathrm{s}}(s_{31})}\,. \tag{4.19}$$

Figure 4.13 showcases the radial triple-wise velocity dispersion in the redshift space. On large separation scales on all three edges of the configuration, the linear theory is able to reproduce the measurement from simulations quite well. One of the caveat is that there is an offset error which needs to be accounted for. However the offset calibration is same as in the case of real space quantity. This is not surprising as the offset is introduced to account for the inaccurate modeling of the one-dimensional velocity dispersion.

4.4 Breaking optical depth degeneracy: bias-independent estimator

The cosmological growth rate measured from pairwise kSZ is perfectly degenerate with the optical depth of galaxies or clusters (Keisler and Schmidt, 2013; Sugiyama, Okumura and D. N. Spergel, 2018)

$$\langle w_{12\parallel}\rangle_{\mathrm{kSZ}} \propto b\tau f\sigma_8^2\,, \tag{4.20}$$

where $\langle w_{12\parallel}\rangle_{\rm kSZ} = (b\tau T_{\rm cmb}/c)\langle w_{12\parallel}\rangle$. The linear bias being scale and mass dependent, and treating optical depth as an effective quantity are few of the assumption going into this formulation. The degeneracy leads to an overall uncertainty in the growth rate measurement and is the limiting systematic for constraining cosmology from kSZ. In principle, it is possible to obtain external constraints on biasing term b from clustering measurements and optical depth τ from X-ray observation to obtain $f\sigma_8^2$. From a cosmological information perspective this is interesting as dynamical probes like RSD constrain $f\sigma_8$ which could be leveraged to break the degeneracy between f and σ_8.

Madhavacheril et al., 2019 proposes a mechanism to break the optical-depth degeneracy by using 'fast radio bursts sources' (FRBs) to measure the optical depth directly by cross correlating the dispersion measures from FRBs with the galaxy sample used in kSZ measurement. FRBs are radio transient events that are (possibly) generated from some high energy astrophysical process. The exact nature of its origin is still not yet understood. Dispersion measure gives the integrated electron column density of free electrons between the observer and FRB.

In this section, we introduce an estimator to break this degeneracy and to be independent of biasing factor by using velocity information only. The basic idea is to take the ratio of velocity components of the mean triple-wise velocity and the new estimator is independent of b, τ, f and σ_8. There have been similar ratio tests in galaxy clustering analysis already wherein the growth rate was measured using the ratio of multipoles of correlation function (and also of power spectrum) (Hamilton, 1998). For simplicity we ignore the RSD effects on the triple-wise velocity in this section. The bias independent estimator (in real space) $\mathcal{E}_{\rm kSZ}$ can be written as

$$\mathcal{E}_{{\rm kSZ},i}(\triangle_{123}) = \frac{\langle w_{12,i}|\triangle_{123}\rangle_{\rm kSZ}}{\langle w_{23,i}|\triangle_{123}\rangle_{\rm kSZ}}\,, \tag{4.21}$$

where i could stand for the radial or the line-of-sight component. We can write down the estimator explicitly for the radial component as

$$\mathcal{E}_{{\rm kSZ},r}(\triangle_{123}) = \frac{\langle w_{12,r}|\triangle_{123}\rangle_{\rm kSZ}}{\langle w_{23,r}|\triangle_{123}\rangle_{\rm kSZ}} = \frac{-aHf\tau b\,\mathcal{I}_{12}(\triangle_{123})}{-aHf\tau b\,\mathcal{I}_{23}(\triangle_{123})} = \frac{\mathcal{I}_{12}(\triangle_{123})}{\mathcal{I}_{23}(\triangle_{123})}\,, \tag{4.22}$$

where

$$\begin{aligned}\mathcal{I}_{12}(\triangle_{123}) \;&=\; \int_0^\infty {\rm d}k\, kP_{\rm m}(k) j_1(kr_{12}) - 0.5\left[\cos\beta\int_0^\infty {\rm d}k\, kP_{\rm m}(k) j_1(kr_{23})\right.\\ &\qquad\left. + \cos\alpha\int_0^\infty {\rm d}k\, kP_{\rm m}(k) j_1(kr_{31})\right]\,,\end{aligned} \tag{4.23}$$

and

$$\begin{aligned}\mathcal{I}_{23}(\triangle_{123}) \;&=\; \int_0^\infty {\rm d}k\, kP_{\rm m}(k) j_1(kr_{23}) - 0.5\left[\cos\beta\int_0^\infty {\rm d}k\, kP_{\rm m}(k) j_1(kr_{12})\right.\\ &\qquad\left. + \cos\gamma\int_0^\infty {\rm d}k\, kP_{\rm m}(k) j_1(kr_{31})\right]\,.\end{aligned} \tag{4.24}$$

The estimator depends on the integral of the matter power spectrum. We have also verified from numerical simulations that the estimator is independent of bias and optical depth. For this we measured

the necessary velocity statistics for DM particles as outlined in chapter 3. To generate mock kSZ triple-wise velocity statistics, we first generated a DM halo catalogue using ROCKSTAR (Behroozi, Wechsler and Wu, 2013). We used the empirical optical depth - halo mass scaling relation obtained from Battaglia, 2016, to associate the optical depth to each DM halo, which is given as

$$\ln(\tau|M) = \ln\tau_0 + m\ \ln(M/M_0)\,, \tag{4.25}$$

where m is the power law slope, τ_0 is the intercept for the given normalization of $M_0 = 10^{14}\ M_\odot$. Battaglia, 2016 used different hydrodynamical simulations with various input cluster astrophysics and showed how the scaling relation depended on each of these input criteria. We make use of their 'AGN feedback' model (which is a model with radioactive cooling, star formation, galactic winds, supernova feedback, cosmic ray physics and AGN feedback) for the scaling relation and used the values: $\tau_0 = -6.83$ and $m = 0.60$, taken from Table 1 in Battaglia, 2016. In our analysis, we only used halos with mass, $M_{500} > 2 \cdot 10^{14}\ M_\odot$. M_{500} was taken as the halo mass proxy to be consistent with Battaglia, 2016. It should be stressed that halo masses are not a direct observable quantity in any observation, however in numerical simulations we can access it directly. We have verified (using quantities measured from simulations) that the ratio between $\mathcal{E}_{\mathrm{DM},r}$[1] and $\mathcal{E}_{\mathrm{kSZ},r}$ is equal to one, thus confirming numerically also that the new estimator is bias and optical depth independent. Being a three-point velocity statistics, the estimator has an added advantage that it is utilising the underlying (triangular configuration) shape information which is not present in the pairwise quantities.

We want to explore how the estimator in equation (4.22) is affected by the cosmological parameters. For this purpose, we make use of the analytical prediction of the mean triple-wise velocities from linear perturbation which was introduced in chapter (3). In figure 4.14, we check the estimator for three varying cosmologies, which are given in table (1.1). The solid (blue), dashed (orange) and dot-dashed (green) line corresponds to Planck, five year result from WMAP and three year result from WMAP respectively. In each panel we fix r_{12} and r_{23}, and let the side r_{31} vary. We chose to plot the triangular configurations in which the estimator has significant difference at large separation scales where linear theory modeling works well. Among the three cosmologies considered here, the amplitude of $\mathcal{E}_{\mathrm{kSZ},r}$ is maximum in the case of Planck. We believe that the estimator is affected the most by the matter density and it is highest in the case of Planck cosmology when compared to WMAP-3 and WMAP-5 cosmology.

In figure 4.15, we want to test this hypothesis and explore the effect of matter density on the estimator $\mathcal{E}_{\mathrm{kSZ},r}$ by varying Ω_{m} in a flat Universe and keeping all the other cosmological parameters fixed (where we have used the Planck cosmology as the reference). The solid (blue) line corresponds to the matter density of the reference cosmology. We increase and decrease the matter density value by 0.05 and see its effect given by dot-dashed (green) and dashed (orange) lines respectively. It is evident that for the configurations considered here, amplitude of the estimator increases along with the matter density. It is encouraging that the difference is maximum (for these configurations) at the largest r_{31} separation where analytical modeling is well captured by linear theory.

We are at an epoch in cosmology where there is a discrepancy in the Hubble constant H_0 measured from the early- (Planck Collaboration, Akrami et al., 2018; Planck Collaboration, Aghanim et al., 2018; Abbott et al., 2018) and late-time Universe (Riess, L. M. Macri et al., 2016; Riess, Casertano, Yuan, L. Macri et al., 2018; Riess, Casertano, Yuan, L. M. Macri et al., 2019; K. C. Wong et al.,

[1] $\mathcal{E}_{\mathrm{DM},r}(\triangle_{123}) = \dfrac{\langle w_{12,r}|\triangle_{123}\rangle_{\mathrm{DM}}}{\langle w_{23,r}|\triangle_{123}\rangle_{\mathrm{DM}}} = \dfrac{-aHf\mathcal{I}_{12}(\triangle_{123})}{-aHf\mathcal{I}_{23}(\triangle_{123})} = \dfrac{\mathcal{I}_{12}(\triangle_{123})}{\mathcal{I}_{23}(\triangle_{123})}$

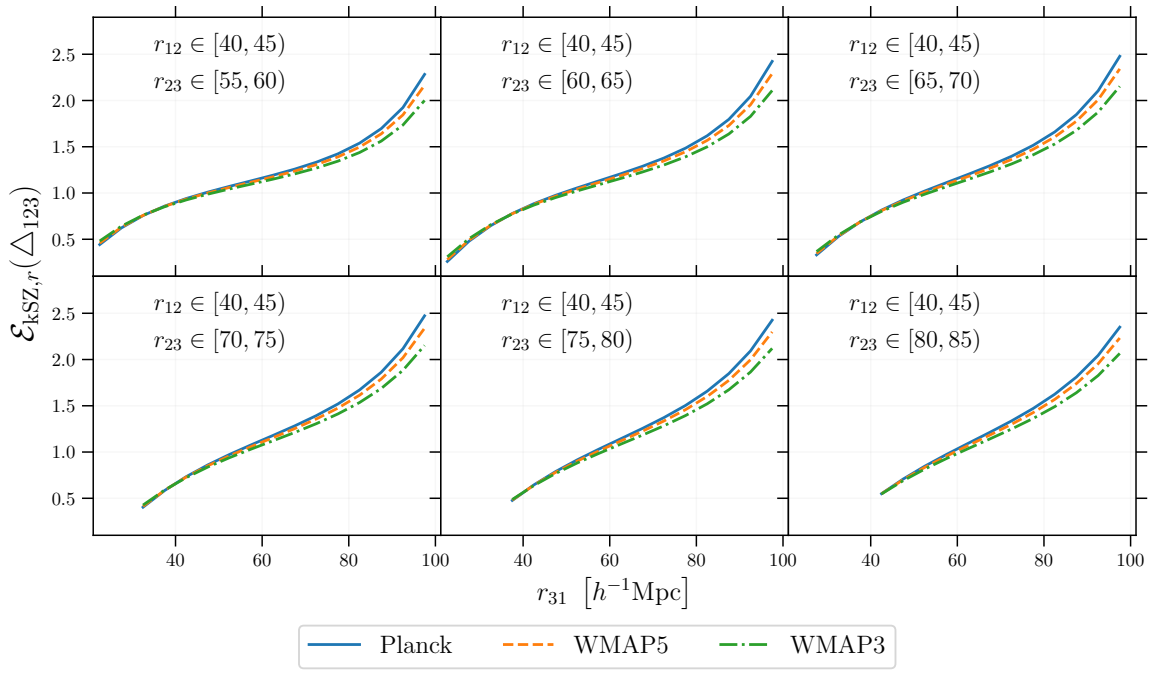

Figure 4.14: Impact of varying cosmology on the estimator $\mathcal{E}_{\mathrm{kSZ},r}$. *Planck* is used as the reference cosmology and is shown by solid (blue) line. The three-year and five-year results from *WMAP* is denoted by dot-dashed (green) and dashed (orange) lines respectively. The length of the side 12 is fixed while allowing separation of side 23 to vary in each panel.

2019). Currently three independent approaches in measuring H_0 from the late-time Universe have a tension of 4.0σ to 5.8σ with that measured from the early Universe (see Verde, Treu and Riess, 2019 for an overview of the current status on the tension). One of the ways to explain the tension could be that an unknown systematic error is affecting the measurement. Another explanation would be to introduce new physics and go beyond our six parameter ΛCDM model, which would result in a major paradigm shift in cosmology. We would like to know if the estimator $\mathcal{E}_{\mathrm{kSZ},r}$ could help in alleviating the tensions and provide an independent probe of measuring the Hubble parameter from the velocity field. We check the sensitivity of $\mathcal{E}_{\mathrm{kSZ},r}$ to H_0 in figure 4.16. However its visually evident that the dependence seems weak. The higher H_0 seems to prefer lower amplitude of $\mathcal{E}_{\mathrm{kSZ},r}$ at the large r_{31} separation in those configurations.

The structure formation in the Universe is affected by the presence of massive neutrinos, leaving imprint on cosmological observables such as galaxy clustering signal, weak lensing, etc (e.g. Lesgourgues and Pastor, 2006; Y. Y. Y. Wong, 2011; Roncarelli, Carbone and Moscardini, 2015; Zennaro et al., 2018). Neutrinos having sub-eV mass behave as a hot component of the DM. They free stream out of high dense regions into low dense regions. This results in the damping of small-scale density perturbations, which in turn suppresses the power spectrum on small scales. Neutrino oscillation experiments have shown that neutrinos have a non-zero mass (Fukuda et al., 1998; Ahn et al., 2006; Ahmad et al., 2001). Cosmological probes are sensitive primarily to the sum of three neutrino masses. Assuming a six-parameter flat ΛCDM cosmology plus the neutrino mass sum as a free parameter, measurement from Planck in combination with lensing and baryon acoustic

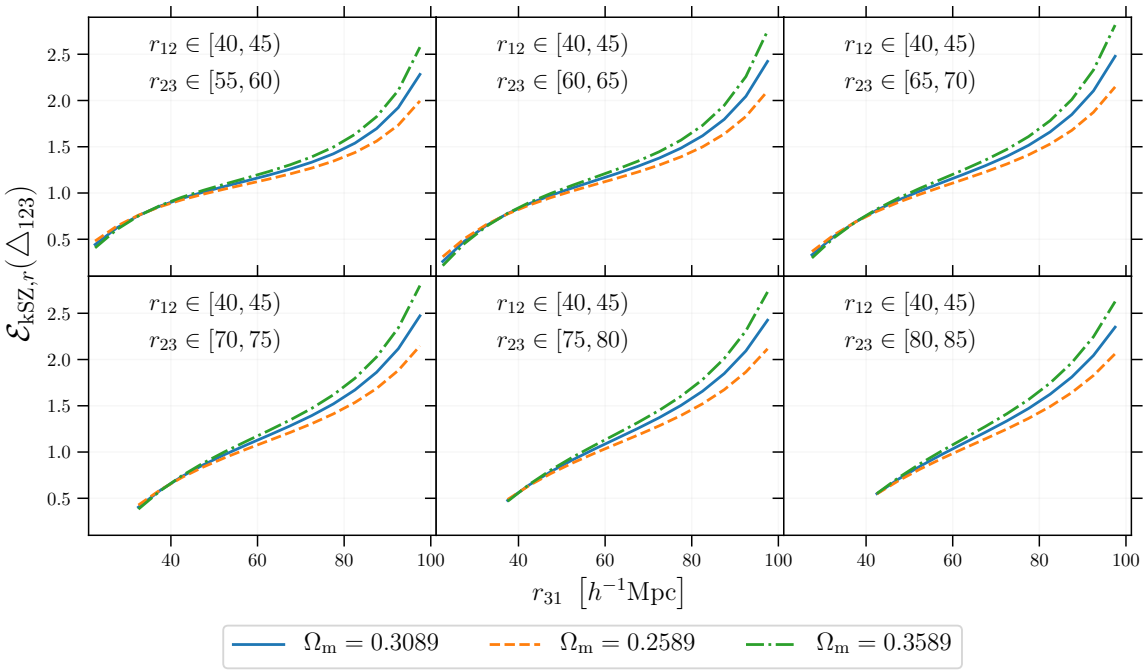

Figure 4.15: The impact of varying matter density in a flat Universe on the estimator $\mathcal{E}_{\mathrm{kSZ},r}$ where the other cosmological parameters are kept fixed. *Planck* is used as the reference cosmology which corresponds to the solid (blue) line. Triangular configurations are same as figure 4.14.

oscillation (BAO) information currently yields an upper limit on the neutrino mass sum of 0.12 eV, i.e $M_\nu < 0.12$ eV at 95% confidence level (Planck Collaboration, Aghanim et al., 2018). This is in agreement with the upper limit obtained from combining BOSS Lyα data with Planck CMB (Palanque-Delabrouille et al., 2015). At early epoch massive neutrinos are relativistic and act as radiation. Later they become non-relativistic and behave as an additional matter component. The energy density of the neutrino is given as

$$\Omega_\nu = \frac{\rho_\nu}{\rho_\mathrm{crit}} = \frac{16\zeta(3)T_\mathrm{cmb}^3}{11\pi H_0^2} M_\nu \simeq \frac{M_\nu}{93.14\, h^2\ \mathrm{eV}}\,, \tag{4.26}$$

where ζ is the Riemann zeta function and $\zeta(3) \simeq 1.202$, $M_\nu = \Sigma m_\nu$ is the sum of neutrino masses and $\Omega_\mathrm{m} = \Omega_\mathrm{cdm} + \Omega_\mathrm{b} + \Omega_\nu$. The impact of varying the sum of neutrino masses on the estimator $\mathcal{E}_{\mathrm{kSZ},r}$ is shown in figure 4.17, which turns out to be quite subtle. We considered three cases, where M_ν to be 0.06, 0.12 and 0.30 eV. A caveat is that in the case of changing the sum of neutrino mass, we let σ_8 value to vary, ensuring that the desired damping feature on small scales of the power spectrum is obtained. Among the two cases which are within current constraints ($M_\nu < 0.12$ eV), difference in the amplitude of the estimator prediction is minimal and hence it indicates that $\mathcal{E}_\mathrm{kSZ}$ may not be able to provide strong constraints on neutrino mass sum.

From figures 4.18 and 4.19 we can conclude that the estimator is insensitive to the equation-of-state parameter w and σ_8, in addition to f, b and optical depth τ. Thus this estimator is mostly sensitive to Ω_m and could provide competitive constraints from future CMB surveys like *SO*, *CMB-S4* and

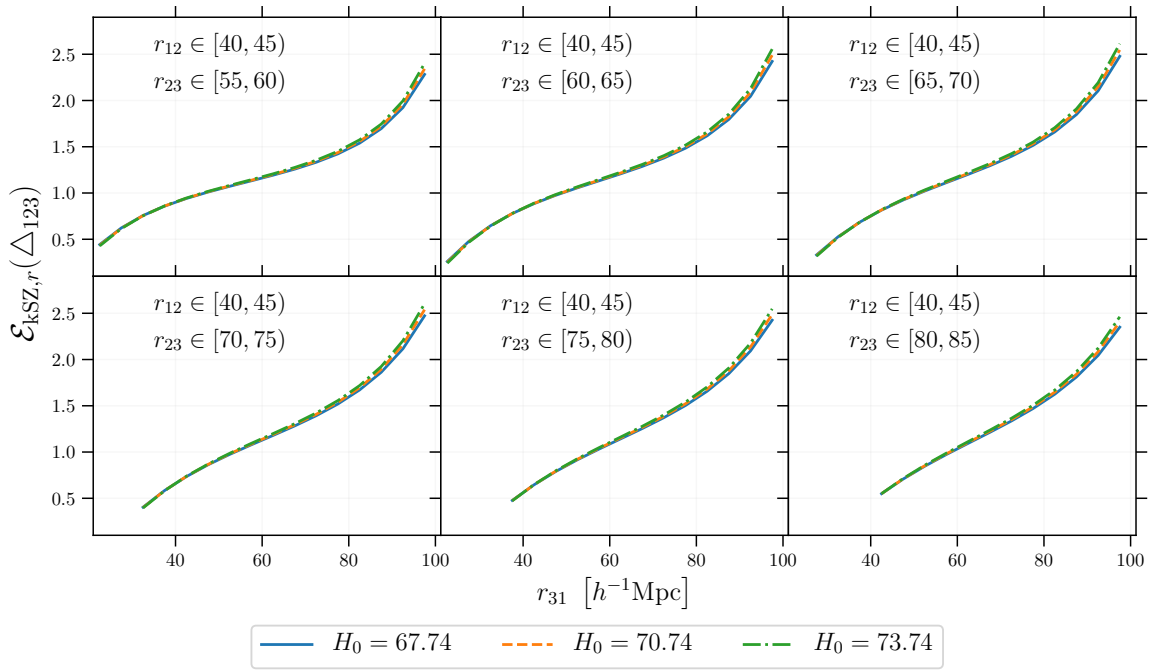

Figure 4.16: The impact of varying H_0 on the estimator $\mathcal{E}_{\mathrm{kSZ},r}$ where the other cosmological parameters are kept fixed. *Planck* is used as the reference cosmology which corresponds to the solid (blue) line. Triangular configurations are same as figure 4.14.

CMB-HD.

4.4.1 Measuring optical depth

kSZ provides a direct way to address the 'missing baryon problem' (which we have introduced in section 1.1.2) by being able to measure the mass dependent optical depth (Hernández-Monteagudo et al., 2015). We explore how triple-wise velocities might be able to tackle this problem. It can be shown that the mean triple-wise velocity from kSZ can be separated into astrophysics- and cosmology-dependent quantities

$$\langle w_{ij,r}(M, \triangle_{123})\rangle_{\mathrm{kSZ}} \propto \underbrace{\tau(M)\, b(M)}_{\text{astrophysics}} \underbrace{Hf\, \mathcal{I}_{ij}(\triangle_{123})}_{\text{cosmology}}, \tag{4.27}$$

where we have relaxed the assumption that the optical depth and biasing factor are independent of mass. The advantage of $\mathcal{E}_{\mathrm{kSZ},r}$ is that it is only affected by the cosmology-dependent quantity. So for the purpose of constraining cosmological information, this is an ideal way to go about it. Assuming we know the cosmological parameters from other probes like CMB, galaxy clustering among others, we can now pose the question of constraining the astrophysical information. Consider the case where we measure the mean triple-wise velocities in n mass bins, going from M_1 being the lowest mass bin to M_n being the highest mass bin. In such a scenario we can propose a new estimator to measure

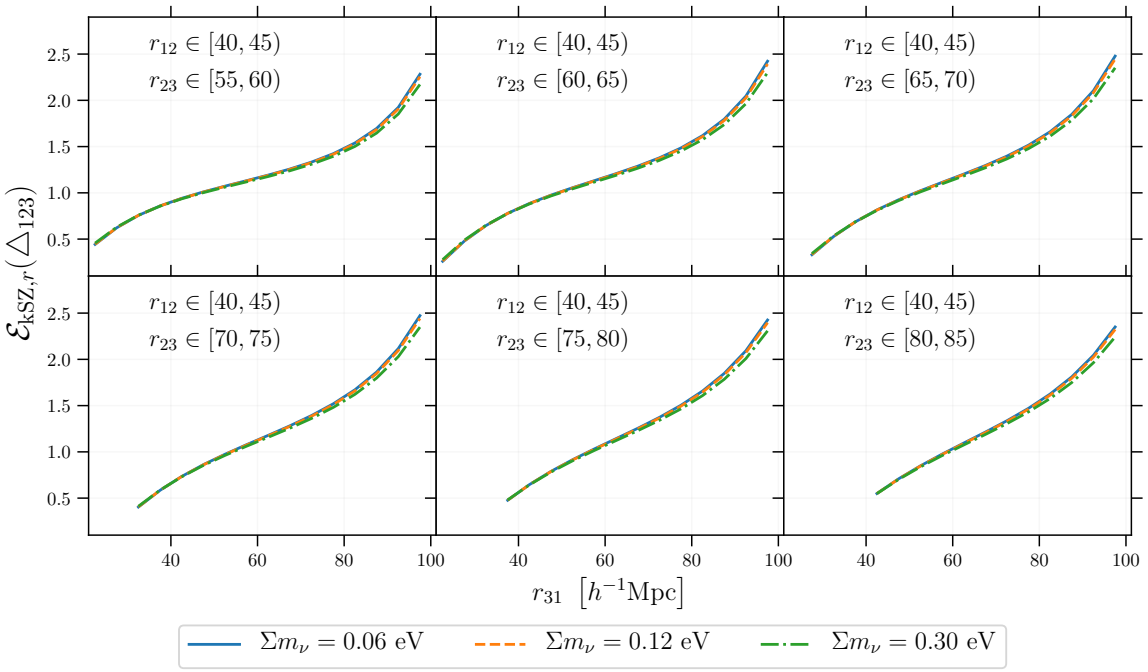

Figure 4.17: The impact of varying sum of neutrino masses on the estimator $\mathcal{E}_{\mathrm{kSZ},r}$. *Planck* is used as the reference cosmology which corresponds to the solid (blue) line. Triangular configurations are same as figure 4.14.

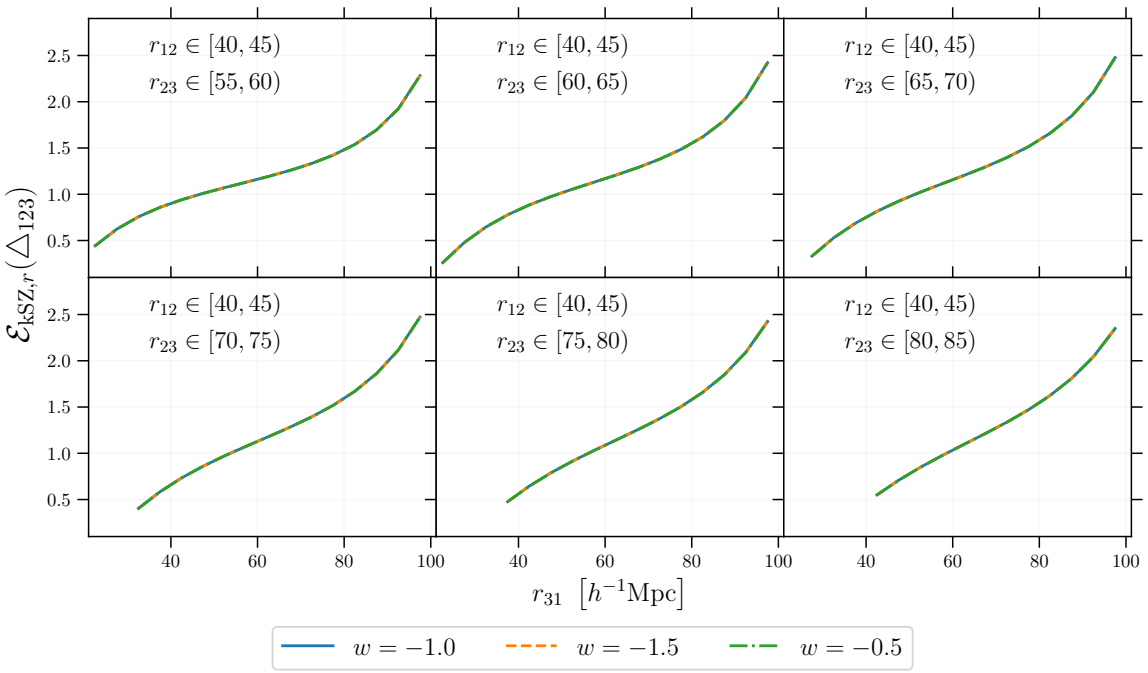

Figure 4.18: The impact of varying equation-of-state w on the estimator $\mathcal{E}_{\mathrm{kSZ},r}$. *Planck* is used as the reference cosmology which corresponds to the solid (blue) line. Triangular configurations are same as figure 4.14.

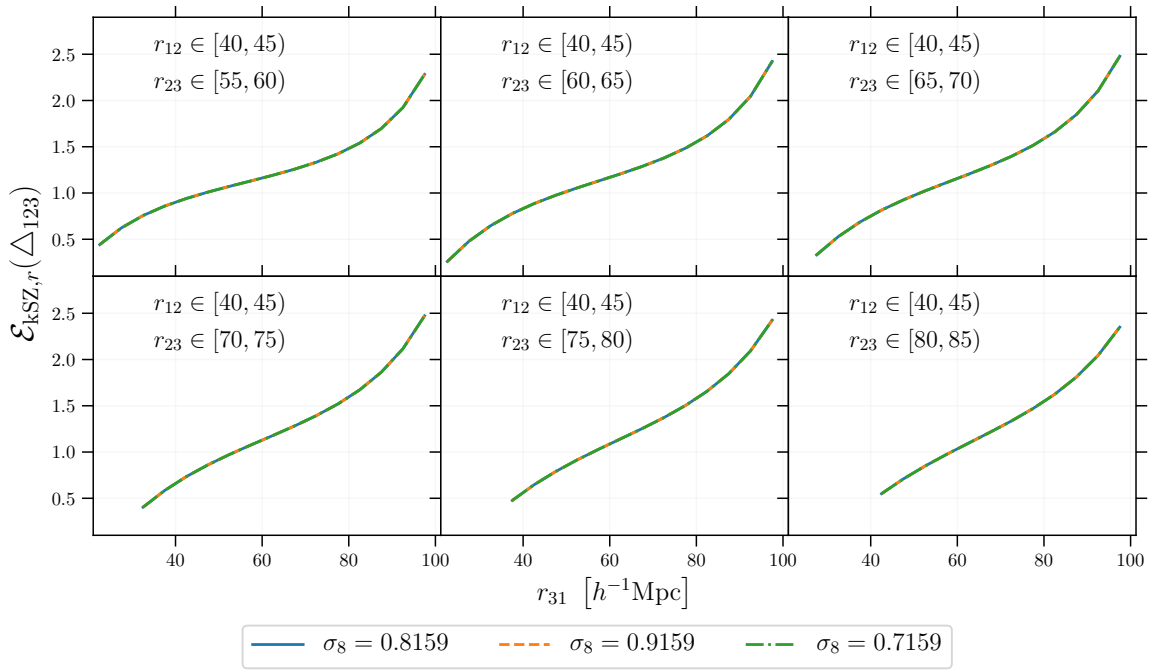

Figure 4.19: The impact of varying σ_8 on the estimator $\mathcal{E}_{\mathrm{kSZ},r}$. *Planck* is used as the reference cosmology which corresponds to the solid (blue) line. Triangular configurations are same as figure 4.14.

mass-dependent optical depth as

$$\mathcal{R}_{\mathrm{kSZ},r}\left(\frac{M_i}{M_n}, \triangle_{123}\right) = \frac{b(M_i)\,\tau(M_i)}{b(M_n)\,\tau(M_n)}\,\mathcal{E}_{\mathrm{kSZ},r}(\triangle_{123})\,, \tag{4.28}$$

where M_i stands for the i^{th} mass bin. The choice of having the mean triple-wise velocity for the pair 23 belonging to the highest mass bin in the denominator is specifically chosen because the optical depth and the biasing factor for the most massive galaxy clusters can be constrained independently from X-ray observations (e.g. Flender, Nagai and M. McDonald, 2017) and galaxy clustering respectively. Thus in the ideal case where we know the cosmological parameters perfectly (thus $\mathcal{E}_{\mathrm{kSZ},r}$ is known), we can map out the normalised optical depth as a function of the mass which will help in directly measuring the baryon content around the outskirts of galaxies or clusters and update the cosmic baryonic budget accordingly, which could address the 'missing baryon problem' atleast partially.. A caveat is that the normalised optical depth is completely degenerate with the mass-dependent bias factor.

4.5 Conclusions

Mean line-of-sight pairwise velocity has been used in recent times to provide evidence for the kinematic Sunyaev-Zeldovich (kSZ) effect. However since what is measured is in the redshift space, this implies that we need to study the pairwise distribution in the redshift space. Okumura et al., 2014 was among

one of the first to take a look into the mean pairwise velocity in the observed frame and showed that there is a sign inversion as one goes to the small scale. This was clearly detected in De Bernardis et al., 2017. To avoid the effects from RSD, Y.-C. Li et al., 2017 restricted their analysis to scales $> 20\,h^{-1}\mathrm{Mpc}$. In this chapter, we looked at the pairwise velocity distribution in redshift space from which the observed mean pairwise velocity quantity is derived. We show how on large scales, there is an equivalence between the real space and redshift space pairwise velocity distribution. However at the small scales, this no longer holds as the redshift space pairwise velocity is obtained as the integral of product real space pairwise velocity distribution with the 'RSD transformation' function. The 'RSD transformation' function at the small scales shows prominent bimodal features, which as a result propagates into the pairwise velocity in redshift space.

We also show the first four moments of this distribution for both 1D and 2D scale dependence in figures 4.4 and 4.5 respectively. At scales $< 40\,h^{-1}\mathrm{Mpc}$, the moments in general suggests a marked departure from their counterparts in real space. The linear theory formulation of the radial component of the mean pairwise velocity is given in equation (4.8). The analytical prediction shows good agreement with that measured from simulation only on scales above $\sim 80\ h^{-1}$ Mpc. We also checked how the redshift space pairwise PDF evolves with time. At earlier epochs, the amplitude of the second peak decreases signifying that the FoG effect and large relative velocities becomes more prominent at late times.

Furthermore, we introduce the redshift-space triple-wise velocity PDF in section 4.3. We express how one can obtain it as mixture PDF of triple-wise PDF in real space and the three-point RSD transformation function in equation (4.9). Similar to the case of pairwise PDF, one of the prominent feature on smaller triplet separations is the bimodality in the case of both the three-point RSD transformation and the redshift-space triple-wise PDF.

In section 4.4, we introduced a new estimator $\mathcal{E}_{\mathrm{kSZ}}$. It is defined by equation (4.22), which is not affected by the optical depth degeneracy that plagues the current pairwise kSZ measurements. Being a purely cosmology dependent estimator, we checked how it is affected by various cosmological parameters in figures 4.14 - 4.19. It seems to be mostly affected by the matter density in the Universe, while being completely independent of biasing factor b, effective optical depth τ, σ_8 and equation-of-state w. This is very advantageous as firstly we get rid of the need for modeling τ and b which are complex in nature, and secondly that the linear theory modeling of $\mathcal{E}_{\mathrm{kSZ}}$ works well at the scales we have checked.

In future work, we would like to quantify the informational gain from combining the two-point and three-point velocity statistics in redshift-space. This could help us in constraining dark energy and modified theories of gravity using the kSZ effect. Thus providing complementary constraints to the galaxy clustering or gravitational lensing probes. Another avenue would be to undertake a forecasting analysis to determine if the future measurements of $\mathcal{E}_{\mathrm{kSZ}}$ would be precise enough to give competitive constraints on the cosmological model when compared to other probes.

CHAPTER 5

Summary and outlook

Redshift-space distortions encode key clues about the formation of cosmological structure and the growth rate offers a key discriminant between cosmological models. For example, dark energy models (with general relativity as the theory of gravity) predict different large-scale structure formation compared to modified gravity models (e.g. Dvali, Gabadadze and Porrati, 2000; Carroll et al., 2004; Joyce, Lombriser and Schmidt, 2016). We have investigated the effects of redshift-space distortion on spatial clustering and velocity statistics in this thesis. It is clearly evident that the analytical modeling of correlation functions and velocity statistics in the redshift space accounting for non-linear effects is a challenging and complex task. We will now summarise our results and provide a short outlook on these topics.

Two-point correlation function

The two-point streaming model describes the mapping between real and redshift space for 2-point clustering statistics. Its key element is the probability density function (PDF) of line-of-sight pairwise peculiar velocities. Following a kinetic-theory approach, we derived the fundamental equations of the streaming model for ordered and unordered pairs as given in equations (2.14) and (2.22) respectively. In the first case, we recovered the classic equation while we demonstrated that modifications were necessary for unordered pairs. We then discussed several statistical properties of the pairwise velocities for DM particles and haloes by using a suite of high-resolution N-body simulations (see section 2.4). We tested the often used Gaussian ansatz for the PDF of pairwise velocities and discussed its limitations in section 2.3.4. Finally, we introduced a mixture of Gaussians which is known in statistics as the generalised hyperbolic distribution and show that it provides an accurate fit to the PDF (see figure 2.10). Once inserted in the streaming equation, the fit yielded an excellent description of redshift-space correlations at all scales that vastly outperformed the Gaussian and exponential approximations (see figure 2.12). Using a principal-component analysis, we reduced the complexity of our model for large redshift-space separations. Our results increase the robustness of studies of anisotropic galaxy clustering and are useful for extending them towards smaller scales in order to test theories of gravity and interacting dark-energy models.

Three-point correlation function

In chapter 3, we presented a generalised streaming model which describes the mapping between real and redshift space in configuration space for n-point clustering statistics using a kinetic-theory approach. One of the important quantities entering the n-point streaming model is the n-tuple wise velocity distribution. In particular we focused on the case where n = 3, to present the three-point streaming model and the triple-wise velocity distribution. We developed an analytical prediction for three-point velocity statistics from linear theory and showed that it achieves high fidelity when compared to N-body simulations. We also introduced the three-point Gaussian streaming model (3pt-GSM) which parameterised the triple-wise velocity distribution using a bivariate Gaussian where its mean and covariance matrix was predicted using the linear theory. We saw that the 3pt-GSM achieved high fidelity in modeling both complete and connected matter redshift-space correlation function at quasi-linear ($\gtrsim 30\,h^{-1}\mathrm{Mpc}$) scales onwards. With the phenomenological model we have introduced, it paves a way in which the higher order redshift-space correlation functions could be utilised to precisely test theories of gravity and interacting dark-energy models for future galaxy surveys like *Euclid*.

Pairwise and triple-wise velocity

Future CMB experiments like *SO*, *CMB-S4*, and *CMB-HD* would offer to be a competitive large-scale data by precisely characterising secondary anisotropies like kinetic Sunyaev-Zeldovich effect (K. M. Smith et al., 2018). The current evidence for the kSZ comes from the mean pairwise velocity in redshift space (e.g. Hand et al., 2012; Planck Collaboration, P. A. R. Ade et al., 2016; Schaan et al., 2016; Soergel et al., 2016; De Bernardis et al., 2017; Y.-C. Li et al., 2017). We studied the pairwise velocity distribution in the observer's frame and saw how it is affected by the redshift-space distortion effect. We explored how the bimodality of this pairwise distribution in small scales comes about from the two-point 'RSD transformation' distribution function. Further we computed the first four moments of this distribution in both one- and two-dimensions, and showed the stark difference they incur due to RSD at the small scales in comparison to the real space pairwise moments. The triple-wise velocity distribution in redshift space was introduced in section 4.3. Similar to the case of pairwise velocity PDF in redshift space, the triple-wise PDF also showcased bimodality. The linear theory prediction of mean and dispersion of triple-wise velocity was shown in section 4.3.1. The kSZ pairwise velocity measurements are plagued with the optical depth degeneracy. We developed an estimator which is devoid of this degeneracy and independent of astrophysical factors, thus has the potential to be a competitive cosmological probe. The estimator is well predicted by linear perturbation theory at triplet separations above 40 h^{-1} Mpc. We hope this would help us to constrain dark energy and modified gravity models from future CMB surveys using kSZ.

Outlook

In the next few years several redshift surveys like *Euclid*, *DESI*, *LSST*, and *WFIRST* will begin their operations. These surveys belonging to the 'stage IV' dark energy experiments are expected to bring atleast an order of magnitude in precision over existing surveys like SDSS. The modeling of redshift-space correlation function using the 'streaming model' framework for three-point statistics,

which we have developed in this thesis, could prove to be the basis for modeling configuration space clustering information and constraining cosmology from third order RSD statistics. We have tested this model on clustering information of dark matter particles. However to apply this model to galaxy redshift survey data, we require to incorporate biasing schemes. For three-point streaming model, our analytical prescriptions were developed from linear perturbation theory. For the cosmological inference, it will be advantageous to extend the streaming model towards non-linear scale by employing higher-order perturbation theories. In the distant future, it is expected that the proposed 'stage V' experiments like *DESI-2* and 'Billion Object Apparatus' (*BOA*) could improve the cosmological constraints by a factor of three over the 'stage IV' experiments (Dodelson et al., 2016). Thus, in the future, higher-order statistics will be able to play an important role in scientifically exploiting the forthcoming data from stage V surveys, in which the n-point streaming model could lead to be a prime framework for these clustering analyses.

Bibliography

Abazajian, K. N. et al. (2016), *CMB-S4 Science Book, First Edition*, ArXiv e-prints, arXiv: 1610.02743 (cit. on pp. 94, 104).

Abbott, T. M. C. et al. (2018), *Dark Energy Survey Year 1 Results: A Precise H_0 Estimate from DES Y1, BAO, and D/H Data*, Mon. Not. R. Astron. Soc. **480** 3879, arXiv: 1711.00403 [astro-ph.CO] (cit. on p. 114).

Abramowitz, M. and I. A. Stegun (1972), *Handbook of Mathematical Functions* (cit. on p. 41).

Adam, R. et al. (2017), *Mapping the kinetic Sunyaev-Zel'dovich effect toward MACS J0717.5+3745 with NIKA*, Astron. Astrophys. **598**, A115 A115, arXiv: 1606.07721 [astro-ph.CO] (cit. on p. 8).

Ade, P. et al. (2019), *The Simons Observatory: science goals and forecasts*, J. Cosmol. Astropart. Phys. **2019**, 056 056, arXiv: 1808.07445 [astro-ph.CO] (cit. on pp. 94, 104).

Agrawal, A. et al. (2017), *Generating Log-normal Mock Catalog of Galaxies in Redshift Space*, ArXiv e-prints, arXiv: 1706.09195 (cit. on p. 26).

Ahmad, Q. R. et al. (2001), *Measurement of the Rate of $\nu_e + d \rightarrow p + p + e^-$ Interactions Produced by ^8B Solar Neutrinos at the Sudbury Neutrino Observatory*, Phys. Rev. Lett. **87** (7) 071301, URL: https://link.aps.org/doi/10.1103/PhysRevLett.87.071301 (cit. on p. 115).

Ahn, M. H. et al. (2006), *Measurement of neutrino oscillation by the K2K experiment*, Phys. Rev. D **74** (7) 072003, URL: https://link.aps.org/doi/10.1103/PhysRevD.74.072003 (cit. on p. 115).

Alam, S., F. D. Albareti et al. (2015), *The Eleventh and Twelfth Data Releases of the Sloan Digital Sky Survey: Final Data from SDSS-III*, Astrophys. J. Suppl. Ser. **219**, 12 12, arXiv: 1501.00963 [astro-ph.IM] (cit. on p. 4).

Alam, S., S. Ho et al. (2015), *Testing general relativity with growth rate measurement from Sloan Digital Sky Survey - III. Baryon Oscillations Spectroscopic Survey galaxies*, Mon. Not. R. Astron. Soc. **453** 1754, arXiv: 1504.02100 (cit. on pp. 20, 31, 55).

Alonso, D. et al. (2016), *Reconstructing cosmic growth with kinetic Sunyaev-Zel'dovich observations in the era of stage IV experiments*, Phys. Rev. D. **94**, 043522 043522, arXiv: 1604.01382 (cit. on p. 98).

Amendola, L. et al. (2013), *Cosmology and Fundamental Physics with the Euclid Satellite*, Living Reviews in Relativity **16**, 6 6, arXiv: 1206.1225 (cit. on pp. 12, 56).

Aragón-Calvo, M. A. et al. (2010), *The Spine of the Cosmic Web*, Astrophys. J. **723** 364, arXiv: 0809.5104 [astro-ph] (cit. on p. 12).

Arnalte-Mur, P., W. A. Hellwing and P. Norberg (2017), *Real- and redshift-space halo clustering in f(R) cosmologies*, Mon. Not. R. Astron. Soc. **467** 1569, arXiv: 1612.02355 (cit. on p. 21).

Babcock, H. W. (1939), *The rotation of the Andromeda Nebula*, Lick Observatory Bulletin **19** 41 (cit. on p. 4).

Bagnold, R. (1941), *The Physics of Blown Sand and Desert Dunes*, Methuen (cit. on p. 42).

Barndorff-Nielsen, O. (1977), *Exponentially Decreasing Distributions for the Logarithm of Particle Size*, Proceedings of the Royal Society of London A: Mathematical, Physical and Engineering Sciences **353** 401, ISSN: 0080-4630, eprint: http://rspa.royalsocietypublishing.org/content/353/1674/401.full.pdf, URL: http://rspa.royalsocietypublishing.org/content/353/1674/401 (cit. on p. 43).

Barndorff-Nielsen, O. and P. Blaesild (1981), "Hyperbolic Distributions and Ramifications: Contributions to Theory and Application", *Statistical Distributions in Scientific Work: Volume 4 — Models, Structures, and Characterizations, Proceedings of the NATO Advanced Study Institute held at the Università degli Studi di Trieste, Trieste, Italy, July 10 – August 1, 1980*, ed. by C. Taillie, G. P. Patil and B. A. Baldessari, Springer Netherlands 19, ISBN: 978-94-009-8549-0, URL: https://doi.org/10.1007/978-94-009-8549-0_2 (cit. on p. 43).

Barndorff-Nielsen, O., J. Kent and M. Sorensen (1982), *Normal variance-mean mixtures and z distributions.*, English, Int. Stat. Rev. **50** 145, ISSN: 0306-7734; 1751-5823/e (cit. on p. 42).

Barreira, A., A. G. Sánchez and F. Schmidt (2016), *Validating estimates of the growth rate of structure with modified gravity simulations*, Phys. Rev. D. **94**, 084022 084022, arXiv: 1605.03965 (cit. on p. 21).

Barriga, J. and E. Gaztañaga (2002), *The three-point function in large-scale structure - I. The weakly non-linear regime in N-body simulations*, Mon. Not. R. Astron. Soc. **333** 443, eprint: astro-ph/0112278 (cit. on p. 85).

Battaglia, N. (2016), *The tau of galaxy clusters*, J. Cosmol. Astropart. Phys. **2016**, 058 058, arXiv: 1607.02442 [astro-ph.CO] (cit. on pp. 8, 114).

Bean, A. J. et al. (1983), *A complete galaxy redshift sample. I - The peculiar velocities between galaxy pairs and the mean mass density of the Universe*, Mon. Not. R. Astron. Soc. **205** 605 (cit. on pp. 20, 30, 56).

Behroozi, P. S., R. H. Wechsler and H.-Y. Wu (2013), *The ROCKSTAR Phase-space Temporal Halo Finder and the Velocity Offsets of Cluster Cores*, Astrophys. J. **762**, 109 109, arXiv: 1110.4372 [astro-ph.CO] (cit. on pp. 22, 114).

Beutler, F. et al. (2012), *The 6dF Galaxy Survey: z 0 measurements of the growth rate and σ_8*, Mon. Not. R. Astron. Soc. **423** 3430, arXiv: 1204.4725 (cit. on pp. 20, 91).

Bhattacharya, S. and A. Kosowsky (2008), *Dark energy constraints from galaxy cluster peculiar velocities*, Phys. Rev. D. **77**, 083004 083004, arXiv: 0712.0034 (cit. on p. 98).

Bianchi, D., M. Chiesa and L. Guzzo (2015), *Improving the modelling of redshift-space distortions - I. A bivariate Gaussian description for the galaxy pairwise velocity distributions*, Mon. Not. R. Astron. Soc. **446** 75, arXiv: 1407.4753 (cit. on pp. 20, 27, 32, 38, 39, 48, 55, 90, 95).

Bianchi, D., W. J. Percival and J. Bel (2016), *Improving the modelling of redshift-space distortions- II. A pairwise velocity model covering large and small scales*, Mon. Not. R. Astron. Soc. **463** 3783, arXiv: 1602.02780 (cit. on pp. 20, 32, 38, 40, 48, 55, 90, 95).

Bond, J. R., S. Cole et al. (1991), *Excursion set mass functions for hierarchical Gaussian fluctuations*, Astrophys. J. **379** 440 (cit. on p. 40).

Bond, J. R., L. Kofman and D. Pogosyan (1996), *How filaments of galaxies are woven into the cosmic web*, Nature **380** 603, arXiv: astro-ph/9512141 [astro-ph] (cit. on p. 12).

Bondi, H. and T. Gold (1948), *The Steady-State Theory of the Expanding Universe*, Mon. Not. R. Astron. Soc. **108** 252 (cit. on p. 6).

Borzyszkowski, M., D. Bertacca and C. Porciani (2017), *liger: mock relativistic light cones from Newtonian simulations*, Mon. Not. R. Astron. Soc. **471** 3899, arXiv: 1703.03407 (cit. on p. 19).
Buckley, M. R. and A. H. G. Peter (2018), *Gravitational probes of dark matter physics*, Phys. Rep. **761** 1, arXiv: 1712.06615 [astro-ph.CO] (cit. on p. 4).
Carlberg, R. G. (1994), *Velocity bias in clusters*, Astrophys. J. **433** 468, eprint: astro-ph/9404005 (cit. on p. 36).
Carlberg, R. G. and H. M. P. Couchman (1989), *Mergers and bias in a cold dark matter cosmology*, Astrophys. J. **340** 47 (cit. on p. 36).
Carlson, J., B. Reid and M. White (2013), *Convolution Lagrangian perturbation theory for biased tracers*, Mon. Not. R. Astron. Soc. **429** 1674, arXiv: 1209.0780 (cit. on pp. 20, 36, 55, 91, 95).
Carroll, S. M. et al. (2004), *Is cosmic speed-up due to new gravitational physics?*, Phys. Rev. D. **70**, 043528 043528, arXiv: astro-ph/0306438 [astro-ph] (cit. on p. 121).
Cautun, M. et al. (2014), *Evolution of the cosmic web*, Mon. Not. R. Astron. Soc. **441** 2923, arXiv: 1401.7866 [astro-ph.CO] (cit. on p. 12).
Cen, R. and J. P. Ostriker (1992), *Galaxy formation and physical bias*, Astrophys. J. Lett **399** L113 (cit. on p. 36).
Chhikara, R. S. and J. L. Folks (1989), *The Inverse Gaussian Distribution: Theory, Methodology, and Applications*, Marcel Dekker, Inc., ISBN: 0-8247-7997-5 (cit. on p. 41).
Chisari, N. E. and M. Zaldarriaga (2011), *Connection between Newtonian simulations and general relativity*, Phys. Rev. D. **83**, 123505 123505, arXiv: 1101.3555 [astro-ph.CO] (cit. on p. 11).
Chuang, C.-H., M. Pellejero-Ibanez et al. (2017), *The clustering of galaxies in the completed SDSS-III Baryon Oscillation Spectroscopic Survey: single-probe measurements from DR12 galaxy clustering – towards an accurate model*, Mon. Not. R. Astron. Soc. **471** 2370, arXiv: 1607.03151 (cit. on pp. 20, 31, 55).
Chuang, C.-H. and Y. Wang (2013), *Using multipoles of the correlation function to measure H(z), $D_A(z)$ and $\beta(z)$ from Sloan Digital Sky Survey luminous red galaxies*, Mon. Not. R. Astron. Soc. **431** 2634, arXiv: 1205.5573 (cit. on pp. 20, 91).
Chudaykin, A. and M. M. Ivanov (2019), *Measuring neutrino masses with large-scale structure: Euclid forecast with controlled theoretical error*, arXiv e-prints, arXiv: 1907.06666 [astro-ph.CO] (cit. on p. 56).
Clowe, D. et al. (2006), *A Direct Empirical Proof of the Existence of Dark Matter*, Astrophys. J. Lett **648** L109, arXiv: astro-ph/0608407 [astro-ph] (cit. on p. 4).
Colberg, J. M., K. S. Krughoff and A. J. Connolly (2005), *Intercluster filaments in a ΛCDM Universe*, Mon. Not. R. Astron. Soc. **359** 272, arXiv: astro-ph/0406665 [astro-ph] (cit. on p. 12).
Colıén, P., A. A. Klypin and A. V. Kravtsov (2000), *Velocity Bias in a Λ Cold Dark Matter Model*, Astrophys. J. **539** 561, eprint: astro-ph/9907337 (cit. on p. 36).
Couchman, H. M. P. and R. G. Carlberg (1992), *Large-scale structure in a low-bias universe*, Astrophys. J. **389** 453 (cit. on p. 36).
Cyburt, R. H. et al. (2016), *Big bang nucleosynthesis: Present status*, Rev. Mod. Phys. **88**, 015004 015004, arXiv: 1505.01076 (cit. on p. 6).
da Cunha, E. et al. (2017), *The Taipan Galaxy Survey: Scientific Goals and Observing Strategy*, Publ. Astron. Soc. Austral. **34**, e047 e047, arXiv: 1706.01246 [astro-ph.GA] (cit. on p. 95).
Danforth, C. W. and J. M. Shull (2008), *The Low-z Intergalactic Medium. III. H I and Metal Absorbers at $z < 0.4$*, Astrophys. J. **679** 194, arXiv: 0709.4030 (cit. on p. 4).

Davis, M. and P. J. E. Peebles (1977), *On the integration of the BBGKY equations for the development of strongly nonlinear clustering in an expanding universe*, Astrophys. J. Suppl. Ser. **34** 425 (cit. on p. 29).

– (1983), *A survey of galaxy redshifts. V - The two-point position and velocity correlations*, Astrophys. J. **267** 465 (cit. on pp. 19, 20, 30).

De Bernardis, F. et al. (2017), *Detection of the pairwise kinematic Sunyaev-Zel'dovich effect with BOSS DR11 and the Atacama Cosmology Telescope*, J. Cosmol. Astropart. Phys. **3**, 008 008, arXiv: 1607.02139 (cit. on pp. 8, 97, 120, 122).

Dodelson, S. et al. (2016), *Cosmic Visions Dark Energy: Science*, arXiv e-prints, arXiv:1604.07626 arXiv:1604.07626, arXiv: 1604.07626 [astro-ph.CO] (cit. on p. 123).

Dore, O. et al. (2014), *Cosmology with the SPHEREX All-Sky Spectral Survey*, arXiv e-prints, arXiv: 1412.4872 [astro-ph.CO] (cit. on p. 56).

Dvali, G., G. Gabadadze and M. Porrati (2000), *4D gravity on a brane in 5D Minkowski space*, Phys. Lett. B **485** 208, arXiv: hep-th/0005016 [hep-th] (cit. on p. 121).

Efstathiou, G., C. S. Frenk et al. (1988), *Gravitational clustering from scale-free initial conditions*, Mon. Not. R. Astron. Soc. **235** 715 (cit. on pp. 20, 27).

Efstathiou, G. and R. I. Jedrzejewski (1984), *Observational constraints on dark matter in the universe*, Advances in Space Research **3** 379 (cit. on p. 56).

Evrard, A. E., F. J. Summers and M. Davis (1994), *Two-fluid simulations of galaxy formation*, Astrophys. J. **422** 11 (cit. on p. 36).

Ferreira, P. G. et al. (1999), *Streaming Velocities as a Dynamical Estimator of* Ω, Astrophys. J. Lett **515** L1, eprint: astro-ph/9812456 (cit. on p. 97).

Fisher, K. B. (1995), *On the Validity of the Streaming Model for the Redshift-Space Correlation Function in the Linear Regime*, Astrophys. J. **448** 494, eprint: astro-ph/9412081 (cit. on pp. 19, 20, 23, 30, 55, 70, 98).

Fisher, K. B. et al. (1994), *Clustering in the 1.2-JY IRAS Galaxy Redshift Survey - Part Two - Redshift Distortions and Xi/r/p, PI*, Mon. Not. R. Astron. Soc. **267** 927, eprint: astro-ph/9308013 (cit. on pp. 19, 20, 27, 30).

Flender, S., D. Nagai and M. McDonald (2017), *Constraints on the Optical Depth of Galaxy Groups and Clusters*, Astrophys. J. **837**, 124 124, arXiv: 1610.08029 [astro-ph.CO] (cit. on p. 119).

Fosalba, P. et al. (2015), *The MICE grand challenge lightcone simulation - I. Dark matter clustering*, Mon. Not. R. Astron. Soc. **448** 2987, arXiv: 1312.1707 [astro-ph.CO] (cit. on p. 85).

Frieman, J. A. and E. Gaztanaga (1994), *The three-point function as a probe of models for large-scale structure*, Astrophys. J. **425** 392, eprint: astro-ph/9306018 (cit. on p. 56).

Fry, J. N. (1994), *Gravity, bias, and the galaxy three-point correlation function*, Phys. Rev. Lett. **73** 215 (cit. on p. 56).

Fukuda, Y. et al. (1998), *Evidence for Oscillation of Atmospheric Neutrinos*, Phys. Rev. Lett. **81** 1562, arXiv: hep-ex/9807003 [hep-ex] (cit. on p. 115).

Fukugita, M., C. J. Hogan and P. J. E. Peebles (1998), *The Cosmic Baryon Budget*, Astrophys. J. **503** 518, eprint: astro-ph/9712020 (cit. on p. 4).

Fukugita, M. and P. J. E. Peebles (2004), *The Cosmic Energy Inventory*, Astrophys. J. **616** 643, eprint: astro-ph/0406095 (cit. on p. 4).

Gaztañaga, E., A. Cabré et al. (2009), *Clustering of luminous red galaxies - III. Baryon acoustic peak in the three-point correlation*, Mon. Not. R. Astron. Soc. **399** 801, arXiv: 0807.2448 (cit. on p. 56).

Gaztañaga, E., P. Norberg et al. (2005), *Statistical analysis of galaxy surveys - II. The three-point galaxy correlation function measured from the 2dFGRS*, Mon. Not. R. Astron. Soc. **364** 620, eprint: astro-ph/0506249 (cit. on p. 56).
Gehrels, N. (1986), *Confidence limits for small numbers of events in astrophysical data*, Astrophys. J. **303** 336 (cit. on p. 45).
Gelb, J. M. and E. Bertschinger (1994), *Cold dark matter. 2: Spatial and velocity statistics*, Astrophys. J. **436** 491, eprint: astro-ph/9408029 (cit. on p. 36).
Giannantonio, T., C. Porciani et al. (2012), *Constraining primordial non-Gaussianity with future galaxy surveys*, Mon. Not. R. Astron. Soc. **422** 2854, arXiv: 1109.0958 [astro-ph.CO] (cit. on p. 19).
Giannantonio, T. and C. Porciani (2010), *Structure formation from non-Gaussian initial conditions: Multivariate biasing, statistics, and comparison with N-body simulations*, Phys. Rev. D. **81**, 063530 063530, arXiv: 0911.0017 [astro-ph.CO] (cit. on p. 56).
Gil-Marıén, H., J. Noreña et al. (2015), *The power spectrum and bispectrum of SDSS DR11 BOSS galaxies - I. Bias and gravity*, Mon. Not. R. Astron. Soc. **451** 539, arXiv: 1407.5668 [astro-ph.CO] (cit. on p. 56).
Gil-Marıén, H., W. J. Percival et al. (2017), *The clustering of galaxies in the SDSS-III Baryon Oscillation Spectroscopic Survey: RSD measurement from the power spectrum and bispectrum of the DR12 BOSS galaxies*, Mon. Not. R. Astron. Soc. **465** 1757, arXiv: 1606.00439 [astro-ph.CO] (cit. on p. 56).
Gil-Marıén, H., C. Wagner et al. (2012), *An improved fitting formula for the dark matter bispectrum*, J. Cosmol. Astropart. Phys. **2012**, 047 047, arXiv: 1111.4477 [astro-ph.CO] (cit. on p. 85).
Gorski, K. (1988), *On the pattern of perturbations of the Hubble flow*, Astrophys. J. Lett **332** L7 (cit. on p. 72).
Groth, E. J. and P. J. E. Peebles (1977), *Statistical analysis of catalogs of extragalactic objects. VII - Two- and three-point correlation functions for the high-resolution Shane-Wirtanen catalog of galaxies*, Astrophys. J. **217** 385 (cit. on p. 56).
Guo, H., C. Li et al. (2014), *Stellar Mass and Color Dependence of the Three-point Correlation Function of Galaxies in the Local Universe*, Astrophys. J. **780**, 139 139, arXiv: 1303.2609 (cit. on p. 56).
Guo, H., Z. Zheng et al. (2015), *Modelling the redshift-space three-point correlation function in SDSS-III*, Mon. Not. R. Astron. Soc. **449** L95, arXiv: 1409.7389 (cit. on p. 56).
Guth, A. H. (1981), *Inflationary universe: A possible solution to the horizon and flatness problems*, Phys. Rev. D. **23** 347 (cit. on p. 1).
Guzzo, L., M. Pierleoni et al. (2008), *A test of the nature of cosmic acceleration using galaxy redshift distortions*, Nature **451** 541, arXiv: 0802.1944 (cit. on pp. 19, 20, 91).
Guzzo, L., M. A. Strauss et al. (1997), *Redshift-Space Distortions and the Real-Space Clustering of Different Galaxy Types*, Astrophys. J. **489** 37, eprint: astro-ph/9706150 (cit. on p. 30).
Hahn, O. and T. Abel (2011), *Multi-scale initial conditions for cosmological simulations*, Mon. Not. R. Astron. Soc. **415** 2101, arXiv: 1103.6031 (cit. on p. 68).
Hale-Sutton, D. et al. (1989), *An extended galaxy redshift survey. II - Virial constraints on Omega0. III - Constraints on large-scale structure*, Mon. Not. R. Astron. Soc. **237** 569 (cit. on pp. 30, 56).
Hamilton, A. J. S. (1998), "Linear Redshift Distortions: a Review", *The Evolving Universe*, ed. by D. Hamilton, vol. 231, Astrophy. Space Sci. Lib. 185, eprint: astro-ph/9708102 (cit. on pp. 19, 22, 55, 57, 113).

Hammerstein, E. A. v. (2011), *Generalized hyperbolic distributions: theory and applications to CDO pricing*, type: Albert-Ludwigs-Universtät Freiburg, URL: https://freidok.uni-freiburg.de/data/7974 (cit. on p. 43).

Hand, N. et al. (2012), *Evidence of Galaxy Cluster Motions with the Kinematic Sunyaev-Zel'dovich Effect*, Phys. Rev. Lett. **109**, 041101 041101, arXiv: 1203.4219 (cit. on pp. 8, 97, 122).

Harrison, E. R. (1974), *Interpretation of Redshifts of Galaxies in Clusters*, Astrophys. J. Lett **191** L51 (cit. on p. 16).

Hashimoto, I., Y. Rasera and A. Taruya (2017), *Precision cosmology with redshift-space bispectrum: A perturbation theory based model at one-loop order*, Phys. Rev. D. **96**, 043526 043526, arXiv: 1705.02574 [astro-ph.CO] (cit. on p. 94).

Hawkins, E. et al. (2003), *The 2dF Galaxy Redshift Survey: correlation functions, peculiar velocities and the matter density of the Universe*, Mon. Not. R. Astron. Soc. **346** 78, eprint: astro-ph/0212375 (cit. on pp. 20, 91).

Hellwing, W. A. et al. (2014), *Clear and Measurable Signature of Modified Gravity in the Galaxy Velocity Field*, Phys. Rev. Lett. **112**, 221102 221102, arXiv: 1401.0706 (cit. on p. 21).

Hernández-Monteagudo, C. et al. (2015), *Evidence of the Missing Baryons from the Kinematic Sunyaev-Zeldovich Effect in Planck Data*, Phys. Rev. Lett. **115**, 191301 191301, arXiv: 1504.04011 [astro-ph.CO] (cit. on p. 117).

Hoffmann, K., J. Bel et al. (2015), *Measuring the growth of matter fluctuations with third-order galaxy correlations*, Mon. Not. R. Astron. Soc. **447** 1724, arXiv: 1403.1259 (cit. on p. 56).

Hoffmann, K., E. Gaztañaga et al. (2018), *Testing the consistency of three-point halo clustering in Fourier and configuration space*, Mon. Not. R. Astron. Soc. **476** 814, arXiv: 1708.08941 [astro-ph.CO] (cit. on p. 85).

Howlett, C., L. Staveley-Smith and C. Blake (2017), *Cosmological forecasts for combined and next-generation peculiar velocity surveys*, Mon. Not. R. Astron. Soc. **464** 2517, arXiv: 1609.08247 (cit. on p. 97).

Hoyle, F. (1948), *A New Model for the Expanding Universe*, Mon. Not. R. Astron. Soc. **108** 372 (cit. on p. 6).

Huang, K. (1987), *Statistical mechanics*, Wiley, 512 pp., ISBN: 9780471815181, URL: https://www.wiley.com/en-us/Statistical+Mechanics%2C+2nd+Edition-p-9780471815181 (cit. on p. 58).

Jackson, J. C. (1972), *A critique of Rees's theory of primordial gravitational radiation*, Mon. Not. R. Astron. Soc. **156** 1P, arXiv: 0810.3908 (cit. on pp. 17, 19, 55, 92).

Jennings, E. et al. (2012), *Redshift-space distortions in f(R) gravity*, Mon. Not. R. Astron. Soc. **425** 2128, arXiv: 1205.2698 [astro-ph.CO] (cit. on p. 21).

Jing, Y. P. and G. Börner (1997), *Three-point correlation function in the quasilinear regime.*, Astron. Astrophys. **318** 667, arXiv: astro-ph/9606122 [astro-ph] (cit. on pp. 83, 85).

– (1998), *The Three-Point Correlation Function of Galaxies Determined from the Las Campanas Redshift Survey*, Astrophys. J. **503** 37, eprint: astro-ph/9802011 (cit. on p. 56).

– (2004), *The Three-Point Correlation Function of Galaxies Determined from the Two-Degree Field Galaxy Redshift Survey*, Astrophys. J. **607** 140, eprint: astro-ph/0311585 (cit. on p. 56).

Jing, Y. P., G. Börner and Y. Suto (2002), *Spatial Correlation Functions and the Pairwise Peculiar Velocity Dispersion of Galaxies in the Point Source Catalog Redshift Survey: Implications for the Galaxy Biasing in Cold Dark Matter Models*, Astrophys. J. **564** 15, eprint: astro-ph/0104023 (cit. on p. 30).

Jørgensen, B. (1982), *Statistical Properties of the Generalized*, vol. 9, Lecture Notes in Statistics, Springer New York, ISBN: 978-0-387-90665-2, URL: https://link.springer.com/book/10.1007%2F978-1-4612-5698-4 (cit. on p. 41).

Joyce, A., L. Lombriser and F. Schmidt (2016), *Dark Energy Versus Modified Gravity*, Annu. Rev. Nucl. Part. Sci. **66** 95, arXiv: 1601.06133 [astro-ph.CO] (cit. on p. 121).

Juszkiewicz, R., K. B. Fisher and I. Szapudi (1998), *Skewed Exponential Pairwise Velocities from Gaussian Initial Conditions*, Astrophys. J. Lett **504** L1, eprint: astro-ph/9804277 (cit. on pp. 20, 29).

Jüttner, F. (1911), *Das Maxwellsche Gesetz der Geschwindigkeitsverteilung in der Relativtheorie*, Annalen der Physik **339** 856, ISSN: 1521-3889, URL: http://dx.doi.org/10.1002/andp.19113390503 (cit. on p. 43).

Kaiser, N. (1987), *Clustering in real space and in redshift space*, Mon. Not. R. Astron. Soc. **227** 1 (cit. on pp. 17, 19, 22, 55).

Karagiannis, D. et al. (2018), *Constraining primordial non-Gaussianity with bispectrum and power spectrum from upcoming optical and radio surveys*, Mon. Not. R. Astron. Soc. **478** 1341, arXiv: 1801.09280 [astro-ph.CO] (cit. on p. 56).

Kardar, M. (2007), *Statistical Physics of Particles*, Cambridge University Press, 330 pp., ISBN: 9780521873420, URL: http://www.cambridge.org/de/academic/subjects/physics/statistical-physics/statistical-physics-particles?format=HB&isbn=9780521873420 (cit. on p. 58).

Kayo, I. et al. (2004), *Three-Point Correlation Functions of SDSS Galaxies in Redshift Space: Morphology, Color, and Luminosity Dependence*, Publ. Astron. Soc. Jap. **56** 415, eprint: astro-ph/0403638 (cit. on p. 56).

Kazin, E. A., A. G. Sánchez and M. R. Blanton (2012), *Improving measurements of $H(z)$ and $D_A(z)$ by analysing clustering anisotropies*, Mon. Not. R. Astron. Soc. **419** 3223, arXiv: 1105.2037 [astro-ph.CO] (cit. on p. 82).

Keisler, R. and F. Schmidt (2013), *Prospects for Measuring the Relative Velocities of Galaxy Clusters in Photometric Surveys Using the Kinetic Sunyaev-Zel'dovich Effect*, Astrophys. J. Lett **765**, L32 L32, arXiv: 1211.0668 [astro-ph.CO] (cit. on p. 112).

Kepner, J. V., F. J. Summers and M. A. Strauss (1997), *A new statistic for redshift surveys: the redshift dispersion of galaxies*, New Astronomy **2** 165, eprint: astro-ph/9607097 (cit. on p. 38).

Koda, J. et al. (2014), *Are peculiar velocity surveys competitive as a cosmological probe?*, Mon. Not. R. Astron. Soc. **445** 4267, arXiv: 1312.1022 (cit. on p. 97).

Komatsu, E. et al. (2009), *Five-Year Wilkinson Microwave Anisotropy Probe Observations: Cosmological Interpretation*, Astrophys. J. Suppl. Ser. **180** 330, arXiv: 0803.0547 (cit. on pp. 15, 21, 98).

Kopp, M., C. Uhlemann and I. Achitouv (2016), *Gaussian streaming with the truncated Zel'dovich approximation*, Phys. Rev. D. **94**, 123522 123522, arXiv: 1606.02301 (cit. on p. 20).

Kragh, H. (2013), *Big Bang: the etymology of a name*, Astronomy and Geophysics **54** 2.28, ISSN: 1366-8781, URL: https://doi.org/10.1093/astrogeo/att035 (cit. on p. 6).

Kulkarni, G. V. et al. (2007), *The three-point correlation function of luminous red galaxies in the Sloan Digital Sky Survey*, Mon. Not. R. Astron. Soc. **378** 1196, eprint: astro-ph/0703340 (cit. on p. 56).

Kuruvilla, J. and C. Porciani (2018), *On the streaming model for redshift-space distortions*, Mon. Not. R. Astron. Soc., arXiv: 1710.09379 (cit. on pp. 55, 58, 59, 90, 95, 98, 102).

Kwan, J., G. F. Lewis and E. V. Linder (2012), *Mapping Growth and Gravity with Robust Redshift Space Distortions*, Astrophys. J. **748**, 78 78, arXiv: 1105.1194 (cit. on p. 20).

Larson, D. et al. (2011), *Seven-year Wilkinson Microwave Anisotropy Probe (WMAP) Observations: Power Spectra and WMAP-derived Parameters*, Astrophys. J. Suppl. Ser. **192**, 16 16, arXiv: 1001.4635 [astro-ph.CO] (cit. on pp. 4, 7).

Lesgourgues, J. and S. Pastor (2006), *Massive neutrinos and cosmology*, Phys. Rep. **429** 307, arXiv: astro-ph/0603494 [astro-ph] (cit. on p. 115).

Levi, M. et al. (2013), *The DESI Experiment, a whitepaper for Snowmass 2013*, ArXiv e-prints, arXiv: 1308.0847 [astro-ph.CO] (cit. on pp. 12, 56).

Lewis, A., A. Challinor and A. Lasenby (2000), *Efficient Computation of Cosmic Microwave Background Anisotropies in Closed Friedmann-Robertson-Walker Models*, Astrophys. J. **538** 473, eprint: astro-ph/9911177 (cit. on p. 68).

Lewis, A. D., D. A. Buote and J. T. Stocke (2003), *Chandra Observations of A2029: The Dark Matter Profile Down to below 0.01r_{vir} in an Unusually Relaxed Cluster*, Astrophys. J. **586** 135, arXiv: astro-ph/0209205 [astro-ph] (cit. on p. 4).

Li, C., Y. P. Jing, G. Kauffmann, G. Börner, X. Kang et al. (2007), *Luminosity dependence of the spatial and velocity distributions of galaxies: semi-analytic models versus the Sloan Digital Sky Survey*, Mon. Not. R. Astron. Soc. **376** 984, eprint: astro-ph/0701218 (cit. on p. 30).

Li, C., Y. P. Jing, G. Kauffmann, G. Börner, S. D. M. White et al. (2006), *The dependence of the pairwise velocity dispersion on galaxy properties*, Mon. Not. R. Astron. Soc. **368** 37, eprint: astro-ph/0509874 (cit. on p. 20).

Li, Y.-C. et al. (2017), *Measurement of the pairwise kinematic Sunyaev-Zeldovich effect with Planck and BOSS data*, ArXiv e-prints, arXiv: 1710.10876 (cit. on pp. 8, 97, 120, 122).

Libeskind, N. I. et al. (2018), *Tracing the cosmic web*, Mon. Not. R. Astron. Soc. **473** 1195, arXiv: 1705.03021 [astro-ph.CO] (cit. on p. 12).

Lin, J. (1991), *Divergence measures based on the Shannon entropy*, IEEE Trans. Inf. Theory **37** 145, ISSN: 0018-9448 (cit. on p. 81).

Linder, E. V. (2005), *Cosmic growth history and expansion history*, Phys. Rev. D. **72**, 043529 043529, arXiv: astro-ph/0507263 [astro-ph] (cit. on p. 11).

Loveday, J. et al. (1996), *The Stromlo-APM Redshift Survey. III. Redshift Space Distortions, Omega, and Bias*, Astrophys. J. **468** 1, eprint: astro-ph/9505099 (cit. on p. 30).

LSST Science Collaboration et al. (2009), *LSST Science Book, Version 2.0*, arXiv e-prints, arXiv: 0912.0201 [astro-ph.IM] (cit. on pp. 12, 56).

Ma, Y.-Z. and G.-B. Zhao (2014), *Dark energy imprints on the kinematic Sunyaev-Zel'dovich signal*, Physics Letters B **735** 402, arXiv: 1309.1163 (cit. on p. 98).

Madhavacheril, M. S. et al. (2019), *Cosmology with kSZ: breaking the optical depth degeneracy with Fast Radio Bursts*, arXiv e-prints, arXiv: 1901.02418 [astro-ph.CO] (cit. on p. 113).

Marıén, F. (2011), *The Large-scale Three-point Correlation Function of Sloan Digital Sky Survey Luminous Red Galaxies*, Astrophys. J. **737**, 97 97, arXiv: 1011.4530 (cit. on p. 56).

Marıén, F. A. et al. (2013), *The WiggleZ Dark Energy Survey: constraining galaxy bias and cosmic growth with three-point correlation functions*, Mon. Not. R. Astron. Soc. **432** 2654, arXiv: 1303.6644 (cit. on p. 56).

Marulli, F., M. Baldi and L. Moscardini (2012), *Clustering and redshift-space distortions in interacting dark energy cosmologies*, Mon. Not. R. Astron. Soc. **420** 2377, arXiv: 1110.3045 [astro-ph.CO] (cit. on p. 21).

Marzke, R. O. et al. (1995), *Pairwise Velocities of Galaxies in the CfA and SSRS2 Redshift Surveys*, Astronomical Journal **110** 477, eprint: astro-ph/9504070 (cit. on p. 30).
Matarrese, S., L. Verde and A. F. Heavens (1997), *Large-scale bias in the Universe: bispectrum method*, Mon. Not. R. Astron. Soc. **290** 651, eprint: astro-ph/9706059 (cit. on p. 56).
Mathews, G. J., M. Kusakabe and T. Kajino (2017), *Introduction to big bang nucleosynthesis and modern cosmology*, Int. J. Mod. Phys. E **26**, 1741001 1741001, arXiv: 1706.03138 (cit. on p. 6).
Matsubara, T. (2008), *Nonlinear perturbation theory with halo bias and redshift-space distortions via the Lagrangian picture*, Phys. Rev. D. **78**, 083519 083519, arXiv: 0807.1733 (cit. on p. 19).
Matsubara, T. (1994), *Peculiar Velocity Effect on Galaxy Correlation Functions in Nonlinear Clustering Regime*, Astrophys. J. **424** 30 (cit. on p. 93).
McBride, C. K. et al. (2011), *Three-point Correlation Functions of SDSS Galaxies: Luminosity and Color Dependence in Redshift and Projected Space*, Astrophys. J. **726**, 13 13, arXiv: 1007.2414 [astro-ph.CO] (cit. on p. 56).
McCullagh, N., D. Jeong and A. S. Szalay (2016), *Toward accurate modelling of the non-linear matter bispectrum: standard perturbation theory and transients from initial conditions*, Mon. Not. R. Astron. Soc. **455** 2945, arXiv: 1507.07824 [astro-ph.CO] (cit. on p. 85).
Mead, A. J. et al. (2016), *Accurate halo-model matter power spectra with dark energy, massive neutrinos and modified gravitational forces*, Mon. Not. R. Astron. Soc. **459** 1468, arXiv: 1602.02154 [astro-ph.CO] (cit. on p. 83).
Mo, H. J., Y. P. Jing and G. Borner (1993), *On the Pairwise Velocity Dispersion of Galaxies*, Mon. Not. R. Astron. Soc. **264** 825 (cit. on p. 30).
Moresco, M., F. Marulli, M. Baldi et al. (2014), *Disentangling interacting dark energy cosmologies with the three-point correlation function*, Mon. Not. R. Astron. Soc. **443** 2874, arXiv: 1312.4530 (cit. on p. 56).
Moresco, M., F. Marulli, L. Moscardini et al. (2017), *The VIMOS Public Extragalactic Redshift Survey (VIPERS) . Exploring the dependence of the three-point correlation function on stellar mass and luminosity at $0.5 < z < 1.1$*, Astron. Astrophys. **604**, A133 A133, arXiv: 1603.08924 [astro-ph.CO] (cit. on p. 56).
Mueller, E.-M. et al. (2015a), *Constraints on Gravity and Dark Energy from the Pairwise Kinematic Sunyaev-Zel'dovich Effect*, Astrophys. J. **808**, 47 47, arXiv: 1408.6248 (cit. on p. 98).
– (2015b), *Constraints on massive neutrinos from the pairwise kinematic Sunyaev-Zel'dovich effect*, Phys. Rev. D. **92**, 063501 063501, arXiv: 1412.0592 (cit. on p. 98).
Nichol, R. C. et al. (2006), *The effect of large-scale structure on the SDSS galaxy three-point correlation function*, Mon. Not. R. Astron. Soc. **368** 1507, eprint: astro-ph/0602548 (cit. on p. 56).
Okumura, T. et al. (2014), *Peculiar velocities in redshift space: formalism, N-body simulations and perturbation theory*, J. Cosmol. Astropart. Phys. **5**, 003 003, arXiv: 1312.4214 (cit. on pp. 98, 101, 119).
Palanque-Delabrouille, N. et al. (2015), *Neutrino masses and cosmology with Lyman-alpha forest power spectrum*, Journal of Cosmology and Astroparticle Physics **2015** 011, URL: https://doi.org/10.1088%2F1475-7516%2F2015%2F11%2F011 (cit. on p. 116).
Pandey, B. and S. Sarkar (2015), *Testing homogeneity in the Sloan Digital Sky Survey Data Release Twelve with Shannon entropy*, Mon. Not. R. Astron. Soc. **454** 2647, arXiv: 1507.03124 [astro-ph.CO] (cit. on p. 2).
Park, C. et al. (1994), *Power spectrum, correlation function, and tests for luminosity bias in the CfA redshift survey*, Astrophys. J. **431** 569 (cit. on pp. 20, 91).

Peacock, J. A. (1992), *Statistics of Cosmological Density Fields*, ed. by V. J. Martinez, M. Portilla and D. Saez, vol. 408 1 (cit. on p. 91).

Peacock, J. A., S. Cole et al. (2001), *A measurement of the cosmological mass density from clustering in the 2dF Galaxy Redshift Survey*, Nature **410** 169, eprint: astro-ph/0103143 (cit. on p. 19).

Peacock, J. A. and S. J. Dodds (1994), *Reconstructing the Linear Power Spectrum of Cosmological Mass Fluctuations*, Mon. Not. R. Astron. Soc. **267** 1020, eprint: astro-ph/9311057 (cit. on pp. 19, 20, 91).

Peacock, J. A. and M. J. West (1992), *The power spectrum of Abell cluster correlations*, Mon. Not. R. Astron. Soc. **259** 494 (cit. on pp. 20, 91).

Peebles, P. J. E. (1976), *A cosmic virial theorem*, Astrophy. Space Sci. **45** 3 (cit. on pp. 30, 40).

– (1979), *The mean mass density estimated from the Kirshner, Oemler, Schechter galaxy redshift sample*, Astronomical Journal **84** 730 (cit. on p. 30).

– (1980), *The large-scale structure of the universe*, Princeton Series in Physics, Princeton University Press, 422 pp. (cit. on pp. 13, 19, 23, 55, 56, 82, 98).

– (1981), *The mass of the universe*, Annals of the New York Academy of Sciences **375** 157 (cit. on p. 56).

– (1982), *Large-scale background temperature and mass fluctuations due to scale-invariant primeval perturbations*, Astrophys. J. Lett **263** L1 (cit. on p. 3).

– (2001), "The Galaxy and Mass N-Point Correlation Functions: a Blast from the Past", *Historical Development of Modern Cosmology*, ed. by V. J. Martıénez, V. Trimble and M. J. Pons-Borderıéa, vol. 252, Astronomical Society of the Pacific Conference Series 201, arXiv: astro-ph/0103040 [astro-ph] (cit. on p. 13).

Peebles, P. J. E. and E. J. Groth (1975), *Statistical analysis of catalogs of extragalactic objects. V - Three-point correlation function for the galaxy distribution in the Zwicky catalog*, Astrophys. J. **196** 1 (cit. on pp. 56, 82).

Perlmutter, S. et al. (1999), *Measurements of Ω and Λ from 42 High-Redshift Supernovae*, Astrophys. J. **517** 565, arXiv: astro-ph/9812133 [astro-ph] (cit. on p. 4).

Peter, A. H. G. (2012), *Dark Matter: A Brief Review*, arXiv e-prints, arXiv: 1201.3942 [astro-ph.CO] (cit. on p. 4).

Pillepich, A., C. Porciani and O. Hahn (2010), *Halo mass function and scale-dependent bias from N-body simulations with non-Gaussian initial conditions*, Mon. Not. R. Astron. Soc. **402** 191, arXiv: 0811.4176 (cit. on pp. 21, 22, 98).

Planck Collaboration, R. Adam et al. (2016), *Planck 2015 results. I. Overview of products and scientific results*, Astron. Astrophys. **594**, A1 A1, arXiv: 1502.01582 (cit. on pp. 22, 67).

Planck Collaboration, P. A. R. Ade et al. (2016), *Planck intermediate results. XXXVII. Evidence of unbound gas from the kinetic Sunyaev-Zeldovich effect*, Astron. Astrophys. **586**, A140 A140, arXiv: 1504.03339 (cit. on pp. 8, 97, 122).

Planck Collaboration, N. Aghanim et al. (2018), *Planck 2018 results. VI. Cosmological parameters*, arXiv e-prints, arXiv: 1807.06209 [astro-ph.CO] (cit. on pp. 114, 116).

Planck Collaboration, Y. Akrami et al. (2018), *Planck 2018 results. I. Overview and the cosmological legacy of Planck*, arXiv e-prints, arXiv: 1807.06205 [astro-ph.CO] (cit. on pp. 4, 7, 13, 15, 114).

Prause, K. (1999), *The Generalized Hyperbolic Model: Estimation, Financial Derivatives, and Risk Measures*, type: Albert-Ludwigs-Universtät Freiburg, URL: https://freidok.uni-freiburg.de/data/15 (cit. on p. 43).

Rao, C. (1987), *Differential Geometry in Statistical Inference*, IMS-Lectures Notes **10** 217 (cit. on p. 81).

Refregier, A. (2003), *Weak Gravitational Lensing by Large-Scale Structure*, Annu. Rev. Astron. Astrophys. **41** 645, arXiv: astro-ph/0307212 [astro-ph] (cit. on p. 4).

Reid, B. A., L. Samushia et al. (2012), *The clustering of galaxies in the SDSS-III Baryon Oscillation Spectroscopic Survey: measurements of the growth of structure and expansion rate at $z = 0.57$ from anisotropic clustering*, Mon. Not. R. Astron. Soc. **426** 2719, arXiv: 1203.6641 (cit. on pp. 20, 31, 55).

Reid, B. A. and M. White (2011), *Towards an accurate model of the redshift-space clustering of haloes in the quasi-linear regime*, Mon. Not. R. Astron. Soc. **417** 1913, arXiv: 1105.4165 (cit. on pp. 19, 20, 27, 29, 30, 40, 55, 76, 90, 95).

Riess, A. G., S. Casertano, W. Yuan, L. Macri et al. (2018), *Milky Way Cepheid Standards for Measuring Cosmic Distances and Application to Gaia DR2: Implications for the Hubble Constant*, Astrophys. J. **861**, 126 126, arXiv: 1804.10655 [astro-ph.CO] (cit. on p. 114).

Riess, A. G., S. Casertano, W. Yuan, L. M. Macri et al. (2019), *Large Magellanic Cloud Cepheid Standards Provide a 1% Foundation for the Determination of the Hubble Constant and Stronger Evidence for Physics beyond ΛCDM*, Astrophys. J. **876**, 85 85, arXiv: 1903.07603 [astro-ph.CO] (cit. on p. 114).

Riess, A. G., A. V. Filippenko et al. (1998), *Observational Evidence from Supernovae for an Accelerating Universe and a Cosmological Constant*, Astron. J. **116** 1009, arXiv: astro-ph/9805201 [astro-ph] (cit. on p. 4).

Riess, A. G., L. M. Macri et al. (2016), *A 2.4% Determination of the Local Value of the Hubble Constant*, Astrophys. J. **826**, 56 56, arXiv: 1604.01424 [astro-ph.CO] (cit. on p. 114).

Roncarelli, M., C. Carbone and L. Moscardini (2015), *The effect of massive neutrinos on the Sunyaev-Zel'dovich and X-ray observables of galaxy clusters*, Mon. Not. R. Astron. Soc. **447** 1761, arXiv: 1409.4285 (cit. on p. 115).

Ross, A. J., R. J. Brunner and A. D. Myers (2006), *Precision Measurements of Higher Order Angular Galaxy Correlations Using 11 Million SDSS Galaxies*, Astrophys. J. **649** 48, arXiv: astro-ph/0605748 [astro-ph] (cit. on p. 56).

Rostoker, N. and M. N. Rosenbluth (1960), *Test Particles in a Completely Ionized Plasma*, The Physics of Fluids **3** 1, eprint: https://aip.scitation.org/doi/pdf/10.1063/1.1705998 (cit. on p. 26).

Rubin, V. C. and W. K. Ford Jr. (1970), *Rotation of the Andromeda Nebula from a Spectroscopic Survey of Emission Regions*, Astrophys. J. **159** 379 (cit. on p. 4).

Rubin, V. C., W. K. Ford Jr. and N. Thonnard (1980), *Rotational properties of 21 SC galaxies with a large range of luminosities and radii, from NGC 4605 /R = 4kpc/ to UGC 2885 /R = 122 kpc/*, Astrophys. J. **238** 471 (cit. on p. 4).

Sabiu, C. G. et al. (2016), *Probing scalar tensor theories for gravity in redshift space*, Astron. Astrophys. **592**, A38 A38, arXiv: 1603.05750 (cit. on p. 21).

Samushia, L. et al. (2014), *The clustering of galaxies in the SDSS-III Baryon Oscillation Spectroscopic Survey: measuring growth rate and geometry with anisotropic clustering*, Mon. Not. R. Astron. Soc. **439** 3504, arXiv: 1312.4899 (cit. on pp. 20, 31, 55).

Sánchez, A. G. et al. (2013), *The clustering of galaxies in the SDSS-III Baryon Oscillation Spectroscopic Survey: cosmological constraints from the full shape of the clustering wedges*, Mon. Not. R. Astron. Soc. **433** 1202, arXiv: 1303.4396 [astro-ph.CO] (cit. on p. 82).

Sargent, W. L. W. and E. L. Turner (1977), *A statistical method for determining the cosmological density parameter from the redshifts of a complete sample of galaxies*, Astrophys. J. Lett **212** L3 (cit. on pp. 17, 19, 55, 92).

Sarkar, P. et al. (2009), *The scale of homogeneity of the galaxy distribution in SDSS DR6*, Mon. Not. R. Astron. Soc. **399** L128, arXiv: 0906.3431 [astro-ph.CO] (cit. on p. 2).

Satpathy, S. et al. (2017), *The clustering of galaxies in the completed SDSS-III Baryon Oscillation Spectroscopic Survey: on the measurement of growth rate using galaxy correlation functions*, Mon. Not. R. Astron. Soc. **469** 1369, arXiv: 1607.03148 (cit. on pp. 20, 31, 55).

Sayers, J. et al. (2013), *A Measurement of the Kinetic Sunyaev-Zel'dovich Signal Toward MACS J0717.5+3745*, Astrophys. J. **778**, 52 52, arXiv: 1312.3680 [astro-ph.CO] (cit. on p. 8).

Schaan, E. et al. (2016), *Evidence for the kinematic Sunyaev-Zel'dovich effect with the Atacama Cosmology Telescope and velocity reconstruction from the Baryon Oscillation Spectroscopic Survey*, Phys. Rev. D. **93**, 082002 082002, arXiv: 1510.06442 (cit. on pp. 8, 97, 122).

Schaller, M. et al. (2015), *The EAGLE simulations of galaxy formation: the importance of the hydrodynamics scheme*, Mon. Not. R. Astron. Soc. **454** 2277, arXiv: 1509.05056 [astro-ph.GA] (cit. on p. 12).

Schneider, P. (2005), *Weak Gravitational Lensing*, arXiv e-prints, astro-ph/0509252 astro, arXiv: astro-ph/0509252 [astro-ph] (cit. on p. 4).

Schrödinger, E. (1915), *Zur Theorie der Fall-und Steigversuche an Teilchen mit Brownscher Bewegung*, Physikalische Zeitschrift **16** 289 (cit. on p. 40).

Schumann, M. (2019), *Direct Detection of WIMP Dark Matter: Concepts and Status*, arXiv e-prints, arXiv: 1903.03026 [astro-ph.CO] (cit. on p. 3).

Scoccimarro, R. (2004), *Redshift-space distortions, pairwise velocities, and nonlinearities*, Phys. Rev. D. **70**, 083007 083007, eprint: astro-ph/0407214 (cit. on pp. 20, 23, 26, 27, 33, 66, 98).

Scoccimarro, R., H. M. P. Couchman and J. A. Frieman (1999), *The Bispectrum as a Signature of Gravitational Instability in Redshift Space*, Astrophys. J. **517** 531, eprint: astro-ph/9808305 (cit. on pp. 56, 78, 93).

Scoccimarro, R. and H. M. P. Couchman (2001), *A fitting formula for the non-linear evolution of the bispectrum*, Mon. Not. R. Astron. Soc. **325** 1312, arXiv: astro-ph/0009427 [astro-ph] (cit. on p. 85).

Scoccimarro, R., E. Sefusatti and M. Zaldarriaga (2004), *Probing primordial non-Gaussianity with large-scale structure*, Phys. Rev. D **69** (10) 103513, URL: https://link.aps.org/doi/10.1103/PhysRevD.69.103513 (cit. on p. 56).

Sefusatti, E., M. Crocce et al. (2006), *Cosmology and the bispectrum*, Phys. Rev. D. **74**, 023522 023522, eprint: astro-ph/0604505 (cit. on p. 56).

Sefusatti, E. and E. Komatsu (2007), *Bispectrum of galaxies from high-redshift galaxy surveys: Primordial non-Gaussianity and nonlinear galaxy bias*, Phys. Rev. D **76** (8) 083004, URL: https://link.aps.org/doi/10.1103/PhysRevD.76.083004 (cit. on p. 56).

Sehgal, N., S. Aiola et al. (2019), "CMB-HD: An Ultra-Deep, High-Resolution Millimeter-Wave Survey Over Half the Sky", vol. 51 6, arXiv: 1906.10134 [astro-ph.CO] (cit. on pp. 94, 104).

Sehgal, N., H. N. Nguyen et al. (2019), *Science from an Ultra-Deep, High-Resolution Millimeter-Wave Survey*, **51**, 43 43, arXiv: 1903.03263 [astro-ph.CO] (cit. on pp. 94, 104).

Seljak, U. and P. McDonald (2011), *Distribution function approach to redshift space distortions*, J. Cosmol. Astropart. Phys. **11**, 039 039, arXiv: 1109.1888 (cit. on p. 26).

Senatore, L. and M. Zaldarriaga (2014), *Redshift Space Distortions in the Effective Field Theory of Large Scale Structures*, ArXiv e-prints, arXiv: 1409.1225 (cit. on p. 19).
Seshadri, V. (1999), *The inverse Gaussian distribution: statistical theory and applications*, Lecture notes in statistics, Springer, ISBN: 9780387986180, URL: https://link.springer.com/book/10.1007%2F978-1-4612-1456-4 (cit. on p. 41).
Shepherd, C. W. et al. (1997), *The Real Space and Redshift Space Correlation Functions at Redshift z = 1/3*, Astrophys. J. **479** 82 (cit. on p. 30).
Sheth, R. K. (1996), *The distribution of pairwise peculiar velocities in the non-linear regime*, Mon. Not. R. Astron. Soc. **279** 1310, eprint: astro-ph/9511068 (cit. on pp. 20, 37, 38).
Sheth, R. K. and A. Diaferio (2001), *Peculiar velocities of galaxies and clusters*, Mon. Not. R. Astron. Soc. **322** 901, eprint: astro-ph/0009166 (cit. on pp. 20, 37, 38).
Shull, J. M., B. D. Smith and C. W. Danforth (2012), *The Baryon Census in a Multiphase Intergalactic Medium: 30% of the Baryons May Still be Missing*, Astrophys. J. **759**, 23 23, arXiv: 1112.2706 [astro-ph.CO] (cit. on p. 4).
Sichel, H. S. (1974), *On a distribution representing sentence-length in written prose*, Journal of the Royal Statistical Society, Series A 25 (cit. on p. 41).
Slepian, Z. and D. J. Eisenstein (2015), *Computing the three-point correlation function of galaxies in O(N^2) time*, Mon. Not. R. Astron. Soc. **454** 4142, arXiv: 1506.02040 (cit. on p. 82).
– (2017), *Modelling the large-scale redshift-space 3-point correlation function of galaxies*, Mon. Not. R. Astron. Soc. **469** 2059, arXiv: 1607.03109 (cit. on p. 56).
Slepian, Z., D. J. Eisenstein et al. (2017), *The large-scale three-point correlation function of the SDSS BOSS DR12 CMASS galaxies*, Mon. Not. R. Astron. Soc. **468** 1070 (cit. on p. 56).
Smith, K. M. et al. (2018), *KSZ tomography and the bispectrum*, arXiv e-prints, arXiv: 1810.13423 [astro-ph.CO] (cit. on p. 122).
Soergel, B. et al. (2016), *Detection of the kinematic Sunyaev-Zel'dovich effect with DES Year 1 and SPT*, Mon. Not. R. Astron. Soc. **461** 3172, arXiv: 1603.03904 (cit. on pp. 8, 97, 122).
Spergel, D. et al. (2013), *Wide-Field InfraRed Survey Telescope-Astrophysics Focused Telescope Assets WFIRST-AFTA Final Report*, arXiv e-prints, arXiv: 1305.5422 [astro-ph.IM] (cit. on p. 56).
Spergel, D. N. et al. (2007), *Three-Year Wilkinson Microwave Anisotropy Probe (WMAP) Observations: Implications for Cosmology*, Astrophys. J. Suppl. Ser. **170** 377, arXiv: astro-ph/0603449 [astro-ph] (cit. on p. 15).
Springel, V. (2005), *The cosmological simulation code GADGET-2*, Mon. Not. R. Astron. Soc. **364** 1105, eprint: astro-ph/0505010 (cit. on pp. 11, 21, 67, 98).
Springel, V., N. Yoshida and S. D. M. White (2001), *GADGET: a code for collisionless and gasdynamical cosmological simulations*, Nature **6** 79, eprint: astro-ph/0003162 (cit. on pp. 11, 21, 98).
Steigman, G. (2007), *Primordial Nucleosynthesis in the Precision Cosmology Era*, Ann. Rev. Nucl. Part. Sci. **57** 463, arXiv: 0712.1100 (cit. on p. 6).
Sugiyama, N. S., T. Okumura and D. N. Spergel (2016), *Understanding redshift space distortions in density-weighted peculiar velocity*, J. Cosmol. Astropart. Phys. **7**, 001 001, arXiv: 1509.08232 (cit. on p. 98).
– (2018), *A direct measure of free electron gas via the kinematic Sunyaev-Zel'dovich effect in Fourier-space analysis*, Mon. Not. R. Astron. Soc. **475** 3764, arXiv: 1705.07449 [astro-ph.CO] (cit. on p. 112).

Summers, F. J., M. Davis and A. E. Evrard (1995), *Galaxy Tracers and Velocity Bias*, Astrophys. J. **454** 1, eprint: astro-ph/9505080 (cit. on p. 36).

Sunyaev, R. A. and Y. B. Zeldovich (1970), *Small-Scale Fluctuations of Relic Radiation*, Astrophy. Space Sci. **7** 3 (cit. on pp. 8, 97).

– (1972), *The Observations of Relic Radiation as a Test of the Nature of X-Ray Radiation from the Clusters of Galaxies*, Comments on Astrophysics and Space Physics **4** 173 (cit. on pp. 8, 97).

– (1980), *The velocity of clusters of galaxies relative to the microwave background - The possibility of its measurement*, Mon. Not. R. Astron. Soc. **190** 413 (cit. on pp. 8, 97).

Szapudi, I. and A. S. Szalay (1998), *A New Class of Estimators for the N-Point Correlations*, Astrophys. J. Lett **494** L41 (cit. on p. 82).

Takada, M. et al. (2014), *Extragalactic science, cosmology, and Galactic archaeology with the Subaru Prime Focus Spectrograph*, Publ. Astron. Soc. Jap. **66**, R1 R1, arXiv: 1206.0737 [astro-ph.CO] (cit. on p. 56).

Takahashi, R. et al. (2019), *Fitting the nonlinear matter bispectrum by the Halofit approach*, arXiv e-prints, arXiv: 1911.07886 [astro-ph.CO] (cit. on p. 85).

Taruya, A., T. Nishimichi and F. Bernardeau (2013), *Precision modeling of redshift-space distortions from a multipoint propagator expansion*, Phys. Rev. D. **87**, 083509 083509, arXiv: 1301.3624 [astro-ph.CO] (cit. on p. 19).

Taruya, A., T. Nishimichi, F. Bernardeau et al. (2014), *Regularized cosmological power spectrum and correlation function in modified gravity models*, Phys. Rev. D. **90**, 123515 123515, arXiv: 1408.4232 (cit. on p. 21).

Taruya, A., T. Nishimichi, S. Saito et al. (2009), *Nonlinear evolution of baryon acoustic oscillations from improved perturbation theory in real and redshift spaces*, Phys. Rev. D. **80**, 123503 123503, arXiv: 0906.0507 [astro-ph.CO] (cit. on p. 19).

Tellarini, M. et al. (2016), *Galaxy bispectrum, primordial non-Gaussianity and redshift space distortions*, J. Cosmol. Astropart. Phys. **2016**, 014 014, arXiv: 1603.06814 [astro-ph.CO] (cit. on p. 56).

Tinker, J. L. (2007), *Redshift-space distortions with the halo occupation distribution - II. Analytic model*, Mon. Not. R. Astron. Soc. **374** 477, eprint: astro-ph/0604217 (cit. on pp. 20, 37, 38).

Tinker, J. L., D. H. Weinberg and Z. Zheng (2006), *Redshift-space distortions with the halo occupation distribution - I. Numerical simulations*, Mon. Not. R. Astron. Soc. **368** 85, eprint: astro-ph/0501029 (cit. on pp. 27, 38).

Tweedie, M. C. K. (1956), *Some statistical properties of Inverse Gaussian distribution*, Virginia Journal Science **7** 160 (cit. on p. 41).

Tyson, J. A., G. P. Kochanski and I. P. Dell'Antonio (1998), *Detailed Mass Map of CL 0024+1654 from Strong Lensing*, Astrophys. J. Lett **498** L107, arXiv: astro-ph/9801193 [astro-ph] (cit. on p. 4).

Uhlemann, C., M. Kopp and T. Haugg (2015), *Edgeworth streaming model for redshift space distortions*, Phys. Rev. D. **92**, 063004 063004, arXiv: 1503.08837 (cit. on pp. 21, 26, 32, 55, 76, 90, 95).

Vallois, P. (1991), *La loi gaussienne inverse genŕalise comme premier ou dernier temps de passage de diffusions*, Bull. Sc. Math. **115** (cit. on p. 41).

Verde, L., T. Treu and A. G. Riess (2019), *Tensions between the Early and the Late Universe*, arXiv e-prints, arXiv: 1907.10625 [astro-ph.CO] (cit. on p. 115).

Vlah, Z., E. Castorina and M. White (2016), *The Gaussian streaming model and convolution Lagrangian effective field theory*, J. Cosmol. Astropart. Phys. **12**, 007 007, arXiv: 1609.02908 (cit. on pp. 20, 31, 55, 91, 95).
Vlah, Z. and M. White (2019), *Exploring redshift-space distortions in large-scale structure*, J. Cosmol. Astropart. Phys. **2019**, 007 007, arXiv: 1812.02775 [astro-ph.CO] (cit. on pp. 66, 67).
Wang, L., B. Reid and M. White (2014), *An analytic model for redshift-space distortions*, Mon. Not. R. Astron. Soc. **437** 588, arXiv: 1306.1804 (cit. on pp. 20, 31, 32, 36, 76, 91).
Wang, Y. et al. (2004), *The three-point correlation function of galaxies: comparing halo occupation models with observations*, Mon. Not. R. Astron. Soc. **353** 287, eprint: astro-ph/0404143 (cit. on p. 56).
Weinberg, D. H. et al. (2013), *Observational probes of cosmic acceleration*, Phys. Rep. **530** 87, arXiv: 1201.2434 [astro-ph.CO] (cit. on p. 4).
White, M. (2014), *The Zel'dovich approximation*, Mon. Not. R. Astron. Soc. **439** 3630, arXiv: 1401.5466 (cit. on p. 20).
White, M., B. Reid et al. (2015), *Tests of redshift-space distortions models in configuration space for the analysis of the BOSS final data release*, Mon. Not. R. Astron. Soc. **447** 234, arXiv: 1408.5435 (cit. on p. 55).
White, M., Y.-S. Song and W. J. Percival (2009), *Forecasting cosmological constraints from redshift surveys*, Mon. Not. R. Astron. Soc. **397** 1348, arXiv: 0810.1518 (cit. on p. 19).
Wong, K. C. et al. (2019), *H0LiCOW XIII. A 2.4% measurement of H_0 from lensed quasars: 5.3σ tension between early and late-Universe probes*, arXiv e-prints, arXiv: 1907.04869 [astro-ph.CO] (cit. on p. 114).
Wong, Y. Y. Y. (2011), *Neutrino Mass in Cosmology: Status and Prospects*, Annual Review of Nuclear and Particle Science **61** 69, arXiv: 1111.1436 [astro-ph.CO] (cit. on p. 115).
Xu, L. (2015), *Constraints on f (R) gravity through the redshift space distortion*, Phys. Rev. D. **91**, 063008 063008, arXiv: 1411.4353 (cit. on p. 21).
Yadav, J. et al. (2005), *Testing homogeneity on large scales in the Sloan Digital Sky Survey Data Release One*, Mon. Not. R. Astron. Soc. **364** 601, arXiv: astro-ph/0504315 [astro-ph] (cit. on p. 2).
Yankelevich, V. and C. Porciani (2019), *Cosmological information in the redshift-space bispectrum*, Mon. Not. R. Astron. Soc. **483** 2078, arXiv: 1807.07076 (cit. on pp. 56, 59, 71, 76, 78, 83).
Yu, Y. (2011), *On Normal Variance-Mean Mixtures*, ArXiv e-prints, arXiv: 1106.2333 [math.ST] (cit. on p. 42).
Yvon, J. (1935), Actualites Sci. et Ind. **203** (cit. on pp. 24, 58).
Zehavi, I. et al. (2002), *Galaxy Clustering in Early Sloan Digital Sky Survey Redshift Data*, Astrophys. J. **571** 172, eprint: astro-ph/0106476 (cit. on p. 30).
Zennaro, M. et al. (2018), *Cosmological constraints from galaxy clustering in the presence of massive neutrinos*, Mon. Not. R. Astron. Soc. **477** 491, arXiv: 1712.02886 (cit. on p. 115).
Zu, Y. and D. H. Weinberg (2013), *The redshift-space cluster-galaxy cross-correlation function - I. Modelling galaxy infall on to Millennium simulation clusters and SDSS groups*, Mon. Not. R. Astron. Soc. **431** 3319, arXiv: 1211.1379 [astro-ph.CO] (cit. on p. 27).
Zu, Y., D. H. Weinberg et al. (2014), *Galaxy infall kinematics as a test of modified gravity*, Mon. Not. R. Astron. Soc. **445** 1885, arXiv: 1310.6768 (cit. on p. 21).
Zurek, W. H. et al. (1994), *Large-scale structure after COBE: Peculiar velocities and correlations of cold dark matter halos*, Astrophys. J. **431** 559 (cit. on pp. 27, 30).

Zwicky, F. (1933), *Die Rotverschiebung von extragalaktischen Nebeln*, Helvetica Physica Acta **6** 110 (cit. on p. 3).

List of Figures

List of Tables